UNDERSTANDING HIGH SPEED MIXING LAYERS WITH LES AND EVOLUTION OF URANS MODELING

A Thesis

Submitted for the degree of

Doctorate of Philosophy

In the Faculty of Engineering

by

IYER ARVIND SUNDARAM

Combustion Gassification and Propulsion Laboratory
Department of Aerospace Engineering
Indian Institute of Science
BANGALORE - 560012

AUGUST 2013

I dedicate this work to my parents for their support and blessings, my wife for her support, my brother for his joyful company and my wonderful teachers by whose grace I was able to complete this work

Acknowledgements

I must pay respects first to Late. Prof. P. J. Paul, who in the first seven years guided me, with a wealth of deep knowledge, clear mindedness and kindness. Prof. Paul gave limitless freedom in exploring the choice of methods to solve the problem, and time to learn the tools required for the same. Without the patience that he showed, it would have been impossible for me to master most of the tools used in this work. Prof. Paul was a man of soft words never raised his voice, and the I still remember the strongest words were "Hello sir! Where have you been?", and this was when I was struggling for three months trying to make OpenFOAM work with IBM-BlueGene supercomputer, without reporting.

The passing away of Prof. Paul was extremely unfortunate, a jolt which left his students direction less. At this difficult time Prof H.S. Mukunda, who almost adopted all of Prof PJP's students, and guided them, and made sure they sail through their course. Dr. Rajan at the same time lent a extremely supporting hand. Perhaps without them I would have discontinued my doctoral work after the passing away of Prof. Paul. I am thankful to God who got me associated with Prof. Paul, Dr. Rajan and Prof Mukunda, I bow down in respect to you, this association has been and will always be the highlight of my life.

I must thank all my colleagues. I had the privilege of debating out several issues with Abhishek Bhat, who has been a close friend of mine since 15 years. I thank Varun Shivakumar, Anand Shivapuji, Ashutosh Sharma who all participated in discussions which helped clear my understanding of various subjects.

Thanks are are due to my parents for their blessings, prayers, and their bring up, which had got me enthusiastic in science since a very young age. Special thanks to my father for helping in improving the readability of the thesis. I must thank my wife for enduring the long duration of the PhD and supporting me all through. I thank my brother who has been a very joyful company which helped keep my spirits high, and also for helping out in proof-reading and corrections.

Abstract

This thesis is concerned with studies on spatially developing high speed mixing layers with twin objectives: (a) to provide enhanced and detailed understanding of spatial development of two-dimensional mixing layer emanating from splitter plate through large eddy simulation (LES, from now on) technique and (b) to evolve a consistent strategy for Unsteady Reynolds Averaged Navier-Stokes (URANS) approach to mixing layer calculations.

The inspiration for this work arose out of the explanations that were being developed for the reduction in the mixing layer thickness with compressibility (measured by a parameter called convective Mach number, M_c). The reasons centered around increased stability, increase in compressible dissipation that was later discounted in favor of reduction in production and pressure-strain terms (with M_c, of course). These were obtained with direct numerical simulations (DNS) or LES techniques with homogeneous shear flow or temporal mixing layer. As apart, there was also a wide held view that using RANS (steady) techniques did not capture the compressibility effects when used in a way described above and so classical industrial codes for computing mixing-layer-embedded flows are unsuitable for such applications.

Other important aspects that come out of the examination of literature are: the mixing layer growth is controlled in the initial stages by the double-boundary layer profile over the splitter plate and results in the mixing layer growth that is somewhat irregular due to doubling and merging of vortical structures. The view point of a smooth growth of the mixing layer is a theoretical approximation arising out of the use of a smooth tan-hyperbolic profile that results at larger distances from the splitter plate. For all practical applications, it is inferred that the initial development is what is important because the processes of ignition and stable combustion occur close to the splitter plate. For these reasons, it was thought that understanding the development of the mixing layer is best dealt with using accurate spatial simulation with the appropriate initial profile.

The LES technique used here is drawn from an OpenFOAM approach

for dissimilar gases and uses one-equation Eddy Model for SGS stresses. The temporal discretization is second order accurate backward Euler and spatial discretization is fourth order least squares; the algorithm used for solving the equations is PISO and the parallelized code uses domain decomposition approach to cover large spatial domain.

The calculations are performed with boundary layer profiles over the splitter plate and an initial velocity field with white noise-like fluctuations to simulate the turbulence as in the experiments. Grid independence studies are performed and several experimental cases are considered for comparison with measured data on the velocity and temperature fields as well as turbulent statistics. These comparisons are excellent for the mean field behavior and moderately acceptable for turbulent kinetic energy and shear stress.

To further benefit from the LES approach, the details of the mixing layer are calculated as a function of four independent parameters on which the growth depends: convective Mach number ($M_c = (U_1 - U_2)/(a_1 + a_2)$), stream speed ratio ($r = U_2/U_1$), stream density ratio ($s = \rho_2/\rho_1$) and the average velocity of the two streams ($(U_1+U_2)/2$) and examine the various terms in the equations to enable answering the questions discussed earlier. It is uncovered that r has significant influence on the attainment of self similarity (which also implies on the rate of removal of velocity defect in the double-boundary layer profile) and other parameters have a very weak influence. The minimum velocity variation with distance from the splitter plate has the $1/\sqrt{\text{axial distance}}$ behavior like in wakes; however, after a distance, departure to linear rise occurs and the distance it takes for this to appear is delayed with M_c. Other features such as the coherent structures, their merger or break up, the area of the structures, convective velocity information extraction from the coherent structures, the behavior of the pressure field in the mixing layer through the field are elucidated in detail; the behavior of the correlations between parameters (like pressure, velocity etc) at different points is used to elucidate the coherence of their fluctuating field. The effects of the parameters on the energy spectra have expected trends.

An examination of the kinetic energy budget terms reveals that

- The production term is the main source of the xx turbulence stress, whereas it is not significant in the yy component.

- A substantial portion of this is carried by the pressure-velocity coupling from the xx direction to the yy direction, which becomes the main source term in the yy component.

- Both, the production term as well as the pressure-velocity term show a clear decrease with increase in M_c

The high point of the thesis is related to using the understanding derived from an analysis of various source terms in the kinetic energy balance to evolve an unsteady Reynolds Averaged Navier Stokes (URANS) model for calculating high speed mixing layers, a subject that has eluded international research till now. It recognizes that the key feature affected by compressibility is related to the anisotropy of the stress tensor. The relationship between stress component (τ_{xy}) and the velocity gradient (S_{xy}) as obtained from LES is set out in the form of a simple relationship accounting for the effects of other parameters obtained earlier in this thesis. A minor influence due to τ_{yy} is extracted by describing its dependence on S_{xy} again as gleaned from LES studies. The needed variation of Prandtl and Schmidt numbers through the field is extracted. While the detailed variations can in fact be taken into account in URANS simulations, a simple assumption of these values being around 0.3 is chosen for the present simulations of URANS. Introduction of these features into the momentum equation gives the much expected variation of the reduction in the growth rate of the mixing layer with convective Mach number as in experiments. The relationships that can be used in high speed mixing layers are

$$\frac{\tau_{xy}}{\bar{\rho}(\Delta U)^2} = \frac{S_{xy}}{(\Delta U)/x}\left(0.00294e^{(-6.756M_c)}\right)$$

$$\frac{\tau_{yy}}{\rho(\Delta U)^2} = 0.02 + \frac{0.03}{\left(\dfrac{M_c+0.01}{0.25}\right)^2}\left(S^2(S+0.4)^2\right)^{0.125} \pm 0.01\left(S^2 - S^4\right)^{0.125}$$

Where, $S = \dfrac{S_{xy}}{30((\Delta U)/x)}$, $\bar{\rho}$ is the average density, and x the stream-wise distance from the splitter plate.

Introduction of these features into the momentum equation gives the much expected variation of the reduction in the growth rate of the mixing layer with convective Mach number as in experiments. This is then a suggested new approach to solve high speed mixing layers.

While it can be thought that the principal contributions of the thesis are complete here, an additional segment is presented related to entropy view of the mixing layer. This study that considers the mixing layer with two different species expresses various terms involved in the entropy conservation equation and obtains the contribution of various terms on the entropy change for various M_c. It is first verified that the entropy derived from the conservation equation matches with those calculated from fluid properties, entropy being a state variable. It is shown that irreversible diffusion comes down the most with convective Mach number.

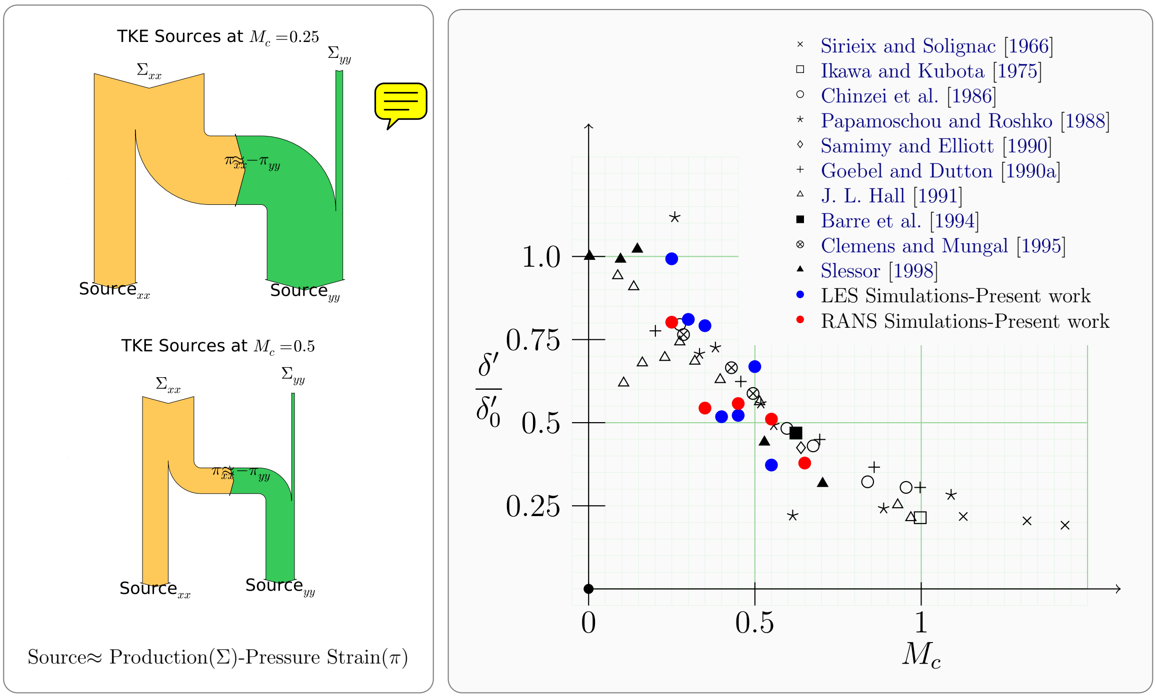

Left: This image shows pictorially the flow of source of turbulent stress from the axial to the cross wise turbulent stress. Production (Σ) of turbulence happens mainly in the xx direction, a part of it is carried by the pressure-velocity correlation to the yy direction, which itself has a low production. With increasing M_c, both the production as well as the pressure-velocity correlation decrease.
Right: This image shows the growth rate obtained from simulations scaled with the incompressible growth rate, of LES and RANS in the background of experiments (others). As is clear, the growth rate obtained is well within the band of experimental results.

Contents

List of Figures

List Of Symbols

Table 1: List of Symbols, Abbreviations and Conventions

Symbol	Meaning
Directions	
x	Distance from the splitter plate along the stream-wise direction
y	Distance from the splitter plate along the cross-wise direction
z	Distance from the splitter plate along the span-wise direction
η	Scaled cross-wise distance (y normalized with δ)
Subscripts	
$(\cdot)_1$	Primary Stream
$(\cdot)_2$	Secondary Stream
$(\cdot)_c$	Convective (eg. U_c, M_c)
$(\cdot)_{,i}$	Tensor notation derivative with respect to direction i
Operators	
$\langle\cdot\rangle$	Ensemble average
$\cdot'$	Fluctuating component after removal of average
$\{\cdot\}$	Favre average (density weighted average)
$\cdot''$	Fluctuating component after removal of Favre average
Symbols	
t	Time
p	Pressure
T	Temperature
ρ	Density
U	Velocity
h	Enthalpy
h	Internal energy
Y_a	Mass fraction of species a
s	Entropy
U_{avg}	Average velocity $(U_1 + U_2)/2$

Continued on next page

Table 1 – *Continued from previous page*

Symbol	Meaning
r	Velocity ratio U_2/U_1
s	Density ratio ρ_2/ρ_1
M_c	Convective Mach Number $(U_1 - U_2)/(a_1 + a_2)$
γ	Ratio of specific heats
μ	Viscosity of the fluid
δ	The width of the mixing layer
θ	The momentum thickness of the mixing layer
δ'	Growth rate:variation of δ wrt x,
δ'_0	Incompressible growth rate
ΔU	Difference in the velocities of the two streams
a	Speed of sound
M	Mach number
S	Strain rate tensor
R	Velocity correlation tensor
τ	Turbulent shear stress tensor
ν_{sgs}	Sub-grid scale viscosity
Σ	Production tensor
π	Pressure velocity correlation tensor
Non dimensional numbers	
Re	Reynolds number
Pr	Prandtl number
Sc	Schmidt number
Le	Lewis number
St	Strouhal number
$\mathrm{Pr_t}$	Turbulent Prandtl number
$\mathrm{Sc_t}$	Turbulent Schmidt number
$\mathrm{Le_t}$	Turbulent Lewis number

Part I

Background and Setup

Chapter 1

Introduction

1.1 Background

Nearly all civilian air travel over the last five decades has occurred at speeds just below the speed of sound. The essential idea is to enable as high a speed as possible with minimal overheads on fuel efficiency. Improving the benefits perceived of air travel has occurred over the last several decades through innovation in propulsion. This has resulted in the evolution of turbofan engines with high bypass ratio to reduce the specific fuel consumption while ensuring that the travel speeds are not compromised. The limitation for this travel speed comes from the fact that the aircraft experiences sharp increase in drag due to compressibility effects in which sonic speeds occur over parts of the wing (the coefficient of drag increases sharply through sonic speed).

An exceptional effort made in an Anglo-French effort resulted in Concorde aircraft that would fly at twice the speed of sound (Mach number, M of 2) at extremely high altitudes (20 km) to reduce drag influences as well as undesirable effects of shockwaves on the ground, called sonic bang. The aim of this effort was to cut-down by half the trans-atlantic air travel time of 6 to 7 hours by airliners currently in vogue. This provided attraction to business executives in the initial stage. However, the operations became expensive and the fare considered exhorbitant by most travellers. The primary reason for such an eventuality is that the fuel consumption at supersonic speeds turns out to be double of that at subsonic speeds. This aircraft operated commercially in such a weak mode for several years that the operations were finally shut down.

An alternate thinking emerged in the early eighties in the USA. Moving from 900 km/h (the high subsonic speeds of civil airliners today) to 1800 km/h (Concorde) appeared a small gain for whatever problems the fuel consumption posed. Would it be possible to increase the civilian air travel speed to 12000 km/h ($M \sim 15$)? If this proved difficult, at least to 8000 km/h ($M \sim 10$)? This led NASA to conceive of a project called National Aerospace Plane (NASP). The project was politically "sold" as an exciting new technological approach to ensure New York-to-Tokyo travel in less than two and a half hours. The propulsion system in this approach works vastly differently from those of subsonic aircraft.

In gas turbine combustion chamber (in a turbofan), the fuel is injected into an air stream at highly subsonic conditions. The airstream is at a M of 0.2 generally, 0.3 at most and a temperature of 450 to 500 K and a pressure of 10 to 30 atm (the compressor pressure ratios have improved over years from 20 to 40). All the heat released by combustion goes to raise the temperature of the gases to 1700 to 1900 K and the hot gases move on to run the turbine.

In the case of NASP design, the flight Mach numbers of the order of 10 to 15 (more optimally close to 10) at extremely high altitudes (of 30 km and above where the ambient pressures are less than 0.01 atm and static temperatures of 220 K), the exit conditions achieved after flow diffusion from hypersonic flight speeds through a suitably designed air intake are at $M = 2$ to 3, static temperatures of 1400 to 1600 K and static pressures of 0.5 to 1 atm, the higher temperatures and pressures being a consequence of compression through shock wave systems through the forebody. The fact that static temperatures in such a condition are not far from the combustion temperatures in a classical air-breathing engine subsonic combustor that has a maximum peak temperature of 2300 K, implied that further deceleration of the air stream to subsonic conditions would be unhelpful in generating positive thrust from the propulsion system. Building any practical combustion system at such flight conditions demands that combustion be performed at supersonic conditions only. This new regime of combustion has been the focus of examination experimentally, theoretically as well as computationally over the last three decades. Briefly stated, the issues are that the residence time available for completing combustion is of the order of a millisecond or less. This is coupled with low static pressures (0.1

MPa or less) that makes chemical reaction rates low is only partly modulated by higher static temperatures of air stream of 1200 K to 1500 K even if combustion temperatures are about 2500 K. These conditions are vastly different from those of a gas turbine main combustor where the residence times are about 4 to 5 ms and pressures are very high as already indicated. The conditions are also vastly different from rocket engine combustion chamber where the reidence times are about a millisecond, but pressures and temperatures are very high - 10 MPa and 3000 K.

The supersonic combustor that is limited to about a meter in length with velocities of a 1000 m/s has issues related to mixing. The combustion process must be conducted in a gradual manner rather than very sharply because the sharp pressure rise will lead to the flow acquiring substantial regions of subsonic flow that eventually leads to a strong coupling between the combustor and the air intake. Such an intimate coupling is most undesirable since combustion will largely be controlled by subsonic heat release causing unsteady flow processes that may lead to the air intake going sub-critical, something that is disastrous for thrust generation. Also the flow processes become unsteady. Avoidance of such a coupling and achieving gradual combustion calls for *mixing processes* to be designed with equal care since *mixing* precedes combustion. Studies of mixing between high speed fuel and air streams (the subject of this thesis to be detailed later) have shown that this process is impeded and controlled by a parameter called convective Mach number M_c defined as the difference between the stream speeds divided by the sum of the acoustic speeds of the two streams. The period of early nineties was dominated by discussion of how to deal with this bottleneck that appears only in high speed combustion processes. Even though practical combustors use the configuration of laterally injected fuel jets in streams, *the early mixing phenomena in such a configuration is best modeled by two-dimensional mixing layer to help unravel the physical processes involved in controlling the mixing phenomena*. Justifiably, mixing layers with different velocities with similar gases have been studied extensively first. Subsequently, the effects of different temperatures of the streams, densities and gases have been treated through experiments and some simpler analyses like temporal mixing layers and linear stability of spatial mixing layers. The development of spatial mixing layers has still several questions that will be brought out in this thesis.

1.1.1 A brief history of scramjet development

A simple thermodynamic analysis of a ramjet propulsion system will lead to

$$\frac{F}{\dot{m}_a a_o} = M_o \left[\sqrt{\frac{\theta_b}{\theta_o}} - 1 \right] \tag{1.1}$$

where $F/\dot{m}_a a_o$ is the dimensionless thrust per unit air flow rate with a_o being the acoustic speed at the flight altitude, M_o, the flight Mach number, $\theta_b = T_b/T_o$, the ratio of combustion chamber temperature to the ambient temperature and $\theta_o = 1 + (\gamma - 1)M_o^2$, the ratio of stangnation temperature to the static temperature expressed in terms of flight Mach number. For a given ramjet engine, the thrust per unit flow rate which is reflective of the compactness of the engine increases initially with flight Mach number, but eventually will drop down because the first tem in the bracket comes down. This is because the stagnation temperature approaches the combustor temperature and the system can no longer accept fuel energy. Typically, the peak in $\frac{F}{\dot{m}_a a_0}$ is obtained at $M_o \sim 2.5$ to 3. Further, calculation of the thrust itself (dimensionless thrust is $F/p_o A_e$ where p_o is the ambient pressure ad A_e is the exit area of the nozzle designed for optimum expansion) has also a peak at a slightly shifted flight Mach number. A further feature not accounted for in the above analysis is that the aerodynamics that reflects itself in terms of drag since it is the balance between the two that leads to steady, accelerated or decelerated modes of functioning. The net effect after this is accounted is that subsonic combustion based devices have an upper limit of operational flight speed not far above 4 under the best circumstances.

The first major contribution in the realization of an engine based on supersonic combustion appears in Ferri [1959] which discusses the practicality of supersonic combustion (an example shown in **Fig 1.1**). The path breaking work was presented in Ferri et al. [1962], which presented experimental attainment of combustion of coaxial stream of hydrogen (subsonic) jet in a supersonic stream of air at $M = 3$ *without* the presence of shocks. Later, Ferri and Fox [1969] described the design of scramjet engines, and provided an en-

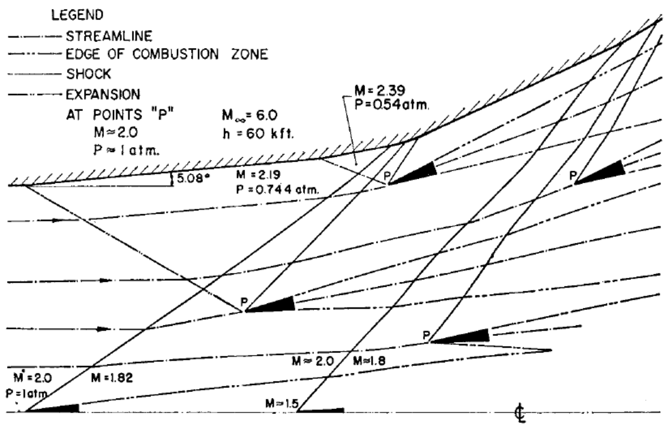

Figure 1.1: Combustor design with thermal compression.
[*Image extracted from Ferri and Fox [1969]*]

gineering approach to the study of mixing and boundary layer approximations in such an engine. His designs were one of the first in trying to address the problem of mixing. Heppenheimer [2007] has presented the detailed historical perspective of the hypersonic research.

The NASA HREP (Hypersonic Research Engine Project) was initiated in 1964 for integrating the then available information into a complete engine. The main aim was to demonstrate the thrust performance over a Mach range of 4 to 8. The last phase of the project was flight tests using the X-15 test airplane which was cancelled in January 1968, which changed the focus of HREP to mainly ground tests. A list of the documents generated is presented in Andrews [1994]. The HREP generated a lot of information pertaining to ground tests. The AIM (Aerothermodynamic Integration Model) designed and tested under HREP was able to perform at about 70% the theoretical efficiency in the range of Mach 5-7.

While the HREP concentrated mainly on axisymmetric engines, NASA also researched in airframe integrated rectangular channel engines. Notably John and Griffin [1973] and Edwards [1974] presented a configuration similar to the one shown in **Fig 1.2** and **Fig 1.3**.

Another project was that of Supersonic Combustion Ramjet Missile or

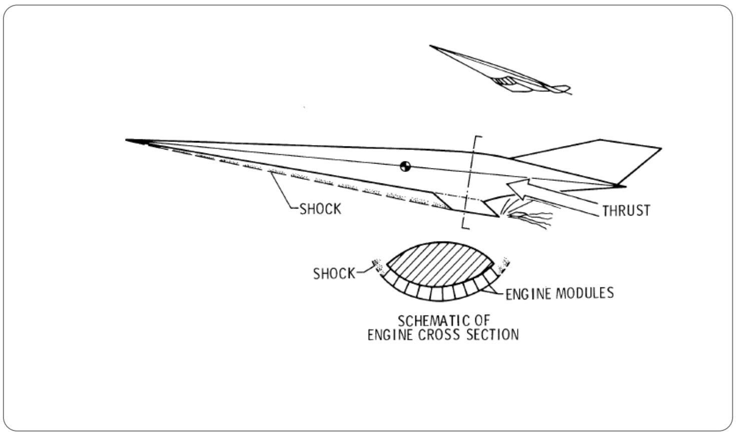

Figure 1.2: Body integrated scramjet airplane.
[*Image extracted from John and Griffin [1973]*]

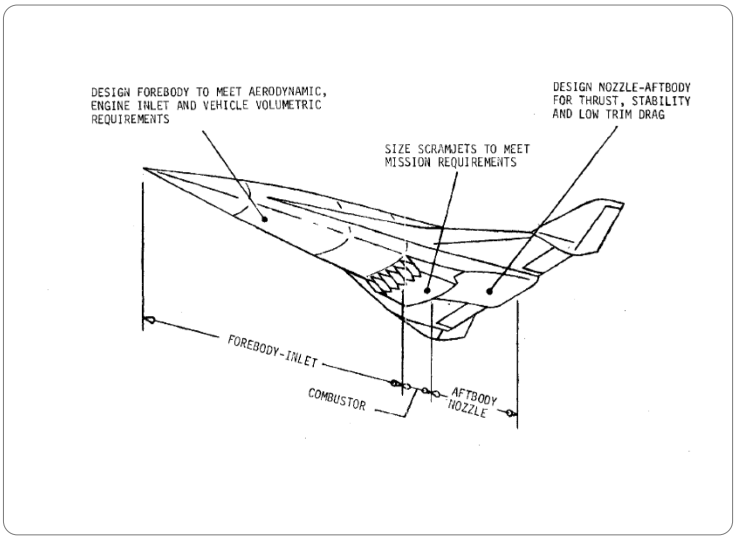

Figure 1.3: Body integrated scramjet airplane.
[*Image extracted from Edwards [1974]*]

(SCRAM) detailed in Billig [1993] at the Johns Hopkins University. This program was successfully able to complete the ground testing of engines in the range M = 5-7.3. This program used a highly reactive fuel HiCal-3-D ($C_{3.2}H_{20.3}B_{10}$). On the basis of these experiments it was predicted that SCRAM would have approximately twice the range of a rocket, and that it would also outperform a subsonic combustion ramjet at hypersonic speeds because of its higher fuel specific impulse.

The year 1984 saw the start of the National Aerospace Plane (NASP) for the development of the Single Stage To Orbit (SSTO) vehicle X-30. The aim of the program under NASP was to develop a hydrogen fuelled scramjet engine which would operate over the range of $M = 4$ to 15. In 1993 the proposed flight experiments were cancelled after they were decided to be too expensive. The NASP program was terminated in 1995. Following this, the Hyper-X program to develop a vehicle to allow tests at speeds approaching Mach 10 was launched. The X-43A research vehicle was designed to be the smallest flight vehicle that could demonstrate scramjet performance. In 2004, X-43A demonstrated in two separate flights, reached near Mach 7 and Mach 10 respectively [Harsha et al., 2005].

Experimental work in Australia has over a period of time matured from design and testing of simple combustors to the testing of scramjet models demonstrating a net positive thrust. Hydrogen fuel is the main fuel candidate in most of the experiments in Australia. These efforts are recorded in Paull et al. [1995]. The continued efforts resulted in HyShot program between 2001 and 2007, further leading to HyCAUSE from 2007 onwards. These flight mainly based of a Ballistic trajectory, which include a portion of supersonic combustion demonstrator with Hydrogen after reentry and reorientation.

Japan built a test facility at National Aerospace Laboratory,Kakuda Research Center (NAL-KRC) for testing of supersonic combustion ramjet engines. The Japanese research included those on fuel injection from side walls and parallel injection with and without using struts. Tests were conducted using shock generators for isolating the effects of the combustion chamber from the inlet to prevent un-start.

Sosounov [1993], Curran et al. [1996], Curran [2001] and others have presented insightful historical perspective of the development of scram jet engines over the years.

1.2 Mixing and its role in Scram jet engines

Mixing is the precursor to combustion and mixing. The purpose of an fuel injection system is to have an efficient distribution of the fuel in the flow field, which will lead to subsequent molecular mixing. As discussed earlier, this has to happen at just the right rate for high efficiency. The mixing process in supersonic combustion poses a central problem. The typical techniques of injecting fuel in the air stream are

Cross injection through walls Fuel injection directly into the flow field through the side walls. The obstruction caused by the incoming jet of fuel into the supersonic stream of air, causes the formation of shock, and subsequent mixing. Due to the total pressure losses to the shock and non uniform distribution causes, this technique is seldom used.

Supersonic wake These are class of intrusive technique wherein a strut or a pylon protrude into the flow field from the wall and deliver the fuel parallel or near parallel to the flow field at various locations. The supersonic wake formation behind such structures provides the intense vorticity and turbulence needed for rapid mixing as well as for flame holding.

Alternating ramps and wedges These provide alternating ramps to increase the area of contact between the air and the fuel. The fuel is injected at the end of the ramp and the contact surface includes all the three surfaces of the ramp.

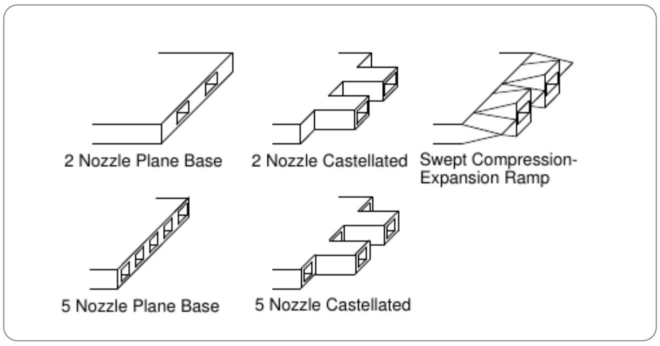

Figure 1.4: Few common injectors used in practice

Some of the common injectors design is shown in **Fig 1.4**. We see that the techniques mentioned above involve streams of fuel and air mixing in the combustion chamber due to shear and turbulence. A mixing layer of two parallel streams is formed when the stream of fuel is from of a rectangular slit. Even in the case where it is injected in the form of a jet, in the early part, the curvature of the flow becomes insignificant compared to the other relevant dimensions of the flow. The conditions from axial flows becomes a two dimensional flow in this limit, and a supersonic coaxial jet degenerates to a two dimensional mixing layer.

Thus the supersonic mixing layer is the most fundamental unit for the study of mixing, and results from this can be extrapolated to most of the mixing devices used in supersonic combustion.

1.3 The Mixing Layer

The mixing layer or more specifically, a plane two dimensional mixing layer is basically two parallel streams at different velocities, initially separated from each other by a splitter plate interacting beyond this region in the test section leading to mixing (**Fig** 1.5). The planar mixing layer is the two dimensional analogue of a circular single jets and annular jets. This makes the mixing layer the simplest approximation to the mixing of two parallel streams.

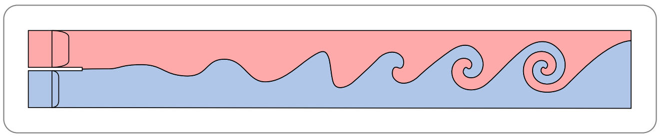

Figure 1.5: Model Mixing Layer
[*Instability and consecutive roll up is depicted. Red color indicates primary stream, and blue the secondary stream.*]

Besides, the mixing layer being largely two dimensional, enables the study of the same experimentally much more viable through shadow graphs or Schlieren images.

1.3.1 The velocity profile

The initial velocity profile of the flow over the splitter plate is the same as that of a boundary layer over a flat plate. Hence at the end of the splitter plate the flow is composed of a double boundary layer profiles of either side of the splitter plate. Of course, in a realistic experiment, boundary layers will form on the top and bottom walls of the channel and also in the span-wise direction.

This initial profile immediately after the splitter plate forms a profile which evens out the sharp changes due to the effect of viscosity. For the laminar flow, the profile approaches a tanh profile but with a velocity deficit initially caused due to the wake of the splitter plate and the boundary layer formed over the splitter plate. As the distance increases, the wake component monotonically decreases. As shown below

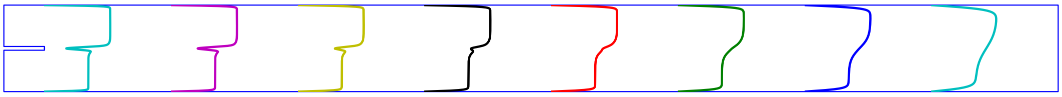

When the wake component becomes unidentifiable and the velocity profile becomes almost a tanh profile, the average parameters become *self-similar*. This is detailed in **Sect 1.3.3**. Very similar is the case when we talk of the average velocity field of a turbulent flow.

1.3.2 The width of the mixing layer

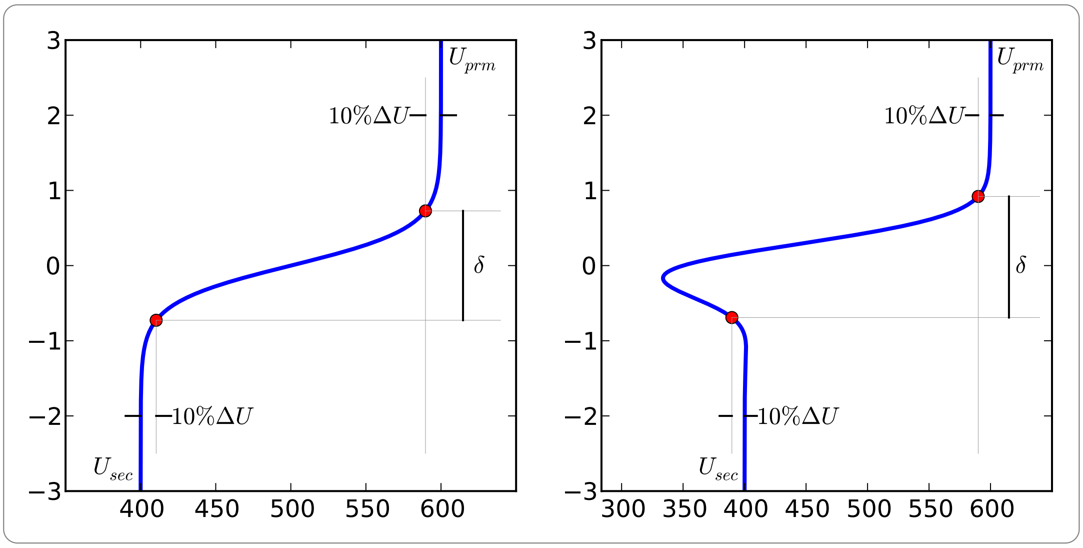

Figure 1.6: Definition of δ
[*Notice that this definition of δ accommodates even flows without (**Left**) and with (**Right**) a deficit velocity*]

A measure of how much the momentum has diffused through the mixing layer is the *width* of the mixing layer. Broadly speaking, the width of the mixing layer is the distance to which each stream feels the presence of the other stream. One measure of the width of the mixing layer is the width where the velocity has changed by more than say 10% of the difference in the free stream velocities. This is shown in **Fig 1.6**.

Another definition of the mixing layer growth is called the *vorticity thickness* shown in **Fig 1.7**. This measure is valid primarily for self-similar profiles, with a single peak in the derivative of velocity. The width is defined as that distance which is required to cover the velocity difference at the greatest gradient in the profile. It must be noted that this technique has the disadvantage that it is not not valid in the early part of the mixing layer where there is a double shear, because there are two peak derivatives, one positive and another negative. Also this technique has a drawback that it takes into consideration only a single point information for the measurement. On the other hand, it does not have any ambiguity as in the case of δ where the threshold is arbitrarily chosen.

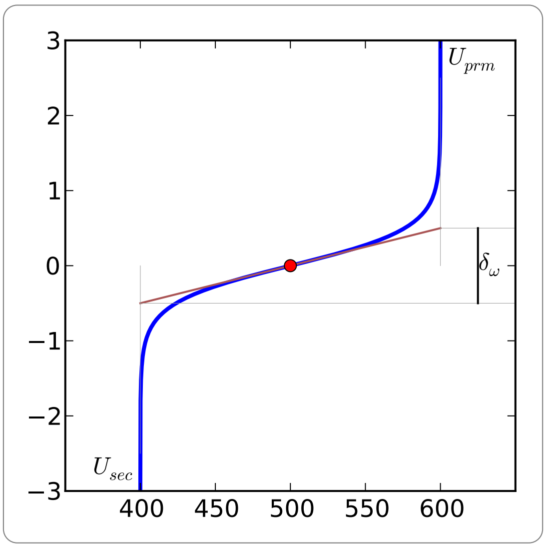

Figure 1.7: Vorticity thickness

A third technique is aimed at arriving at a robust technique that overcomes the local nature of other measurements. This technique involves fitting a tanh profile on the mixing layer, with the best least squared fit, and using that curve to determine the 10% deviations. This technique uses the entire information of the flow velocity and is hence not susceptible to local fluctuations. On the other, hand this technique needs a-priori the form of the velocity field to be expected, and it does not work well with flows with velocity deficit.

A very important parameter is the *growth rate* which is the local rate of increase of $\delta(x)$ with the stream-wise direction x. That is $\delta'(x) \equiv d\delta(x)/dx$. This parameter is of special interest because this parameter gives the rate of diffusion of momentum, and from Reynold's analogy, a measure of rate of turbulent heat transfer and mass diffusion rate.

1.3.3 Self-Similarity

Self-similarity is a phenomenon in which the effect of two or more independent parameters influences the dependent parameters only in a particular combination. Hence that combination can be taken as a single independent variable.

In the case of a mixing layer, when the cross-wise (y) coordinate axis is scaled with the width of the mixing layer at that location, all velocity profiles collapse into one curve. In fact with the definition

$$\eta = y/\delta(x) \tag{1.2}$$

all average parameters become a function of η alone and not that of x and y separately. It can be said that the flow *forgets* the presence of the splitter plate and loses equivalent to one independent parameter. It is also evident that the velocity profile with a velocity deficit cannot be self-similar. This is clear from **Fig** 1.8 where initially we can see the profiles as a function of x as well as η, but after certain distance, it becomes a function of η alone.

In practice, however, the self-similarity is only an approximation because of the presence of the side walls and the presence of the top and bottom walls. The boundary layers growing on these surfaces eventually start influencing the mixing layer and the flow parameters no longer are functions of η alone.

It must also be noted that there is an ambiguity as to where the self-similarity has actually occurred. It may be said to have attained self-similarity

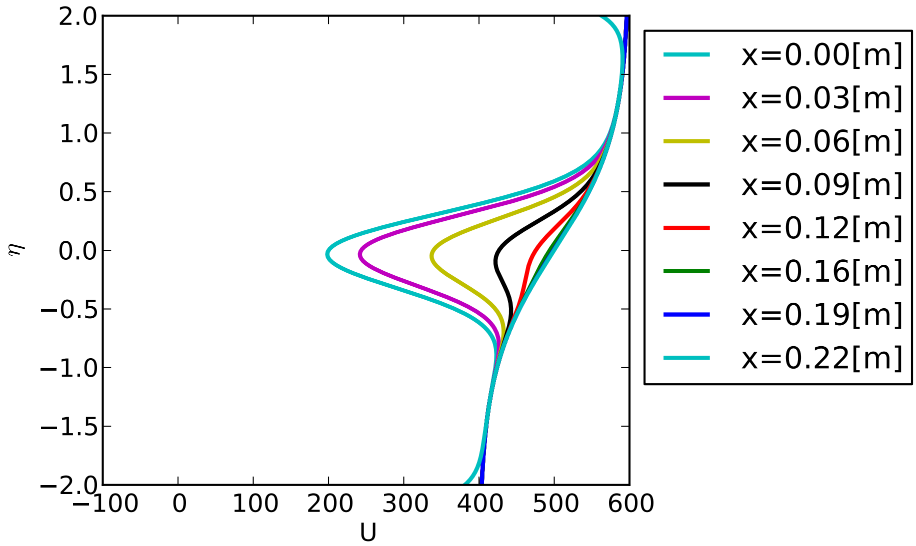

Figure 1.8: Attainment of Self Similarity
[*Stream-wise velocities collapse when* y *is scaled with* δ]

when the average plots *reasonably* collapse on to a single curve. Further, once the averages have attained self-similarity does not mean that the second order statistics (like $\langle u'u'\rangle$) have attained self-similarity. In fact there is no simple technique to estimate the distance required for the second order statistics to attain self-similarity given the distance needed for the first order statistics to attain self-similarity.

When self-similar, all the measures of mixing layer thickness are proportional to each other and grow linearly with x. Hence the growth rate of each of these measures differ by only fixed constants.

1.4 Research in Mixing, a literature survey

1.4.1 Experimental developments

Abramowitz [1963] in a monograph provided an appraisal of theoretical and experimental data published over earlier ten years. It gives a systematic analysis of numerous experimental data on velocity profiles, temperature, and the impurity concentration. The theory of free turbulence in a gas, suitable in principle for any degree of compressibility, is revised, and the equations are derived for motion and heat exchange in the boundary layer of a jet at very high temperature. It also dealt with spreading of jets in finite and semi-finite space. He derived the first relation for the growth rate of a mixing layer as

$$\delta' \propto \frac{U_1 - U_2}{U_1 + U_2} \tag{1.3}$$

Where

$\delta(x)$	is the width of the mixing layer
δ'	$\equiv d\delta(x)/dx$
U_1	is the velocity of the primary stream
U_2	is the velocity of the secondary stream

The above equation is easy to understand. In the frame of reference of the instability, the only time scale is $\delta/\Delta U$. Hence the rate of change of delta i.e. $d\delta/dt$ must be proportional to ΔU. To transfer this to the stationary frame of reference, if the convective velocity is U_c, we get

$$\delta' \equiv \frac{d\delta}{dx} = \frac{d\delta}{dt}\frac{1}{U_c} = \frac{\Delta U}{U_c} \tag{1.4}$$

If we further assume that the convective velocity is the mean velocity, which must be a very good estimate in the case of both the streams with the same fluid density, we get

$$\boxed{\delta' \propto \frac{U_1 - U_2}{U_1 + U_2}} \tag{1.5}$$

The above equation, however, is not valid for streams with dissimilar densities. And, of course, it is meant only for incompressible mixing layer.

By the beginning of 1970s it was known that increase in the Mach number causes the decrease in the growth, or the spread of supersonic jets. This was generally attributed to the decreasing temperature with increased Mach number in experimental studies and hence the increasing density of the stream.

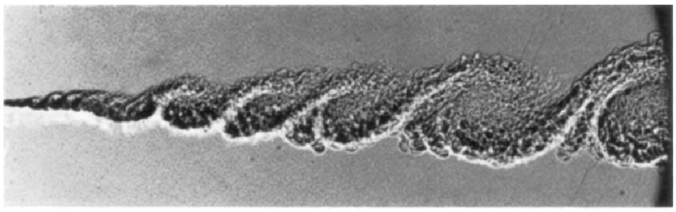

Figure 1.9: Shadow graph sample from Brown and Roshko [1974]
[*Notice the well formed coherent large scale structures*]

To verify this claim and to see the effects of density variation, Brown and Roshko [1974] conducted experiments with a mixing layer (subsonic) with different gases to be able to have a density ratio significantly different from unity and thus emulate the effects of varying density ratio related to the increasing Mach number in other experiments. The test cases for the verification is presented in **Table 1.1**. These test cases were selected to be able to emulate the effects of differing density ratios in cases where the Mach number of the primary stream would be up to 5. The experiment demonstrated present of span-wise structures, as shown in **Fig 1.9**.

The results of these experiments (presented in **Fig 1.10**) clearly showed that although the increasing density ratio does decrease the mixing layer growth rate, the decrease caused in the experiments when the M_c is increased is much more than what is expected solely due to the density ratio change. It was hence concluded that the density ratio alone *does not* explain the reduced growth of the mixing layer at high Mach numbers.

The reduced growth rate was again observed and presented by Ikawa and Kubota [1975]. This experiment, with the primary stream Mach number as 2.47, found that there is a reduction in the mixing process, growth rate, normalized shear stress, and other measures of turbulence. Comparison was made with an incompressible mixing layer, and the reduction of growth rate was found to be from 0.035 in the case of incompressible mixing layer, to 0.0073 in the case of a compressible mixing layer.

To be able to make predictions regarding the compressible mixing layers, it was necessary to have a measure of the compressibility effects. To this end

Parameter	**Case 1**		**Case 2**		**Case 3**	
	Primary	Secondary	Primary	Secondary	Primary	Secondary
Fluid	Helium	Nitrogen	Nitrogen	Air	Nitrogen	Helium
Velocity $[m/s]$	5	1.9	5	1.9	5	1.9
Pressure$[atm]$	4		4		4	
Density Ratio	7		≈ 1		$1/7$	
Velocity Ratio	$\approx 1/\sqrt{7}$		$\approx 1/\sqrt{7}$		$\approx 1/\sqrt{7}$	
ρU^2 **Ratio**	≈ 1		$\approx 1/7$		$\approx 1/49$	
$\lambda \equiv \frac{U_1-U_2}{U_1+U_2}$	0.45		0.45		0.45	

Parameter	**Case 4**		**Case 5**		**Case 6**	
	Primary	Secondary	Primary	Secondary	Primary	Secondary
Fluid	Helium	Nitrogen	Nitrogen	Air	Nitrogen	Helium
Pressure$[atm]$	4		4		4	
Density Ratio	7		≈ 1		$1/7$	
Velocity Ratio	≈ 7		≈ 7		≈ 7	
ρU^2 **Ratio**	≈ 343		≈ 49		≈ 7	
$\lambda \equiv \frac{U_1-U_2}{U_1+U_2}$	0.75		0.75		0.75	

Table 1.1: Test cases of Brown and Roshko [1974]

Bogdanoff [1983] presented a measure M^+. This is the geometric mean of the two Mach numbers that the frame moving with the coherent structures see, M_{c1} and M_{c2}. The results of this study were compared with the analysis of Blumen et al. [1975], and were found to be corroborating with the linear stability results. This comparison is shown in **Fig 1.11**.

Now that it was certain that the effect of the growth rate reduction was not solely due to the density or the velocity ratio, but was a compressibility effect, there was a need for a systematic characterization of the effect based on experimental evidence and quantification of its effect. This was done by Papamoschou and Roshko [1988] who experimentally investigated the growth rate and the turbulence structure of supersonic mixing layers with similar and dissimilar gasses. The experiments performed ranged from Mach numbers from 0.2 to 3.4. The Schlieren images and the details are shown in **Fig 1.12** to enable

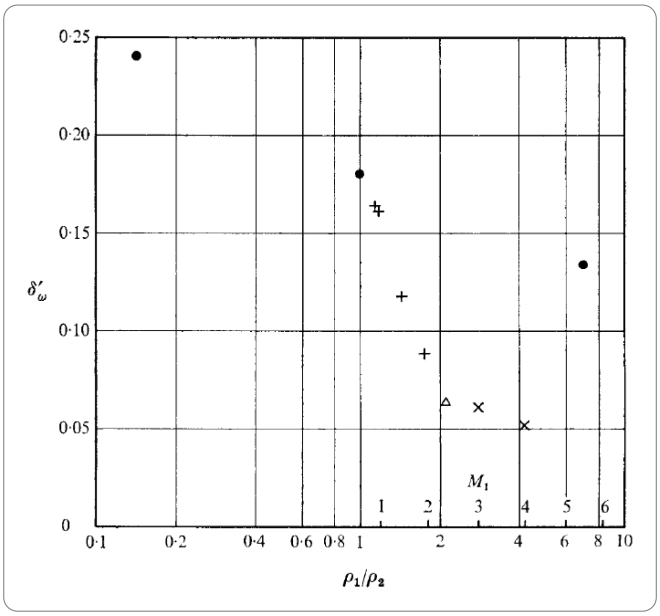

Figure 1.10: Effect of density ratio on spreading rate
[*Image extracted from Brown and Roshko [1974]. Symbols: • represents the incompressible case and experiments: △, Ikawa [1973];+, Maydew and Reed [1963]; ×, Sirieix and Solignac [1966]. Note that the decrease in the growth rate is much smaller due to density variations than what is caused due to increased* M_c]

further analysis of the behavior of the mixing layers.

It can be seen that the images of the experiments reveal very low growth rates and presence of large scale structures. To quantify the compressibility effect, the authors introduced a compressibility parameter which would unify all the results obtained. This parameter which was the Mach number convecting with the velocities of the structures, came to be known as the convective Mach numbers (plural indicates the two numbers, one with respect to each stream). To be able to calculate the convective Mach number, it was necessary to calculate the velocity of the convecting structures. For this the authors matched the total pressures from both the streams in the convecting frame of reference. This gives

$$\left(1 + \frac{\gamma_1 - 1}{2} M_{c1}^2\right)^{\dfrac{\gamma_1}{\gamma_1 - 1}} = \left(1 + \frac{\gamma_2 - 1}{2} M_{c2}^2\right)^{\dfrac{\gamma_2}{\gamma_2 - 1}} \tag{1.6}$$

This relation is plotted in **Fig 1.13**, which shows that for moderate M_{c1}

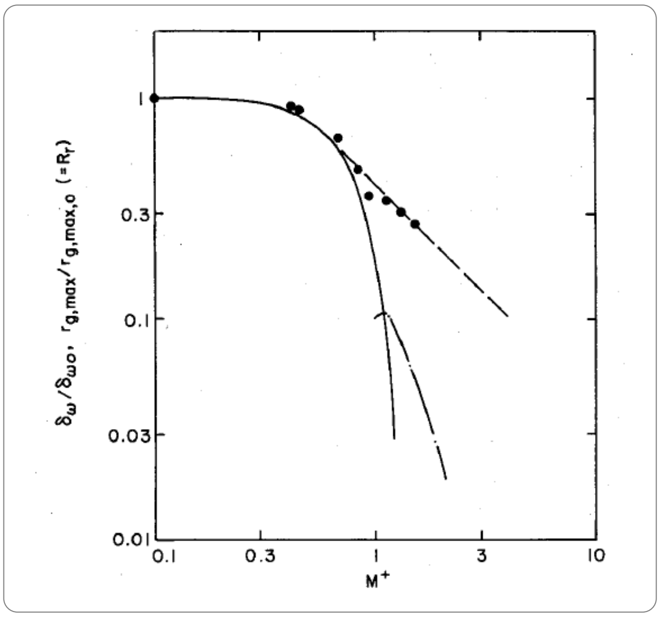

Figure 1.11: The Mach number M^+
[*Image extracted from Bogdanoff [1983]. • represents experimental values, and curves represent maximum inviscid instability amplification rates*]

the difference in M_{c1} and M_{c2} is less than 9%. This may not hold true for large M_cs. Since the difference between the two convective Mach numbers is not large, the definition of the term "convective Mach number" (M_c) changed in most of the later papers, which used the single mean value $M_c = \dfrac{U_1 - U_2}{a_1 + a_2}$.

For $\gamma_1 = \gamma_2$, $M_{c1} = M_{c2}$, **Eqn 1.6** yields

$$U_c = \frac{a_2 U_1 + a_1 U_2}{a_1 + a_2} \tag{1.7}$$

The next thing was to isolate the effects of compressibility. For this it was assumed that the effect of compressibility will be in the *variable separable* form. That is, they assumed

$$\delta' = \underbrace{\delta'_0(r,s)}_{\text{incompressible effects}} \times \underbrace{f(M_{c1})}_{\text{compressibility effects}} \tag{1.8}$$

Papamoschou and Roshko [1988] then modelled the incompressible growth rate for various density ratios (s) and velocity ratios (r) from the data of Brown

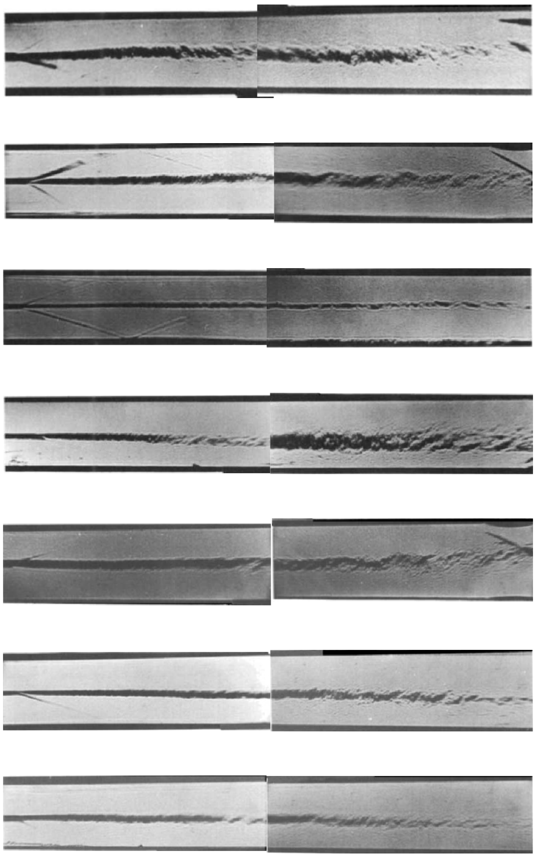

Case	Fluid	$U[m/s]$	$\rho[kg/m^3]$	M	M_c	r	s
Case 1	N2	459.41	0.12	1.60	0.08	0.9291	4.37
	Ar	494.73	0.52	3.30			
Case 3	N2	640.33	0.23	3.10	0.33	0.75	0.54
	N2	477.81	0.12	1.70			
Case 4	N2	616.94	0.20	2.80	0.38	0.75	1.81
	Ar	465.00	0.36	2.60			
Case 6	He	1236.43	0.02	1.70	0.64	0.51	9.98
	N2	633.03	0.22	3.00			
Case 7	Ar	487.76	0.47	3.10	0.89	0.13	0.24
	Ar	64.09	0.11	0.20			
Case 8	He	1469.02	0.04	2.60	1.08	0.42	5.52
	N2	616.94	0.20	2.80			
Case 9	He	1572.82	0.05	3.40	1.49	0.29	2.18
	N2	459.41	0.12	1.60			

Figure 1.12: Schlieren sample from Papamoschou and Roshko [1988]

and Roshko [1974], as

$$\delta_0' = 0.14\frac{(1-r)\left(1+s^{1/2}\right)}{1+rs^{1/2}} \tag{1.9}$$

Using the definition of M_{c1}, and using a model for the growth rate, it was scaled with the incompressible growth rate for the same s and r as that of the compressible counterpart and the effect of compressibility so obtained is shown in **Fig 1.14**. It is seen that all the points, more or less fall on the same curve which shows insignificant decrease till $M_c \approx 0.3$ and then decreases with increase in M_c to an asymptotic value of about 0.2 at about $M_c \approx 0.75$. Identification of M_c as a measure of compressibility was one of the important contributions of Papamoschou and Roshko [1988]. This measure of compress-

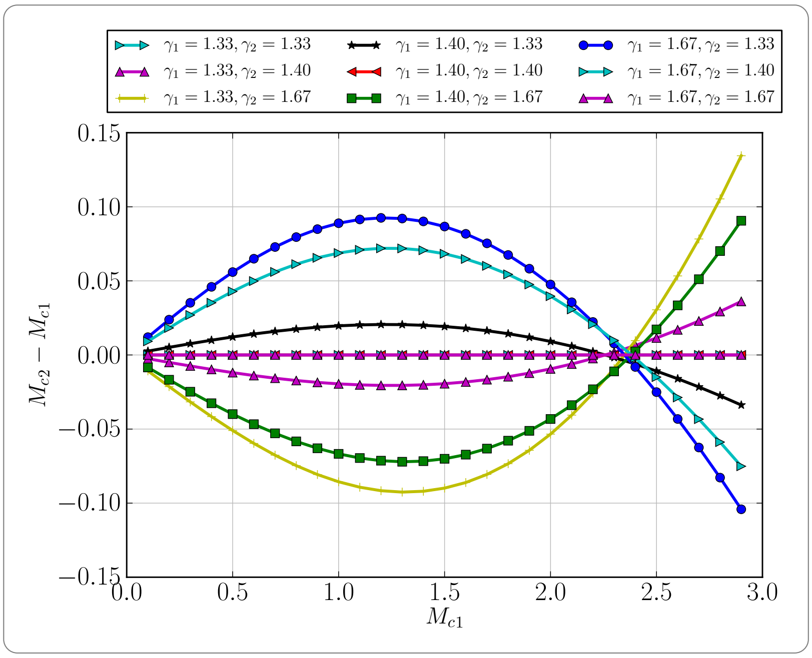

Figure 1.13: Convective Mach numbers
[*Notice that the difference between* M_{c1} *and* M_{c2} *for* $M_{c1} < 2.5$ *is less than 9%*]

ibility differs from the one presented by Bogdanoff [1983] (the latter is the geometric mean of the two Mach numbers M_{c1} and M_{c2}).

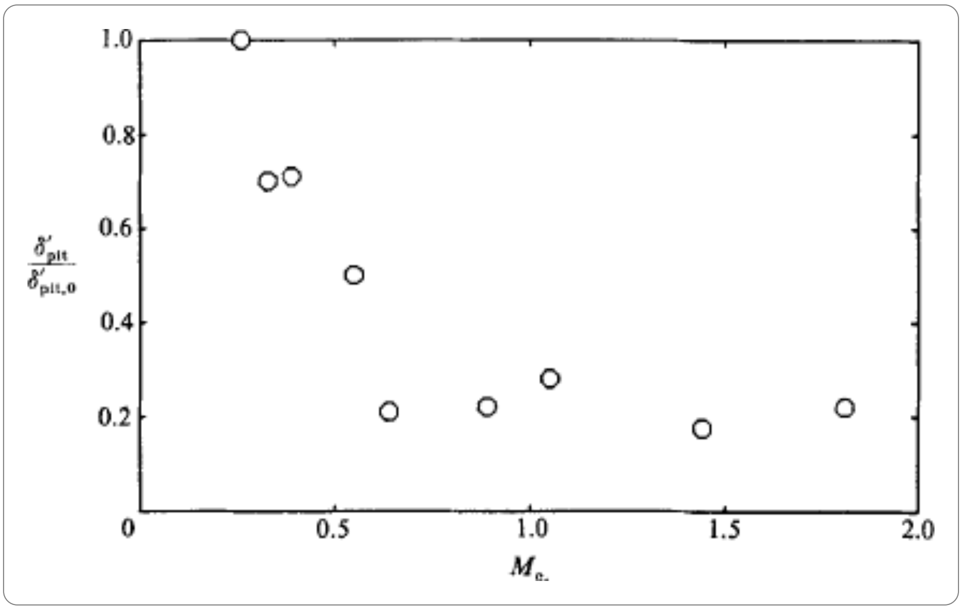

Figure 1.14: Scaled growth rate from pitot measurements vs M_c
[*Image extracted from Papamoschou and Roshko [1988]*]

The schlieren images are examined further here. The Schlieren image also represents an average in the span-wise direction. Being so the envelope of the fringes of the Schlieren images is indicative of the average growth δ of the mixing layer at that point. This δ was measured directly from the images present in Papamoschou and Roshko [1988]. This plot is shown in **Fig 1.15**. The left of the images has the plot of the measured δ, and the right one is scaled to counter the effects of r and s. It can be seen that increase in M_c almost monotonically decreases the scaled δ and this effect is the compressibility effect.

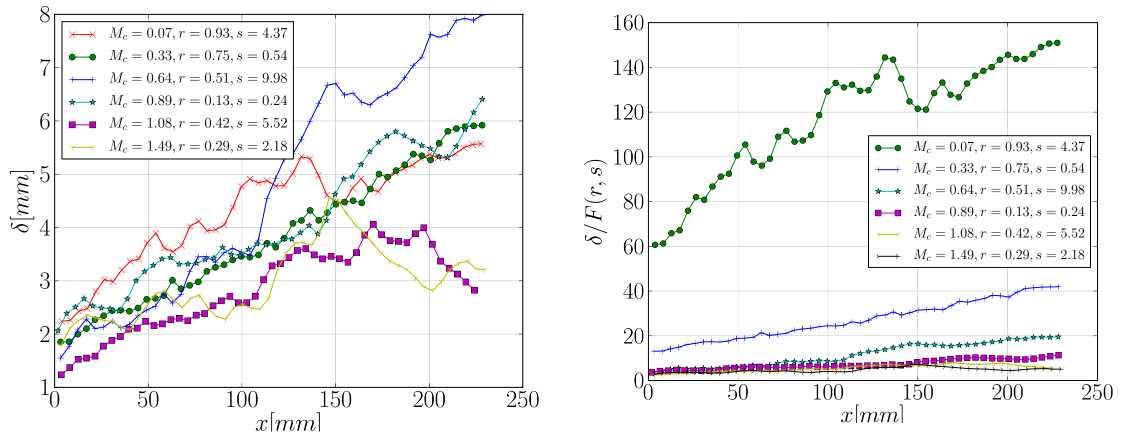

Figure 1.15: Measured δ (left) and scaled to remove effect of r and s (right) [*Note that the scaled δ shows a distinct decrease with M_c for a given x*]

The following are some observations that can be made from **Fig 1.15**.

- The decrease in the scaled growth rate is monotonic with increase in M_c.
- The influence of the incompressible effects is large and can actually offset the influence of M_c. For example M_c of 0.64 has a greater growth than M_c of 0.3 because r increased from 0.51 to 0.75 for the same two cases.
- The growth is not very linear, especially with increasing M_c. This further means that self-similarity may not have been attained even in the first order statistics, because self-similarity would imply a constant growth rate.

The experiments prior to the 90's could use only Schlieren images as the visualization technique. These could, at best, guess the three dimensional structures. However, the beginning of the 90's saw the advent of better visualization techniques. Planar Mie Scattering was one such technique, which was employed by Clemens and Mungal [1990], for the direct visualization of the three dimensional structures. Clemens and Mungal [1990] performed experiments of mixing with Air-Argon supersonic streams at the conditions shown in **Table 1.2**.

Parameter	**Case 1**		**Case 2**		**Case 3**	
	Primary	Secondary	Primary	Secondary	Primary	Secondary
Fluid	Air	Air	Air	Air	Air	Argon
Mach Number	1.64	0.91	1.97	0.42	2.15	0.38
Velocity $[m/s]$	430	275	480	130	508	110
Total Temperature $[K]$	265	260	265	260	265	260
ρ $[kg/m^3]$	2.04	1.58	2.35	1.40	2.59	1.96
T $[K]$	172.8	222.3	150.1	251.6	136.3	248.4
Density Ratio	0.77		0.59		0.77	
Velocity Ratio	0.63		0.28		0.22	
M_{c1}	0.29		0.62		0.79	
M_{c2}	0.29		0.62		0.73	
Mc	0.29		0.62		0.75	

Table 1.2: Test cases of Clemens and Mungal [1990]

A part of their work was the comparison of the average velocity profiles for comparison with the previous growth rate measurements. This was presented in the background of the results of Papamoschou and Roshko [1988] (shown in **Fig 1.16**), indicating that the compressibility parameter M_c introduced by the latter held true.

A major part of the work, however, was the visualizations of the turbulence structures using planar Mie scattering. The imaging were done with two techniques, product formation (where ethanol vapour in warmer slow speed stream condenses and becomes visible when it in contact with cold high speed stream), and passive scalar (where the high speed stream is seeded with vapour which condenses into fog in the nozzle). Some of the results are shown in **Fig 1.17**. The experiments showed that the low M_c cases indicate to the regular two dimensional coherent structures, whereas for high M_c cases, the mixing layer becomes highly three dimensional. Low M_c cases show the formation of *fat braids*, which are almost absent in the high M_c cases. Also the presence of

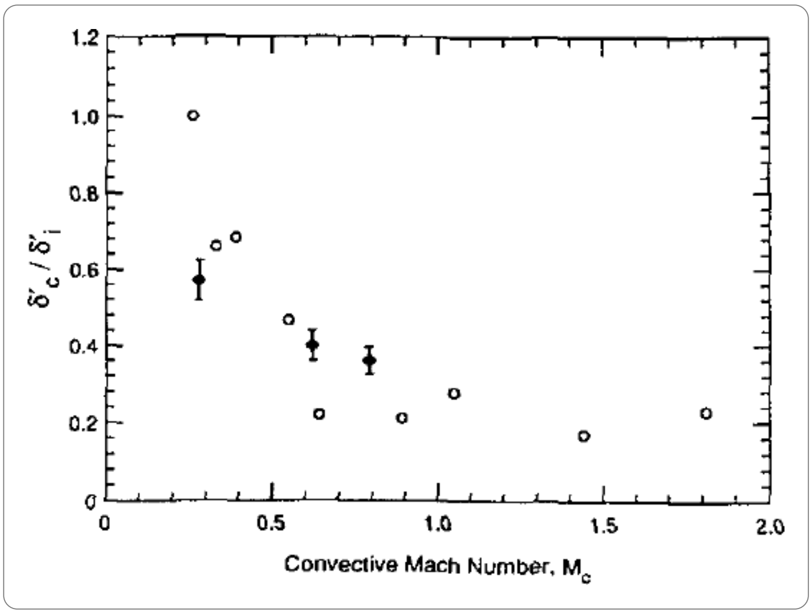

Figure 1.16: Results of Clemens and Mungal [1990] compared with Papamoschou and Roshko [1988]
[*Figure extracted from Clemens and Mungal [1990]. ○ represents results of Papamoschou and Roshko [1988] and • represents results of Clemens and Mungal [1990] with error bars.*]

dark streamwise streaks in the high M_c flows, which are not present in the low M_c flows suggests the presence of streamwise vortical structures. Furthermore, they reported that this structure carries predominantly the low stream fluid and *does not* cause entrainment.

The velocity measurements in all these experiments were made usually using pitot static tube or hot wire anemometer. Also, the run times of the experimental setup were small due to the limitation of pressurized bottled gasses. Messersmith et al. [1988] presented the experimental facility for studying supersonic mixing layers with long run times. Also a precise measurement technique, Planar Laser Doppler Velocimeter (PLDV) was used to make the measurements of the velocity field. Whereas Messersmith et al. [1988] presented the case M_c=0.2, Goebel and Dutton [1990a] and Goebel and Dutton [1990b] provided experimental results on the same setup with many test cases. The setup also had the facility for Schlieren images and pressure measurements.

The PLDV measurements allowed for measurements of turbulence in-

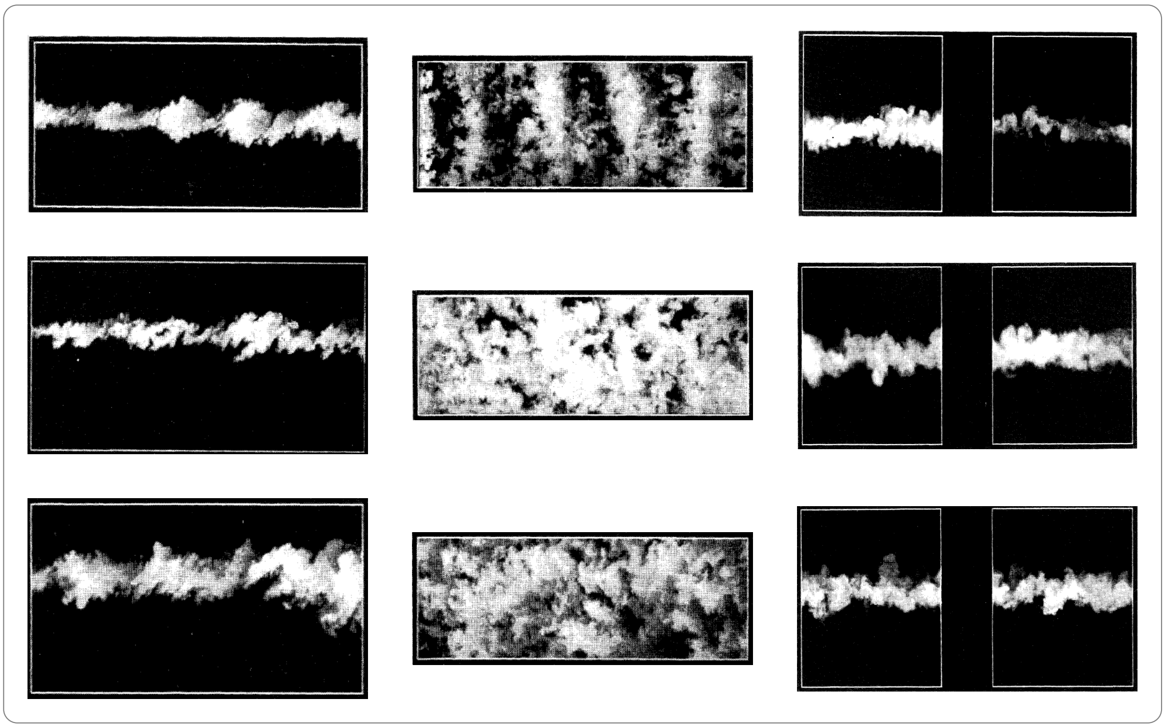

Figure 1.17: Mie scattering images from Clemens and Mungal [1990] [*Side View (Left), Top View (Center) and End View (Right) of flows at* $M_c = 0.28$*(Top),* $M_c = 0.62$*(Middle) and* $M_c = 0.79$*(Bottom) from Clemens and Mungal [1990]*]

tensities along with the mean velocity profiles. The cases had relative Mach numbers ranging from 0.4 to 1.97.

The results of this case is presented in **Fig 1.18** where it can be seen that

1. $\sigma_v\,(\equiv \langle v'v' \rangle)$ shows a distinct reduction with M_c.
2. $\sigma_u\,(\equiv \langle u'u' \rangle)$ shows no particular trend with increasing M_c.
3. The shear stress shows reduction with increasing M_c.
4. The anisotropy, which is the ratio of the turbulent stresses in stream-wise direction to the cross-wise direction, increases with increase in M_c.

Besides, it was observed from Schlieren pictures that organized structures were not present. This was in contrast to the observations made by Papamoschou and Roshko [1988] who stated that the large scale structures were present. Such large scale structures were also clearly demonstrated in the work

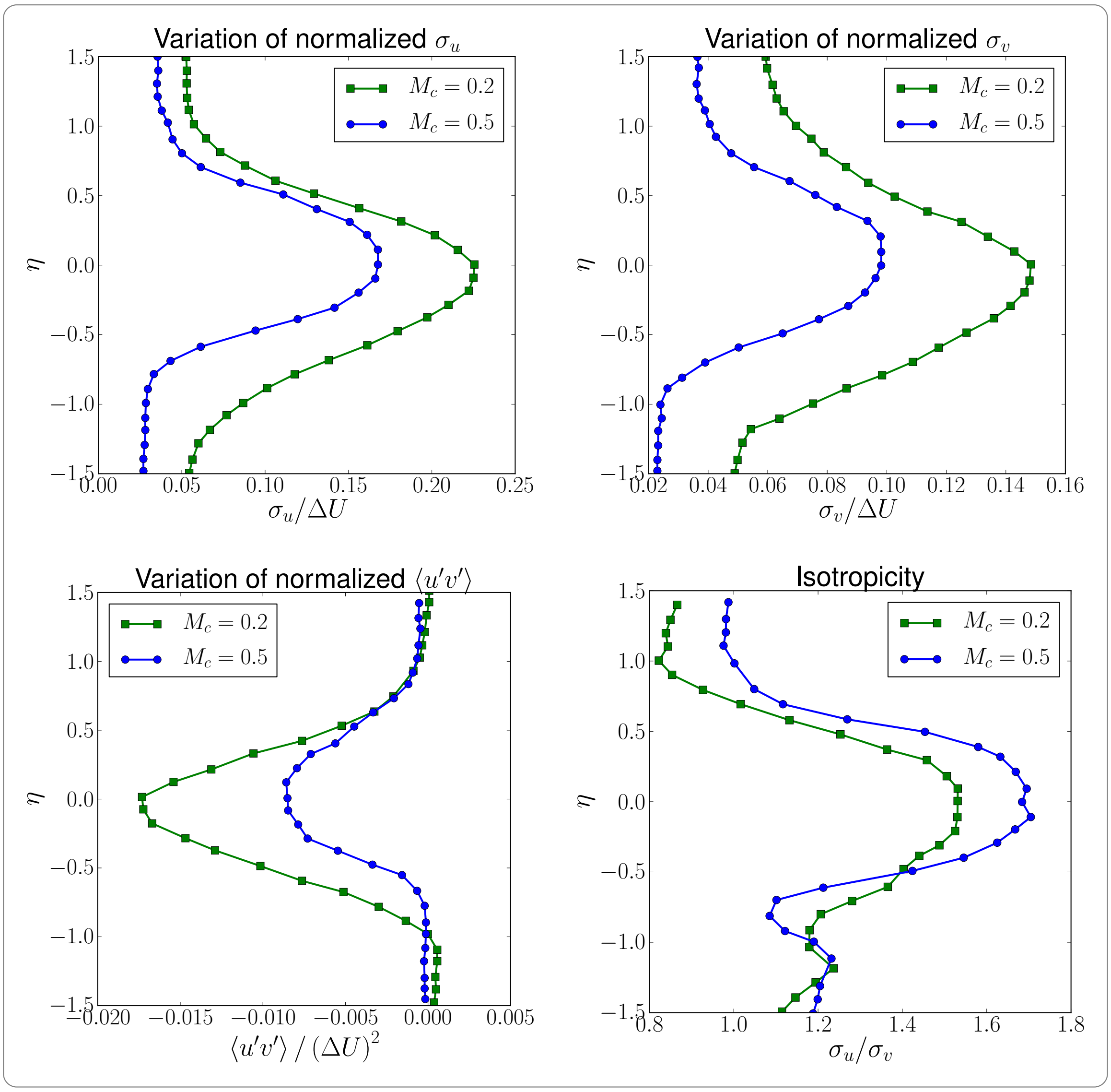

Figure 1.18: Stress tensor components from the experiments of Goebel and Dutton [1990b]

[Plotted above are the $\sigma_{xx}(u_x{}', u_x{}')$ correlation (top left), the $\sigma_{yy}(u_y{}', u_y{}')$ correlation (top-right), $\sigma_{xy}(u_x{}', u_y{}')$ velocity correlation (bottom left) and the ratio of σ_u and σ_v(bottom right). It can be seen that $\langle u'u' \rangle$ does not show much of a trend, $\langle v'v' \rangle$ does show a clear trend of decreasing magnitude with M_c]

of Clemens and Mungal [1990] and Elliott and Samimy [1990]. The present work also confirms the presence of such structures.

Also, through a set of experiments, the authors claimed that higher level of free stream turbulence and shock waves apparently inhibited development.

Around the same time as Goebel and Dutton [1990a], a similar setup was made at Ohio state university, and the observations were presented in Samimy and Elliott [1990] and Elliott and Samimy [1990]. The test cases were of high speed flows with M_c values 0.51, 0.64 and 0.86. A two component LDV was used for velocity measurements.

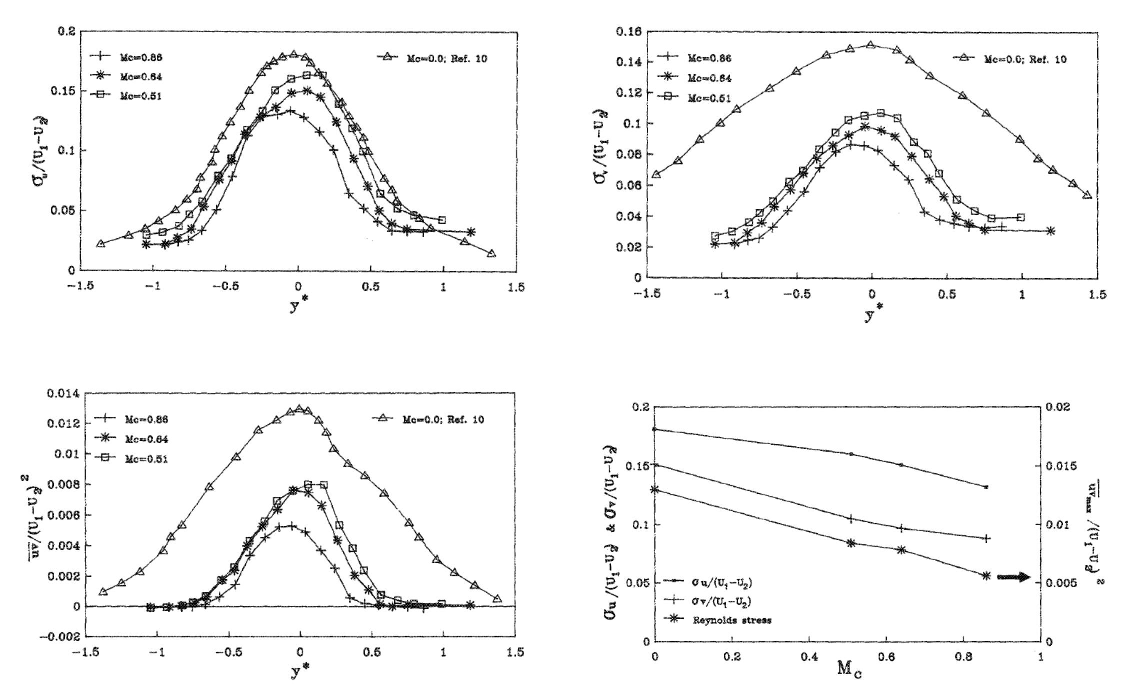

Figure 1.19: Results from Samimy and Elliott [1990]
[*Plotted above are the* $\sigma_{xx}(u_x{}', u_x{}')$ *correlation (top left), the* $\sigma_{yy}(u_y{}', u_y{}')$ *correlation (top-right),* $u_x{}', u_y{}'$ *velocity correlation (bottom left) and* σ_u *and* σ_v *with respect to* M_c*(bottom right). In these plots* $\triangle$ *is* $M_c = 0$ $+$ *is* $M_c = 0.88$, $\star$ *is* $M_c = 0.64$ *and* $\Box$ *is* $M_c = 0.51$ *for the top plots and the bottom left*]

The results showed that for the lower convective Mach number case, the vorticity thickness growth rates were over 20% higher and the momentum thickness growth rate was over 30% higher than those of the higher convective Mach number case. The lateral turbulence intensity, shear stress, and lateral transport of kinetic energy were all non-dimensionalized, with the velocity difference across the shear layer. These were plotted against the normalized y coordinate, shown in **Fig 1.19**. It can be seen that these show reduced levels for the higher convective Mach number case. It must be noted that this is in contrast with the reports of Goebel and Dutton [1990a], with respect to the transverse and the shear components, which show no particular trend with increasing M_c for these components. Also the reduction in the case of the stream-wise fluctuations with respect to the incompressible values was found to be much less than in the case of the cross-wise or the shear components, which show a significant decrease.

It was also seen by the authors that the normalized turbulent quantities *do not* become self-similar even in the regions where the velocity profiles become self-similar. This, using analogy to the analysis of Lumley [1986], was explained as due to the fourth order fluctuations which have a large influence over the mean turbulent quantities. If the turbulent shear were to be back-calculated from the mean velocity profiles, using eddy-viscosity hypothesis, they would obviously be self-similar (and were shown to be so by Samimy and Elliott [1990]), and was hence argued by Lumley [1986] that the eddy viscosity *certainly cannot* describe the evolution of the shear layer.

An interesting viewpoint of the mixing layer is from the aspect of frequency measurement. Frequency measurement of the perturbation gives a picture of the presence of coherent waves and an idea size of structures. This was done by Demetriades and Brower [1990] who presented the experimental analysis of laminar flow profiles in high speed shear layers, intensity and frequency of the fluctuations in laminar flow. Two test cases were selected with stream Mach numbers $M_1 = 2.9$, $M_2 = 2.29$ and $M_1 = 2.76$, $M_2 = 1.87$. Both streams were of Air. The RMS of the fluctuations measured is shown in **Fig 1.21**

Figure 1.20 shows the development of the free shear layer (FSL) and the development of the boundary layers (BL) with the stream-wise direction. It is seen from **Fig 1.20** that for about 200 momentum thicknesses (θ) of high speed stream equivalent of length, there is a relative quiescent region. After that there is a region of approximately the same distance of intensified instability. The observations are summarized in **Table 1.3**. It is apparent from the measurements that the increase in M_c has actually decreased the distance where the amplifications occur, however it must be pointed out that the two streams do not have the same r or s. Hence an isolated statement regarding stability depending on M_c alone cannot be made.

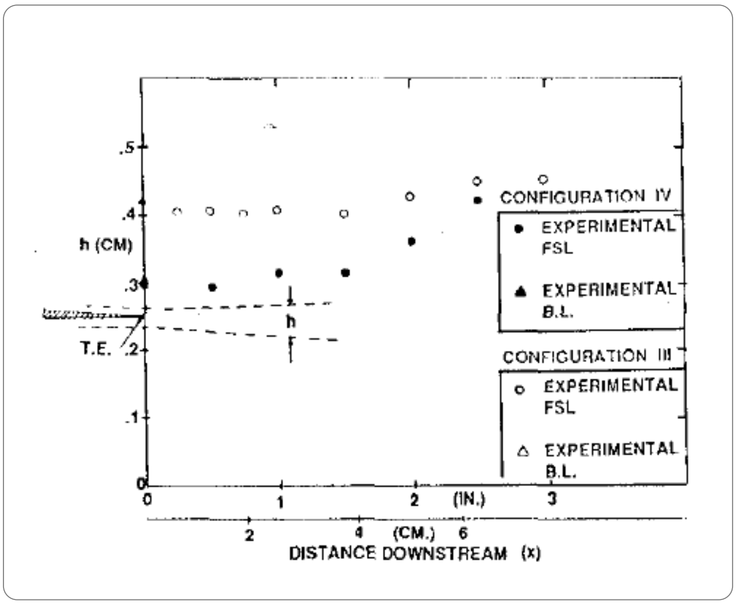

Figure 1.20: Growth of the mixing layer from Demetriades and Brower [1990] [*It is seen that there is an initial quiescent region after which the growth starts.*]

	Parameter	Config III Primary	Config III Secondary	Config IV Primary	Config IV Secondary
	Fluid	Air	Air	Air	Air
	Mach Number	2.9	2.29	2.76	1.87
	Velocity $[m/s]$	653	583	627	514
	Velocity Ratio (r)	0.89		0.82	
	Density Ratio (s)	0.94		0.909	
	M_c	0.145		0.225	
Start of growth	**from** δ **measurement**$[cm]$	4.6		3.8	
	from Schlieren images$[cm]$	5.8		3.8	
	from RMS measurement$[cm]$	5.1		1.8	
	from Spectrum$[cm]$	4.4		2.5	
	from $170[kHz]$ **frequency measurement**$[cm]$	5.7		4.6	
	Average$[cm]$	**5.1**		**3.3**	

Table 1.3: Test cases and transition distance of the cases of Demetriades and Brower [1990]

This instability was measured in their setup to be around $120[kHz]$. After this it is reported that the intensity of the instability decreases, the spectrum disperses, and flow width increases. The initial instability develops due to Kelvin Helmholtz instability, which occurs at a certain frequency, which in the

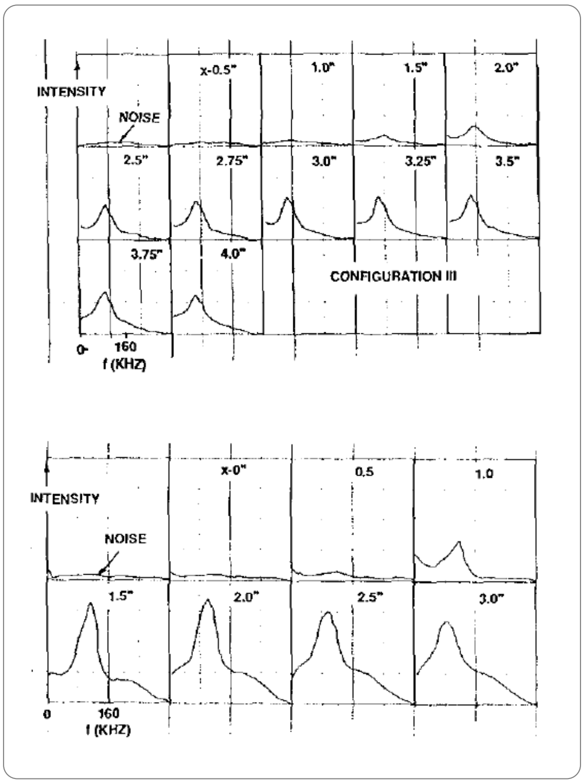

Figure 1.21: Frequency measurements from Demetriades and Brower [1990] [*Note the instability developing at about* $120[kHz]$ *and gradually spreading*]

present case happens at $120[kHz]$. This frequency for a characteristic velocity of $113[m/s]$ (the difference in the stream velocities) and a characteristic length of from $0.3[mm]$ where frequency is around $120[Hz]$ has a Strouhal Number of $St = fL/V \approx \frac{120\times10^3\cdot0.3\times10^{-3}}{113} = 0.318$. However, with process of growth of the structures and their merging, the frequency decreases and the bandwidth increases. It is estimated that 1000 θ distance is required to be able to attain completely random flows.

The above results tend to indicate that the beginning of growth is actually earlier in the case of higher M_c, however, the two cases are not at the same velocity ratio, and are not very far apart in M_c too. Hence, no generalization may be possible. However, the frequency distribution, and the intensity measurements of the velocity fluctuations at various locations is of value. The pattern indicates that the evolution of the flow first starts as a band limited instability which grows and becomes more and more broad banded with evolution.

All experiments till this point had the density ratio close to unity, at least not far from unity. So as to validate if the observations at usual laboratory conditions hold for conditions far from unity, Erdos et al. [1992] carried out experiments with mixing layers at hypervelocity conditions with different gasses, and M_c of 0.8 and 2.8.

Case	**N_2/N_2**		**H_2/N_2**		**H_2/Air**		**H_2O**	
Stream	Primary	Secondary	Primary	Secondary	Primary	Secondary	Primary	Secondary
Species	N_2	N_2	N_2	H_2	Air	H_2	O_2	H_2
$U[m/s]$	3807	640	3807	2387	3810	2387	3805	2387
$T[K]$	2444	102	2444	103	2443	103	2398	103
M	3.93	3.12	3.93	3.05	4.00	3.05	4.27	3.05
$p[Pa]$	21373		21373		21373		21373	
M_c	2.70		0.81		0.82		0.85	
r	0.17		0.63		0.63		0.63	
s	24.04		1.70		1.65		1.46	

Table 1.4: Test cases of Erdos et al. [1992]

The different test cases of Erdos et al. [1992] are presented in **Table 1.4**. The test conditions were chosen by them to be able to demonstrate the effect of high M_c and the effect of heat release. Laser holographic interferometer (LHI) was used to study the initial development. A typical case of H_2/N_2 case is shown in **Fig 1.22** which shows a distinct and a preferential growth on the secondary side of the stream.

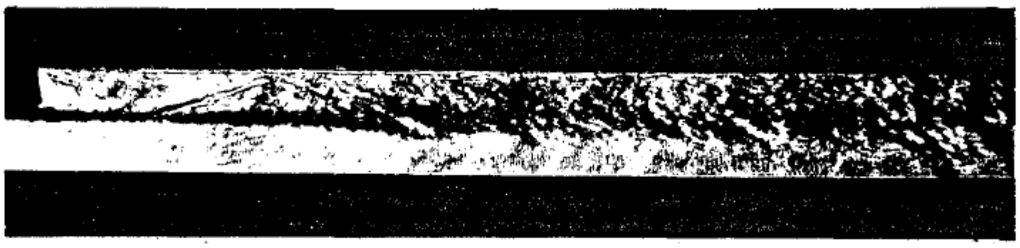

Figure 8c. Laser Holographic Schlieren for H_2/N_2 Case

Figure 1.22: Image of LHI from Erdos et al. [1992]
[*Note the asymmetric growth towards the secondary stream*]

The instrumentation of the experiment carried pressure transducers and heat flux measurement devices on the top and the bottom walls. These measurements, an example of which is show in **Fig 1.23**, indicate again a pronounced asymmetry in the heat transfer, but in a direction opposite to that of the visual growth. The heat transfer happens to the wall much later on the side of secondary stream than on the side of the primary stream.

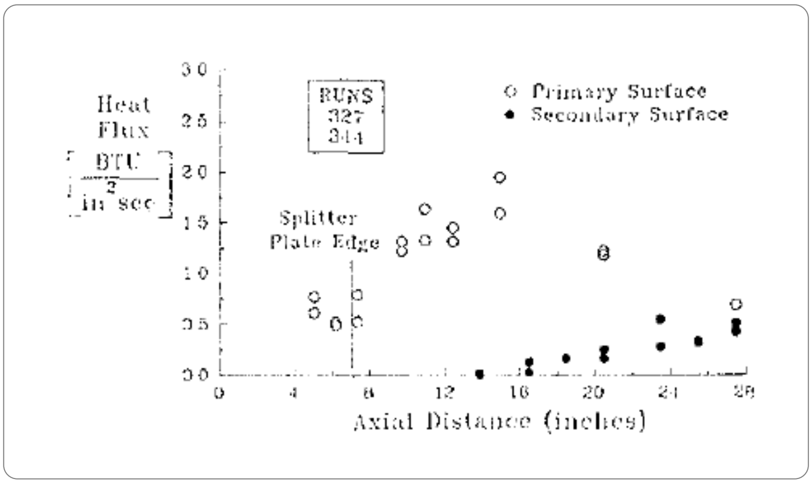

Figure 1.23: Heat flux measurements from the measurements of Erdos et al. [1992] $[1[BTU/(in^2 s)] \approx 1.635[MW/m^2]]$

Miller et al. [1993] studied the structure of a plane mixing layer between a supersonic, high-temperature, oxidizing stream and a subsonic, ambient-temperature, hydrogen-containing stream under compressible conditions and with low heat release. Visualization was done with OH/acetone PLIF (Planar Laser Induced Fluorescence). The structural features of the flow were presented. Subsequently, Miller et al. [1994] presented results where the increasing three dimensionality of the flow with increase in the M_c is demonstrated. Also the entrainment rates were investigated and it is shown that the entrainment ratio is closer to unity unlike in a incompressible mixing layer.

1.4.2 Theoretical and computational developments

Approximations and extensions to the incompressible mixing layer

The earliest approximations to predict the behaviour were presented by Favre [1964] who presented the Markovin hypothesis. This states that for boundary layers and wakes with free stream Mach numbers up to 5, and jets with Mach numbers up to 1.5, turbulence structures are close to the constant density flows, and the density fluctuations can be neglected. This was later modified by Bradshaw [1977] who reviewed Markovin hypothesis and substantiated the claims for boundary layers, free shear flows and duct flows. Citing the work of Papamoschou and Roshko [1988], it is stated that the density ratio plays a minimal role in determining the spread rate of a compressible mixing layer. Further, the paper claimed that, the breakdown of the Markovin hypothesis happens primarily due to pressure fluctuations and not due to density fluctuations. This article also has provided information on the skin friction coefficient, the correlation coefficients, and the spectrum shapes for different flows.

The implicit presence of the density term in the conservation equation makes the equations extremely unwieldy when the usual (Reynold's) averaging is used. Instead as Favre [1971] introduced, considerable simplification of the equations can be obtained if the averages of properties are density weighted. This removes the density fluctuations from the conservation equations. However the physical meaning of *Favre average* was unclear, and was considered to be an approximation to the Reynold's average. Laufer (see Birch et al. [1972]), however, reasoned that the pitot-static measurements of the flows are in fact the Favre averaged quantities rather than the conventional averages, thus giving a physical meaning to the Favre average.

An early attempt to predict the growth rate of the incompressible mixing layer, was made by Abramowich. However, as mentioned before, this did not consider the density differences. To be able to delineate the incompressible effects and the compressible effects, it was necessary to have a model for the incompressible growth rate at different density ratios. Dimotakis [1986] using simple arguments based on the geometrical properties of the large-scale flow structures derived expressions for the growth of two dimensional incompressible turbulent mixing layer. Konrad [1977] provided measurements of entrainment of different gasses for a mixing layer. Based on this, the author found that that the entrainment is approximately of the form

$$E_v(r,s) = s^{1/2} f(r) \tag{1.10}$$

Where

$$s \equiv \frac{\rho_2}{\rho_1} \text{ and } r \equiv \frac{U_2}{U_1}$$

It must be noted that the entrainment rates were investigated by Dimotakis [1986] experimentally had shown that the entrainment ratio is closer to unity unlike in a incompressible mixing layer, which is different from the assumption made here.

Assuming that in the frame of reference of the vortices, the entrainment velocities (v_{ix} where x is 1 for primary stream and 2 for secondary stream) would be a function of the respective characteristic velocity, it was proposed that

$$\frac{-v_{i1}}{U_1 - U_c} = \frac{v_{i2}}{U_c - U_2} = \epsilon(r,s) \implies \frac{-v_{i1}}{v_{i2}} = \frac{1-r_c}{r_c - r} \text{where } r_c \equiv \frac{U_c}{U_1} \tag{1.11}$$

Next assuming the match of the dynamic pressures, r_c was estimated to be

$$r_c(r,s) = \frac{1 + rs^{1/2}}{1 + s^{1/2}} \tag{1.12}$$

Assuming a geometric progression for the position of the vortices, that is $x_{n+1} = (1 + l/x)\, x_n$, and extrapolating from the available incompressible results, it was found that

$$\frac{l}{x} = 0.68 \frac{1-r}{1+r} \tag{1.13}$$

The product of the rate of growth of mixing layer and the distance between the adjacent vortices must be equal to the total entrainment volume. Thus

$$\frac{A_n}{t} = \frac{1}{2}\delta_n \left(x_{n+1} - x_{n-1}\right) = \epsilon \left(U_1 - U_c\right)\left(x_{n+1} - x_n\right) + \epsilon \left(U_c - U_2\right)\left(x_n - x_{n-1}\right) \tag{1.14}$$

Simplifying this, and substituting the values of r_c, $\frac{x}{l}$ and ϵ and transforming the equations to the frame of reference of the splitter plate, one arrives at

$$\boxed{\frac{d\delta}{dx} = \epsilon \left(\frac{1-r}{1+s^{1/2}r}\right)\left(1 + s^{1/2} - \frac{1 - s^{1/2}}{1 + 2.9\left(\frac{1+r}{1-r}\right)}\right)} \tag{1.15}$$

These predictions were shown, by the author to be in good agreement with measurements till then. At first, the equation 1.15 which depends on the velocity ratio and the density ratio alone, and not on the average velocity may seem surprising. The point to be noted in the derivation is that the rate of entrainment is directly proportional to the velocity, hence, canceling out the effect of the average velocity. This latter assumption is central to the growth rate equation.

For compressible turbulent mixing layers, the growth rate is assumed to be formed out of two effects, the incompressible effects, which accounts for the velocity ratio and the density ratio and the compressibility effects. **Eqn 1.15** is very often used in literature to provide a model for the incompressible effects.

Causes for reduced mixing layer growth rate with increased M_c

The reasoning behind the decreasing growth rates with increasing Mach number has been a topic of research for quite some time. Many researchers have approached the problem from the instability point of view.

The average velocity profile of the mixing layer is close to the tanh profile (in the case of a spatial mixing layer this state is reached at a distance of about 1000× momentum thickness (θ) as investigated by Demetriades and Brower [1990]). The flow profile, and the derivatives are shown in **Fig 1.24**.

It can be seen from **Fig 1.24**(c) that the velocity profile has an inflection point, and hence satisfies the Rayleigh [1879] criteria for instability . Further it can be seen from **Fig 1.24**(d) that Fjørtoft's criteria (Fjortoft [1950]) that $\dfrac{\partial^2 U}{\partial y^2}(U - U_I)$ must be negative at some point in the flow field, is also satisfied. These are necessary conditions for instability (though not sufficient). Hence a mixing layer becomes a strong candidate for instability. In fact the mixing layer undergoes the well known Kelvin Helmholtz instability.

Blumen [1970] extended the Rayleigh stability criterion and Howards semi-circle theorem to compressible flows. A subsonic neutral solution of the

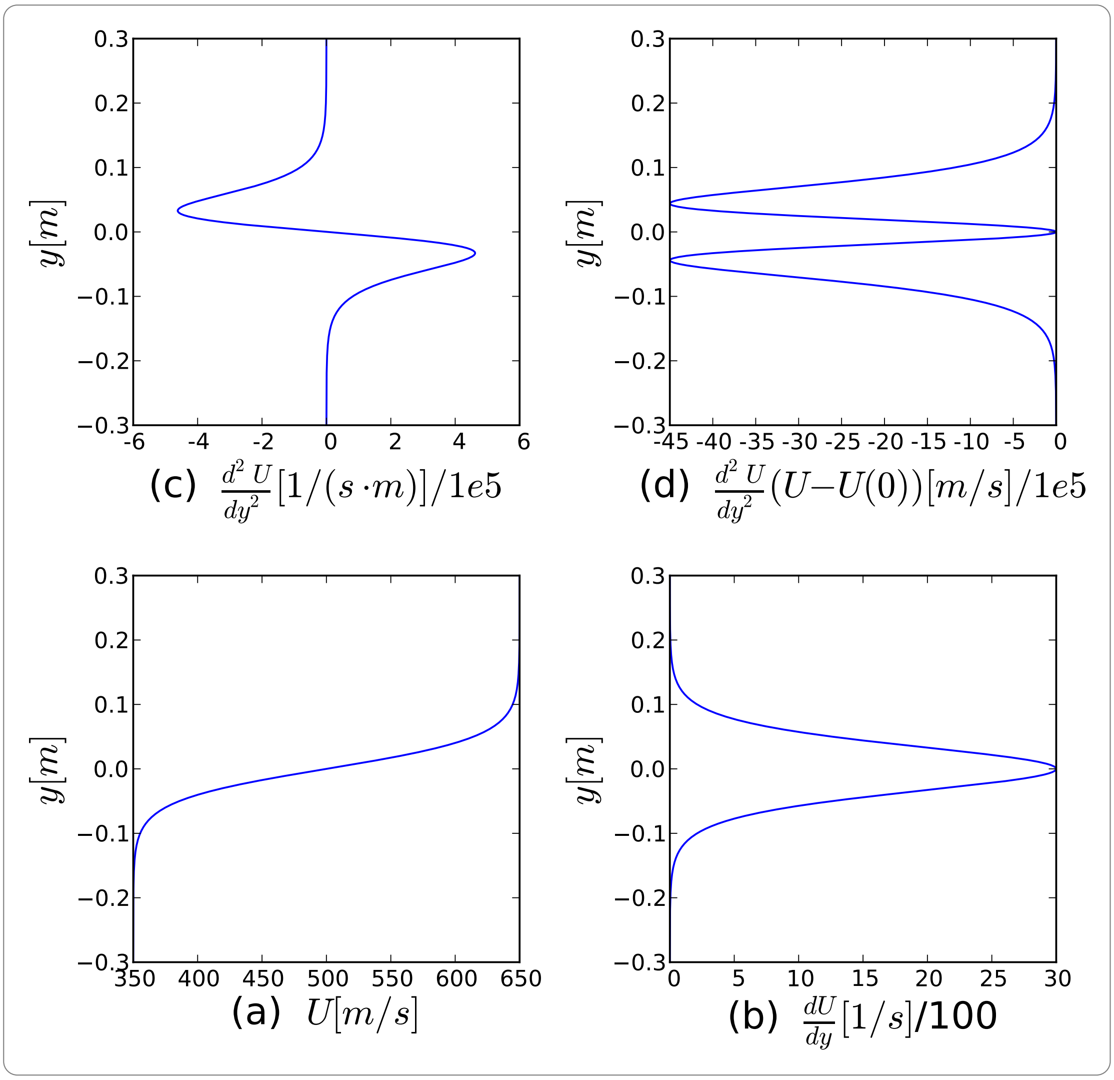

Figure 1.24: Instability Criteria
[*The velocity profile(a), the derivative of the velocity profile(b), the second derivative(c) and* $(U - U(0))\times$ *the second derivative(d)*]

stability equation was found for the hyperbolic-tangent velocity profile. With this he presented the unstable eigenvalues, eigenfunctions and Reynolds stresses by numerical methods. Blumen et al. [1975] describes the presence of a second supersonic mode. Blumen used a hyperbolic tangent profile as the base flow and a constant temperature fluid for the analysis. He showed that that the hyperbolic tangent profile is unstable for any value of Mach number, however large. The second mode occurs only at Mach number greater than 1. However, the amplification factor of this mode was shown to be one order less than the first mode. Later Drazin and Davey [1977] augmented the findings of Blumen et al. [1975] and presented a third mode of instability.

In addition to the contribution of Bogdanoff [1983] to the definition of convective Mach number M^{+}, he compared the results of the experiments with linear stability analysis and argued that the reduction in the growth rates at high convective Mach numbers is strongly coupled to the reduction in the amplification rates of the most unstable Kelvin-Helmholtz instability waves. He suggested that linear stability theory as an important tool for the understanding the reduced growth rate phenomenon. On these lines, Sandham and Reynolds [1989] performed linear stability analysis of small perturbations for the compressible mixing layer. The perturbations used by the author were of Blassius type laminar profile. The author compared the results with two and three dimensional temporal mixing layers. It was further shown by the author (see **Fig 1.25**) that the amplification rate of the most unstable wave decreases with M_c. They also showed that below M_c of about 0.6, two dimensional modes are more unstable than the three dimensional modes.

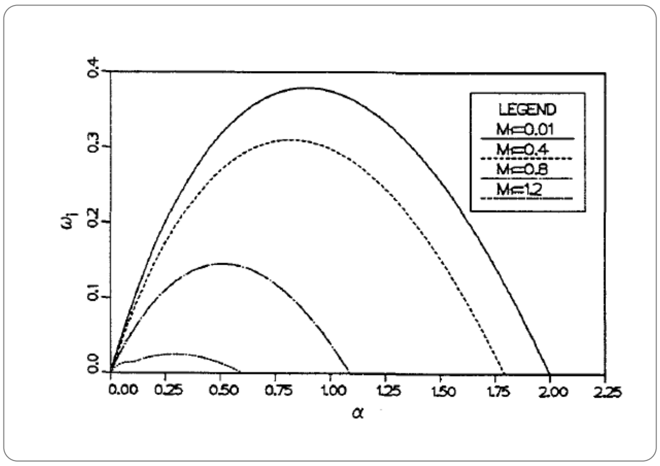

Figure 1.25: Temporal mixing layer amplification rates at different M_c from Sandham and Reynolds [1989]

Parallel to the linear stability approach, Papamoschou [1990] offered a physical explanation to the stabilizing effects of compressibility in shear layers. His line of argument was related to the region of influence of a perturbation in the field of supersonic mixing layer. Assuming that the wavelength of the disturbance is smaller than the characteristic dimension of the mixing layer, he calculated the radiation propagation of acoustic disturbances from a sender plane to a receiver plane, in the base field of averaged mixing layer, shown in **Fig 1.26**. By calculating the tubes of radiation, he made estimates of the energy reaching the receiver plane from the sender plane. He suggested that the compressibility distorts the rays from an acoustic source. This causes a *hindrance* in the communication of disturbances providing an inherent stability to the mixing layer.

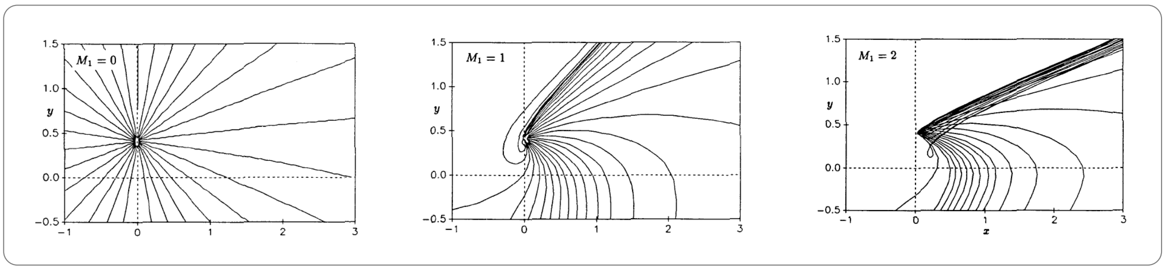

Figure 1.26: Ray diagrams from Papamoschou [1990]
[*Notice that the rays become skewed as M_1 increases*]

Later Papamoschou [1993] presented a quasi one-dimensional model for planar shear layer and estimated the total pressure loss due to turbulent mixing. Entropy production was found to be strongly coupled to the compressibility, and total pressure losses become significant with M_c increasing beyond 1.

This work was extended by Zhuang and Dimotakis [1995]. They extended the linear stability analysis for wake dominated flows, as in the case of a realistic spatial mixing layer. They performed the linear stability on flows with varying degrees of wake, and found that the presence of wake has a large influence on the mixing layer. They observed that the two dimensional modes are more dominant in the case of flows with wake. Further, a greater wake component can produce a larger amplification rates. A remarkable result was that the amplification rate of a flow with wake, *does not* decrease monotonically with increase in the M_c, unlike flows with no wake component.

The advent of digital computers, and development of the field of Computational Fluid Dynamics gave rise to the possibility of numerical simulations of the mixing layer. However the initial attempts using RANS computations failed to capture the reduced growth rate effect. Launder et al. [1972] compared the various turbulent models and showed that the RANS computations over predict the growth rate of the mixing layer.

Vreman [1995] presented Large Eddy and Direct Simulations of a temporal mixing layer and Vreman et al. [1996] presented the direct numerical simulation of a temporal mixing layer of M_c ranging from 0.2 to 1.2. The study showed the presence of two dimensional structures up to a M_c of 0.6, and oblique modes beyond M_c of 0.8.

One of the most important contributions of this work was the demonstration of the insignificance of dilatation dissipation and a demonstration that turbulence models based on the dilatation dissipation do not work for shear flows especially beyond a M_c of 0.3. It was shown that compressibility affects the production terms much more than the dissipation. By performing integrated analysis of the statistics of the flow, it was shown that the pressure strain term is responsible for the reduction in the growth rate.

Increase in the available computational power over the years paved way for the possibility of Direct Numerical Simulation of the flow, though not nearly so for a full spatial mixing layer, but for a homogeneous shear flow. One of the first contributions in the direction of the DNS of homogeneous mixing layer was by Sarkar et al. [1991b] who showed the importance of the *compressible dissipation*.

The authors claimed that the turbulence Mach number defined as

$$M_t \equiv \frac{q}{\langle c \rangle} \quad \begin{array}{l} \text{where } q^2 = 2\times \text{ T.K.E. } (\langle u_i' u_i' \rangle) \text{ , and} \\ \langle c \rangle \text{ is local average mean sonic speed} \end{array} \tag{1.16}$$

was expected to be a better measure of the compressibility effect, and showed through DNS of homogeneous turbulent flows that the compressible dissipation is directly related to M_t. The compressible dissipation arises out of the turbulent dissipation term $\left\langle \sigma_{ij}{}' u_{i,j}{}' \right\rangle$ which can be written for compressible isotropic turbulence as

$$\left\langle \sigma_{ij}{}' u_{i,j}{}' \right\rangle = \underbrace{\langle \mu \rangle \left\langle \omega_i{}' \omega_i{}' \right\rangle}_{\langle \rho \rangle \epsilon_s} + \underbrace{\frac{4}{3} \langle \mu \rangle \left\langle d'^2 \right\rangle}_{\langle \rho \rangle \epsilon_c} \tag{1.17}$$

Here ϵ_s represents solenoidal dissipation and ϵ_c represents compressible dissipation. Using asymptotic analysis and DNS for a homogeneous compressible turbulence it was shown that a good model for the ϵ_c term is

$$\epsilon_c = \alpha_1 M_t^2 \epsilon_s \tag{1.18}$$

The effect of the compressible dissipation is shown in **Fig 1.27**. It can be seen that the incorporation of the dilatation terms causes a decrease in the growth rate. However, it can also be seen that the decrease caused thus is much later, and lesser than what is observed experimentally.

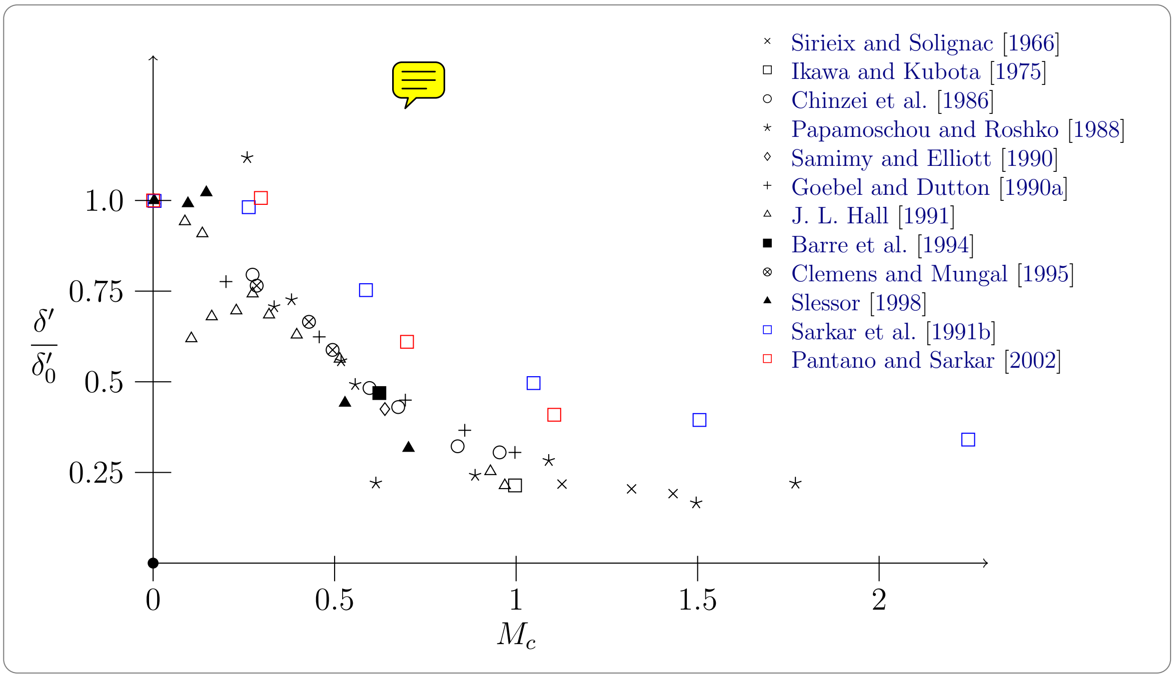

Figure 1.27: Results of Sarkar et al. [1991b] in light of experiments

This claim was however refuted by the same author in Sarkar [1995]. In this paper, the author defined the gradient Mach Number M_g for a homogeneous shear flow as

$$M_g \equiv \frac{Sl}{c} \text{ where } S \equiv \frac{\partial U}{\partial y} \text{ and } l \text{ is an integral length scale of turbulence} \tag{1.19}$$

The author describes two series of simulations, first with varying gradient Mach number, and second in with the turbulent Mach number is changed.

Conditions of the test (where $_0$ represents the initial conditions) are:

Case	M_{g0}	M_{c0}	Case	M_{g0}	M_{c0}
A1	0.22	0.40	**B1**	0.22	0.13
A2	0.44	0.40	**B2**	0.22	0.20
A3	0.66	0.40	**B3**	0.22	0.40
A4	1.32	0.40			

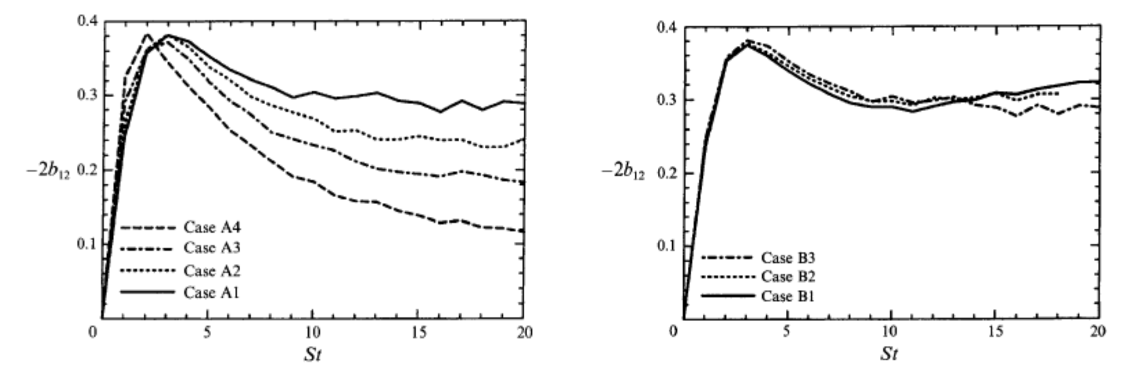

Figure 1.28: Cases of Sarkar [1995] and the influence of M_c and M_g on production
[b_{12} *refers to the normalized production term*]

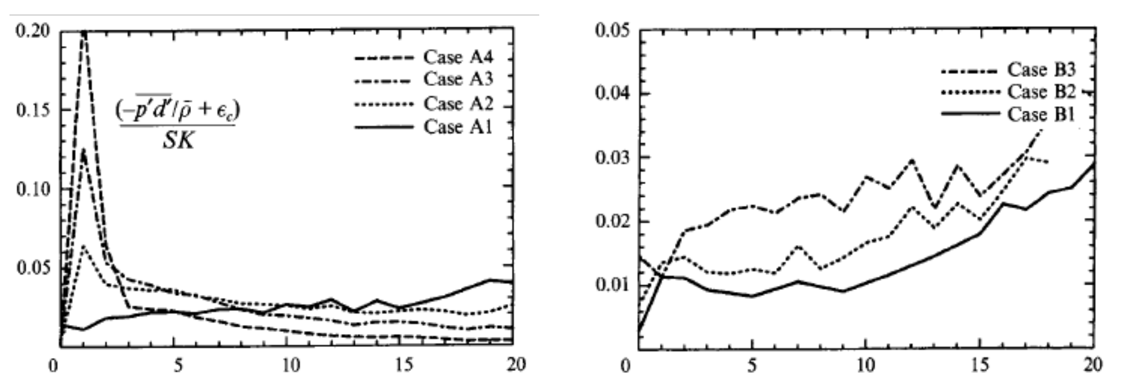

Figure 1.29: Dilatation effects observed in Sarkar [1995]
[*Notice that the dilatation effects are small*]

As shown in **Fig 1.28** the primary influence of M_{g0} is on the production, where as **Fig 1.29**, the compressible dilatation effect was shown to have little influence on the reduction of the growth rate. It is further shown that increase in M_g causes a decrease in the overall turbulent kinetic energy on the flow. This paper concluded that the compressibility effect of reduced turbulent energy growth rate in homogeneous shear flow is primarily due to the reduced level of turbulence production, and that explicit dilatation of the terms have little influence on the growth rate of the flow.

This stand was again changed by the same author in Pantano and Sarkar [2002] on the lines of Vreman et al. [1996]. They performed DNS simulations of a temporal mixing layer, with a *tanh* type initial velocity profile. The plot of the momentum thickness θ, with respect to normalized time is shown in **Fig 1.30**.

It can be seen from **Fig 1.30** that the compressibility effect of increase in the M_c is captured for the given mixing layer, and that the decrease matches with the *Langley curve*, though it over-predicts the growth rate in comparon to many other experiments. Even more discrepancies are visible when many other experimental results are plotted as in **Fig 1.27**.

The turbulent kinetic energy budget was performed to identify the parameter which was responsible for the decrease in the growth rate. This budget is shown in **Fig 1.31**. This figure clearly shows that there is a decrease in the production term with increase in M_c, where as the dissipation is almost unaffected.

The work also claimed that the normalized pressure-strain term decreases with increasing M_c, which is stated to lead to inhibited energy transfer from the stream-wise to cross-stream fluctuations, to the reduced turbulence production observed in DNS to finally lead to reduced turbulence levels as well as reduced growth rate of the shear layer. They also presented an analysis which shows that the pressure strain term decreases monotonically with increasing Mach number. The present work investigates these claims for the case of a spatial mixing layer.

Sankaran and Menon [2005] studied the mixing of passive scalars for a spatial mixing layer with LES. They simulated a single mixing layer with $M_c = 0.62$. They presented the comparison of the Gradient diffusion sub-grid

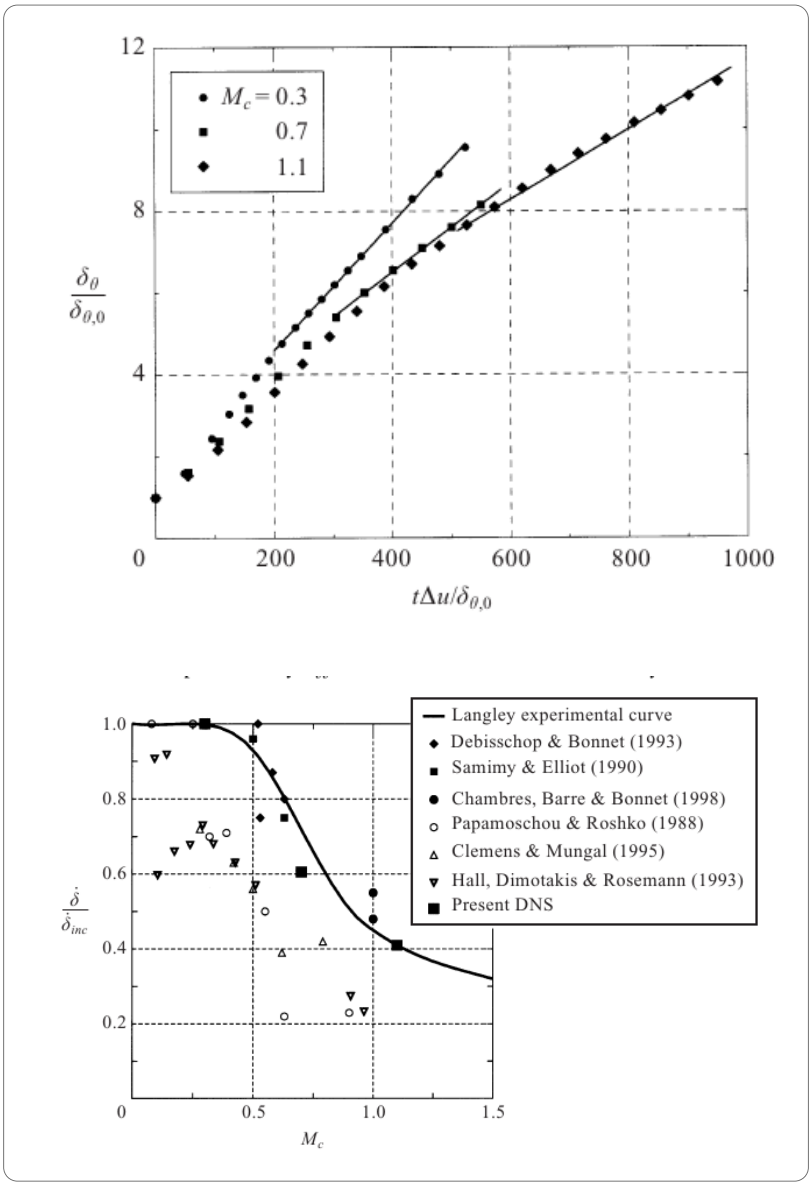

Figure 1.30: Growth of momentum thickness from Pantano and Sarkar [2002] [**Present DNS** *in the above refers to the work of Pantano and Sarkar [2002]*]

scale model with a new sub-grid scale model *LES-LEM* or the Linear Eddy Model. They validated the model with several experiments, and showed better predictions than the gradient diffusion methods. This work, however, does not focus on the issue of reduced growth rate in a spatial mixing layer.

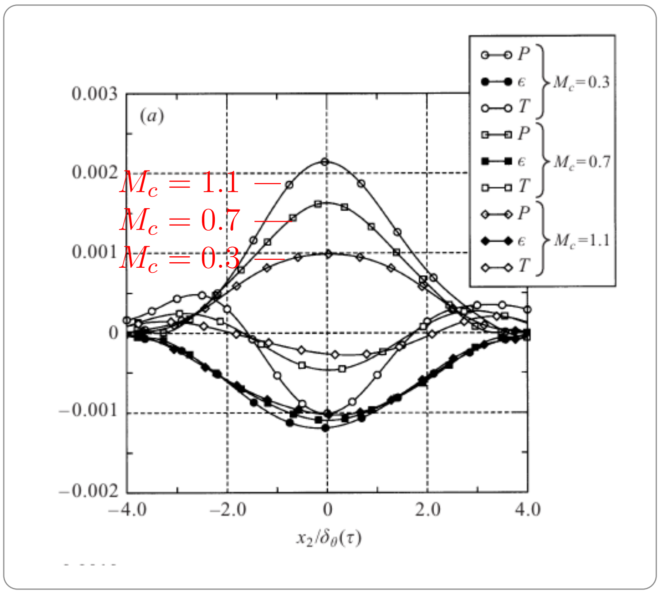

Figure 1.31: Turbulent Kinetic Energy budget from Pantano and Sarkar [2002] [**Note:** Here P represents the Production, T the transport and ϵ the dissipation]

1.5 Temporal and Spatial Mixing Layers

As was discussed in the previous sections, temporal mixing layers have been used by many researchers because they allow the implementation of periodic boundary conditions in the stream-wise direction, effectively reducing the size of the domain required for the computation. This allowed Sarkar et al. [1991a] to perform a direct simulation of a uniform shear flow. This was followed by Vreman [1995], who simulated a temporal mixing layer using both DNS as well as LES techniques. Later Pantano and Sarkar [2002] performed the temporal mixing layer analysis. The temporal mixing layer analysis provided valuable understanding of the behaviour of the mixing process. In summary, the understanding obtained from the above studies are that

- the growth rate reduction effect with increasing M_c of the mixing layer is captured by a temporal mixing layer,
- the initial thought that the dilatation dissipation plays a significant role in this effect was later shown to be not so,
- the turbulence production and pressure-strain coupling are the most important effects responsible for the growth rate reduction effect and

- the eddy viscosity is anisotropic.

However, there are certain limitations of a temporal mixing layer in that some effects of a spatial mixing layer cannot be captured by a temporal mixing layer. Mapping the results of a temporal mixing layer with periodic boundary conditions in the stream-wise directions to a realistic spatial mixing layer is not straight forward, and can be considered at best an approximation. Furthermore, temporal mixing layer cannot provide any information regarding the temporal statistics at a point in the flow field of a spatial mixing layer. For that a large set of simulations need to be performed and noting that a mixing layer is statistically stationary, the ensemble average can be stated to be the temporal average. However, computation intensity of DNS makes this approach infeasible. Another critical issue is that most of the studies presuppose and rely on self-similarity. In a temporal mixing layer, self-similarity may be attained in due course of time, but in the case of a spatial mixing layer, the distance available may not be sufficient to attain self-similarity, unless the conditions are favourable for this to happen. However, attainment of self-similarity is of much less concern for combustion, flame holding and mixing very close to the splitter plate are of greatest importance for initiating and sustaining supersonic combustion. Temporal mixing layers provide absolutely *no* way to incorporate this effect of a splitter plate.

1.6 Conclusions

It can be seen from the literature survey, that there is undeniable evidence for compressibility effects measured by the convective Mach number, delaying the instability of the mixing layer. The experimental works of Brown and Roshko [1974] clearly indicated that the effect was not of that related to the density ratio. Papamoschou and Roshko [1988] verified that the is indeed a compressibility effect which causes a reduction in the growth rate, and this was verified by other experiments of Goebel and Dutton [1990a], Samimy and Elliott [1990], Erdos et al. [1992] amongst others. All experimental evidence has been with spatial mixing layers. Linear stability does provide a few hints to the stability of the flow. However, it is known that the assumption for the linear stability of small perturbations, is almost immediately violated because of intense turbulent regimes. The processes that follow include roll up of the vortex sheet, formation of larger structures, merging of vortices, growth of the size of the structures and other phenomena which are not even remotely linear in nature. On the other hand, RANS calculations with the usual eddy viscosity model, have been shown to be of little use in predicting the growth rate of the spatial mixing layer. Direct numerical simulation results are very expensive, and even with the great strides in the computation capabilities in the recent years, remain to be untenable, especially for realistic domain sizes. Hence most of the DNS simulations performed, use the homogeneous turbulence as the model for mixing layer or temporal mixing layer. In the recent years the reason for the decrease in the growth rate with increasing M_c have pointed to important directions that have been widely debated. The inherent shortcomings of a temporal mixing layers have already been discussed in the previous sections.

On the other hand, where RANS does not provide the adequate prediction unless the critical modelling questions are addressed, and DNS appears not economical, Large Eddy Simulation provides a possible intermediate strategy for solution and provide inputs of value for modelling. LES of supersonic spatial mixing layer which is realistic with boundary layers over a splitter plate has not been performed with the aim to study the turbulence and reduction of growth rate with increasing M_c. The current work is aimed at filling up this gap.

The thesis consists of the following chapters, Chapter 2 introduces the reader to the governing equation in raw as well as the LES formulation, the boundary conditions and the methodology of solution. It then presents the grid dependence studies. Following this it presents the comparison with many of the existing experimental results. Finally, this chapter lays out the list of simulation cases which were used in the rest of the thesis. Chapter 3 presents many features of the mixing layer pertaining to the velocity field, the pressure field and the fluctuations of parameters. The frequency component is finally studied with respect to the flow parameters. Chapter 4 specifically studies the evolution of the turbulent stresses. This first presents the evolution equation of the shear stresses. This is followed by results obtained from the extraction and tracking the energy transactions in the flow. Chapter 5 first identifies the important terms needed to model the shear stresses, and then using the LES results formulates the model for the important components of the shear stress. The effective Prandtl number and Schmidt number too is obtained from the LES simulations. Using these a set of cases using URANS is simulated for tuning the constants of the model. Finally the tuned model is presented with the sensitivity analysis of the model constants. Chapter 6 first presents the evolution equation of entropy. This evolution equation is verified by convecting this field and comparing with the entropy obtained from the flow parameters. This is followed by a careful extraction and presentation of each source of entropy, and its variation with M_c. Chapter 7 takes an overview of the work accomplished, and throws some light on how the work may go forward.

Chapter 2

Simulation Methodology and Code Validation

As was discussed in the previous chapter, the crucial problem to be solved is the case of a spatial mixing layer at realistic conditions. The configuration of a mixing layer was also presented. This chapter lays the foundation of the rest of the work, where first, the equations describing the problem and the different models are described. This chapter then describes the methodology for solving these equations. The working of the solver, grid independence and comparisons with experiments are presented. The chapter closes with the enlisting of the test cases used to study the mixing layer.

The sections of this chapter are as follows

Section 2.1 discusses the mathematical equations which model the problem to be solved.

Section 2.2 describes the Large Eddy Simulation methodology, the details of the technique and its suitability for the current problem.

Section 2.3 describes the computation domain used for the calculation and the specifications of the mesh.

Section 2.4 describes the computation domain used for the calculation and the specifications of the mesh.

Section 2.5 describes the solution technique adopted for solving the set of equations. This describes the implementation of the solver as well as the boundary conditions.

Section 2.6 describes the technique adopted and the analysis of the time required to obtain the estimate of averages with the required level of confidence.

Section 2.7 shows the influence of the mesh size on the results, which is a necessary condition for confidence in precision of the results.

Section 2.8 describes the results obtained by simulating conditions similar to some experiments and comparing the results with those experiments.

Section 2.9 describes the fundamental parameters of the problem and the determination of the configuration of numerical experiments. Using this, three sets of cases used for further analysis are listed.

2.1 Governing Equations

The mathematical equations which govern the problem of supersonic flows, including the supersonic mixing layer are listed in **Table 2.1**

2.1.1 Property Models

The fluid properties are generally considered to be a function of the temperature. Many models exist for the modelling of these properties. The property model used in the current simulation are described below.

Viscosity is modelled with the model provided by Sutherland [1893], which is perhaps the most commonly used model for viscosity. The model is

$$\boxed{\mu = \mu_0 \frac{T_0 + C}{T + C} \left(\frac{T}{T_0} \right)^{2/3}} \tag{2.16}$$

Where μ_0 is the reference viscosity at T_0, the reference temperature, and C is a constant. The constants used are shown in **Table 2.2**.

Thermodynamic Property of C_p is modelled according to the model provided by McBride et al. [1993]. This model is shown in **Table 2.3**

Equation Name		Equation	
Continuity equation		$\frac{\partial \rho}{\partial t} + \frac{\partial \rho u_i}{\partial x_i} = 0$	(2.1)
Momentum Conservation		$\frac{\partial \rho u_i}{\partial t} + \frac{\partial \rho u_j u_i}{\partial x_j} = -\frac{\partial p}{\partial x_i} + \frac{\partial \sigma_{ij}}{\partial x_j}$	(2.2)
	Reduced to	$\rho\left(\frac{\partial u_i}{\partial t} + u_j \frac{\partial u_i}{\partial x_j}\right) = -\frac{\partial p}{\partial x_i} + \frac{\partial \sigma_{ij}}{\partial x_j}$	(2.3)
	Where	$\sigma_{ij} \equiv 2\mu\left(S_{ij} - \frac{1}{3} S_{kk}\delta_{ij}\right)$	(2.4)
		$S_{ij} \equiv \frac{1}{2}\left(\frac{\partial u_i}{\partial x_j} + \frac{\partial u_j}{\partial x_i}\right)$	(2.5)
Energy Equation in e_t		$\rho\left(\frac{\partial e_t}{\partial t} + u_i \frac{\partial e_t}{\partial x_i}\right) = -\frac{\partial u_i p}{\partial x_i} + \frac{\partial u_j \sigma_{ij}}{\partial x_i} + \frac{\partial}{\partial x_i} k \frac{\partial T}{\partial x_i}$	(2.6)
	Where	$de = c_v dT$	(2.7)
		$e_t = e + \frac{u_i u_i}{2}$	(2.8)
Energy Equation in e		$\rho\left(\frac{\partial e}{\partial t} + u_i \frac{\partial e}{\partial x_i}\right) = -p\frac{\partial u_i}{\partial x_i} + \sigma_{ij}\frac{\partial u_j}{\partial x_i} + \frac{\partial}{\partial x_i} k \frac{\partial T}{\partial x_i}$	(2.9)
Energy Equation in h		$\rho\left(\frac{\partial h}{\partial t} + u_i \frac{\partial h}{\partial x_i}\right) = \left(\frac{\partial p}{\partial t} + u_i \frac{\partial p}{\partial x_i}\right) + \sigma_{ij}\frac{\partial}{\partial x_j} u_i + \frac{\partial}{\partial x_i} k \frac{\partial T}{\partial x_i}$	(2.10)
	Where	$h \equiv e + \frac{p}{\rho}$	(2.11)
		$dh = c_p dT$	(2.12)
Ideal Gas equation		$p = \rho R T$	(2.13)
	Where	$R = \frac{\mathcal{R}}{W}$	(2.14)
Mass diffusion equation		$\rho\left(\frac{\partial Y_j}{\partial t} + u_i \frac{\partial Y_j}{\partial x_i}\right) = \frac{\partial}{\partial x_i}\mathcal{D}\frac{\partial Y_j}{\partial x_i}$	(2.15)

Table 2.1: List of governing equations

The value of the coefficients a_1 to a_7 are presented in MacBride [1963]. This model provides equations which map the temperature to the different properties. In the case where the reverse mapping is required, as in the case of obtaining the temperature from enthalpy, Newton-Raphson technique is generally employed.

Fluid	$C[K]$	$T_0[K]$	$\mu_0[Pa.s]$
Air	120	291.15	18.27×10^{-6}
Nitrogen	111	300.55	17.81×10^{-6}
Argon	110	300.55	1.458×10^{-6}
Hydrogen	72	293.85	8.76×10^{-6}
Helium	79.4	273	19×10^{-6}

Table 2.2: Sutherland Coefficients

Parameter	Model	
	$\frac{c_{p0}}{R} = a_1 + a_2T + a_3T^2 + a_4T^3 + a_5T^4$	(2.17)
	$\frac{h_0}{RT} = a_1 + a_2\frac{T}{2} + a_3\frac{T^2}{3} + a_4\frac{T^4}{4} + a_5\frac{T^4}{5} + \frac{a_6}{T}$	(2.18)
	$\frac{s_0}{R} = a_1 \ln(T) + a_2T + a_3\frac{T^2}{2} + a_4\frac{T^3}{3} + a_5\frac{T^4}{4} + a_7$	(2.19)

Table 2.3: Thermodynamic models for c_p, h_0 and s_0 [McBride et al., 1993]

2.2 Large Eddy Simulation (LES)

The mixing layer is a flow which is known to be unstable by the Kelvin-Helmholtz instability, which causes a roll up of the contact surface. This forms distinct large scale structures, which have been widely reported in the experiments. These large scale structures carry most of the energy and the bulk of the turbulent mixing of momentum, energy and species happens due to these large scale structures. The largest scales of turbulence are typically the same scale as that of the cross-wise height of the domain. These scales obtain their energy from the mean flow and they pass on this energy through the turbulence cascade to the smallest sizes where the viscosity effects are strong and the energy is dissipated into random fluctuations meaning sensible heat. It is known that the formation of larger structures is an inviscid process and hence the energy passed down the cascade too is. The larger the turbulent energy production the smaller the smallest scales are. To be able to obtain the *com-*

plete picture of the turbulent flows, it is necessary to simulate accurately *all* the scales of turbulence, right up to the smallest scales. This is called Direct Numerical Simulation (DNS). With increase in the Reynolds number of the flow, the disparity of the scales goes on increasing. Given the largest scales in the flow are of the scale l, and the characteristic Reynolds number is Re, the Kolmogorov scale η is given by

$$\frac{\eta}{l} \sim \mathrm{Re}^{-3/4} \tag{2.20}$$

We can see that as the Reynolds number increases the size of the smallest scale goes on decreasing. A typical supersonic combustion chamber has a Reynolds number of the order of 10^6 to 10^7 and a Kolmogorov length scale of about $1\mu m$ [1]. To be able to resolve all the scales, one needs a mesh size of approximately one tenth of the smallest scales. This means a mesh size of the order of $0.1\mu m$ is required for DNS which is prohibitively small even for modest domain sizes. It is also seen that while most of the energy is contained in the larger eddies and mixing process and turbulence cascade process also starts at the larger scales, in DNS a large effort is spent in simulating the smallest scales.

In most engineering applications, the mean flow parameters are the most important ones. The closure problem of turbulence makes solving only for the mean flow properties, which would have been extremely useful, impossible. However the unclosed terms can be closed using models. This set of equations is called the Reynold's Averaged Navier Stokes equations, and a vast variety of models are available for closing the set of equations. However, this technique has its drawbacks due to the fact that all models are at best, approximations based on assumptions. These models are seldom universal, and often assume conditions like isotropy of turbulence, which is far from the prevailing conditions in a practical flow. Being so, these closure models cannot be considered universal, and often have to be tuned for each class of problems. In particular, Launder et al. [1972] shows that the growth rate in compressible regimes is

[1] To give an example of how small the Kolmogorov scales are, in a typical supersonic combustion chamber, where the velocity scales are about 500m/s, the viscosity is say 1e-5, and length scale is 0.1m for the mixing eddies, Re $\approx 5 \times 10^-6$ and $\eta \approx 1 \times 10^{-6} m$

over-predicted by the RANS closure models.

It is here that Large Eddy Simulations (LES) try to strike an optimum. LES simulates accurately the larger scales and models only the smaller ones [Smagorinsky, 1963]. Furthermore, the larger scales are often anisotropic. As the energy cascades down the turbulence scales, the turbulence becomes more isotropic [Tennekes and Lumley, 1972]. This makes the sub-grid scale models more universal and less influenced by the boundary conditions than in the case of RANS modelling, where all the scales are modelled [Piomelli, 1997].

Jimenez and Moser [2000] and Lucor et al. [2007] have conducted detailed study on the working of the SGS models, in particular the Smagorinsky class of models. They have shown that the SGS models predict the sub-grid scale stresses rather poorly, however the dissipation provided by these models, more or less matches the production by the large scale. In LES, since the large scales are exactly computed, hence the production calculations are quite accurate. The sub-grid scale models tend to mop up whatever energy is passed down to it through the energy cascade. Hence even if the stress calculations at the grid level are inaccurate, the large scale structures are captured pretty accurately by LES, even if the flow fields at length scale close to the grid scale may be inaccurate. In fact, Jimenez and Moser [2000] showed that the SGS models are extremely robust even to the choice of the model constants, as far as the large scale averages and the large scale structures are concerned.

In the case of a spatial mixing layer, this has an added advantage. The errors developed in the flow field are washed away in course of the simulations, and do not accumulate, which would have caused a divergence in the results as in the case of a temporal mixing layer.

2.2.1 Filtering

Filtering is the process in which the Larger scales (spatial as well as temporal) of turbulence are retained and the smaller scales are rejected. Thus filtering in the sense of LES is the application of a high pass filter in spatial and temporal domain (and hence a low pass filter in frequency and wave number domain). Filtering is mathematically defined as the convolution

$$\overline{\phi}\,(\boldsymbol{x},t) = G\,(\boldsymbol{x},t) \star \phi\,(\boldsymbol{x},t) = \int\limits_{t=-\infty}^{\infty} \iiint\limits_{\xi=-\infty}^{\infty} \phi\,(\boldsymbol{\xi},t')\,G(\boldsymbol{x}-\boldsymbol{\xi},t-t')d^3\xi dt \quad (2.21)$$

Where $\star$ represents convolution and G the convolution kernel which is characteristic of the filter. The same can be represented in Fourier space as

$$\widehat{\overline{\phi}}\,(\boldsymbol{k},\omega) = \widehat{\phi}\,(\boldsymbol{k},\omega)\,\widehat{G}\,(\boldsymbol{k},\omega) \text{ or simply, } \widehat{\overline{\phi}} = \widehat{\phi}\widehat{G} \quad (2.22)$$

We further define the *unresolved* as the difference between the original parameter and the resolved component that is

$$\phi'\,(\boldsymbol{x},t) = \phi\,(\boldsymbol{x},t) - \overline{\phi}\,(\boldsymbol{x},t) \quad (2.23)$$

Thus

$$\phi'\,(\boldsymbol{x},t) = (1 - G\,(\boldsymbol{x},t)) \star \phi\,(\boldsymbol{x},t) \quad (2.24)$$

Properties of Filtering Kernel

This convolution has certain properties which need to be noted (Germano et al. [1992], Sagaut [2006])

Conservation of Constants Filtering a constant yields the same value

$$\overline{a} = a \Longleftrightarrow \int\limits_{t=-\infty}^{\infty} \iiint\limits_{\xi=-\infty}^{\infty} G(\boldsymbol{x}-\boldsymbol{\xi},t-t')d^3\xi dt = 1 \quad (2.25)$$

Linearity The filtering operation is linear

$$\overline{\phi+\psi} = \overline{\phi} + \overline{\psi} \quad (2.26)$$

Commutation with derivative The filtering operation is expected to be commutating with derivative

$$\overline{\frac{\partial \phi}{\partial s}} = \frac{\partial \overline{\phi}}{\partial s} \tag{2.27}$$

To analyse the commutation property we define the commutator $[\cdot, \cdot]$ of two operators $\mathcal{G}$ and $\mathcal{H}$ as the difference caused in changing the order of application

$$[\mathcal{G}, \mathcal{H}] (\phi) \equiv \mathcal{G} (\mathcal{H} (\phi)) - \mathcal{H} (\mathcal{G} (\phi)) \tag{2.28}$$

With this definition the above criteria with $\mathcal{G} = G\star$ and $\mathcal{H} = \dfrac{\partial}{\partial s}$ implies

$$\left[G\star, \frac{\partial .}{\partial s} \right] = 0 \tag{2.29}$$

After the enumeration of the properties the filters have, we now observe a property a filter in general does not have

$$\overline{\overline{\phi}} \neq \overline{\phi} \implies G \star G \star \phi \neq G \star \phi \tag{2.30}$$

Also

$$\overline{\phi'} \neq 0 \implies G \star (1 - G) \star \phi \neq 0 \tag{2.31}$$

Favre Filtering

In the case of compressible flows addition of the weight of density to the filter makes the equation easier to solve. Hence we define

$$\widetilde{\phi} \equiv \frac{\overline{\rho \phi}}{\overline{\rho}} \implies \overline{\rho \phi} = \overline{\rho}\, \widetilde{\phi} \tag{2.32}$$

An important point to be borne in mind is that in actual calculation the filter is dictated by the numerical schemes and is not explicitly provided for the simulation. The variables that we solve for are in fact the filtered variables, and the dissipation effect is provided by the SGS model, which provents the pile up of the energy near the effective cutoff frequency.

2.2.2 Filtering of Governing equations

Filtering the Compressible Navier Stokes equations gives the equations of the filtered variables. We seek a closed form equation in terms of the filtered variables [Piomelli, 1997].

Continuity Equation

Filtering the mass conservation equation (**Eqn 2.1**) yields

$$\boxed{\frac{\partial \overline{\rho}}{\partial t} + \frac{\partial \overline{\rho}\, \widetilde{u}_i}{\partial x_i} = 0} \tag{2.33}$$

This shows that Favre averaged velocity and average density field satisfy the continuity equation.

Momentum Equation

Filtering the momentum equation (**Eqn 2.2**) gives

$$\frac{\partial \overline{\rho}\, \widetilde{u}_i}{\partial t} + \frac{\partial \overline{\rho}\, \widetilde{u_j u_i}}{\partial x_j} = -\frac{\partial \overline{p}}{\partial x_i} + \frac{\partial \overline{\sigma_{ij}}}{\partial x_j} \tag{2.34}$$

We define a term

$$\tau_{ij}^{\text{sgs}} \equiv \overline{\rho}\,(\widetilde{u_i u_j} - \widetilde{u}_i\, \widetilde{u}_j) \tag{2.35}$$

Substituting this in **Eqn 2.34** we get

$$\frac{\partial \overline{\rho}\, \widetilde{u}_i}{\partial t} + \frac{\partial \overline{\rho}\, \widetilde{u}_j\, \widetilde{u}_i}{\partial x_j} = -\frac{\partial \overline{p}}{\partial x_i} + \frac{\partial \overline{\sigma_{ij}}}{\partial x_j} - \frac{\partial \tau_{ij}^{\text{sgs}}}{\partial x_j} \tag{2.36}$$

On using **Eqn 2.33** we get

$$\boxed{\overline{\rho}\left(\frac{\partial \widetilde{u}_i}{\partial t} + \widetilde{u}_j \frac{\partial \widetilde{u}_i}{\partial x_j}\right) = -\frac{\partial \overline{p}}{\partial x_i} + \frac{\partial \overline{\sigma_{ij}}}{\partial x_j} - \frac{\partial \tau_{ij}^{\text{sgs}}}{\partial x_j}} \tag{2.37}$$

The term τ^{sgs} itself cannot be expressed in terms of the filtered quantities and this must be modelled. This term appears due to the closure problem of turbulence. There are various models proposed for the modelling of this term few of which are briefly discussed in **Sect 2.2.3**

Energy equation

Filtering **Eqn 2.9** we get

$$
\begin{aligned}
\overline{\rho}\left(\frac{\partial \widetilde{e}}{\partial t}+\widetilde{u}_i\frac{\partial \widetilde{e}}{\partial x_i}\right) &= -\,\overline{p}\,\frac{\partial \widetilde{u}_i}{\partial x_i}-\underbrace{\left(\overline{p\frac{\partial u_i}{\partial x_i}}-\overline{p}\,\frac{\partial \widetilde{u}_i}{\partial x_i}\right)}_{\text{SGS pressure dilatation term}} \\
&+\overline{\sigma_{ij}}\,\frac{\partial\,\overline{u}_j}{\partial x_i}+\underbrace{\left(\overline{\sigma_{ij}\frac{\partial u_j}{\partial x_i}}-\overline{\sigma_{ij}}\,\frac{\partial\,\overline{u}_j}{\partial x_i}\right)}_{\text{SGS dissipation}} \\
&\underbrace{-\frac{\partial}{\partial x_i}\left(\overline{\rho}\,\widetilde{u_i e}-\overline{\rho}\,\widetilde{u}_i\,\widetilde{e}\right)}_{\text{SGS energy flux term}} \\
&+\frac{\partial}{\partial x_i}k\frac{\partial\overline{T}}{\partial x_i}
\end{aligned}
\tag{2.38}
$$

Where the terms to be modelled are

SGS energy flux term is the most dominant term to be modelled. This represents the flux of energy due to sub-grid scale velocities.

SGS dissipation term represents the conversion of the kinetic energy to heat due to sub grid scale viscous dissipation. This term is considered small and usually neglected.

SGS pressure dilatation term represents the work done due to sub grid scale pressure fluctuations coupling with the sub grid scale dilatations. Even this terms is often neglected.

Vreman [1995] and Vreman et al. [1995] showed that for high Mach numbers the SGS dissipation term, and the SGS pressure dilatation terms are reasonable large and should be considered for better match with DNS results, and proposed a scale similar model for these terms.

The energy equation can also be written in the form of enthalpy, as in **Eqn 2.10**. When this equation is filtered we get

$$
\begin{aligned}
\overline{\rho}\left(\frac{\partial \widetilde{h}}{\partial t} + u_i \frac{\partial h}{\partial x_i}\right) &= \frac{\partial \overline{p}}{\partial t} + \widetilde{u}_i \frac{\partial \overline{p}}{\partial x_i} \\
&+ \underbrace{\left(\overline{u_i \frac{\partial p}{\partial x_i}} - \widetilde{u}_i \frac{\partial \overline{p}}{\partial x_i}\right)}_{\text{SGS velocity pressure gradient coupling}} \\
&+ \overline{\sigma_{ij}} \frac{\partial \overline{u}_j}{\partial x_i} + \underbrace{\left(\overline{\sigma_{ij} \frac{\partial u_j}{\partial x_i}} - \overline{\sigma_{ij}} \frac{\partial \overline{u}_j}{\partial x_i}\right)}_{\text{SGS dissipation}} \\
&\underbrace{- \frac{\partial}{\partial x_i}\left(\overline{\rho}\, \widetilde{u_i h} - \overline{\rho}\, \widetilde{u}_i \widetilde{h}\right)}_{\text{SGS enthalpy flux term}} \\
&+ \frac{\partial}{\partial x_i} k \frac{\partial \overline{T}}{\partial x_i}
\end{aligned}
\tag{2.39}
$$

The above formulation gives the SGS velocity-pressure gradient term and the SGS enthalpy flux term , which can be shown to be related to the SGS pressure dilatation terms and the SGS energy flux term.

2.2.3 Sub-grid Scale Models

The closure problem of turbulence, gives rise to the terms like τ^{sgs} which cannot be exactly expressed as closed form expression in terms of the filtered variables. This leads to the next step of being able to model this term in terms of known filtered quantities. This models are aptly called the sub-grid scale models. The most researched and the most important model is the model for the sub-grid scale stress term τ^{sgs}, which appears both in the compressible as well as the incompressible momentum equation. The first model for SGS was the Smagorinsky model [Smagorinsky, 1963], of which variations were worked out like the dynamic model of Germano et al. [1991] and Lilly [1992], and the scale similarity model of Bardina et al. [1980]. A mixture of the models was proposed by Leonard [1974]. Erlebacher et al. [1992] provided a foundation to the LES of compressible flows and presented a mixed model for the compressible isotropic turbulence. We describe here only the *One Equation Eddy Viscosity Model*, which is used in the present work.

One Equation Eddy Viscosity Model

Schumann [1975], Yoshizawa and Horiuti [1985] and Kim and Menon [1999] proposed another model for the sub-grid scale stresses. This method is based on calculating the sub-grid scale viscosity based on the sub-grid scale kinetic energy. This method basically states

$$\nu_{sgs} = C_m \Delta \sqrt{q_{\text{sgs}}} \tag{2.40}$$

Where

$$q^2_{\text{sgs}} = \frac{1}{2}\left(u_i{}' u_i{}'\right) \tag{2.41}$$

q_{sgs} itself is solved with a separate evolution equation, with models for turbulent dissipation and the turbulent diffusion terms.

$$\frac{\partial q^2_{\text{sgs}}}{\partial t} + \frac{\partial \widetilde{u_j}\, q^2_{\text{sgs}}}{\partial x_j} = -\tau_{ij}\,\overline{S}_{ij} - C_1 \frac{(q^2_{\text{sgs}})^{\frac{3}{2}}}{\overline{\Delta}} + C_2 \frac{\partial}{\partial x_j}\left(\Delta \sqrt{q^2_{\text{sgs}}}\frac{\partial q^2_{\text{sgs}}}{\partial x_j}\right) + \nu \frac{\partial^2 q^2_{\text{sgs}}}{\partial x_j \partial x_j} \tag{2.42}$$

Where the model constants C_1, and C_2 were given as 1 and 0.1 respectively by Yoshizawa and Horiuti [1985] and 1 and 0.094 respectively by Schumann [1975].

The obvious advantage of models where the eddy is considered to be a proportional to the turbulent kinetic energy is that in the regions where the flow tends to become laminar with respect to the grid scales, the eddy viscosity tends to become zero, as must be the case. It was observed that as predicted by Jimenez and Moser [2000], the average quantities were rather insensitive to the selection of the SGS model, at least for the current class of simulations of a spatial mixing layer. The model in this study was the one equation eddy model as Kim and Menon [1999] had proven this model to be quite accurate for temporal mixing layer simulations.

2.3 Domain And Mesh

2.3.1 Domain and conventions

The domain for the solution is rectangular, with a splitter plate on the inlet side separating the primary and the secondary streams. The bounding surfaces of the domain of interest are shown in **Fig 2.1**. Also shown is the direction of the coordinate system, and the names of the direction. These direction name convention is used throughout the work. Also to be mentioned is that the origin is at the center of the trailing face of the splitter plate, both in the span-wise direction as well as in the cross-wise direction.

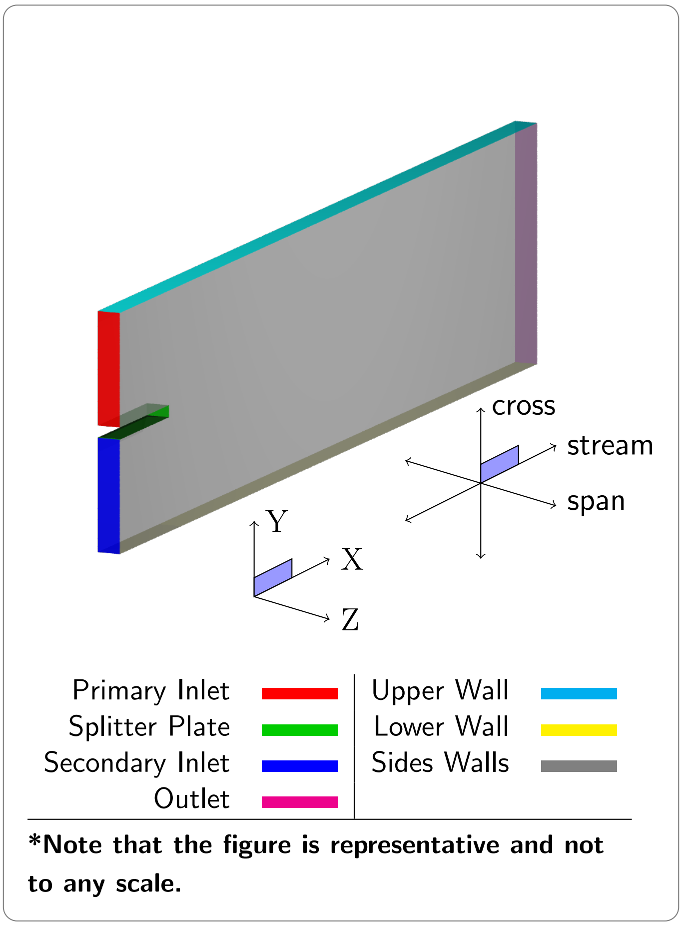

Figure 2.1: Domain bounding surfaces, coordinate system and directions

The flow enters the domain through the primary and the secondary inlet surfaces, mixes in the domain and flows out of the domain through the outlet.

As we shall see later, the growth of the boundary layer primarily, causes an increase in the pressure in the stream-wise direction. To be able to maintain a near zero stream-wise pressure gradient, in some of the simulations, a slight divergence is provided in the upper and lower walls. The divergence is attained through a region of smooth bend of a relatively large radius of curvature, to prevent causing strong expansion fans and to disturb the flow minimally.

2.3.2 Mesh

The mesh used is Cartesian mesh, all elements are rectangular elements.

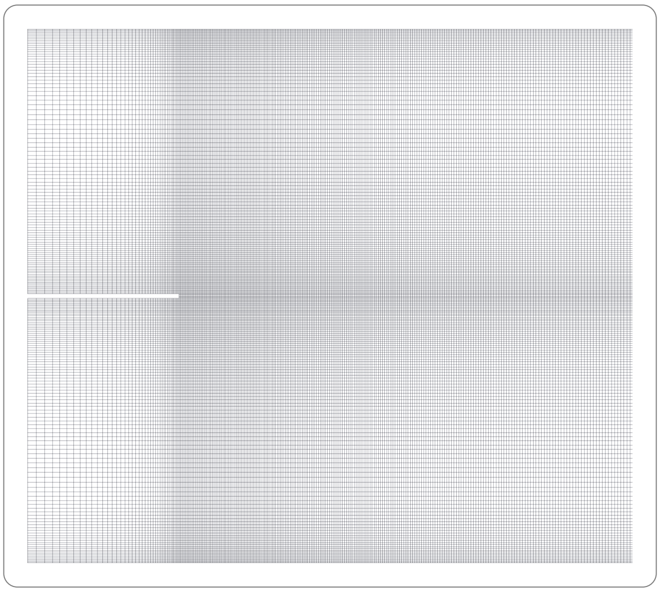

Figure 2.2: Mesh near splitter plate
[*Notice the fine mesh near the trailing edge of the splitter plate*]

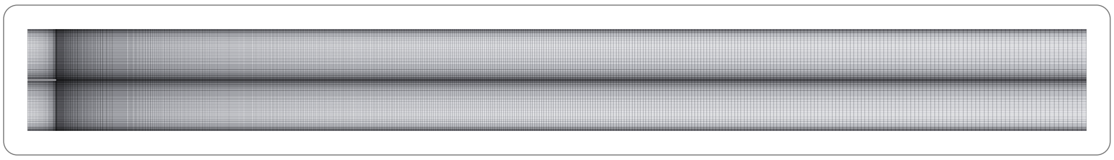

Figure 2.3: Full Mesh
[*Notice the fine mesh in the central region and near the walls*]

Figure 2.2 and **Fig 2.3** show a typical mesh used in the current work. The mesh is finer near the walls and the splitter plate. The mesh is coarser downstream since both the size of the smallest eddies as well as the size of the largest structures increase as they proceed downstream. Also the sharp gradients present in the initial parts of the mixing become smoother as they recede from the splitter plate.

2.4 Boundary Conditions

2.4.1 Primary and Secondary inlets

Velocity boundary condition is implemented by imposing a random noise about a mean which is profiled to emulate a largely uniform flow with boundary condition, with a modifiable temporal correlation and a given standard deviation(see Appendix A.1 on Page182 for details)

Pressure at a major section of the inlet is fixed, because the inlet has largely inward supersonic flow. In the regions where the flow is not supersonic, that is the places where there is the presence of a boundary layer, either due to the presence of the top or bottom walls, or due to the splitter plate, the pressure is determined by the use of characteristics.

Static Temperature is determined from the total temperature which is constant throughout the boundary. This total temperature is selected so as to produce a defined mean static temperature in the quiescent part of the flow.

Mass fraction in the case of dissimilar gasses is constant close to unity (but not exactly 1 to prevent some singularities in computation) for one of the species for a stream and close to zero for the other species and vise-versa for the other stream.

2.4.2 Walls and Splitter plate

Velocity is imposed $\boldsymbol{U} = \boldsymbol{0}$ for the splitter plate for all cases, and those cases with no slip on the top and bottom walls. In those cases where the top and bottom walls are prescribed to be slip, only the velocity component normal to the surface is imposed to be zero, while the tangential component of the velocity has no gradient in such cases. This is roughly valid for cases where there is no strong shock impinging on the surface.

Pressure at upper and lower walls and the splitter plate is assumed to have zero gradient normal to the surface of the flow. This too is reasonable since the current flow does not have strong shock waves impinging on the surface.

Temperature at the upper and lower walls and the splitter plate is considered to have a zero normal gradient, since it is assumed that these are adiabatic surfaces.

Mass fractions at the upper and lower walls and the splitter plate is considered to have a zero normal gradient, since it is assumed that these surfaces are closed and there is no surface reaction.

2.4.3 Outlet

Pressure and Velocity are implemented such that it is a non reflecting surface. Since most of the boundary surface sees supersonic outgoing fluid, the pressure is dictated only from the domain. However this is not true in the regions near to the walls where the Mach number reduces to below unity. Here the pressure and velocity are decided on the basis of the characteristics to result in a non reflecting boundary.

Temperature and Mass fraction at the outlet is implemented as zero gradient for flow going outside the domain, however for incoming flow, which is extremely rare and an isolated event near to the walls, the temperature of the incoming stream is a fixed constant value.

2.5 Solution methodology

All simulations have been performed using OpenFOAM [Jasak et al., 2007]. OpenFOAM is a free and open source toolkit which provides a set of libraries for data handling, mesh handling, implicit and explicit calculus, boundary handling, parallellization and a large set of in built solvers and utilities. However, the present work utilizes the package as a library and a specific code was written for LES of supersonic flow of dissimilar gasses using the utilities provided.

The algorithm to solve the set of coupled equations was done using the PISO algorithm of Issa [1986] (which is an improvisation of the SIMPLE [Patankar, 1980]). The basic steps of the algorithm are

1. Set the boundary conditions.
2. Solve the discretized momentum equation to compute an intermediate velocity field.
3. Compute the mass fluxes at the cells faces.
4. Solve the pressure equation.
5. Correct the mass fluxes at the cell faces.
6. Correct the velocities on the basis of the new pressure field.
7. Update the boundary conditions.
8. Repeat from 3 for the prescribed number of times.
9. Solve for energy equation, mass fraction equation.
10. Do all the post processing steps.
11. Increase the time step and repeat from 1.

2.5.1 The solution method in detail

OpenFOAM provides two basic methods of calculus called

Finite Volume Calculus which provides for the *time explicit* computation of gradients of fields using many schemes

Finite Volume Method which provided for the *time implicit* computation of gradients of fields using many schemes

Time explicit methods provide directly the calculated field. The time implicit schemes provide sparse matrix which when solved provides the gradient of the field. The temporal scheme decides the *implicitness* of the field, and a range of temporal schemes are provided. It is to be noted that the matrix so produced can be solved using different iterative techniques which are special sparse matrix solvers

Type of Matrix	Method	Name
Symmetric	Incomplete-Cholesky preconditioned conjugate gradient	ICCG
	Diagonally preconditioned conjugate gradient	DCG
	Algebraic multi-grid	AMG
Asymmetric	Incomplete-Cholesky preconditioned biconjugate gradient	BICCG
	Diagonally preconditioned biconjugate gradient	BDCG
	Gauss-Seidel	GaussSeidel

An important point to be noted that since the matrix solvers are iterative in nature, and the matrix solution for implicit solution, it is necessary for the update of the coefficients corresponding boundary condition after every iterative step of the matrix solver.

The parallel implementation of the OpenFOAM library is of distributed memory architecture with OpenMPI. Being so, the parallelization is achieved by domain decomposition, which in the current work has been done using the metis algorithm. Being of distributed memory architecture, the coefficient information has to be transmitted across processor boundaries after every iteration of the sparse matrix solver, so that the matrix solution is consistent.

2.5.2 Selection for the simulations

The following selection is made for all the LES simulations

Type	Parameters	Scheme	Specs
Temporal Scheme	All	Second order Backward Euler	
Gradients	Basic parameters	Fourth order least squares	
	Post Processing	Second order Gauss	
Matrix Solvers	ρ	PCG with DIC[2] pre-conditioner	Tolerance of 1e-10
	All others	PBiCG with DILU[3] pre-conditioner	Tolerance of 1e-10
LES Subgrid-Scale Model		One-Equation Eddy model	

A second order temporal scheme is needed to have time accurate solutions. Greater than the second order solutions require prohibitively large memory requirement, and hence are generally not used. Second order spatially accuracy was initially tried, but was found to be more diffusive than what would be acceptable, where as fourth order scheme was found to be adequate. The order of accuracy greater then the fourth order was not sought because a greater order of accuracy involves a much larger information required to be transmitted between the computation nodes, which become the bottlenecks for computation. A compact scheme of higher order, or a spectral scheme would have been a possible solution. However an aim for future expansion towards three dimensional simulations with complex geometries with unstructured mesh made distributed memory architecture a necessity, and in this architecture compact schemes or spectral schemes algorithms are both complex as well as unsuited.

In all the cases the time stepping has been such to maintain the Courant number to below 0.1.

2.6 Averaging

The averaging of flow field is done by performing the summation of the required variables. This summation is done incrementally at every time step after the solution stage. Thus the calculation of any of the averages is simply done as

$$\langle Q \rangle = \frac{\sum\limits_{i \in \mathcal{I}} Q_i}{\sum\limits_{i \in \mathcal{I}} 1} \tag{2.43}$$

where $\mathcal{I}$ is the list of time steps representing the desired time range of averaging. Favre averaging is accomplished by performing the density weighted sums as

$$\{Q\} = \frac{\sum\limits_{i \in \mathcal{I}} \rho_i Q_i}{\sum\limits_{i \in \mathcal{I}} \rho_i} \tag{2.44}$$

For the quantities which are products of fluctuations, we use

$$\langle P'Q' \rangle = \langle PQ \rangle - \langle P \rangle \langle Q \rangle \tag{2.45}$$

And hence for quantities like $\langle P'Q' \rangle$ sums of PQ, P and Q are all maintained, and the averaging is performed at the end of the time duration.

2.6.1 Time required for averaging

Two important parameters as far as averaging is concerned are

1. The initial offset required for the arbitrary initial conditions to have insignificant effect
2. The time required to be able to estimate a given measure of average with a reasonable level of confidence.

This subsection describes the way in which these two times were estimated. The average measurement of U_x and τ_{xy} at a point about $0.4[m]$ from the splitter plate is shown in **Fig 2.4**. This figure shows how the averages change with different window sizes Δt and different offsets in time from the initial time. The right side plot shows the probability density of the average. It can be seen that the measurement of the average velocity with 95% interval of confidence $4[m/s]$ when we use a time duration of about $2[ms]$. With this same duration for Δt, however, we see that an estimation of τ_{xy} with 95% level of confidence is still about $80[m^2/s^2]$ which is prohibitively large. An interval of $5[ms]$, however reduces it to about $36[m^2/s^2]$, which is about 7% of the peak value.

Another fact that is noticed is that there is a lot of variation in the initial measurement of τ due to the initial conditions, however, this value settles after about $4[ms]$, after which measurements can be taken without having the influence of the initial condition.

In all calculations, the average is calculated for $\approx 0.01[s]$, which amounts to around 8 sweeps of the convective structures, with an initial delay of $\approx 6[s]$, which amounts to about 5 sweeps of the convective structures.

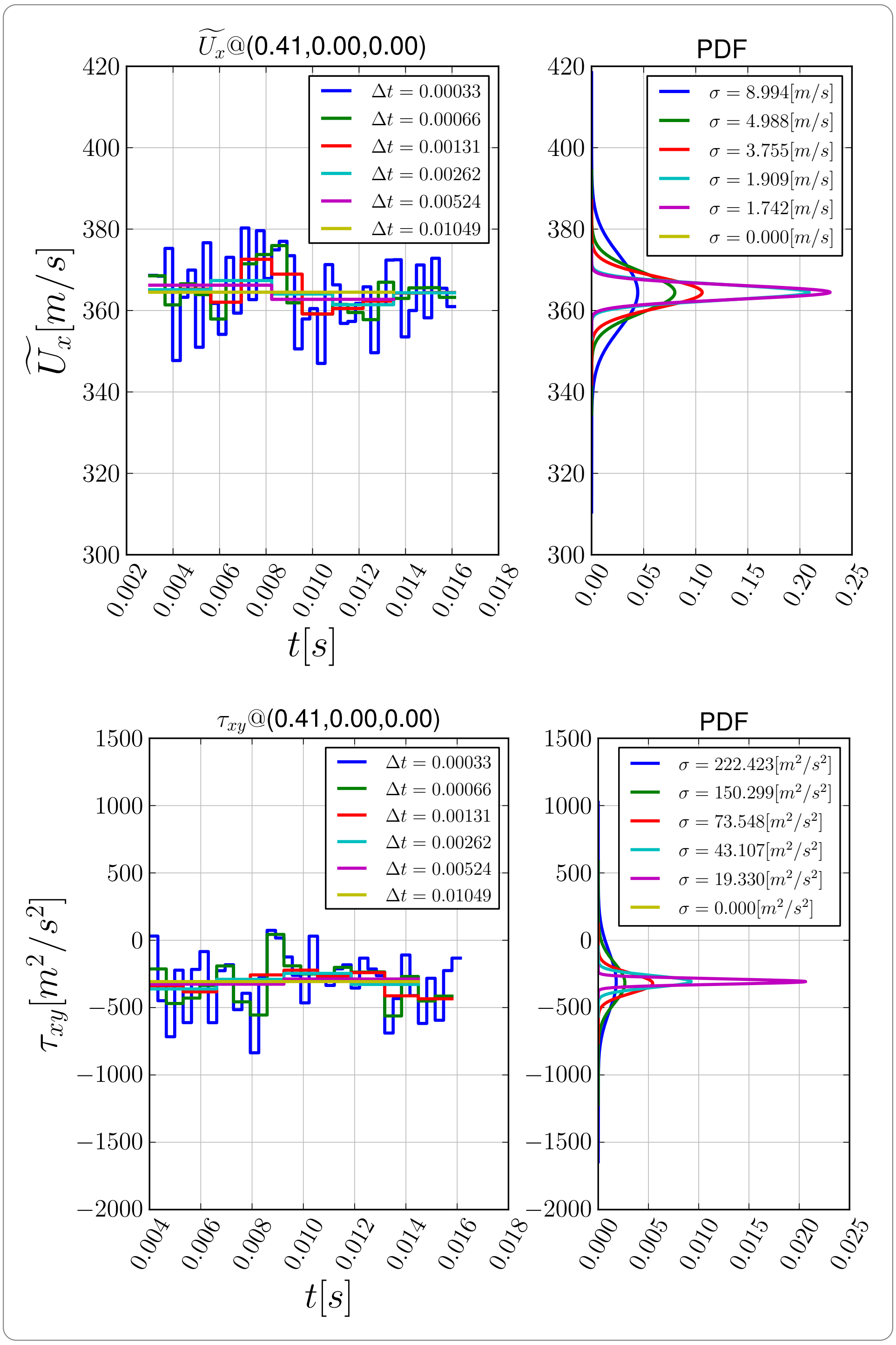

Figure 2.4: Precision vs Time of average for U_x and τ_{xy}
[*It is seen that we can attain a good precision if we collect data for more than* $0.005[s]$ *for averaging*]

2.7 Grid Dependence

In order to make the predictions by the simulations with a high degree of confidence, and with precision, it is necessary to demonstrate that the mean profiles of the parameters are independent of the mesh resolution. For this the same simulation was performed with three different meshes. The parameters for the simulations and the mesh sizes are shown in **Table 2.4**. These simulations were of the multi-species type, and used exactly the same schemes and procedures used in the rest of the thesis.

Parameter	Primary	Secondary
Fluid	N_2	Ar
Velocity $[m/s]$	727.2	472.7
Temperature $[K]$	405.7	289.27
Mach Number	1.7	1.4
Pressure$[kPa]$	46	
$\rho[kg/m^3]$	0.38	0.76
Velocity Ratio	0.65	
Density Ratio	2	
M_c	0.35	

Mesh Name	Mesh Size
Fine Mesh	1200×260
Medium Mesh	800×200
Coarse Mesh	600×160

Table 2.4: Flow conditions and mesh sizes used for grid dependence studies

2.7.1 Mean Velocity Profile

The mean velocity profile with the simulations with three grids is shown in **Fig 2.5**.

It can be seen from **Fig 2.5** that the average stream-wise velocity plots are almost coincident. This plot clearly shows that the solution of the average velocity profile can be predicted precisely, and independent of the resolution in the range. The fact that the actual grid used is similar to the *Medium mesh*, lays to rest concerns regarding the dependence of the solution on the quality of the mesh.

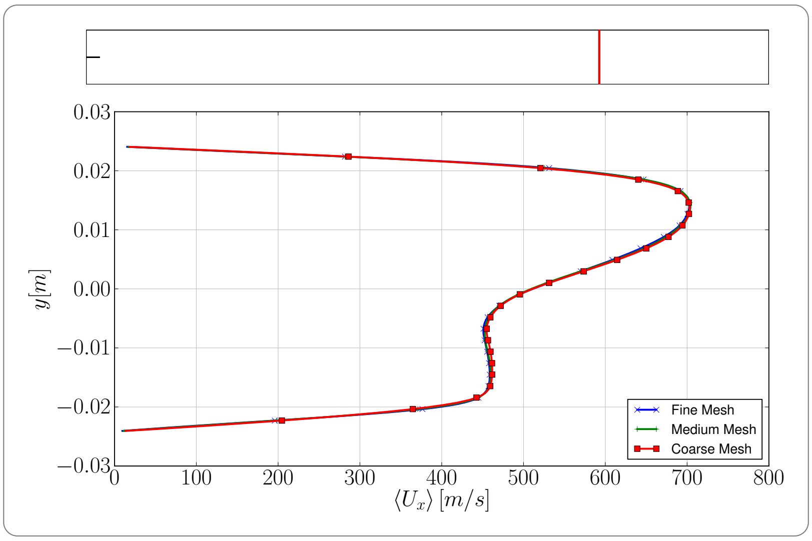

Figure 2.5: Mean velocity profiles for different grids
[*All the curves are almost coincident, indicating almost independence of the mesh. The rectangular section on the top indicates the section in the domain where the data is presented*]

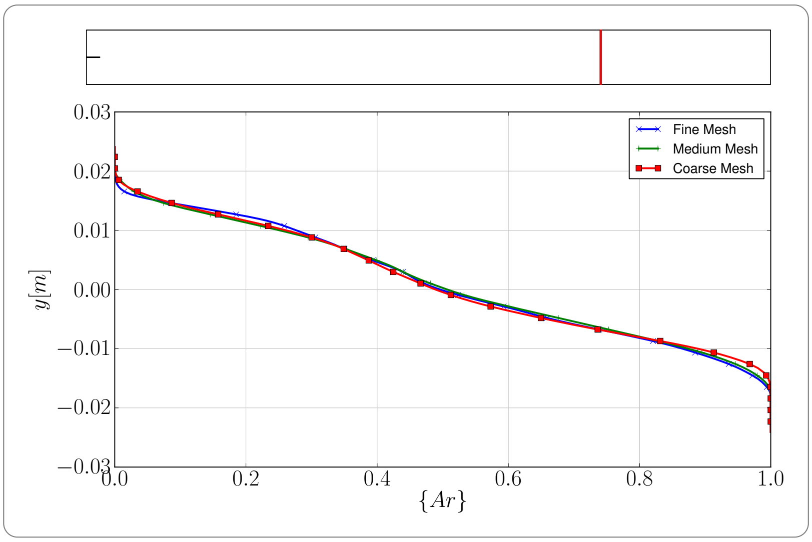

Figure 2.6: Mean Ar mass fraction profiles for different grids
[*The top figure indicates where in the domain the curves are plotted.All the curves are almost coincident, again, indicating almost independence of the mesh*]

2.7.2 Mean Species Profile

Shown in **Fig 2.6** is the cross-wise species distribution of Ar. It is again seen that the three curves are almost coincident and there is little scope for doubt regarding the independence of the solution from the quality of the mesh which is of quality similar to the *Medium Mesh*.

2.7.3 Mean Temperature Profile

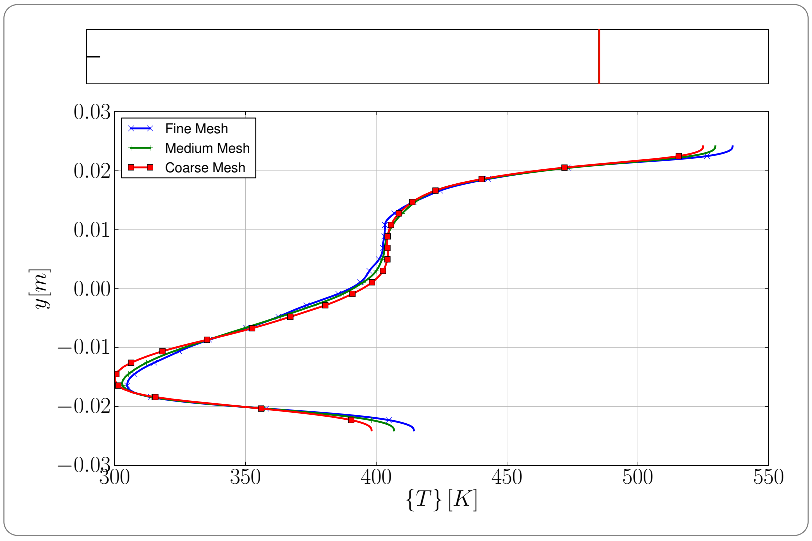

Figure 2.7: Mean temperature profiles for different grids
[*All the curves are coincident except near the walls*]

Like the other profiles, the mean temperature profiles shown in **Fig 2.7** is almost coincident for most of the flow, except very close to the walls, where they show about 5% deviation of the maximum variation. In the region of the mixing the deviation is less than 3% of the total variation.

2.7.4 Turbulent Kinetic Energy Spectrum

The turbulent kinetic energy spectrum of the velocity field is a useful indicator of the mesh, and its adequacy. A coarse mesh filters out lower frequencies more than finer mesh. It is needed that the energy carrying low energy spectrum be largely unaffected by mesh, but the effect of mesh on higher frequency content is unavoidable.

The turbulent kinetic energy spectrum is plotted in **Fig 2.8**. The left figure shows that near to the splitter plate the frequency as well as the peak is captured for all the grids, while far away, the coarse grid gives lesser energies for higher frequencies. It can this be clearly inferred that grid independence has adequately been achieved, and that the Medium Mesh is sufficiently fine to be used with LES to have precise simulations which does not depend on the grid resolution.

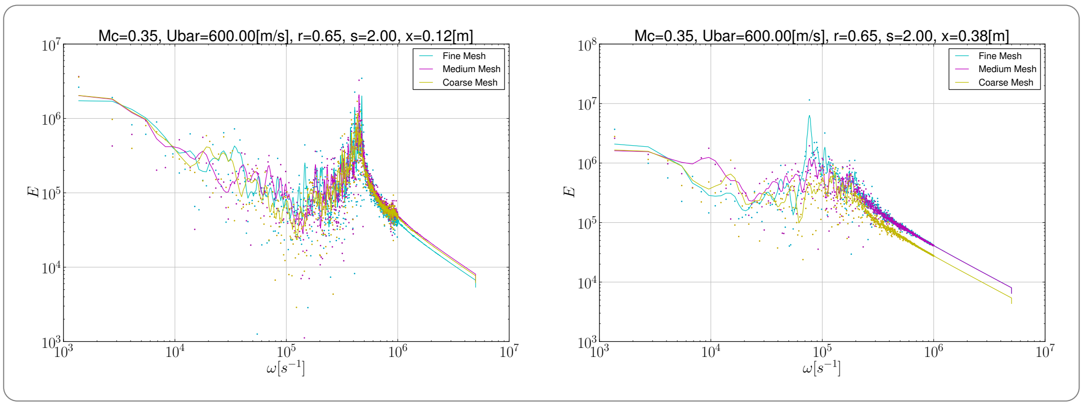

Figure 2.8: Turbulent Kinetic Energy spectrum at two different downstream locations along the centerline

[*At the nearer station(left) there is no difference and the frequency is accurately captured along with the peak value, and at 75% the flow distance (right), also the peak frequency and value is similarly captured for Medium Mesh and Fine Mesh, coarse mesh gives slightly lower energies at higher frequencies*]

It must be noted that Oh and Loth [1994] has indicated that a minimum of 20 grid points are needed across the mixing layer to be able to obtain grid independence. In the current work more than twice the grid points than is required by the criteria have been used. Oh and Loth [1994] however used IES (Inviscid Eddy Simulation) which is quite different from the Large Eddy Simulation, with the latter being expected to provide better convergent results.

2.8 Experimental Comparison

The simulation methodology was compared with experimental cases, established trends in growth rate and turbulence levels. The first set of test cases used were the supersonic cases of Goebel and Dutton [1990a], the next set of

Parameter	Case 1		Case 2	
Fluid	Air	Air	Air	Air
Velocity $[m/s]$	515	700	404	399
Temperature $[K]$	162	339	214	215
Mach Number	2.01	1.89	1.37	1.35
Pressure$[kPa]$	46		49	
$\rho[kg/m^3]$	0.980	0.50	0.75	0.79
Velocity Ratio	0.780		0.57	
Density Ratio	0.760		1.57	
M_c	0.202		0.45	

Table 2.5: Flow conditions of Goebel and Dutton [1990a]

experimental results which were used were from Papamoschou and Roshko [1988].

2.8.1 Comparison with experiments of Goebel and Dutton [1990a]

Goebel and Dutton [1990a] conducted compressible mixing layer experiments with air as the fluid, and M_c varying from 0.2 to 0.99. Two representative test cases were selected for the verification as outlined in **Table 2.5**.

Self Similar Velocity Profile

The first parameter compared is the self similar velocity profile. **Figure 2.9** shows the self similar profiles obtained from the simulation in a background of the experimental self similar profile.

The x axis of the plot is the velocity scaled between 0 and 1, and the y axis is scaled and shifted so that $U_1 - 0.1\Delta U$ and $U_2 + 0.1\Delta U$ fall at 0.5 and -0.5 respectively (so that the length between these points is scaled to 1 and are equidistant from 0). It can be seen that the profiles match almost exactly, except for a small difference near the secondary stream. The self similar velocity profiles are expected to attain a error function for the incompressible flows [Herrmann Schlicting, 2000]. Though the attainment of such a profile is only

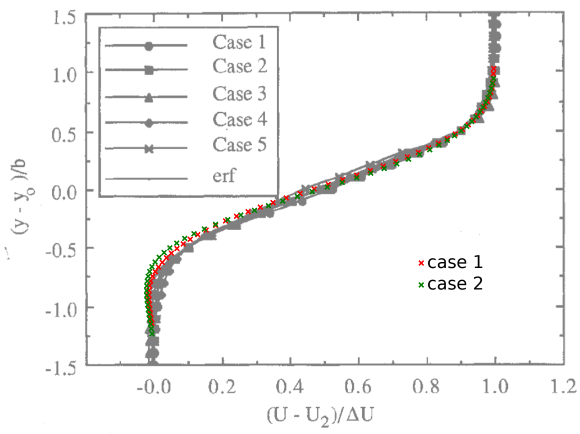

Figure 2.9: Comparison of average Velocity obtained from the experiments compared with the simulations
[*The faded background image is from Goebel and Dutton [1990a]*]

asymptotic, the nearness to the error function is an indication of attainment of self similarity, at least in the first order statistics. It was observed by Goebel and Dutton [1990a] that even for high M_c cases, the mean velocity profile was not significantly different than that of an incompressible mixing layer and the same has been observed in the simulations.

Reynold's stresses

The next parameter compared are the turbulence intensities in the self similar region. This defined as in the experiment as

$$\sigma_{ij} \equiv \frac{\sqrt{\langle u_i{}' u_j{}' \rangle}}{\Delta U} \tag{2.46}$$

It can be seen from the **Fig 2.10** that the match for the current case is almost precise in all the components of the turbulence intensities, especially the case of $\langle u'v' \rangle$ which is most critical for the growth rate. In the case of σ_{xx}, the spread is observed to be greater than in the case of the experiment, however the peak value is accurately captured.

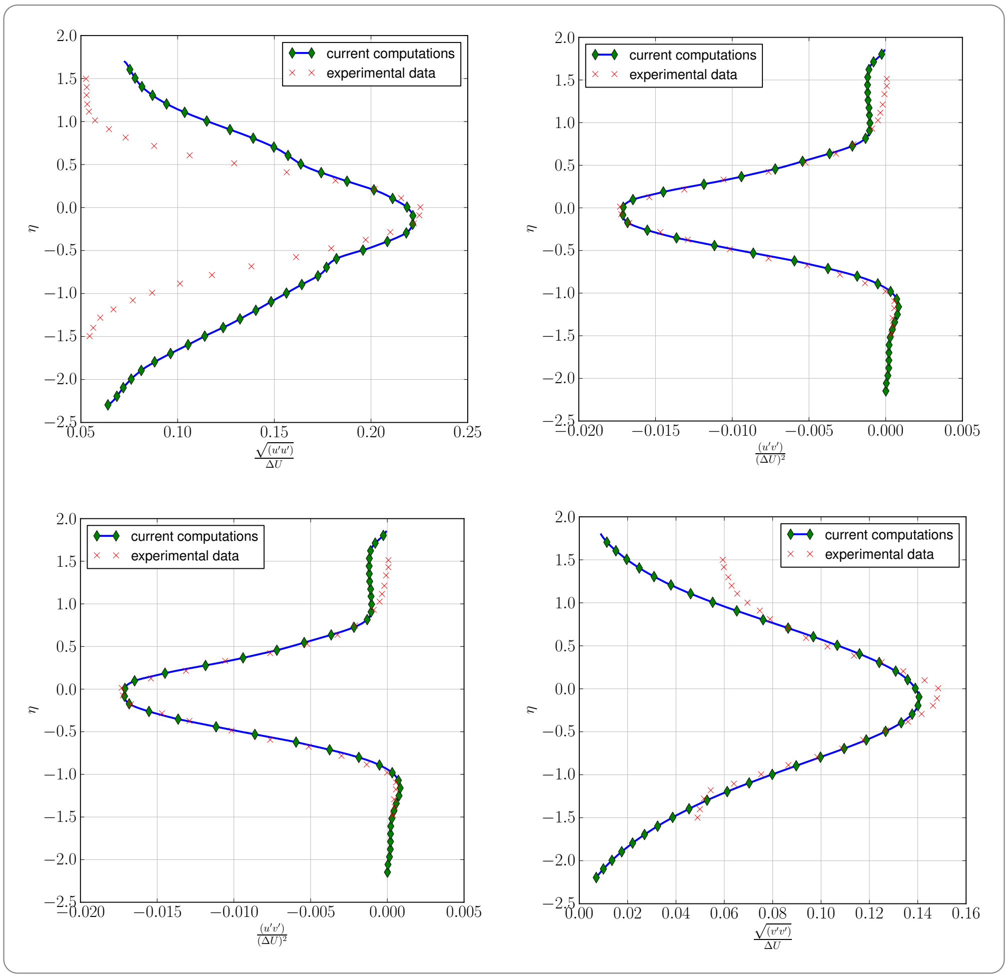

Figure 2.10: Comparison of Turbulence Intensity
[*Plotted above are the* $\sigma_{xx}({u_x}', {u_x}')$ *correlation (top left), the* $\sigma_{yy}({u_y}', {u_y}')$ *correlation (top-right),* $\sigma_{xy}({u_x}', {u_y}')$ *velocity correlation (bottom left) and the ratio of* σ_u *and* σ_v*(bottom right). The experimental data is case 1 of Goebel and Dutton [1990a]*]

Growth Rates

The growth rates obtained from the simulation have been scaled and plotted in **Fig 2.11** in a backdrop of experimental growth rates. It can be clearly seen that

1. The growth rate lies entirely within the band of experimentally obtained growth rates

2. The simulation is clearly able to capture the reduces growth rates phe-

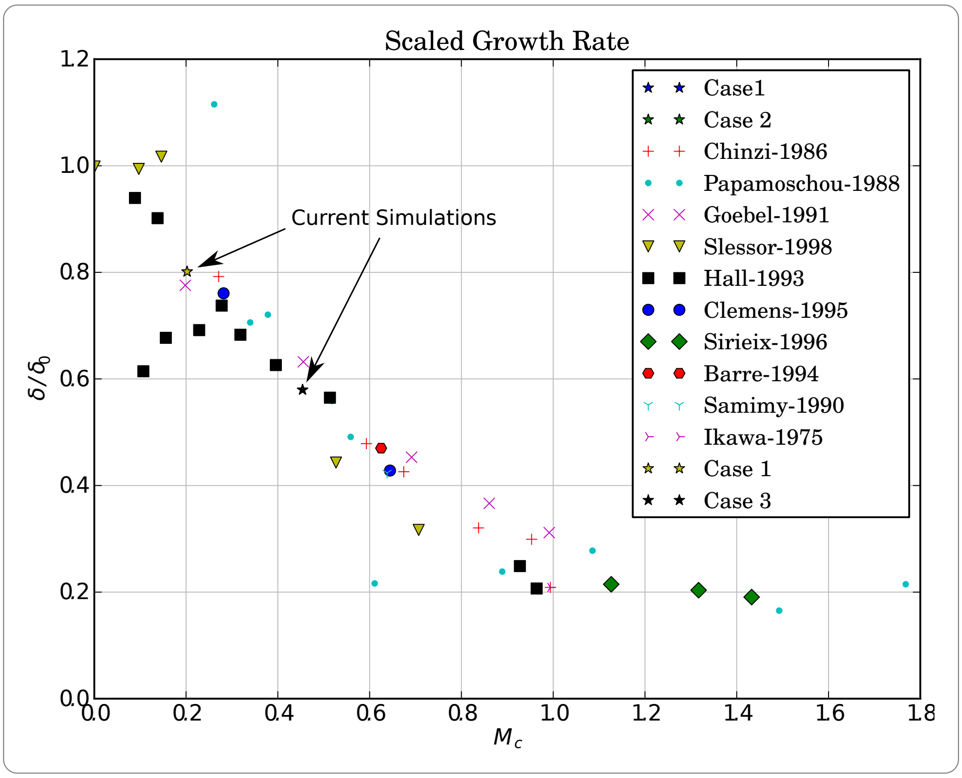

Figure 2.11: Growth Rates form Goebel and Dutton [1990a]
[*The growth rate from simulations of experiments of Goebel and Dutton [1990a] falls within the band of experiments*]

nomenon with increasing M_c

2.8.2 Comparisons with the experiments of Papamoschou and Roshko [1988]

Two test case from Papamoschou and Roshko [1988] were simulated Case 2 and Case 3. The details of the cases are outlined in table **Table 2.6**.

Comparison of growth rates

The growth rates of the simulations of experiments from Papamoschou and Roshko [1988] are plotted along with the simulation results against other experimental results in **Fig 2.12**. It can be again seen that the growth rates lie in the band of experimental results, and that the decrease in the growth rate

Parameter	Case 2		Case 3	
Fluid	Ar	2	Ar	N_2
Velocity $[m/s]$	497.8	640.3	402.6	477.8
Temperature $[K]$	61.8	102.7	144.2	190.14
Mach Number	3.4	3.1	1.8	1.7
Pressure$[kPa]$	7		7	
$\rho[kg/m^3]$	0.54	0.23	0.23	0.12
Velocity Ratio	0.80		0.74	
Density Ratio	0.42		0.54	
M_c	0.26		0.33	

Table 2.6: Flow conditions

is captured by the simulation.

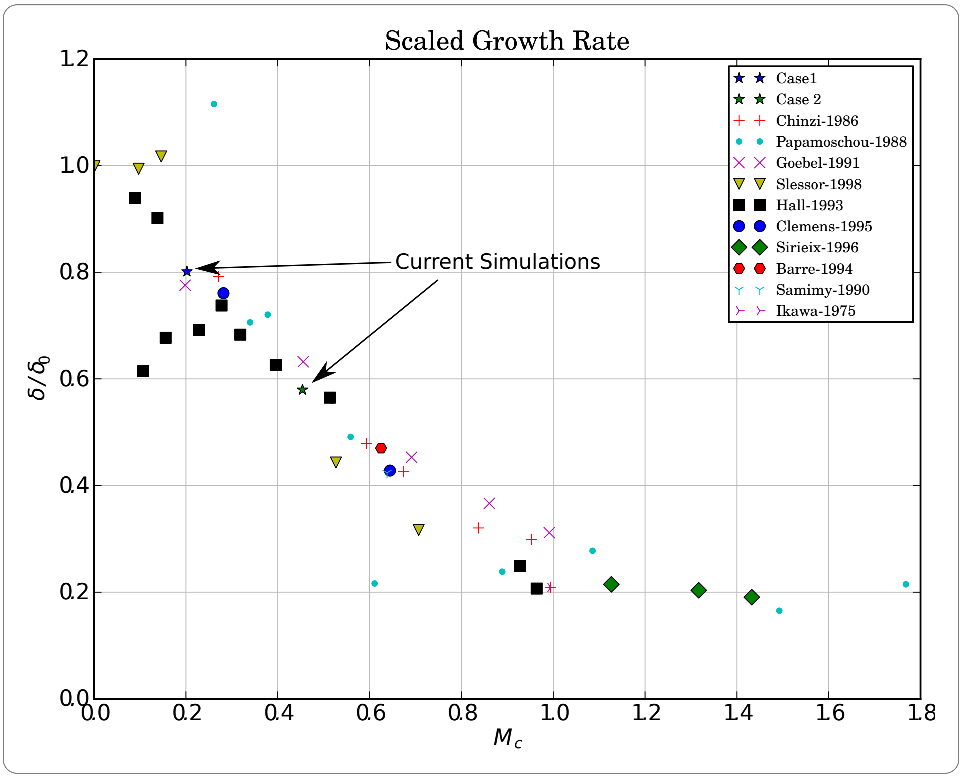

Figure 2.12: Growth Rates from simulations of experiments from Papamoschou and Roshko [1988]

[*The growth rate from simulation of experiments of Papamoschou and Roshko [1988] falls within the band of experiments*]

Pitot measurement

From the simulations, the local average static pressure and the local average Mach number can be calculated. From Reyleigh's pitot equation (**Eqn 2.47**) we can back calculate $\frac{p_t}{p}$ at any location. This is compared with the documented values.

$$\frac{p_0}{p} = \left(\frac{(\gamma+1)^2 M^2}{4\gamma M^2 - 2(\gamma-1)}\right)^{\left(\frac{\gamma}{\gamma-1}\right)} \left(\frac{1-\gamma+2\gamma M^2}{\gamma+1}\right) \tag{2.47}$$

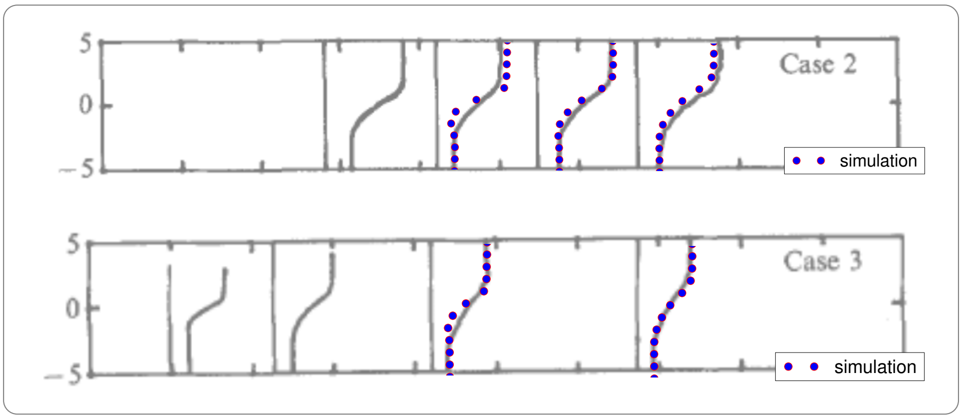

Figure 2.13: Pitostatic measurements
[*The match between the experimental and the simulation pitot measurement is within acceptable limits. The background is the experimental results extracted from Papamoschou and Roshko [1988]*]

It can be seen from **Fig 2.13** that even though at lower distances the match is not very accurate, in the self similar regions, the match is almost perfect with the experiments.

2.8.3 Schlieren Images

Instantaneous density gradient is plotted in gray-scale to simulate the schlieren. This is compared with the schlieren presented in the experiment in **Fig 2.14**.

The differences in the images can be reasoned out as

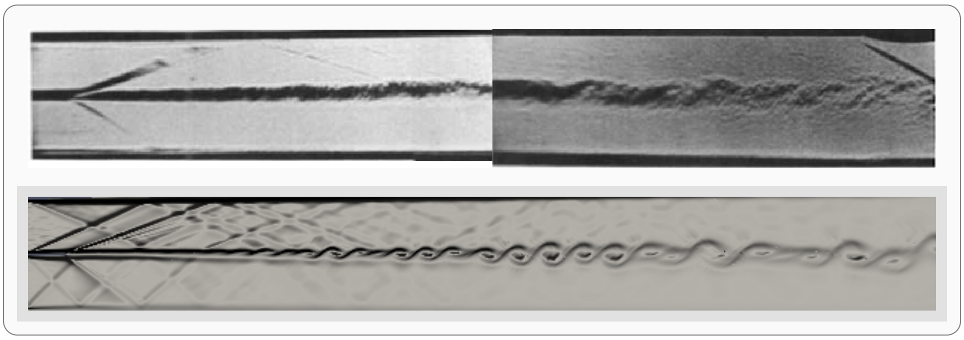

Figure 2.14: Schlieren images from experiment(top) and from simulations(bottom) [Width of the structures roughly match with the presence of similar structures]

1. The schlieren image from the simulation is obtained by plotting on a single plane, while the schlieren is effectively the *spatial average*[4] of the gradient density in the spanwise direction. Hence any small amount of three dimensionality in the density field will cause a smudging in the schlieren obtained. It is not that the structures are completely invisible in the experimental schlieren, and a careful examination of the image, especially on the right side shows the presence of these structures roughly of the same size of those obtained in the simulation

2. The images in the corresponding reference is presented as two separate images, which were taken separately and with slightly differing lighting conditions. It can be easily seen as well as it was commented by the authors that the schlieren images are not very clear and give significantly differing results for slightly differing lighting conditions.

A good match, however, has been obtained in the width of the mixing layer. It can be seen that roughly the positions of the outer edges of the mixing layer match. This is roughly the width of the mixing layer and indicates the growth and mixing.

With this we can conclude that

- The LES simulations are able to capture the mean velocity profiles quite accurately.

[4]The spark in the experiment was of 20ns duration, during which the structures move about $0.02\mu m$. Hence the smudging is not due to temporal averaging

- The simulations capture the reduction in growth rate with increasing M_c observed in experiments.
- The simulations predict the trends in the turbulence levels, where it is observed in experiments.
- The simulations are able to show the large scale structures.

2.9 Test Cases

The most fundamental parameters in the case of a mixing layer, considered in this study are the convective Mach number M_c, the average velocity U_{avg}, the velocity ratio r, and the density ratio s. These parameters have the following definitions.

$$M_c \equiv \frac{U_1 - U_2}{a_1 + a_2} \tag{2.48}$$

$$U_{\text{avg}} \equiv \frac{U_1 + U_2}{2} \tag{2.49}$$

$$r \equiv \frac{U_2}{U_1} \tag{2.50}$$

$$s \equiv \frac{\rho_2}{\rho_1} \tag{2.51}$$

A study of the influence of each of the above parameters on the supersonic mixing layer is to be studied. For the sake of simulations, we need to convert from these parameters to the parameters which are supplied as the boundary conditions.

These dependent parameters can be calculated as (see Appendix **A.2** on Page**184** for derivation)

$$
\begin{aligned}
U_1 &= 2\frac{U_{avg}}{1+r} && (2.52)\\
U_2 &= 2\frac{r}{1+r}U_{avg} && (2.53)\\
T_2 &= \frac{1}{\gamma R}\left(2\left(\frac{1-r}{1+r}\right)\left(\frac{U_{avg}}{M_c\left(s^{\frac{1}{2}}+1\right)}\right)\right)^2 && (2.54)\\
T_1 &= \frac{s}{\gamma R}\left(2\left(\frac{1-r}{1+r}\right)\left(\frac{U_{avg}}{M_c\left(s^{\frac{1}{2}}+1\right)}\right)\right)^2 && (2.55)
\end{aligned}
$$

These equations are suitably modified for calculating the flow field parameters for dissimilar gases. It is important to note that the velocities are uniquely determined by U_{avg} and r alone. Role of M_c comes in determining the temperatures and hence the densities.

2.9.1 Case Specifications

Three sets of test cases were used to analyse the problem. The first and the second test cases use the same species on both the primary as well as the secondary streams. The third and the fourth use different species. The first two test cases are designed to enable a study of the problem with only one of the four flow parameter varying. The second set is different from the first in that the interesting parameter M_c is studied in greater detail, and that the domain is somewhat larger than the first test case. The third test case is meant to study the mixing aspect and the entropy generation.

Case	Species		U_{avg}	M_c	r	s	$U[m/s]$		$T[K]$		M		p	$a[m/s]$	
	P	**S**	$[m/s]$				**P**	**S**	**P**	**S**	**P**	**S**	$[kPa]$	**P**	**S**
1	Ar	Ar	400	0.30	0.74	1.25	459.5	340.4	126.8	101.5	2.19	1.81	7	209.7	187.6
2	Ar	Ar	450	0.30	0.74	1.25	517.0	382.9	160.5	128.4	2.19	1.81	7	236.0	211.0
3	Ar	Ar	500	0.30	0.74	1.25	574.4	425.5	198.2	158.6	2.19	1.81	7	262.2	234.5
4	Ar	Ar	550	0.30	0.74	1.25	631.9	468.0	239.8	191.9	2.19	1.81	7	288.4	258.0
5	Ar	Ar	600	0.30	0.74	1.25	689.3	510.6	285.4	228.3	2.19	1.81	7	314.6	281.4
7	Ar	Ar	500	0.25	0.74	1.25	574.4	425.5	285.4	228.3	1.83	1.51	7	314.6	281.4
8	Ar	Ar	500	0.30	0.74	1.25	574.4	425.5	198.2	158.6	2.19	1.81	7	262.2	234.5
9	Ar	Ar	500	0.35	0.74	1.25	574.4	425.5	145.6	116.5	2.56	2.12	7	224.7	201.0
10	Ar	Ar	500	0.40	0.74	1.25	574.4	425.5	111.5	89.2	2.92	2.42	7	196.6	175.9
11	Ar	Ar	500	0.30	0.74	2.50	574.4	425.5	266.9	106.7	1.89	2.21	7	304.3	192.4
12	Ar	Ar	500	0.30	0.74	1.67	574.4	425.5	225.9	135.5	2.05	1.96	7	279.9	216.8
13	Ar	Ar	500	0.30	0.74	1.25	574.4	425.5	198.2	158.6	2.19	1.81	7	262.2	234.5
14	Ar	Ar	500	0.30	0.74	0.83	574.4	425.5	162.0	194.4	2.42	1.64	7	237.0	259.7
15	Ar	Ar	500	0.30	0.74	0.71	574.4	425.5	149.2	208.9	2.52	1.58	7	227.5	269.2
16	Ar	Ar	500	0.30	0.80	1.25	555.5	444.4	110.3	88.2	2.84	2.54	7	195.6	174.9
17	Ar	Ar	500	0.30	0.77	1.25	565.2	434.7	152.0	121.6	2.46	2.12	7	229.6	205.4
18	Ar	Ar	500	0.30	0.74	1.25	574.4	425.5	198.2	158.6	2.19	1.81	7	262.2	234.5
19	Ar	Ar	500	0.30	0.71	1.25	583.3	416.6	248.2	198.6	1.99	1.59	7	293.4	262.4
20	Ar	Ar	500	0.30	0.69	1.25	591.8	408.1	301.5	241.2	1.83	1.41	7	323.3	289.2

Table 2.7: Specifications of **Set1** designed to study the effect of one of the parameters (U_{avg}, M_c, r and s) at a time

Case	Species		U_{avg}	M_c	r	s	$U[m/s]$		$T[K]$		M		p	$a[m/s]$	
	P	**S**	$[m/s]$				**P**	**S**	**P**	**S**	**P**	**S**	$[kPa]$	**P**	**S**
1	Ar	Ar	400	0.25	0.70	1.25	470.5	329.4	256.5	205.2	1.58	1.23	7	298.28	266.7
2	Ar	Ar	400	0.30	0.70	1.25	470.5	329.4	178.1	142.5	1.89	1.48	7	248.57	222.3
0	Ar	Ar	400	0.35	0.70	1.25	470.5	329.4	130.8	104.6	2.21	1.73	7	213.06	190.5
3	Ar	Ar	400	0.40	0.70	1.25	470.5	329.4	100.2	80.1	2.52	1.98	7	186.43	166.7
4	Ar	Ar	400	0.45	0.70	1.25	470.5	329.4	79.1	63.3	2.84	2.22	7	165.71	148.2
5	Ar	Ar	400	0.50	0.70	1.25	470.5	329.4	64.1	51.3	3.16	2.47	7	149.14	133.4
6	Ar	Ar	400	0.55	0.70	1.25	470.5	329.4	53.0	42.4	3.47	2.72	7	135.58	121.2
7	Ar	Ar	300	0.35	0.70	1.25	352.9	247.0	73.6	58.8	2.21	1.73	7	159.79	142.9
0	Ar	Ar	400	0.35	0.70	1.25	470.5	329.4	130.8	104.6	2.21	1.73	7	213.06	190.5
10	Ar	Ar	400	0.35	0.65	1.25	484.8	315.1	189.0	151.2	1.89	1.38	7	256.10	229.0
0	Ar	Ar	400	0.35	0.70	1.25	470.5	329.4	130.8	104.6	2.21	1.73	7	213.06	190.5
11	Ar	Ar	400	0.35	0.75	1.25	457.1	342.8	85.7	68.6	2.65	2.22	7	172.48	154.2
0	Ar	Ar	400	0.35	0.70	1.25	470.5	329.4	130.8	104.6	2.21	1.73	7	213.06	190.5
15	Ar	Ar	400	0.35	0.70	2.00	470.5	329.4	161.1	80.5	1.99	1.97	7	236.44	167.1
16	Ar	Ar	400	0.35	0.70	3.00	470.5	329.4	188.7	62.9	1.84	2.23	7	255.89	147.7
17	Ar	Ar	400	0.35	0.70	4.00	470.5	329.4	208.7	52.1	1.75	2.45	7	269.08	134.5

Table 2.8: Specifications of **Set2** designed to study effect of M_c to a greater detail, and in a larger domain

Case	Species		U_{avg} $[m/s]$	M_c	r	s	$U[m/s]$		$T[K]$		M		p $[kPa]$	$a[m/s]$	
	P	**S**					**P**	**S**	**P**	**S**	**Prm**	**Sec**		**P**	**S**
1	N2	Ar	400	0.25	0.75	1.25	457.1	342.9	128.9	147.9	2.98	1.52	7	231.37	225.80
2	N2	Ar	400	0.30	0.70	1.25	470.6	329.4	136.5	155.8	2.98	1.42	7	238.17	232.44
3	N2	Ar	400	0.35	0.65	1.25	484.9	315.2	144.9	165.4	2.98	1.32	7	245.39	239.49
4	N2	Ar	400	0.40	0.65	1.25	484.9	315.2	111.0	126.6	2.36	1.50	7	214.72	209.55
5	N2	Ar	400	0.45	0.65	1.25	484.9	315.2	87.7	100.0	2.54	1.69	7	190.86	186.27
6	N2	Ar	400	0.50	0.65	1.25	484.9	315.2	71.0	81.0	2.82	1.88	7	171.77	167.64
7	N2	Ar	400	0.35	0.65	4.00	484.9	315.2	236.9	84.5	1.55	1.84	7	313.73	171.16

Table 2.9: Specifications of **Set3** designed to study the mixing of dissimilar gasses and entropy generation.

2.10 Summary

In this chapter the problem was described mathematically, and the LES setup was explained along with the sub-grid scale model used. The domain was defined for the purpose with the grid and boundary condition specifications. The solution methodology was then explained. It was then shown how the averaging process was arrived at, as to how much of time is required for averaging. Grid independence was then established, and was shown that for grids finer and coarser than the selected grid, there was hardly any difference in the mean profiles, and the turbulence spectrum too showed only the expected difference at high frequencies. Simulations were performed with select cases where experimental values were available, and it was seen that the match was excellent with respect to the mean parameters, moderate for turbulence measures. Finally a strategy was laid out to be able to study each of the influencing flow parameters independently, and all the test cases were listed.

Part II

Results and Discussions

Chapter 3

Features Of The Mixing Layer

In the previous chapter, the validity of the code, and its usefulness in simulating the spatial mixing layer was demonstrated. We now put to use this methodology in studying the mixing layer, starting with the statistical and mean properties.

This chapter is intended to explain some of the intricate features which are observed in a plain mixing layer. It opens with the features based on the instantaneous and mean profiles of velocity (**Sect 3.1**). First the growth rates measured from the simulations are presented in the background of the existing literature (**Sect 3.1.1**). This is followed by a discussion of two closely related phenomena of attainment of self-similarity (**Sect 3.1.2**) and of velocity deficit removal (**Sect 3.1.3**).

The distance it takes for assuming the mean velocities have attained self-similarity and the distance it takes for the velocity deficit to reduce to near zero is studied here. This study is important, because many of the theories existing make the assumption of self-similarity, and it is important to understand under what conditions how much distance it takes to achieve the same. This in turn reflects the practical applicability of the said theory.

This is followed by the study of coherent structures (**Sect 3.1.4**) and the study of the convective velocity (**Sect 3.1.4**). Theory has a number of assumptions made to be able to calculate the convective velocities. A direct measurement of the same from simulation gives an idea of how valid those assumptions are.

This is followed by the observations regarding mean pressure profiles

(**Sect 3.2**). This includes a discussion on the Mach disturbances emanating from the splitter plate (**Sect 3.2.1**). It is observed that the mixing layer has a relatively lower average pressure compared to the free stream and this can be explained through boundary layer equations to be caused by turbulence. This pressure deficit is compared with the expected pressure deficit due to turbulence (**Sect 3.2.2**).This is followed by a comparison of the pressure rise in the domain with parallel walls with the expected pressure rise due to the mixing and due to the boundary layer (**Sect 3.2.3**).

The presence of the coherent structures in the walled channel causes the stream to have coherent fluctuations in pressure and velocity (**Sect 3.3**). The coherent pressure fluctuations are estimated by performing a point-to-point correlation in the cross stream direction. This is followed by velocity correlations and discussions regarding pressure-velocity correlations.

The mixing layer initially is smaller in size and is composed of high frequency disturbances, which coalesce downstream and form larger disturbances and turn to lower frequencies. The spectrum of these disturbances is analysed next (**Sect 3.4**).

3.1 Features based on Mean Velocity

At the inlet of a spatial mixing layer is the splitter plate over which boundary layer develops on both sides. Thus at the point where the two streams meet, the boundary layers cause a velocity deficit. This deficit is removed in due course of mixing, and the mean velocity profile evolves from a double boundary layer profile to a tanh type of a profile, which grows in the streamwise direction. Three important features based on the mean velocity are the Growth rate, the attainment of self similarity and the velocity rate of removal of velocity deficit, which are discussed in the following sections. Besides, based on instantaneous velocity, the structures can be identified which is also studied in detail.

3.1.1 Growth Rate

The growth rate is a parameter of significance because it indicates the amount of momentum mixing, which scales with the species and energy mixing too. The growth of the mixing layer is measured by fitting a tanh profile and measuring the 90% distance, as describe in the introduction chapter. The measured growth is linear (constant growth rate) in the self similar region. Self similarity in the parameters implies a constant rate of growth in the case of a mixing layer with zero pressure gradient. A representative measurement of a typical growth profile is shown in **Fig** 3.1

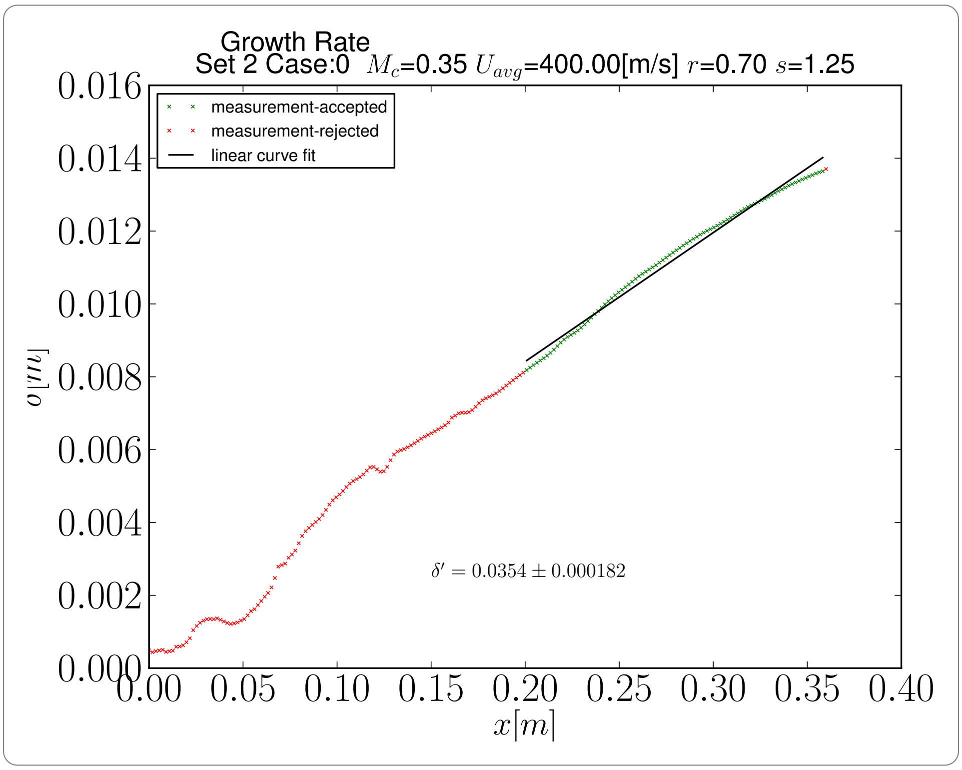

Figure 3.1: Typical Growth of a Mixing layer
[*Notice the linear portion used for the measurement of the growth rate*]

To study the effect of M_c on the growth rate, the effect of the velocity ratio r and the density ratio s must be removed. It is usually assumed that the effect of compressibility can be separated out and expressed as

$$\delta'(M_c; r, s) = \delta'_0(r, s) f(M_c) \tag{3.1}$$

Here the incompressible growth rate $\delta_0'(r,s)$ is the growth rate of the incompressible flow at the same velocity ratio and the density ratio as that of the given problem. This is usually obtained using the expression

$$\frac{d\delta}{dx} = \epsilon\left(\frac{1-r}{1+s^{1/2}r}\right)\left(1+s^{1/2}-\frac{1-s^{1/2}}{1+2.9\left(\frac{1+r}{1-r}\right)}\right) \tag{3.2}$$

Where the value of ϵ is found to be between 0.27 to 0.45 [Slessor et al., 2000]. The scaled growth rate of all the cases are plotted in **Fig 3.2**. It can be seen that the measured growth rate lies well within the band of experimental results and demonstrates the distinct drop in the growth rate with increasing M_c. A very important feature to notice is that the reduction in the growth rate is being captured by LES. It has been known for a while that most RANS simulations were unable to capture the effect of the growth rate reduction with increase in the M_c. This problem is dealt with in greater detail in **Chapter 5**. It is however very clear from the figure that LES is able to capture the effect. It has also been claimed by Vreman [1995] through LES of temporal mixing layers and Sankaran and Menon [2005] through LES of spatial mixing layer that LES was indeed capable of predicting the lowered growth rates.

In the present simulations though neither artificial dissipation nor any term dependent explicitly on the mixing layer has been added. This also goes to show that the reason of the reduction of the mixing layer has to do with the large scales, and not the large scales.

3.1.2 Self-Similarity

Self-similarity, in the present context, is the behaviour of the mixing layer when the profiles collapse into being a function of a single variable η which is a composite of x and y, rather than being functions of x and y independently.

In the case of a mixing layer, the velocity profiles, when scaled in the cross-wise direction with a length proportional to the mixing layer width, collapse into a single profile, which is close to a tanh function. In this section we shall analyse the self-similarity behaviour of the velocity profiles.

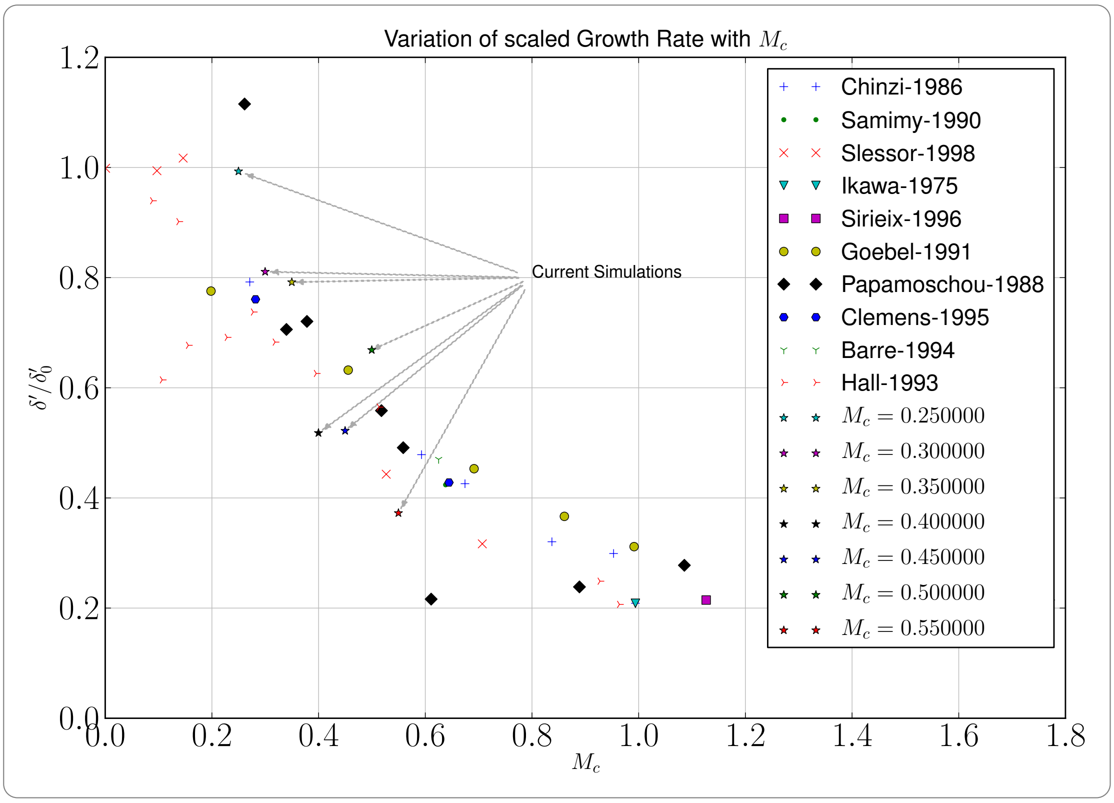

Figure 3.2: Growth rates variation with M_c in relation to experiments
[*The star marks are the measured growth rates*]

An example can be seen in **Fig 3.3**. In this we note that all curves after $x \approx 0.10[m]$ have attained self-similarity. At this distance, it can be said that a length scale (the information of the distance from the splitter plate) is *lost*, or equivalently, the flow has no influence of the splitter plate.

The delay in the attainment of self similarity with increasing M_c was observed by Pantano and Sarkar [2002], but for a temporal mixing layer for which analysis of simplified equations lead to a reasoning for the behaviour. Here we shall analyse a spatial mixing layer, instead of a temporal mixing layer. The departure from the analysis of Pantano and Sarkar [2002] is explained after the analysis.

The momentum thickness is a measure of loss of momentum in the mixing process. It is the extra cross-wise height required (in both directions) to allow the same flux of momentum as the initial flux. Mathematically

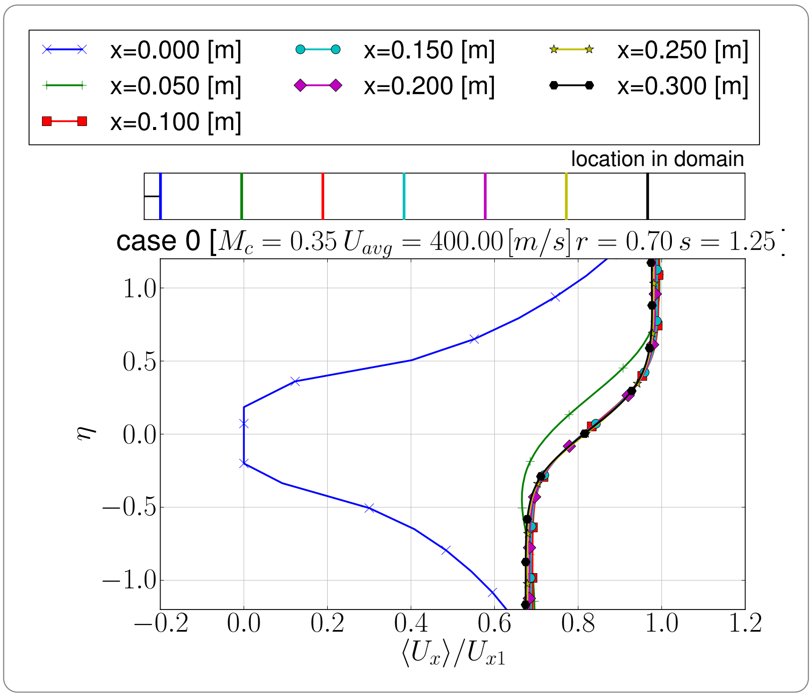

Figure 3.3: Attainment of self-similarity
[*The top figure indicates pictorially at which stream-wise location the measurement is made. Notice that the* tanh *profile is almost attained after* $x \approx 0.10[m]$]

$$\int_{-H}^{0} \rho_2 U_2 U_2 dy + \int_{0}^{H} \rho_1 U_1 U_1 dy = \int_{-H}^{H} \langle\rho\rangle \{u\} \{u\} + \int_{-H-\theta/2}^{-H} \langle\rho\rangle \{u\} \{u\} dy + \int_{H}^{H+\theta/2} \langle\rho\rangle \{u\} \{u\} dy \tag{3.3}$$

Where H is an arbitrarily large distance from the mixing layer. This equation simplifies to

$$\theta = \frac{1}{1+sr^2} \left(\int_{-\infty}^{0} \left(sr^2 - gf^2\right) dy + \int_{\infty}^{0} \left(gf^2 - 1\right) dy \right) \tag{3.4}$$

Where

$$g = g(y) = \frac{\rho(y)}{\rho_1}$$
$$f = f(y) = \frac{u(y)}{U_1}$$

It can be easily seen that as $y \to \pm\infty$ both the integrands reduce to zero, hence the integration converges. Next, taking the derivative of the above wrt x, we get

$$\theta'(x) = \frac{1}{1 + sr^2} \left(\int_{-\infty}^{0} -\frac{\partial g f^2}{\partial x} dy + \int_{\infty}^{0} \frac{\partial g f^2}{\partial x} dy \right) \tag{3.5}$$

With boundary layer approximation, we have

$$\frac{\partial}{\partial x} \langle \rho \rangle \{u\} \{u\} + \frac{\partial}{\partial y} \langle \rho \rangle \{u\} \{v\} \approx -\frac{\partial}{\partial y} \{\rho\} \{u'' v''\} \tag{3.6}$$

neglecting the x gradients as well as the viscous terms in comparison to the turbulent stress for an order of magnitude estimate Integrating the cross-wise direction, we have

$$\rho_1 U_1 U_1 \int_{-\infty}^{0} \frac{\partial g f^2}{\partial x} dy \approx \left(\langle \rho \rangle R_{12} \right) \Big|_{y=0} \tag{3.7}$$

Hence

$$R_{12} \sim U_1 U_1 \theta' \tag{3.8}$$

We now bring in the transformation from y to η as

$$\eta \equiv \frac{y}{\theta(x)} \tag{3.9}$$

This implies that

$$\frac{\partial}{\partial x} = \frac{\eta \theta'}{\theta} \frac{d}{d\eta} \text{ and } \frac{\partial}{\partial y} = \frac{1}{\theta} \frac{d}{d\eta}$$

We also make scaling

$$\begin{aligned}
\langle \rho \rangle &= \rho_1 \hat{\rho}(\eta) && (3.10)\\
\{u\} &= U_1 \hat{u}(\eta) && (3.11)\\
\{v\} &= U_1 \left(\theta'\right)^n \hat{v}(\eta) && (3.12)\\
R_{12} &= U_1^2 \theta' \hat{R_{12}}(\eta) && (3.13)
\end{aligned}$$

Where all $\hat{}$ represent functions of $O(1)$ Substituting this in the continuity equations we get

$$\frac{\partial}{\partial x} \langle \rho \rangle \{u\} + \frac{\partial}{\partial y} \langle \rho \rangle \{v\} = 0 \tag{3.14}$$

$$\rho_1 U_1 \frac{\eta \theta'}{\theta} \frac{d}{d\eta} \hat{\rho}\hat{u} + \rho_1 U_1 \left(\theta'\right)^n \frac{1}{\theta} \frac{d}{d\eta} \hat{\rho}\hat{v} = 0 \tag{3.15}$$

We see that for consistency, we need $n = 1$, hence

$$\{v\} = U_1 \theta' \hat{v}(\eta) \tag{3.16}$$

Substituting this in the boundary layer equations with viscous terms we get

$$\frac{\partial}{\partial x} \langle \rho \rangle \{u\} \{u\} + \frac{\partial}{\partial y} \langle \rho \rangle \{u\} \{v\} \approx -\frac{\partial}{\partial y} \{\rho\} R_{12} + \frac{\partial}{\partial y} \mu \frac{\partial u}{\partial y} \tag{3.17}$$

$$\begin{aligned}
\rho_1 U_1 U_1 \frac{\eta \theta'}{\theta} \frac{d}{d\eta} \hat{\rho}\hat{u}\hat{u} \quad &+ \rho_1 U_1 U_1 \theta' \frac{1}{\theta} \frac{d}{d\eta} \hat{\rho}\hat{u}\hat{v} \\
&\approx -\rho_1 U_1 U_1 \theta' \frac{1}{\theta} \frac{d}{d\eta} \hat{\rho} \hat{R_{12}} + \frac{1}{\theta} \frac{d}{d\eta} \mu \frac{\partial u}{\partial y}
\end{aligned} \tag{3.18}$$

We have the Reynolds number based on θ as

$$\mathrm{Re}_\theta = \frac{\rho u \theta}{\mu} \implies \mu = \frac{\rho_1 U_1 \theta}{\mathrm{Re}_\theta} \hat{\rho}\hat{u} \tag{3.19}$$

And an estimate of $\dfrac{u}{y}$ is $\Delta U / \delta_\omega$ where δ_ω is the vorticity thickness For self-similarity, it is required that the viscous terms become insignificant. Hence for self-similarity,

$$\rho_1 U_1 U_1 \frac{\eta \theta'}{\theta} \gg \frac{\rho_1 U_1 \theta}{\theta \mathrm{Re}_\theta} \frac{U_1}{\delta_\omega} \tag{3.20}$$

Thus for self-similarity

$$\mathcal{E} \equiv \mathrm{Re}_\theta \frac{\theta}{\delta_\omega} \theta' \gg 1 \tag{3.21}$$

The above derivation deviates from the derivation of Pantano and Sarkar [2002] in that in the case of the latter, the equation considered is the temporal mixing layer with a time derivative term in addition, but without the stream-wise derivative. Furthermore instead of the spatial derivative of the spatial mixing layer, the temporal mixing layer has a time derivative. Thus the derivations progress on different lines.

Equation 3.21 shows that the to attain self-similarity $\mathcal{E}$ must be large enough. When we have a closer look at $\mathcal{E}$, we notice that for a given fluid with the same fluid properties (i.e. considering ρ,μ etc as constants)

$$\mathcal{E} \propto U_1 \frac{\theta(x)^2}{\delta_\omega(x)} \theta'(x) \tag{3.22}$$

Thus it is clearly seen that lower the growth rate (hence lower the growth) the distance required to attain self-similarity will be delayed. Hence, increasing M_c is expected to delay the attainment of self-similarity.

Note that in the following sections, when we look at the influence of one of the parameter out of M_c, r, s, and r, the other parameters are kept constant. The procedure was described in **Section 2.9**

Influence of M_c on the attainment of self-similarity

Figure 3.4 shows the plot of the difference between scaled velocity profile and the self-similar profile, as a function of the cross-wise distance scaled with the width of the mixing layer. Each curve is a different M_c. The closer the curve is to 0, one can say, that self-similarity has been attained to a greater degree. At the shown, the flow having a greater M_c has a greater deviation from self-similarity and it is seen that deviation from self-similarity shows a distinct trend for being the least different from being self-similar for the lowest M_c case to being farthest from being self-similar for the highest M_c case. **Figure 3.5**

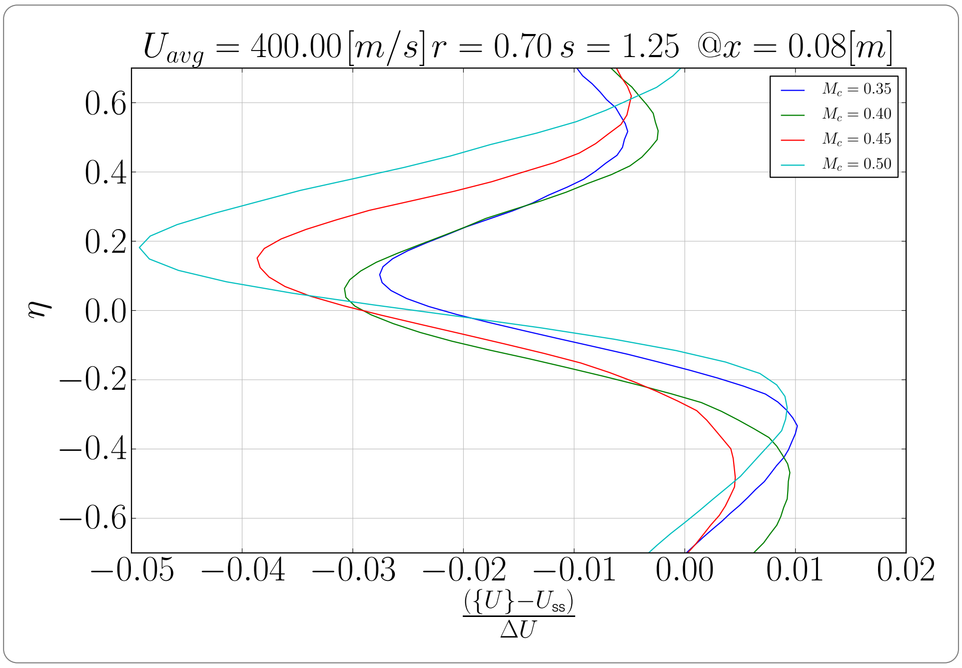

Figure 3.4: Difference in the average velocity profile, and the self-similar profile at a particular distance for varying M_c

[*Note that with increase in the M_c the deviation from self-similarity increases at the same distance from the splitter plate*]

shows the distance it takes for the difference in the self similar profile and the actual profile, normalized with ΔU and δ to reduce till a prescribed percentage. This even more clearly demonstrates that with increasing M_c attainment of self similarity is delayed. This conclusively proves that with increase in the M_c there is a delay in attaining the self-similarity. At distances further from the splitter plate (not shown), the curves become indistinguishable since all have more or less attained self-similarity. This trend of attaining self-similarity with M_c has been observed in experiments by Samimy and Elliott [1990] for the plane mixing layer.

Influence of r on self-similarity

We can at once see from **Fig 3.6** that r has a strong influence on the attainment of self-similarity. This is also reflected in the rate of removal of velocity deficit.

At a stream-wise distance of $x = 0.05[m]$ none of the three profiles is

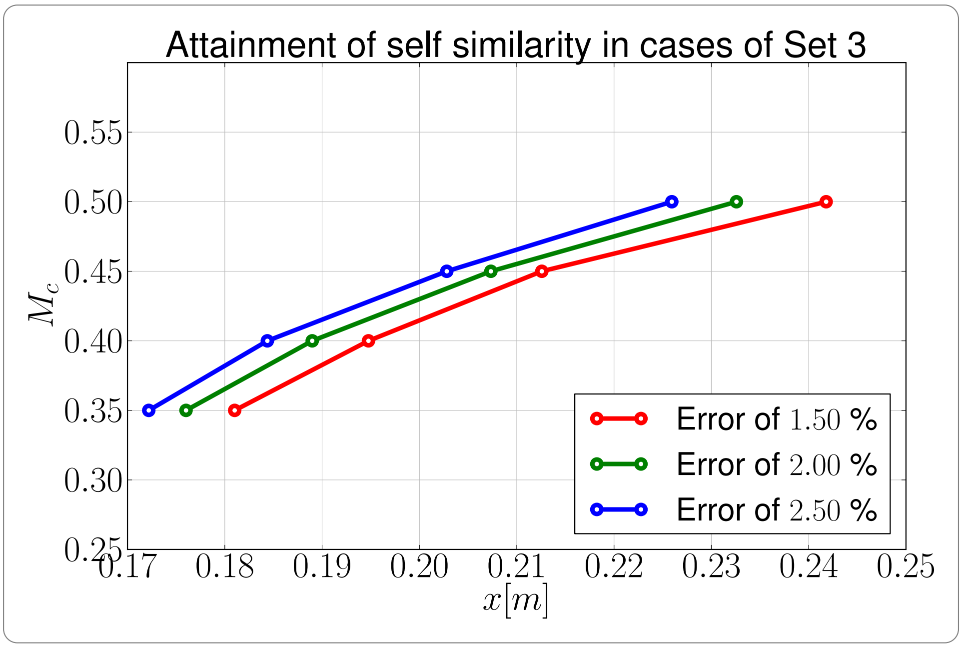

Figure 3.5: Attainment of selft similarity profile
[*Note that with increase in the M_c greater distance is required to attain self similarity*]

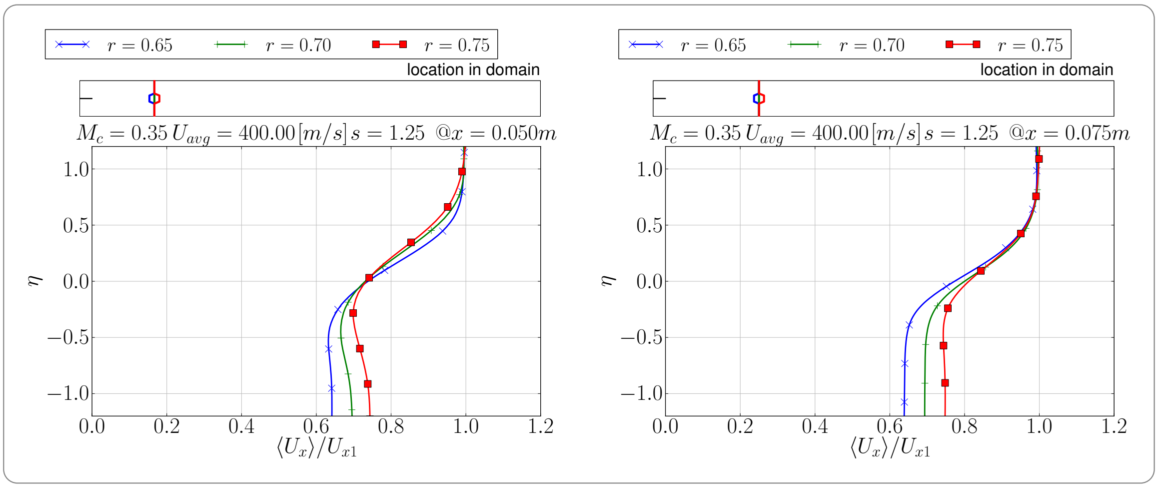

Figure 3.6: Self-similarity collapse of $\{U_x\}$ at a particular distance for varying r
[*The lower r profile attains self-similarity the earliest*]

self-similar. This is particularly indicated by the presence of a velocity deficit. At a distance of $x = 0.75[m]$ the flow with $r = 0.75$ still has not attained self-similarity where as $r = 0.65$ has almost reached to the self-similar state. Finally at $x = 0.1[m]$ all three curves seem to have attained self-similarity.

With increasing r at the same average velocity, the difference in the stream velocities tends to decrease. This directly means that the gradient of the velocity across the mixing layer is small. Hence the vorticity levels too tend to be small with larger values of r. In the limit of $r \to 1$ the mixing layer with a splitter plate becomes the same as that of a wake flow behind the splitter, where the velocity deficit may take a very long time to disappear.

Influence of U_{avg} and s on self-similarity

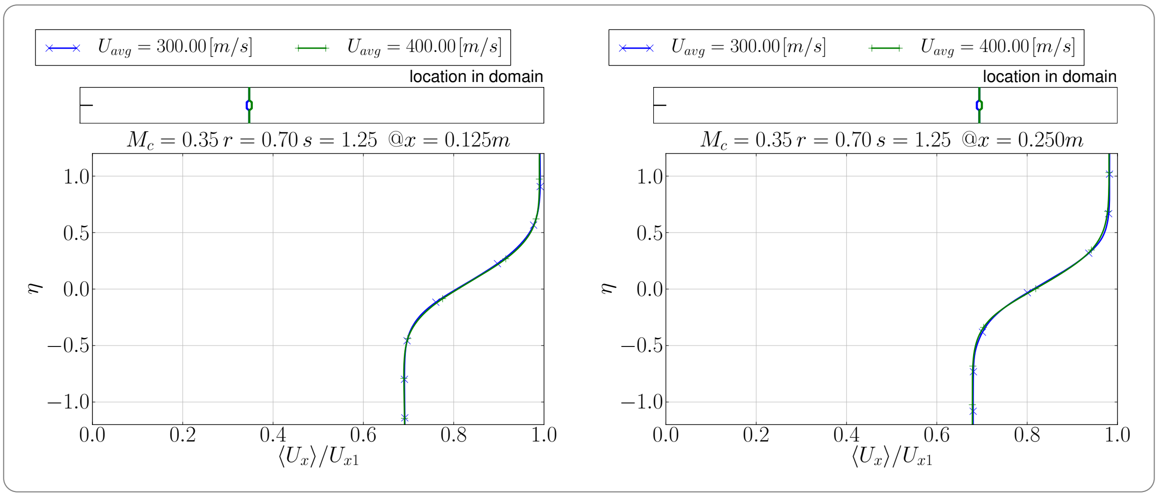

Figure 3.7: Self-similarity collapse of $\{U_x\}$ at a particular distance for varying U_{avg} [*There is hardly any change in the profile with increasing* U_{avg}]

Figure 3.7 and **Fig** 3.8 show the non-dimensionalized velocity profile with respect to the cross-wise coordinate scaled with the mixing layer width, for varying U_{avg} and s respectively. It can be seen from **Fig** 3.7 that U_{avg} has very little influence on the distance required to attain self-similarity. So much so that when non dimensionalized the curves across the cases in fact coincide to a large extent. Again, it is seen that the location where self-similarity is attained is just after $x = 0.08[m]$.

Similarly, **Fig** 3.8 shows that s too has a weak influence on the attainment of self-similarity.

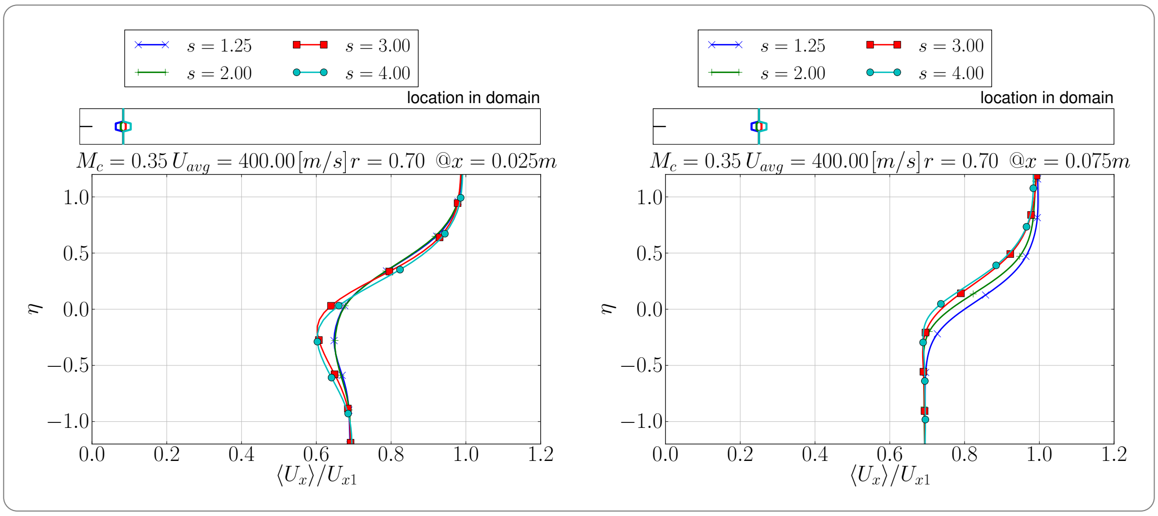

Figure 3.8: Self-similarity collapse of $\{U_x\}$ at a particular distance for varying s [*s has a small influence on the attainment of self-similarity*]

3.1.3 Velocity Deficit Removal

The wake of the splitter plate and the boundary layer over it cause the formation of region of low velocity immediately after the splitter plate. The mixing action and the accompanying momentum flux to this region eventually removes the region of low velocity completely, as the flow proceeds further to attain self-similarity. The removal of the velocity deficit depends on a number of parameters including the thickness of the splitter plate, the local Reynold's number, other than the flow parameters. In the present study, the focus is on the influence of the flow parameters for the same domain. In a flow without any deficit, in the region far from the boundary layers developing at the walls, the minimum velocity is the velocity of the secondary stream, U_2.

Effect of M_c on the rate of removal of velocity deficit

Fig 3.9 shows the sole effect of M_c over the rate at which the velocity deficit is removed. It is clearly seen that the initial portion closely follows the curve $U_{\text{min}} \propto 1 - \dfrac{a}{\sqrt{x}}$, shown in dotted line. In this region, the curves almost overlap each other, showing that there is not much effect of M_c. At some point, each curve switches to a higher rate of removal of the velocity deficit, and this region is almost linear. The point at which this switch happens is clearly delayed by

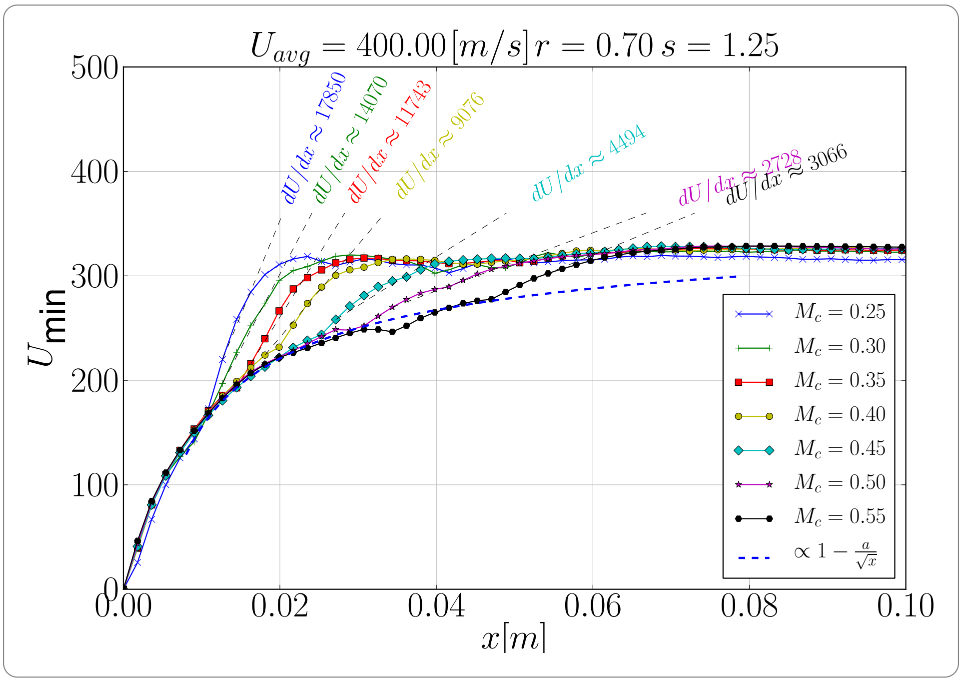

Figure 3.9: Variation of the removal rate of the Velocity

[*Notice the initial part is same for all M_cs, and is close to the wake line $\propto 1 - \frac{const}{\sqrt{x}}$ (which is valid for $x > 0.1$ here). Later it switches to almost linear reduction. The switching point is delayed and the rate of removal (shown as the slope of the linear region) decreases with increase in M_c*]

increase in M_c. The parabolic part of the removal, is basically identical to that of a wake behind the splitter plate. It can be seen that the linear rate begins at the point where the instability in the flow sets in. The fact that the point of switching to the higher rate is delayed with increase in M_c indicates that more the M_c, the more the delay for the instability to set in. Hence, this clearly indicates that a higher M_c provides stability to the flow. Moreover, it can be seen that the slope of the linear section of the curve distinctly decreases with increased M_c (see **Fig 3.10**). The rate of removal of the velocity deficit is proportional to the momentum diffusion present, which in turn is proportional to the amplification rate of the instability. Hence an inference may be drawn that the amplification rate of the instabilities decreases with increase in M_c.

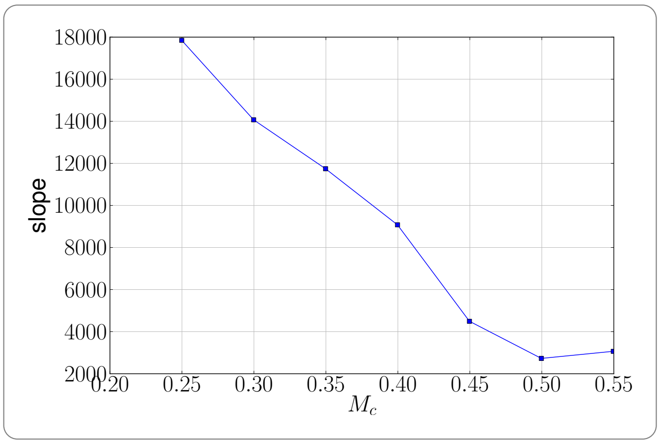

Figure 3.10: Variation of the velocity deficit removal rate in the linear region with M_c

3.1.4 Coherent Structures

To identify the coherent structures Dubief and Delcayre [2000] recommended the usage of the Q parameter. This parameter is calculated as

$$Q \equiv \frac{1}{4}\left(\omega^2 - 2S_{ij}S_{ij}\right) \tag{3.23}$$

It was shown that the Q parameter was capable of sharply marking the coherent vortex structures, of the kind found in Kelvin Helmholtz instability.

The Q contours for two different cases are shown in **Fig 3.11**. The structures are very distinctly seen in this image, and all the more the evolution of the structures from small size, merging and growth can be seen.

It can be clearly seen that as the M_c increases, the size of the structures have definitely decreased. Since the growth of the mixing layer is directly related to the growth of these structures [Sandham and Reynolds, 1989], it can be argued that the decrease in the growth rate is caused by the decrease in the size of the structures.

It can also be seen that the increase in r has a similar effect, that the size of the structures decrease, and hence lead to the decrease in the growth rate, but this effect is the same as that in incompressible flows.

A distinctive advantage of the spatial simulation performed is the possibil-

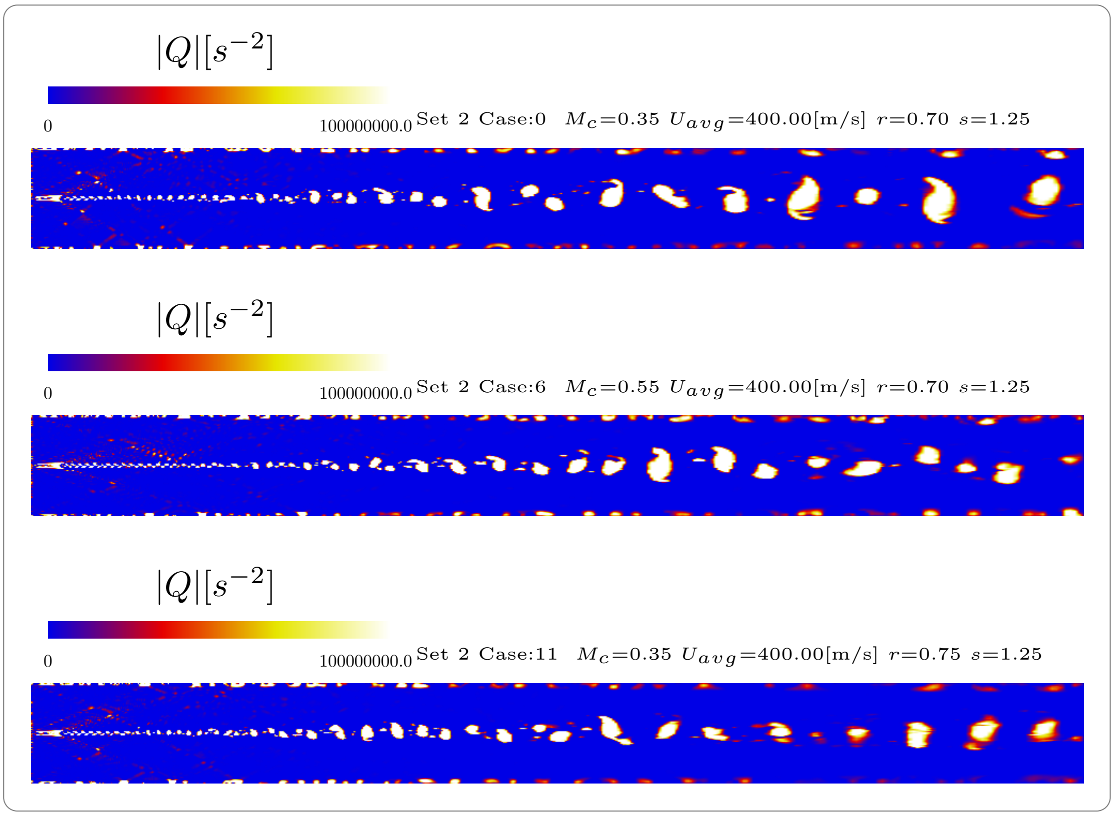

Figure 3.11: Coherent Voritcal Structures
[*The top figure is the central case. The middle figure the case with a higher* M_c *and the bottom with a greater* r. *Notice the distinct decrease in the size of the coherent vortical structures with increasing* M_c]

ity of detection of the coherent structures and following which a host of further calculations can be performed. For the detection of the structures, from the simulations, the Q parameter was calculated. The contours of this parameter, at a single suitable level was plotted. [1] A typical evolution of such a contour is shown in **Fig 3.12**. Once the contours are obtained, the area, centers, the evolution with time and other statistics can be calculated. The following analysis were performed

- The area and center of area of the relevant contours were calculated,
- The time trace of each relevant contour was recorded,

[1]the Q parameter is such that the shapes of the contours is more or less same for a range of threshold values. A value of $5 \times 10^8 [SI units]$ was found to be suitable for most cases

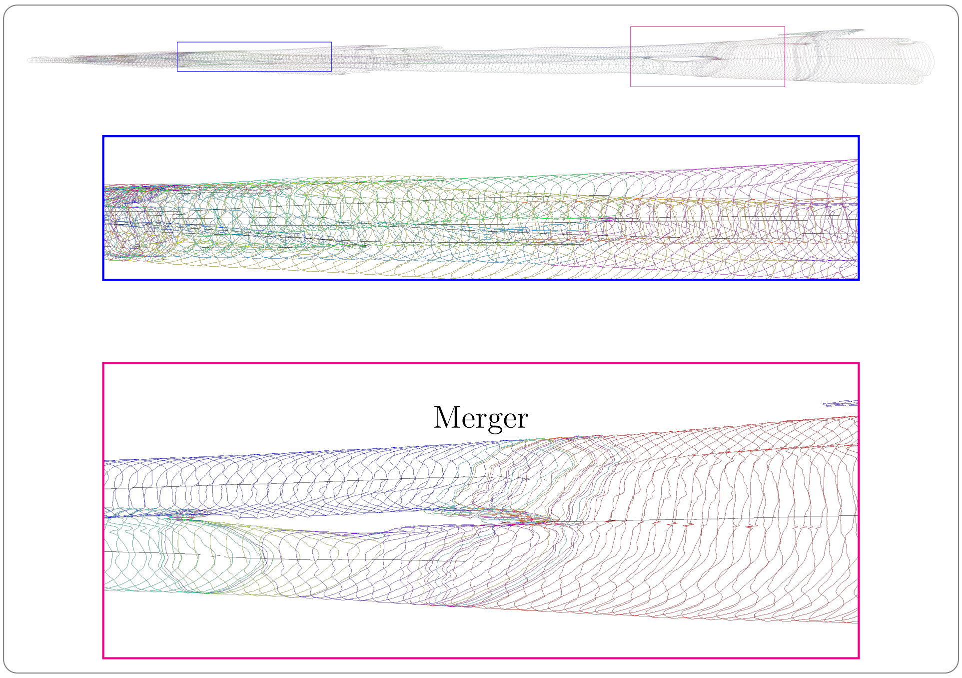

Figure 3.12: Evolution of a structure
[**Note:** The merger of different structures (depicted by different colors), their growth and splitting are all depicted. The contours are captured once every 4 time steps, and plotted once every 20 time steps]

- The velocity of the contours was calculated,
- The mergers of contours and splitting of contours were detected.

Position of centers

The position of the centers of the contours is plotted against the physical coordinates in **Fig 3.13**. This plot shows that most of the structures have the center close to the centerline and the excursions away from the same are not far, and are weakly dependent on the M_c.

It is apparent (admittedly not clear) that the excursions of a structure in either streams have reduced in the case of the higher M_c. The excursions of the contours away from the center, and the size of the contours both contribute to the mixing and the growth rate. It is seen that the reduction of the excursions, *could be* reflected as a reduction in the growth rate, if it is accompanied by a

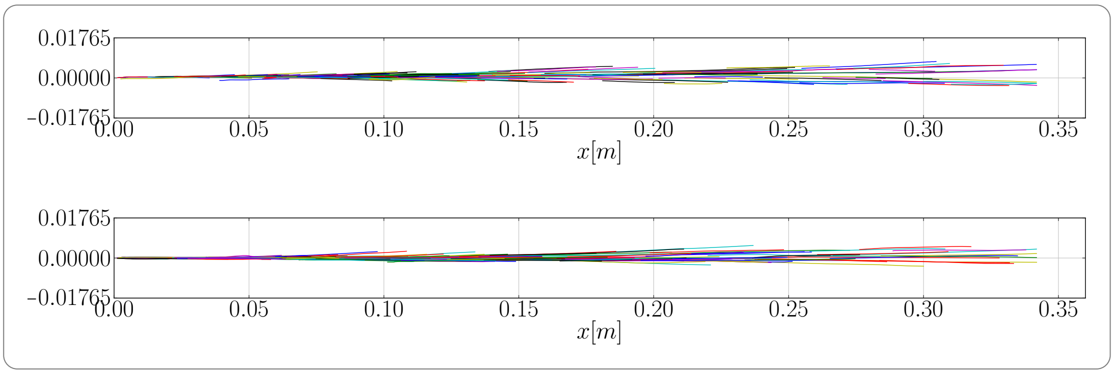

Figure 3.13: Trace of the centers of the structures **top**:$M_c = 0.25$ and **bottom**:$M_c = 0.5$

[*Trace of the position is shows that apparently the higher M_c case has a lower spread than that of higher M_c.*]

decrease in the area. This is later shown to be true.

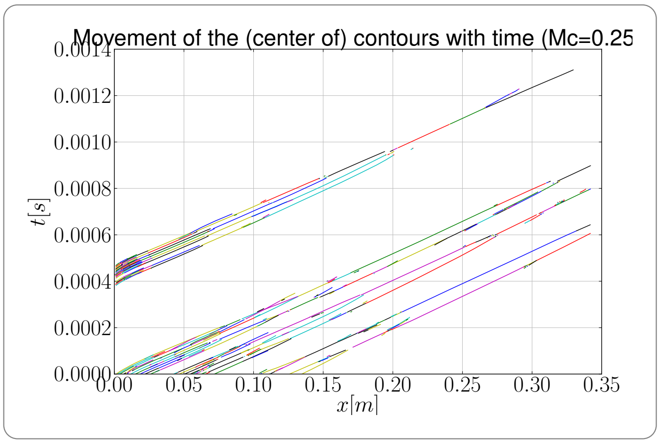

Figure 3.14: The time trace of a few contours at a lower $M_c(0.25)$

[*The mergers and a few splits of the contours are clear*]

Time trace of the position of center **Figure 3.14** shows the time trace ($t[s]$ vs $x[m]$) of a few contours. We can notice that the evolution of a structures involves merging of several contours. While some mergers are artefact of the contour setting, most are indeed genuine. Besides it is seen that most of the lines are quite linear, indicating a constant velocity.

The x-position of the center of the contours with time at a higher M_c is plotted in **Fig 3.15**. In each of the plots, the position of contours associated

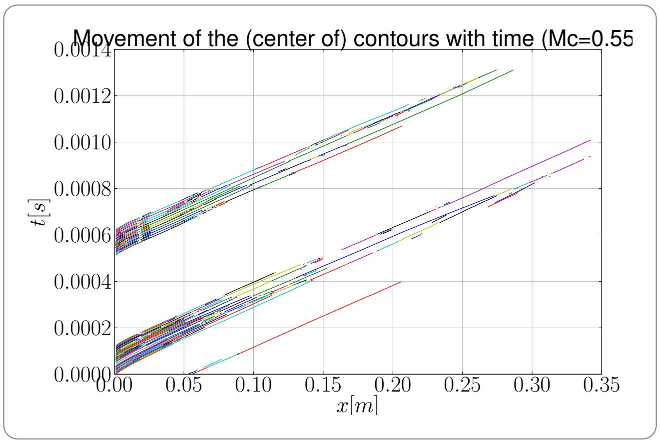

Figure 3.15: Time trace of contours at a higher $M_c(0.55)$
[*Notice that the larger M_c case has a delayed merging as compared to the smaller M_C*]

with 5 random traces is plotted. The fact that all the contours of a given trace is plotted, means, this shows the merging and the splitting of the trace too.

Comparing the time-x trace plots of a higher M_c is plotted, in **Fig 3.15**, it is apparent that the higher M_c has far more lines from the start and these proceed to a large distance before merger happens than in the case of smaller M_c. Hence we may draw the conclusion that *the increase in the M_c delays the merging of structures*. The merging of structures is crucial in the process of growth of structures, which is also indicated by linear stability analysis (eg Sandham and Reynolds [1989]), though the delay in the merging phenomenon cannot itself be predicted by the linear stability analysis.

Size of Structures

The size of the structure is indicative of the excursion of each of the stream into the other. This in turn is indicative of the mixing process. It is hence, useful to investigate the statistics of the size of the structures.

Figure 3.16 shows the average area of the contours versus the stream-wise location. The average is conducted about a thousand contours. It can be seen that

- The average growth rate of the areas of the lower M_c is almost linear

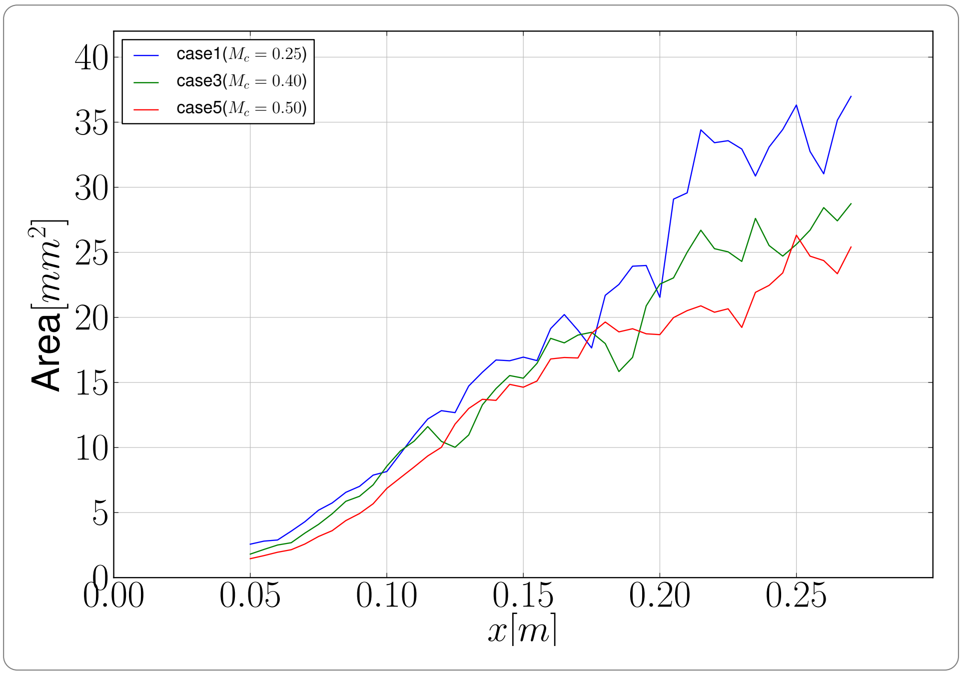

Figure 3.16: Variation of Average Area with x
[*The average area of the contours distinctly decreases with increase in* M_c]

- The average growth rate of the different M_c cases is almost the same initially
- The slopes of higher M_c is reduced, and higher the M_c greater the reduction

Shown in **Fig 3.17** is the history of the area of the same contour shown in **Fig 3.12**. This figure shows the importance of of mergers in the growth of a structure. This figure shows that structures grow at vastly different rates. Some even decrease in size. Many structures grow initially and saturate, and after that merger of the structures cause an effective growth. This is very close to the findings of linear stability analysis, which shows that after a certain growth, the amplification factor becomes zero, after which merger of structures causes a growth, and also allows it to grow further.

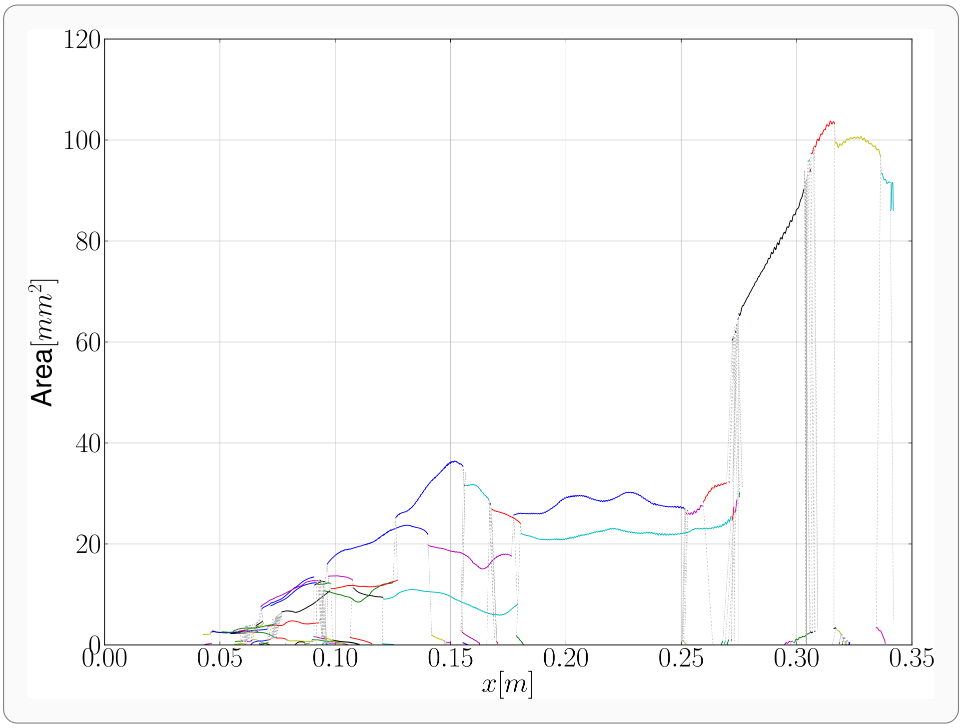

Figure 3.17: Area history of a contour
[**Note:** It can be seen that mergers of contours contribute to the increase in the area of a structure quite significantly]

Convective Velocities

[2] The measurement of the convective velocity is very important, because this is the foundation of many of the theory of the compressible mixing layer, and is generally estimated through empirical relations. The incompressible value of the velocity of the structures of the mixing layer involves the equalization of the dynamic pressures on both sides of the stream in the frame of reference of the structures [Dimotakis, 1984]. This yields

$$\frac{U_c}{U_1} \equiv r_c = \frac{1 + rs^{1/2}}{1 + s^{1/2}} \tag{3.24}$$

For the compressible case Papamoschou and Roshko [1988] equated the total pressures, assuming the stagnation to the frame of reference is isentropic.

[2]**Note:**in this table and the related discussion, σ refers to the standard deviation

This yields for same γ of both streams

$$U_c = \frac{a_2 U_1 + U_2 a_1}{a_1 + a_2} \tag{3.25}$$

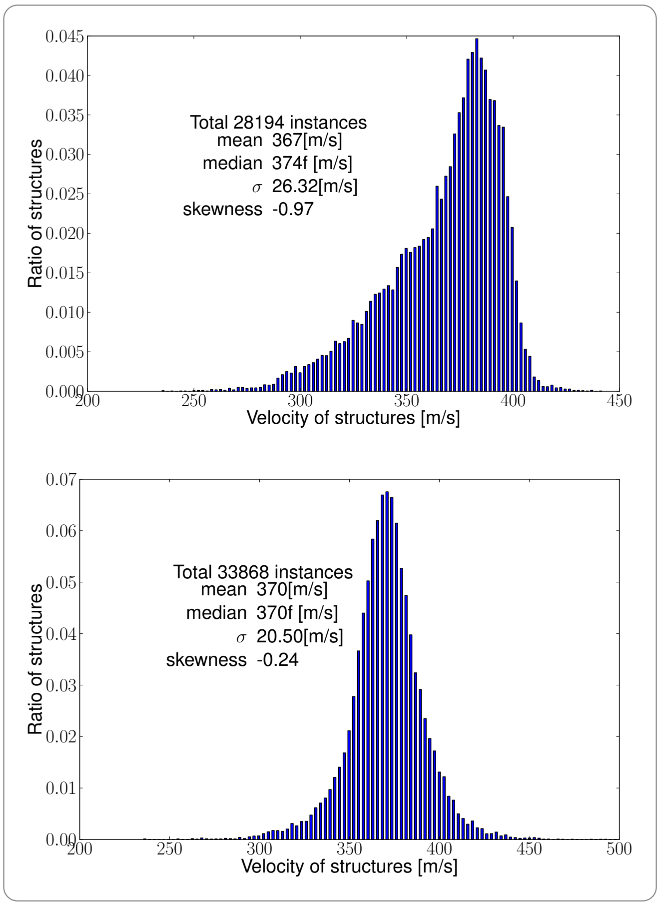

Figure 3.18: Velocity histogram
[*Note that the* **top** *figure with lower* $M_c(0.25)$ *shows a more skewed distribution of the velocity, as compared to the* **lower** *figure which has a greater* $M_c(= 0.55)$*, but roughly the same* σ*. Also the theoretical velocity is about* $396[m/s]$.]

Spatial simulations provide for the possibility of direct measurement of the velocity of the coherent structures. The technique followed here is to find the incremental position change in the position of the center of the contour between consecutive iteration. This introduces an error of apparent movement when the shape of the structure changes. This is found to have a component of less than 5%. Also the iteration which involve splits or mergers, which result in a unphysical change in the position of the centers are ignored. The distribution of the convective velocities of the structures is shown in **Fig 3.18**. Similar measurements were made for all cases and the findings are summarized

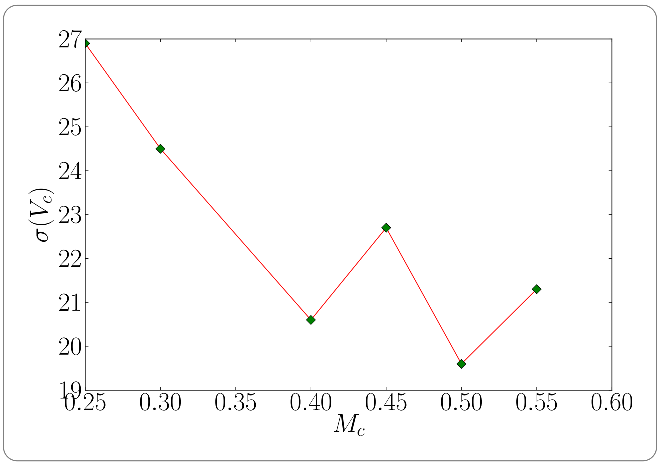

Figure 3.19: Variation of $\sigma(V_c)$ with increasing M_c
[*There is a decrease in the deviation of the velocities with increased* M_c]

The present work shows that for all the cases, the measured convective velocity is consistently *lower* than predicted by theory. Knowing that the range of the possible values of r_c is from r to 1, the measured r_c is about 10–15% lesser [3]

This difference is perhaps due to the non-isentropicity of the flow due to mixing, heat conduction, shear, or even due to the presence of shocklets. However this difference has been quantified to be small in value. Also plotted in **Fig 3.19** is the standard deviation of the measured velocity with increasing M_c. It can be seen that there is a clear trend of decreasing variation of velocity with increasing M_c. This behaviour can be attributed to the fact that the excursions of the structures far away from the centerline is decreased in the higher M_c cases. This also is one of the contributing reasons for the decreased rate of merging of structures, because, when there is a greater variation in the velocities, there is a greater chance that the structures can merge with each other.

[3] calculated as $\dfrac{r_c - r_{c\text{measured}}}{1 - r}$

3.2 Mean Pressure Profiles

Turning the attention to the features of the mixing layer, which we can infer from the pressure field, a typical mean pressure profile is show in **Fig 3.20**

The boundary condition on the splitter plate and the top and bottom walls is that of no slip. This causes the formation of boundary layer. A slight mismatch in the expected pressure profile, and the imposed profile gives rise to the waves right at the inlet. This wave, however is quite weak and dies down after a couple of reflections.

At the edge of the splitter plate a doublet of expansion and compression wave is formed due to the turning of the flow on both sides. These two waves propagate in either direction and are reflected by the walls. The boundary layer on the walls attenuates these waves, and after two or three reflections, these waves more or less die down.

The coherent structures convecting with the flow cause alternate increase and decrease in the pressure. However it is seen that the average flow has a decreased pressure in the region of the mixing layer. This decrease arises due to the momentum balance in the region of turbulence.

Finally there is an increase in the over all pressure in the stream-wise direction. This increase is mainly due to the boundary layer as will be discussed in the following sections.

3.2.1 Mach disturbances from splitter plate

An important feature of the supersonic mixing layer is the presence of the reflecting stationary waves caused mainly due to the splitter plate. These waves have been reported in the experiments of Papamoschou and Roshko [1988] (**Fig 3.21**)

The angle of the wave is the direct indicator of the prevailing Mach number in supersonic flows, and can be used to ascertain the Mach number. This is often used by the experimentalists to *measure* the Mach number of the two streams.

As shown in **Fig 3.22** the angle measured is about $20°$ for the primary

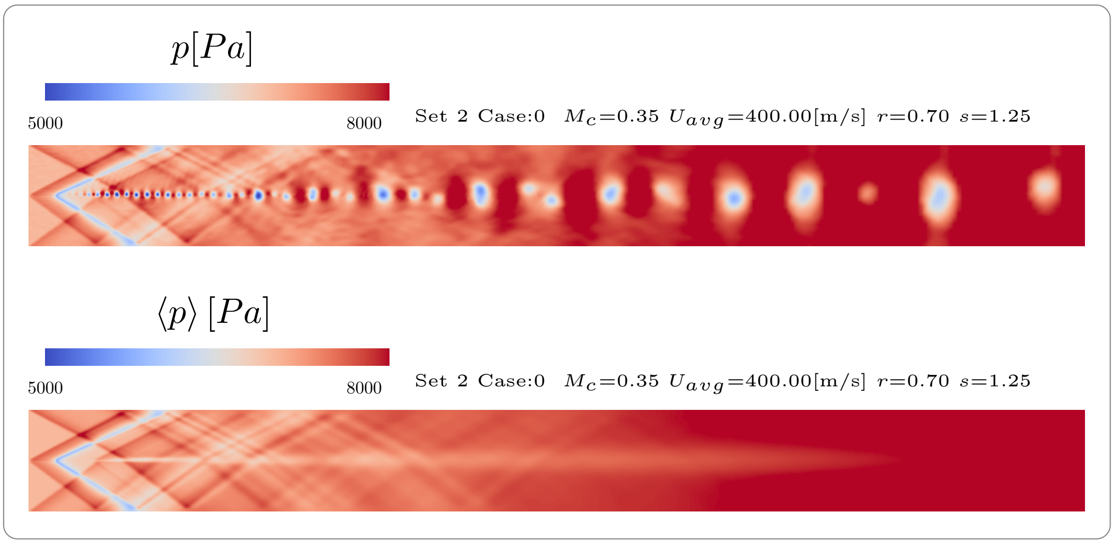

Figure 3.20: Typical p, $\langle p \rangle$ profiles
[*Notice the Mach and weak compression waves emanating from the splitter plate, and reflecting on the walls, a distinct increase in the pressure in the stream-wise direction and a lowered average pressure at the mixing layer*]

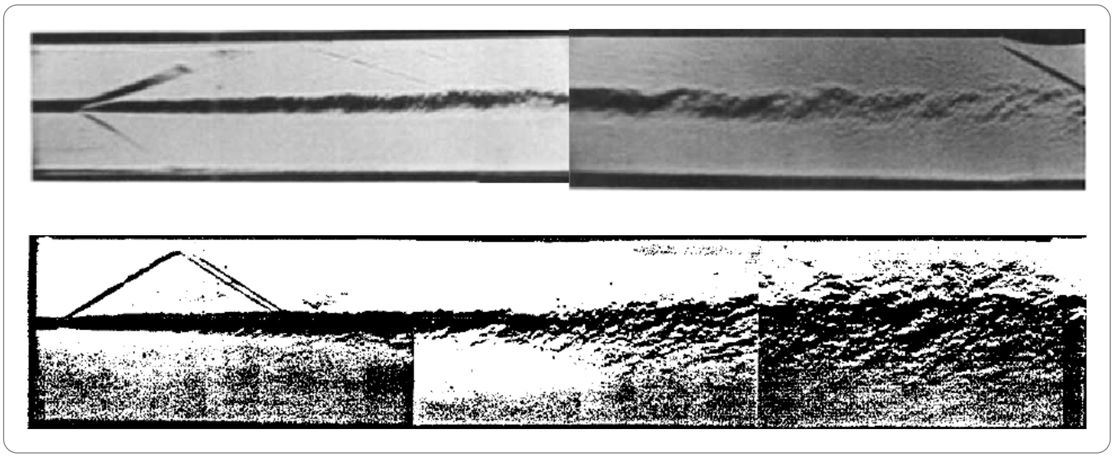

Figure 3.21: Schlieren from Experiments of Papamoschou and Roshko [1988] (top) and Goebel and Dutton [1990b] (bottom)
[*Notice the waves emerging from the edge of the splitter plate*]

stream and about 32° for the secondary stream. This corresponds to Mach numbers $M_1 \approx 2.92$ and $M_2 \approx 1.88$ which is close to the experimental value of $M_1 = 3.1$ and $M_2 = 1.7$. As a cross verification of the simulation, in **Fig 3.23** we draw the mach angles. This turns out to be at angles 25° and 33°, which

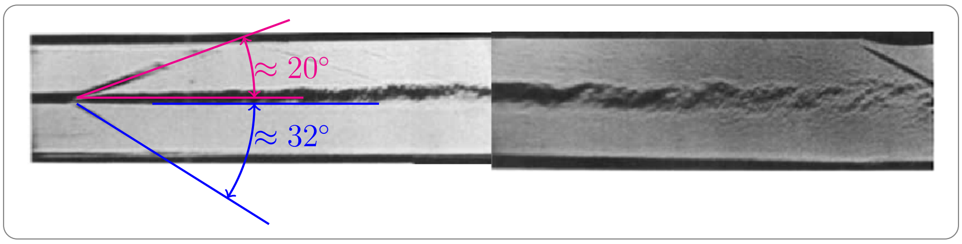

Figure 3.22: Measurement of the angles for an experiment of Papamoschou and Roshko [1988]

corresponds to $M_1 = 2.3$ and $M_2 = 1.8$ which is close to the inlet Mach conditions of $M_1 = 2.2$ and $M_2 = 1.72$. This also goes to show that the waves are not strong oblique shocks. In the given conditions, the Mach number of the flow perpendicular to the direction of the waves is very near unity.

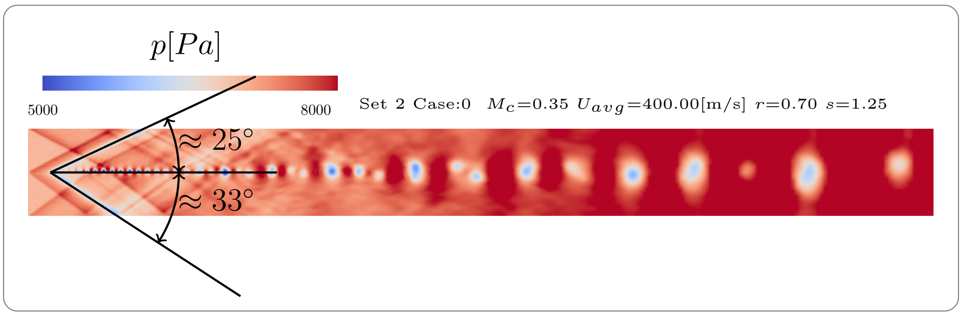

Figure 3.23: Measurement of the angles for an experiment of Papamoschou and Roshko [1988]

3.2.2 Pressure Deficit

When one observes the pressure distribution of the mixing layer, the region of mixing shows a clear indication of a reduction in pressure from the mean stream profile. This deficit in the pressure in the region of the mixing layer is a direct consequence of the momentum equation. The cross stream momentum equation (for two dimensions) reads

$$\rho\frac{\partial v}{\partial t} + \rho u\frac{\partial v}{\partial x} + \rho v\frac{\partial v}{\partial y} = -\frac{\partial p}{\partial y} + \frac{\partial \sigma_{xy}}{\partial x} + \frac{\partial \sigma_{yy}}{\partial y} \tag{3.26}$$

For a statistically stationary flows, averaging yields

$$\langle\rho\rangle \{u\} \frac{\partial \{v\}}{\partial x} + \langle\rho\rangle \{v\} \frac{\partial \{v\}}{\partial y} = -\frac{\partial \langle p\rangle}{\partial y} + \frac{\partial T_{xy}}{\partial x} + \frac{\partial T_{yy}}{\partial y} \tag{3.27}$$

Where T is the sum of the viscous stress and the turbulent stress.

If we make the assumption now that $\{v\}$ and $\dfrac{\partial \{v\}}{\partial y}$ are small, the balance is simply

$$\frac{\partial p}{\partial y} = \frac{\partial T_{xy}}{\partial x} + \frac{\partial T_{yy}}{\partial y} \tag{3.28}$$

Further neglecting the viscous part in comparison to the turbulent part of the total stress, $T_{ij} \approx -\tau_{ij}$

Hence

$$p_{,y} = -\tau_{iy,i} \tag{3.29}$$

We can now compare the two and see if we obtain a match between the deficit of pressure and the divergence of the y components of turbulence stress.

Fig 3.24 shows this comparison. One can clearly see the absolute match between the two curves, which proves beyond doubt that *the pressure drop at the centre of the mixing layer is purely due to turbulence, and that this drop is totally accounted for.*

3.2.3 Pressure Rise due to Boundary Layer and Mixing

We now look at the mean pressure profile in the stream-wise direction. A typical pressure profile is shown in **Fig 3.25**

There can be two reasons for the rise in the pressure.

The Boundary Layer The boundary layers developing on the walls of the chamber reduce the effective channel cross area available for the flow of the mixing layer. This is reduction is the same as that of the displacement thickness. A similar effect happens for the mixing layer, which, also has a displacement thickness in the cross-wise direction. Hence a practical mixing layer domain with parallel walls having no slip boundary

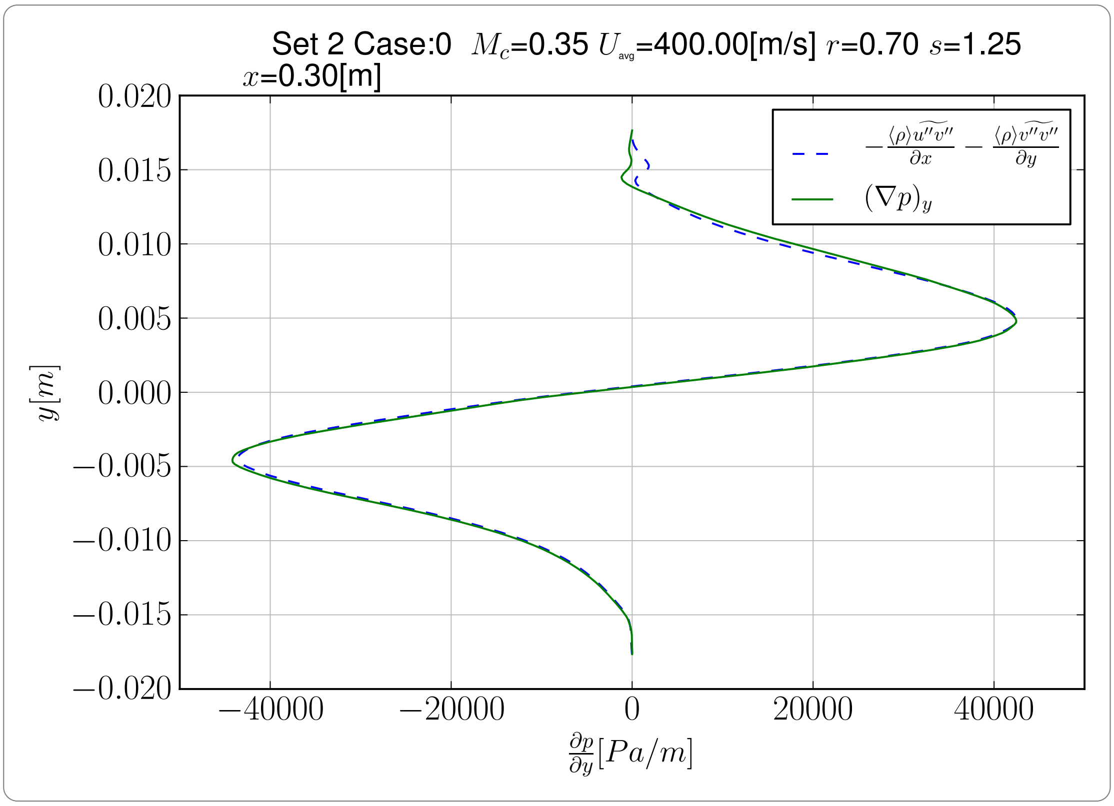

Figure 3.24: Pressure gradient compared with gradient of turbulent stress
[*Notice the almost complete match between the two curves*]

conditions is effectively like a convergent duct, which for a supersonic flow acts as a diffuser, hence the rise in pressure.

The Mixing Process The mixing process itself results in the velocity profile being more evened out. The total area of the curve under the ρu vs y curve must be a constant to account for the mass conservation. Since momentum is proportional to ρu^2, there is a loss in the momentum, which must be accounted for by an increase in the pressure.

The amount each one contributes to the total increase is investigated here. To model the increase, we model the flow to be equivalent to two channel flows as shown in **Fig 3.26** A-priori we know the following parameters

- The effective areas are estimated from the velocity profiles, hence inlet areas are known, the sum of the outlet area is known, individual areas are not known

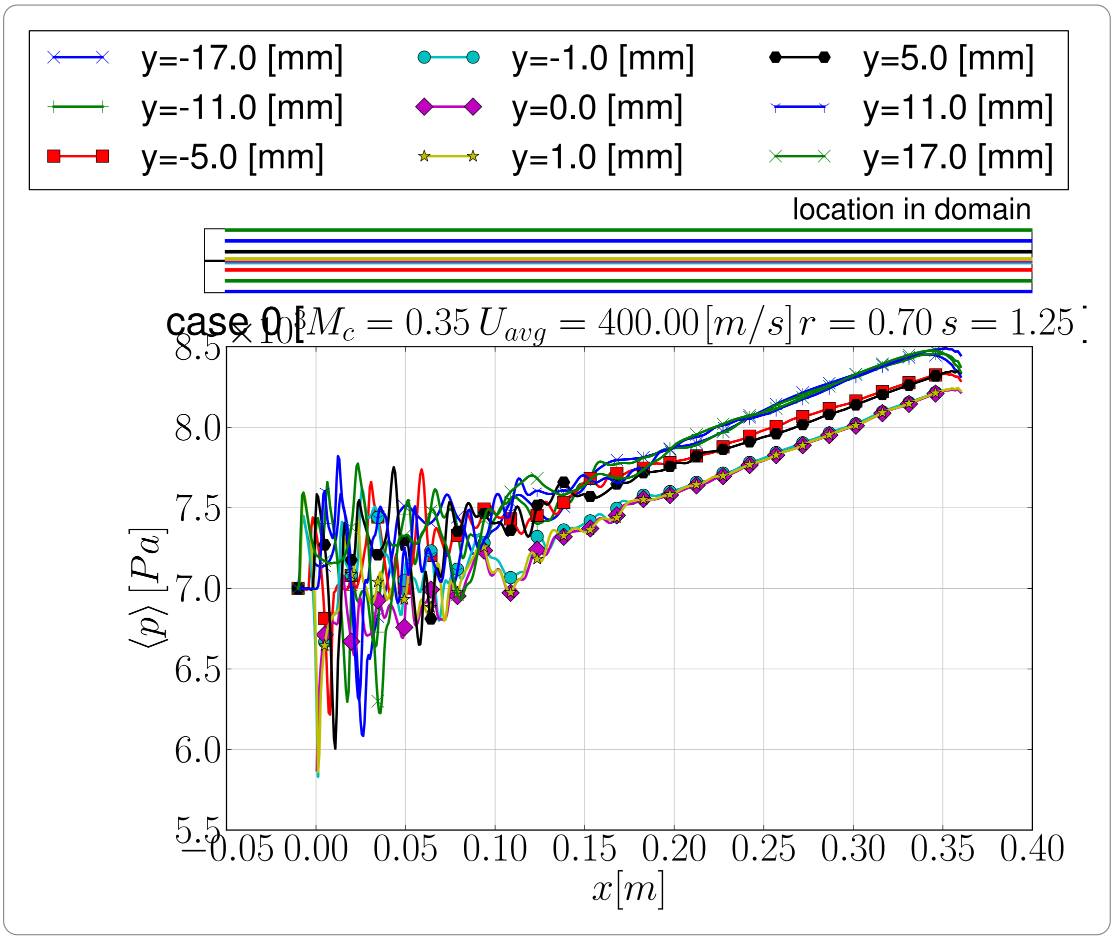

Figure 3.25: Variation in the average pressure in the stream-wise direction
[*The top part of the figure shows pictorially the cross-wise position at which the corresponding measurement is taken.Notice the clear increase in the average pressure at all stations along the cross direction*]

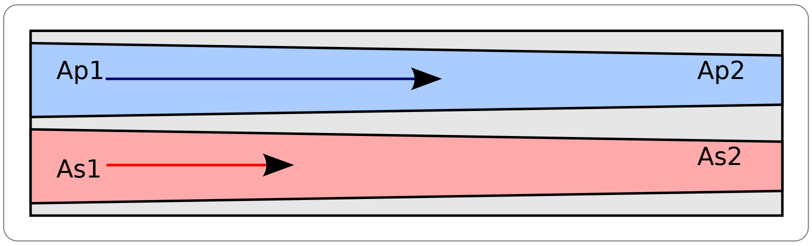

Figure 3.26: Model for reduced area channel
[*The effective blocked area due to mixing layer and due to the boundary layer*]

- Inlet mach numbers are known and inlet pressure is known

The calculation of each of the outlet areas individually is iterative, where we assume an effective outlet Mach number for each of the streams and calculate the exit pressure p_2 using **Eqn 3.30** and exit area a_2 using **Eqn 3.31**

$$\frac{p_2}{p_1} = \left(\frac{1 + \frac{(\gamma - 1)}{2} M_1^2}{1 + \frac{(\gamma - 1)}{2} M_2^2} \right)^{\left(\frac{\gamma}{\gamma - 1} \right)} \tag{3.30}$$

$$\frac{A_2}{A_1} = \frac{M_1}{M_2} \left(\frac{1 + \frac{\gamma - 1}{2} M_2^2}{1 + \frac{\gamma - 1}{2} M_1^2} \right)^{\left(\frac{\gamma + 1}{2\,(\gamma - 1)} \right)} \tag{3.31}$$

Iterations terminate when pressures on both streams match, and the total area on the exit matches with the total effective area obtained from simulations. To obtain the pressure gain due to momentum loss due to mixing, we simply calculate the inlet momentum and the outlet momentum through integration and the difference is the pressure gain due to mixing.

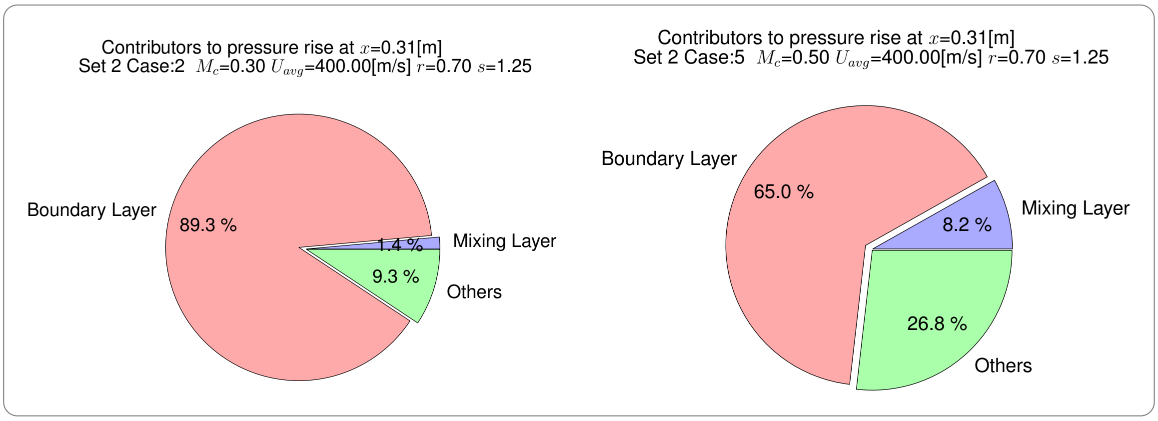

Figure 3.27: Contributors to pressure rise
[*The contribution of the boundary layer decreases with* Mc]

A typical distribution of the pressure rise from two cases is shown in **Fig 3.27**. It can be seen that more than 80% of the pressure rise is due to the growth of the boundary layers, and only about 10% is from the spread of the velocity profile in the mixing layer. It can also be noted that the proportion of the pressure rise due to the boundary layer is greater than in the case of lower M_c.

3.3 Coherence in Fluctuations

This section presents the coherence amongst fluctuations of various parameters in the flow field. In course of analysis of the various parameters, correlations between various parameters were studied. While studying these, some interesting aspects were noticed which are presented in this section.

Firstly, from **Fig 3.28** it can be seen that very early, the region of influence of pressure reaches the walls. This implies that the 'free stream' is no longer free from the influence of the mixing layer, and there is the presence of large scale coherent pressure fluctuations. To be able to quantify this aspect and to be able to see the influence of the same on the velocity field, the two point correlation of the pressure fluctuation was calculated for every two points at the same stream wise location.

Figure 3.29 shows the calculated two point correlations of the pressure field. This plot indicates several features. To be able to explain the different regions of the plot, consider **Fig 3.30**

Region A This region is the correlation of points very close to each other, and hence it is expected to have a very large correlation, as is also seen.

Region B Near the mixing layer, the interaction of the two streams gives rise to alternate compression and rarefaction. This region denotes points within the region of mixing, and shows large correlation as high as 0.85. It is rather interesting to note that this region develops earlier in the case of higher M_c than in the case of lower M_c. This indicates that within the mixing layer, greater correlation is found in the pressure fluctuations, for a higher M_c case than a lower M_c case.

Region C This is the correlation of the near center region to the peripheral point. This shows the least correlation.

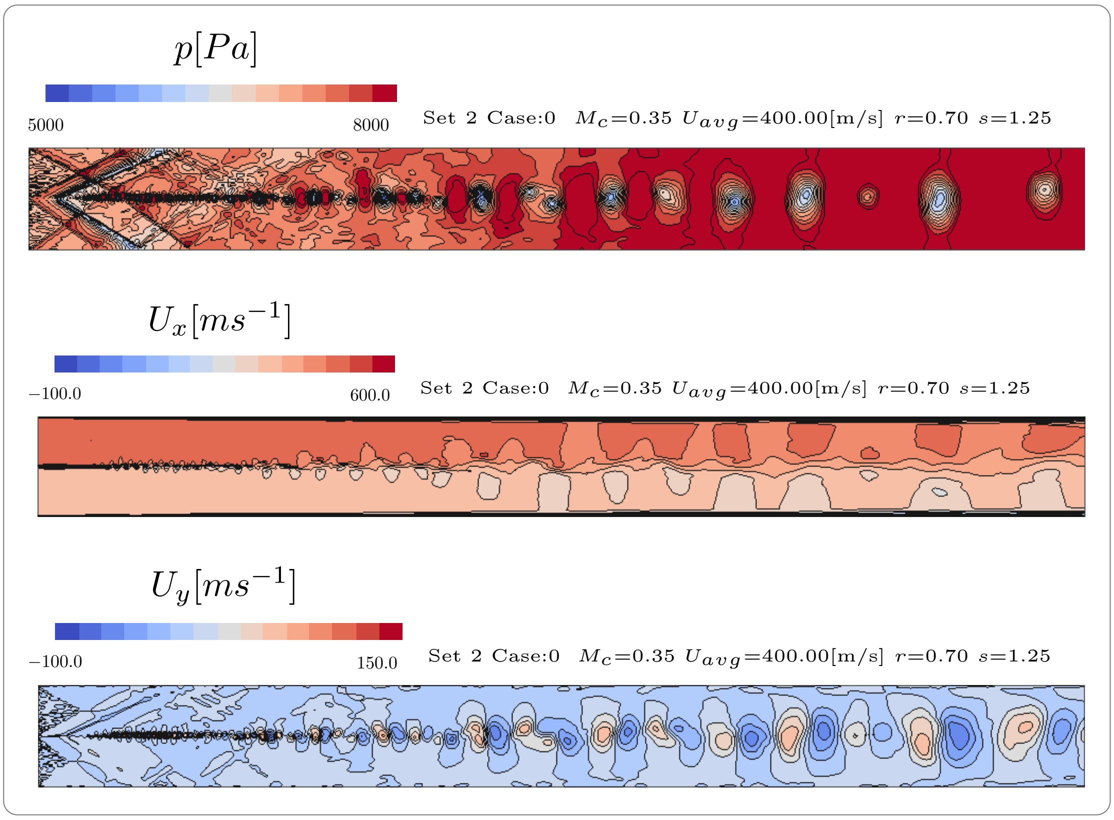

Figure 3.28: Pressure Contours (**Top**), U_x(**Middle**) and U_y(**Bottom**) [*The influence of pressure reaches the boundary earlier, and the influence is in the way of columns*]

Region D This region is the most unusual part,where points at symmetric locations from the center show a large correlation, as high as 0.9. This stem is found to be present in the case of lower M_c case much more prominently than in the case of a higher M_C case.

It must also be noted that at about 0.35[m] of the domain length, almost the entire cross-wise direction has a very large correlation of pressure fluctuations (greater than 0.8 in the smaller M_c case and about 0.5 in the case of larger M_c case). This clearly indicates the presence of large scale coherent oscillations in the flow field. This coherent pressure fluctuations are expected to have an influence on the velocity field by way of increasing the value of τ_{xx}.

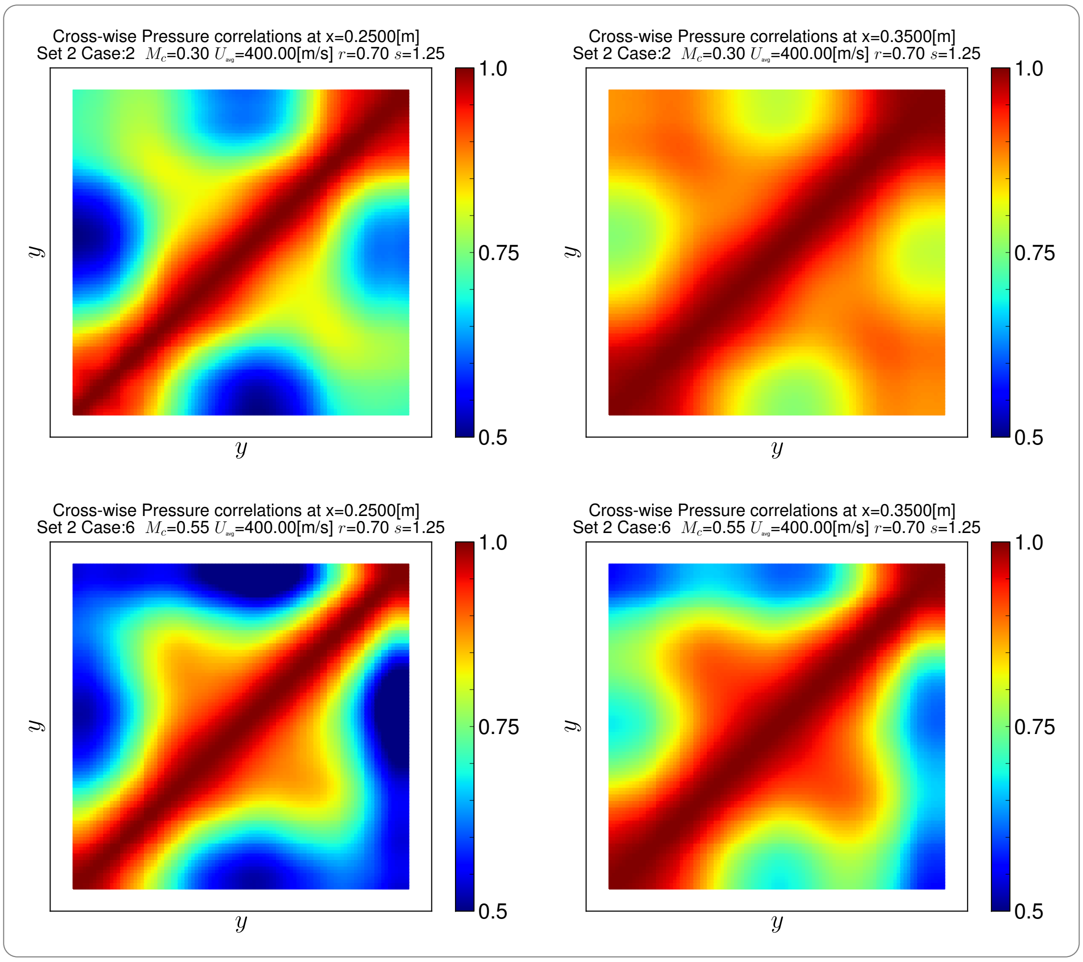

Figure 3.29: Pressure Cross Correlation for $M_c = 0.25$(top),and $M_c = 0.55$(bottom), at $x = 0.25[m]$(left) and $x = 0.35[m]$(right)
[*The area of the correlations increases significantly in the downstream direction. Also note that in the high M_c case the region of influence of p is distinctly smaller than in the case of lower M_c.*]

3.3.1 Pressure Velocity Correlation

Is interesting to analyse the pressure velocity correlation, to see the interdependence of the velocity and the pressure profiles. This correlation is shown for the high M_c case and the low M_c case in **Fig 3.31**. This figure, brings out an interesting fact that the pressure is strongly and positively positively correlated with the secondary side stream-wise velocity fluctuation and strongly negatively correlated with the stream-wise velocity on the primary side. To impress upon this point, **Fig 3.28** shows the pressure contours, and the two

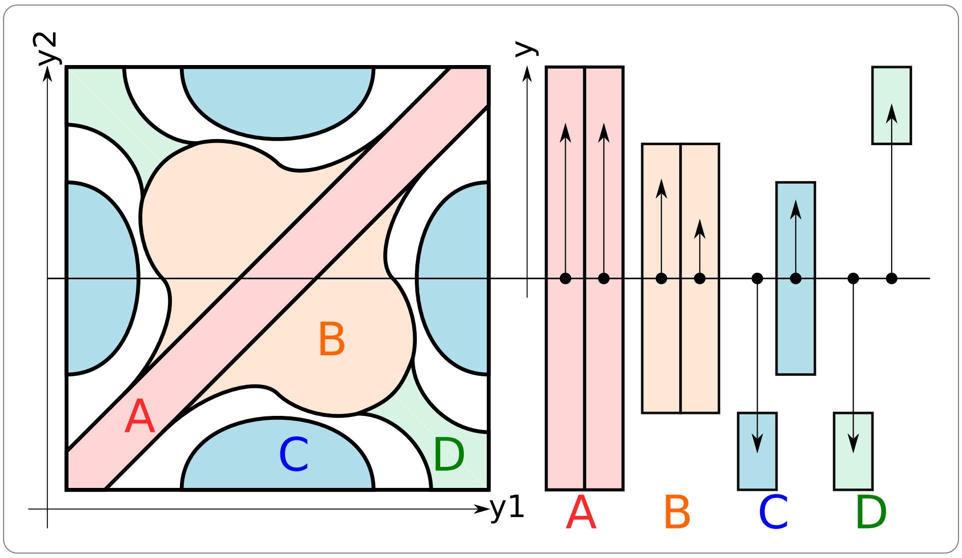

Figure 3.30: Model of the shape of two point correlation of pressure
[**A** *represents correlation between points nearby, throughout the domain,* **B** *represents the correlation between points within the mixing layer,* **C** *represents correlation between one point in the mixing layer and another outside, and* **D** *represents correlation of two points on the opposite ends of the domain*]

components of the velocity profile. A heuristic model helps understand the correlation more clearly. When the pressure and velocity are positively correlated, pressure can be said to be driving the velocity. That is when an increase in the pressure increases the velocity, and vice versa. When pressure and velocity are negatively correlated, velocity (or momentum) can be said to build the pressure. That is, a decrease in the velocity causes increases the pressure, and vice versa. It is clear from the above correlations that velocity fluctuations drives pressure fluctuations on the primary side, and vice versa on the secondary side. This causes a momentum flux from the primary stream to the secondary stream.

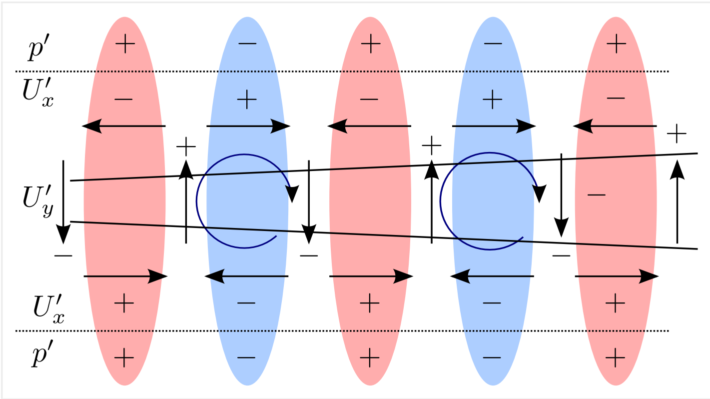

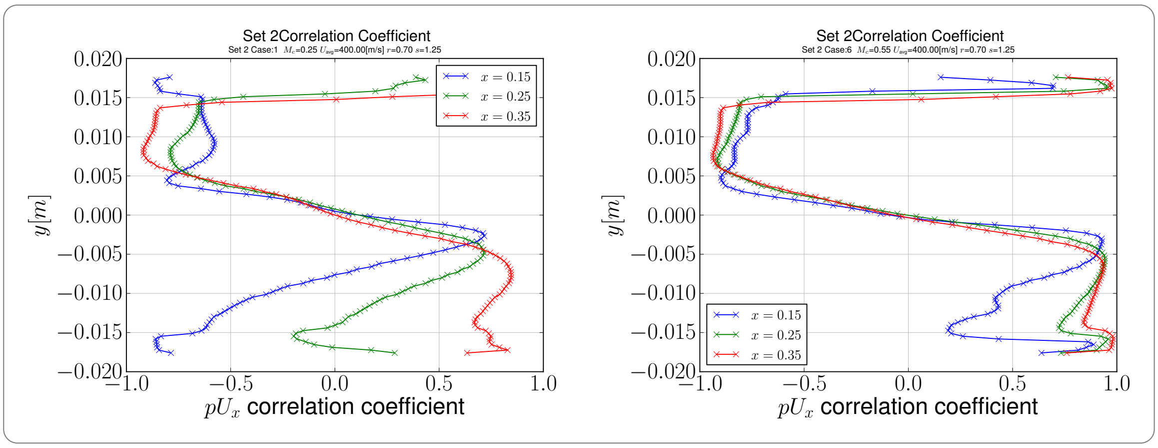

Figure 3.31: p, U_x correlation
[*The pressure is highly positively correlated with the secondary stream, and strongly negatively correlated with the pressure on the primary stream*]

3.3.2 Velocity Correlation

The above model also supports the velocity fluctuation correlations shown in **Fig 3.32**. In the following discussion, the following notation is followed

- +	+ +
- -	+ -

to refer to the different regions of the plot. A few things which can be inferred from the two point correlation plots of **Fig 3.32**

- The $u' - u'$ correlation is large in the ++ and the -- regions of the plot. This region represents the part of the fluid on the same side of the mixing layer The fact that almost the entire quadrants have a large correlation indicates that the regions move as coherent chunks. Note that

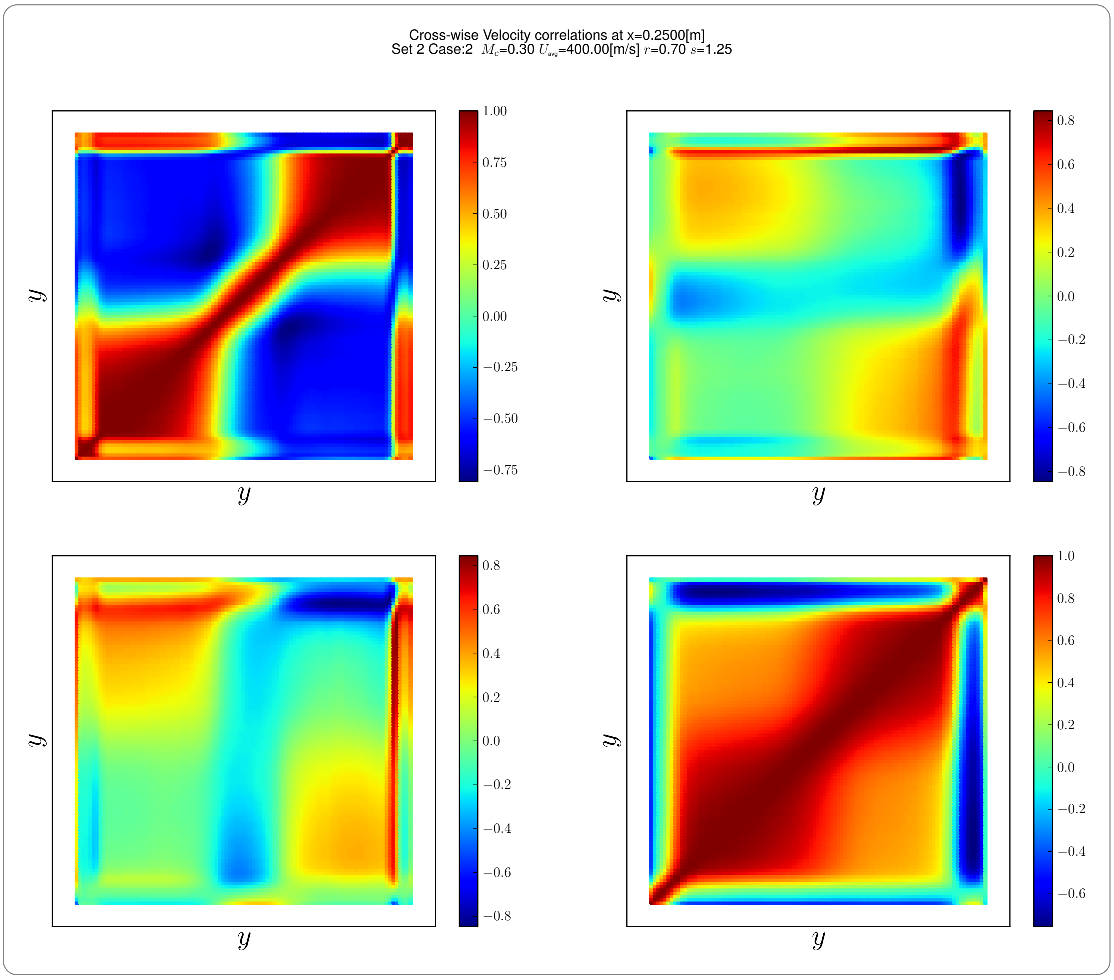

Figure 3.32: Velocity component correlations
[*Note the difference in the correlation forms for different components of velocities*]

this region of high correlation is *outside* the mixing layer. This shows that the influence of the structures are felt almost throughout the cross-wise direction.

- The $u' - u'$ correlation is strong and negative in the +− and the −+ regions. This region represents the correlation of the opposite sides of the mixing layer. The strong negative correlation indicates that the fluid on opposite sides of the mixing layer have opposite direction of fluctuation. That is, when the primary side fluid has a positive fluctuation, the secondary side has a negative fluctuation. This, again, pertains to the region *outside* the mixing layer.

- The $u' - v'$ correlation is quite small and seems larger in the positions symmetrically apart, that is the +- and -+ regions.
- The $v' - v'$ correlation is large almost for the entire domain. It is especially large for the same side of the mixing layer, that is ++ and the -- regions, and around 0.6 for a large portion of the +- and the -+ regions.

The above goes to show that the effect of the structure formation in the mixing layer is not restricted to the mixing layer alone, but extends to almost the entire domain in the way of coherent oscillations. This feature is also seen and explains experimental observations, like the one shown in **Fig 3.33**, where the turbulence value *does not* go to zero even far from the mixing layer.

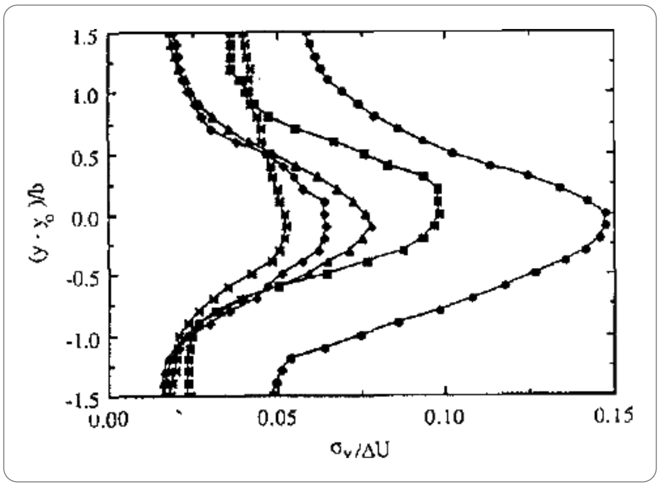

Figure 3.33: Figure of σ_{uu} from Goebel and Dutton [1990b]
[*Note that the free stream values of the*]

3.4 Spectral Analysis

The evolution of the mixing layer involves the initial formation of the instability. The amplitude of the instability waves gets magnified, and roll-up occurs. This increases the physical size of the structure, and when these structures merge, the size grows further. The coherent structures of a mixing layer are the main source of mixing, and growth. The formation and evolution of the structures is studied here from the point of view of spectrum analysis.

3.4.1 Turbulent Energy Spectrum

The turbulent energy spectrum is the spectrum of energy content of turbulent flows. This is the Fourier transform of the autocorrelation function R_{ij} defined for a statistically stationary flow as [Pope, 2000]

$$R_{ij}(t; x, y, z) \equiv \langle u(T; x, y, z)u(T + t; x, y, z)\rangle_T \tag{3.32}$$

And the spectrum of the autocorrelation function is

$$\widehat{R}_{ij}(\omega; x, y, z) \equiv \mathcal{F}(R_{ij}(t; x, y, z)) \tag{3.33}$$

The turbulence energy spectrum is now defined as, the half of contraction of $\widehat{R}$, that is

$$E(\omega; x, y, z) = \frac{1}{2}\widehat{R}_{ii}(\omega; x, y, z) \tag{3.34}$$

We shall now see the effect the flow parameters have on the energy spectrum.

Effect of M_c

It can be seen from **Fig 3.34** that the lower M_c case becomes unstable with a higher energy than that at higher M_c. This clearly shows that the higher M_c case is more stable than the lower M_c case, and it also indicates that the production rates of in the case of lower M_c is higher. This also concurs with finding that the lower M_c case recovers the velocity deficit earlier than the higher M_c case, and this is clearly because of the larger amount of mixing happening in the former.

It is also seen that the frequency of instability is higher in the case of the higher M_c case. It must be noted that this is not in accordance to the linear stability theory, which predicts a slightly lower frequency of peak amplification for the higher M_c case.

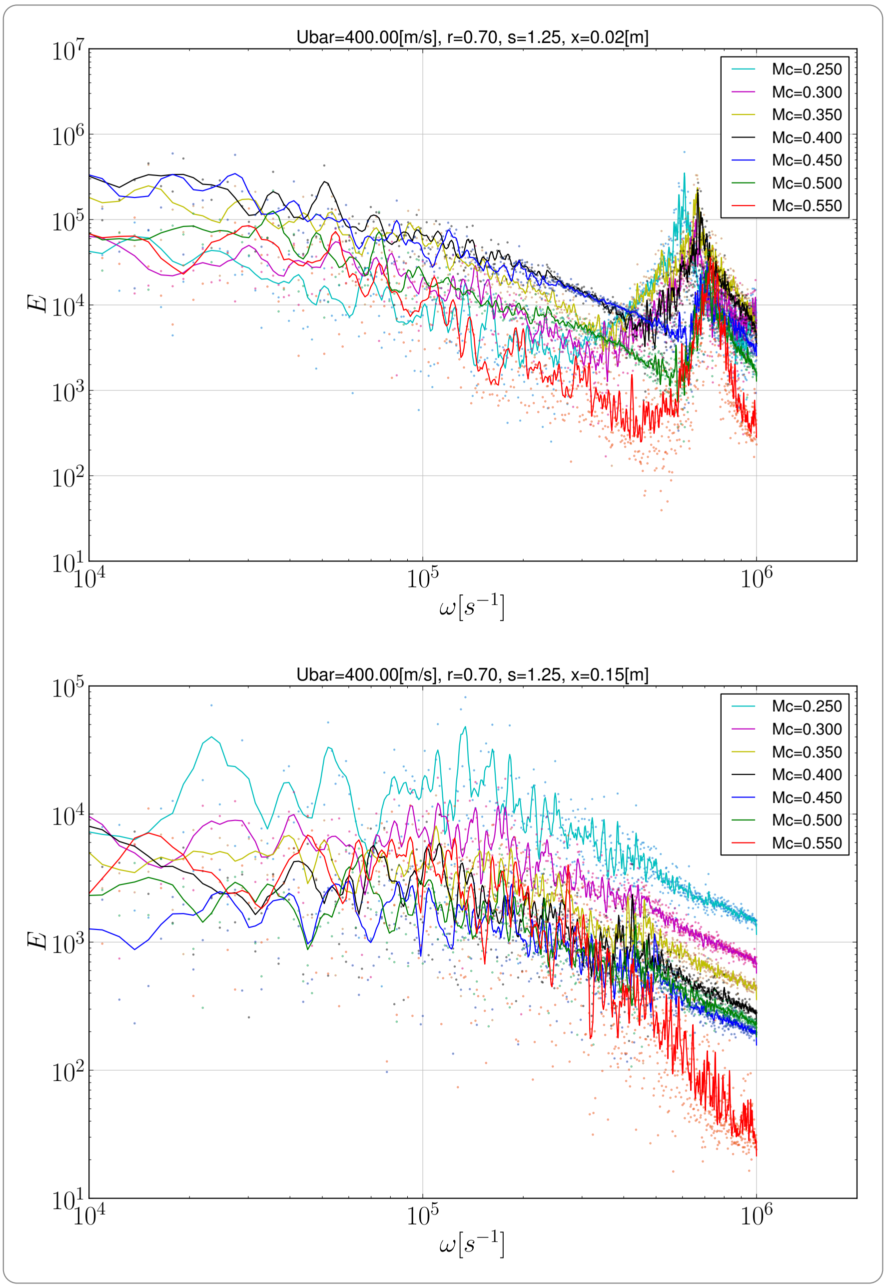

Figure 3.34: Energy Spectrum changes with M_c
[*Close to the splitter plate, the frequency peak of the low M_c is much larger (about an order of magnitude) than that of high M_c. Far from the splitter plate, the overall energy content too is larger in the case of lower M_c than high M_c*]

Effect of r

The effect of change in r as shown in **Fig 3.35** is a reduction on the energy with increasing r. It is of course expected to be the case because a smaller

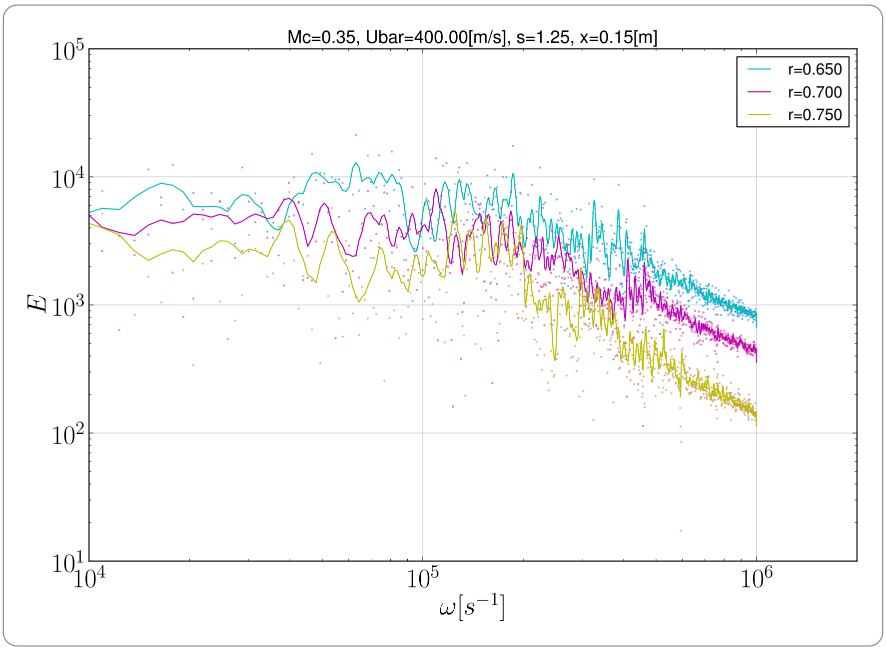

Figure 3.35: Energy Spectrum changes with r
[*Increase in r causes an increase in the overall energy content of the flow*]

velocity ratio, directly means a greater gradients of velocity, which in turn leads to greater production.

Effect of s

The effect of s shown in **Fig 3.36** is even more dramatic. It is clear that increase in the values of s clearly increases the energy content in the entire spectrum. This matches with the predictions of linear stability analysis as well as the incompressible prediction.

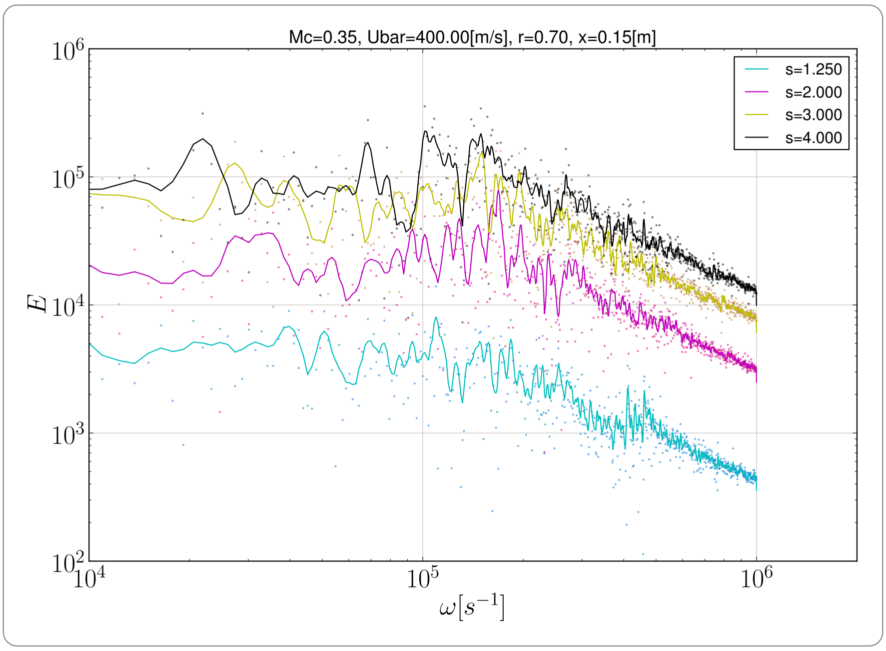

Figure 3.36: Energy Spectrum changes with s
[*Increase in s causes an increase in the overall energy content of the flow*]

3.5 Summary and conclusions

In this chapter interesting features of the mixing layers were studied. The conclusions are:

- The growth rate of the mixing layer is measured, and is shown to be smaller in the self similar regions for higher M_c, as observed in the experiments.
- The dependence of attainment of self similarity on M_c is derived. It is shown that the attainment of self similarity is delayed due to increase in M_c, and that this is shown to be the case in the simulations. Further, it is seen from the simulation that increase in r delays the attainment of self similarity.
- It is clearly demonstrated that increase in M_c delays the removal of velocity deficit. This is attributed to the stability of the mixing layer being greater in the case of higher M_c.
- The coherent structures are captured from the simulations, and the evo-

lution of the same studied. This yielded the conclusions that

  - The coherent excursions of the coherent structures away from the centerline is greater in the case of lower M_c than in the case of higher M_c.
  - Mergers and even splits are common in the evolution of a mixing layer. Mergers increase the area of the structures, and this is a very important part of the growth of the structures.
  - The average area of the structures is shown to be reducing with the increase in the M_c.
  - The velocity of the structures were actually measured from the simulations and were shown to be consistently about 10% to 15% smaller than the predicted velocity from model of Dimotakis [1984].
  - The velocity distribution about the mean showed significant skewness preferential to the smaller velocity side in the case of low M_c. In the case of higher M_c it is found to be symmetrically distributed.

- The mean pressure profiles show the following
  - The waves emanating from the splitter plate. It is confirmed that these are indeed weak waves, at an angle close to that of the Mach angle.
  - A pressure deficit exists in the mixing layer. This is shown to be purely due to the turbulence.
  - The pressure rise in the stream for a parallel side walls shows a gain. This is largely accounted for, and is shown to be mostly due to boundary layer growth.
- The mean pressure profiles show the following
  - Two point correlations of pressure showed the presence of large scale coherence even in the region away from the mixing layer. This is shown to be due to bulk movements, not random turbulent movements.

- The region of coherent fluctuations is shown to be smaller in the case of larger M_c. This is attributed to the smaller structures present.
- The pressure velocity correlations are strongly positive on the secondary side and strongly negative on the secondary side. The reason for the same is discovered through a simple model of the structure, and is confirmed with two point velocity correlations.

• The spectrum of the flow is analysed and showed that

- The increase in M_c reduces significantly the energy content of the instability, and hence shows that mixing layers with greater M_c are indeed more stable.
- The increase in r, as expected, shows a decreased energy content of the most unstable modes.
- Increase in s increases the energy of turbulence, as predicted by the linear stability theory as well as the incompressible theory.

This chapter thus leads the way for a more detailed analysis of the turbulence budgeting, but with cases where the average pressure gradient is maintained through divergence of the walls appropriately.

Chapter 4

Evolution of Turbulent Stresses

4.1 Introduction

The previous chapter dealt with the features of the mixing layer, some related to the mean profiles, and other more intricate quantities. As a step further, this chapter deals exclusively with the evolution of the evolution of turbulent stresses to be able to trace their transactions.

Writing the turbulent stresses in a conservative form, one can obtain the equation of the turbulence stress, which involves the production and the dissipation terms. A study of these terms is expected the reason for the changes in the turbulence levels with increase in M_c. The formulation of the problem is first carried out in **Sect 4.2**.

It is also noticed that the turbulence levels in the stream are influenced by the mean flow conditions. The development of the boundary layer has been shown to be the primary reason for the domain with parallel top and bottom surfaces to act as a diffuser, and cause an increase in the pressure and a decrease in the velocity. This changes the free stream conditions, affecting the shear. To correct this problem, the domain is modified with a slight divergence to compensate for the displacement thickness of the boundary layers. This is discussed in **Section 4.3**.

The **Sect 4.4** presents the findings regarding the factors influencing the different components of the turbulence stresses. This traces the behaviour of the total sources of the shear stresses, where as **Sect 4.5** deals with the components of each of the sources, to determine which particular component has an influence of M_c. Finally **Sect 4.6** discusses the effect of the particular pressure-strain term.

4.2 Kinetic energy Budget

The fact that the turbulence level decreases with M_c leads to the obvious search for the cause for this decrease. To investigate this, the evolution equation of the turbulent kinetic energy is derived, and the source terms are identified. To do this the mechanical energy equation is subtracted from the total kinetic energy equation. After substantial simplifications and mathematical manipulations (see Appendix **A.3** on Page**186**). The final equation obtained is

$$\boxed{\langle\rho\rangle \left\{ \frac{\langle D\rangle R_{ij}}{\langle D\rangle t} + D_{ij} \right\} = \underbrace{\Sigma_{ij} + B_{ij} - \pi_{ij} + X_{ij}^{\mathrm{Diss}} + \frac{2}{3}\delta_{ij} \langle p' u_{k,k}''\rangle}_{\text{Source Terms}}} \tag{4.1}$$

Where

$$\frac{\langle D\rangle}{\langle D\rangle t} \equiv \frac{\partial}{\partial t} + \{U_l\} \frac{\partial}{\partial x_l} \tag{4.2}$$

$$R_{ij} = \{u_i'' u_j''\} \tag{4.3}$$

$$D_{ij} = \frac{1}{\langle\rho\rangle} \frac{\partial}{\partial x_l} \left(\tau_{ijk} + \frac{2}{3}\delta_{ij} \langle p' u_l''\rangle - X_{ij}^{\mathrm{Diff}} \right) \tag{4.4}$$

$$\tau_{ijk} = \langle\rho\rangle \{u_i'' u_j'' u_k''\} \tag{4.5}$$

$$\tau_{ij} = \langle\rho\rangle \{u_i'' u_j''\} \tag{4.6}$$

$$X_{ij}^{\mathrm{Diff}} = (\langle u_i'' \sigma_{jl}\rangle + \langle u_j'' \sigma_{il}\rangle) \tag{4.7}$$

$$\Sigma_{ij} = -\tau_{jl} \{U_{i,l}\} - \tau_{il} \{U_{j,l}\} \tag{4.8}$$

$$B_{ij} = -(\langle p_{,j}\rangle \langle u_i''\rangle + \langle p_{,i}\rangle \langle u_j''\rangle) \tag{4.9}$$

$$\pi_{ij} = \Pi_{ij} - \frac{1}{3}\delta_{ij}\Pi_{ll} \tag{4.10}$$

$$\Pi_{ij} = \langle p_{,j}' u_i''\rangle + \langle p_{,i}' u_j''\rangle \tag{4.11}$$

$$X_{ij}^{\mathrm{Diss}} = -(\langle u_{i,l}'' \sigma_{jl}\rangle + \langle u_{j,l}'' \sigma_{il}\rangle) \tag{4.12}$$

The terms above are identified in **Table 4.1**

Term	Significance
R_{ij}	The velocity correlation
D_{ij}	Diffusion of turbulence
τ_{ijk}	Triple correlation (density weighed)
τ_{ij}	Turbulent correlation
X_{ij}^{Diff}	Turbulence diffusion due to viscosity
Σ_{ij}	Production
B_{ij}	Mean Pressure Velocity fluctuation coupling
π_{ij}	Fluctuation of pressure and velocity coupling
X_{ij}^{Diff}	Dissipation
$p'u''_{kk}$	Pressure dilatation coupling

Table 4.1: Terms in the Turbulence evolution equation

4.2.1 Other equivalent derivations

We shall discuss some other forms of the derivation by other authors.

Neglecting the large scale viscosity

Under certain conditions, the large scale viscous effects can be neglected, hence

$$\{u\}_{,i} \approx 0$$

This results in the approximations as made by Canuto [1997]

$$X_{ij}^{Diff} = \left(\langle {u_i}''\sigma_{jl}\rangle + \langle {u_j}''\sigma_{il}\rangle\right)_{,l} \approx \left(\langle U_i\sigma_{jl}\rangle + \langle U_j\sigma_{il}\rangle\right)_{,l} \tag{4.13}$$

$$X_{ij}^{Diss} = -\left(\langle {u_{i,l}}''\sigma_{lj}\rangle + \langle {u_{j,l}}''\sigma_{li}\rangle\right) \approx -\left(\langle U_{i,l}\sigma_{lj}\rangle + \langle U_{j,l}\sigma_{li}\rangle\right) \tag{4.14}$$

Not splitting p'

Another variation of the τ_{ij} equation is found in some literature, for example Pantano and Sarkar [2002]. This formulation differs from **Eqn A.42** as

$$\begin{aligned}
\langle F_i U_j \rangle - \langle F_i \rangle \{U_j\} = \langle F_i u_j'' \rangle &= \langle (-p_{,i} + \sigma_{il,l})\, u_j'' \rangle \\
&= -\langle p_{,i} \rangle \langle u_j'' \rangle - \langle p_{,i}' u_j'' \rangle + \langle \sigma_{il,l} u_j'' \rangle \\
&= -\langle p_{,i} \rangle \langle u_j'' \rangle - \langle p' u_j'' \rangle_{,i} + \langle p' u_{j,i}'' \rangle + \langle \sigma_{il,l} u_j'' \rangle
\end{aligned} \tag{4.15}$$

Further, the term $\langle \sigma_{jl,l} u_i'' \rangle$ is decomposed as

$$\begin{aligned}
\langle \sigma_{jl,l} u_i'' \rangle &= \langle (\langle \sigma_{jl,l} \rangle + \sigma_{jl,l}')\, u_i'' \rangle \\
&= \langle \sigma_{jl,l} \rangle \langle u_i'' \rangle + \langle \sigma_{jl,l}' u_i'' \rangle \\
&= \langle \sigma_{jl,l} \rangle \langle u_i'' \rangle + \left\langle \sigma_{jl}' u_i'' \right\rangle_{,l} - \left\langle \sigma_{jl}' u_{i,l}'' \right\rangle
\end{aligned} \tag{4.16}$$

And similarly

$$\langle \sigma_{il,l} u_j'' \rangle = \langle \sigma_{il,l} \rangle \langle u_j'' \rangle + \langle \sigma_{il}' u_j'' \rangle_{,l} - \langle \sigma_{il}' u_{j,l}'' \rangle \tag{4.17}$$

The diffusion terms are collected as

$$T_{ijl} = \left(\tau_{ijl} + \langle p' u_j'' \rangle \delta_{il} + \langle p' u_i'' \rangle \delta_{jl} - \left\langle \sigma_{jl}' u_i'' \right\rangle - \langle \sigma_{il}' u_j'' \rangle \right) \tag{4.18}$$

Thus **Eqn A.39** becomes

$$\begin{aligned}
\frac{\langle D \rangle \tau_{ij}}{\langle D \rangle t} + T_{ijl,l} &= \Sigma_{ij} \underbrace{- \left\langle \sigma_{jl}' u_{i,l}'' \right\rangle - \langle \sigma_{il}' u_{j,l}'' \rangle}_{\epsilon} \\
&\quad + \underbrace{\langle p' (u_{j,i}'' + u_{i,j}'') \rangle}_{\Psi} \\
&\quad + \underbrace{(\langle \sigma_{jl,l} \rangle - \langle p_{,j} \rangle) \langle u_i'' \rangle + (\langle \sigma_{il,l} \rangle - \langle p_{,i} \rangle) \langle u_j'' \rangle}_{\Phi}
\end{aligned} \tag{4.19}$$

Where the terms Σ, Ψ and Φ the respectively labelled as P, Φ and Σ of Pantano and Sarkar [2002]

4.3 Domain for analysis

It was seen in the previous chapter that the development of the boundary layer reduces the effective area for the stream. This is sought to be corrected in the current set of experiments by making the top and the bottom walls slightly divergent, just enough to compensate for the reduction in the flow area due to the boundary layer. Though we have an estimate of how much the walls are to be diverged to be able to remove the pressure gradient, it was found that this approximation removed only a part of the pressure gradient.

In the present case, the (almost) zero pressure gradient was attained through iterations of modifying the divergence angle and measurement of the pressure gradient after two sweeps of the flow. The divergence of the plates cannot be from the inlet itself, because that will give rise to unrealistic expansion fans right at the inlet zone. The divergence also cannot be done in a way that it creates a sudden change of angle, because even then it will give rise to expansion fans into the domain. Hence, the domain was diverged through a smooth arc with a large radius of curvature, as shown below.

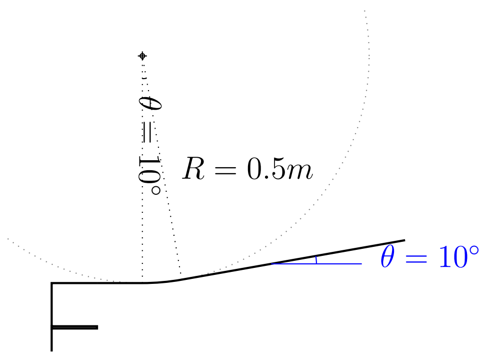

Note that the figure above shows the angle of divergence of 10° only for clarity, whereas in reality the angle was found to vary from 0.125° to 0.3°

The effect of this divergence is shown in **Fig 4.1**, where it is clearly seen that most of the pressure gradient has been mitigated using divergence of the side walls. Similar pressure distribution is created in almost all the cases in this set of experiments.

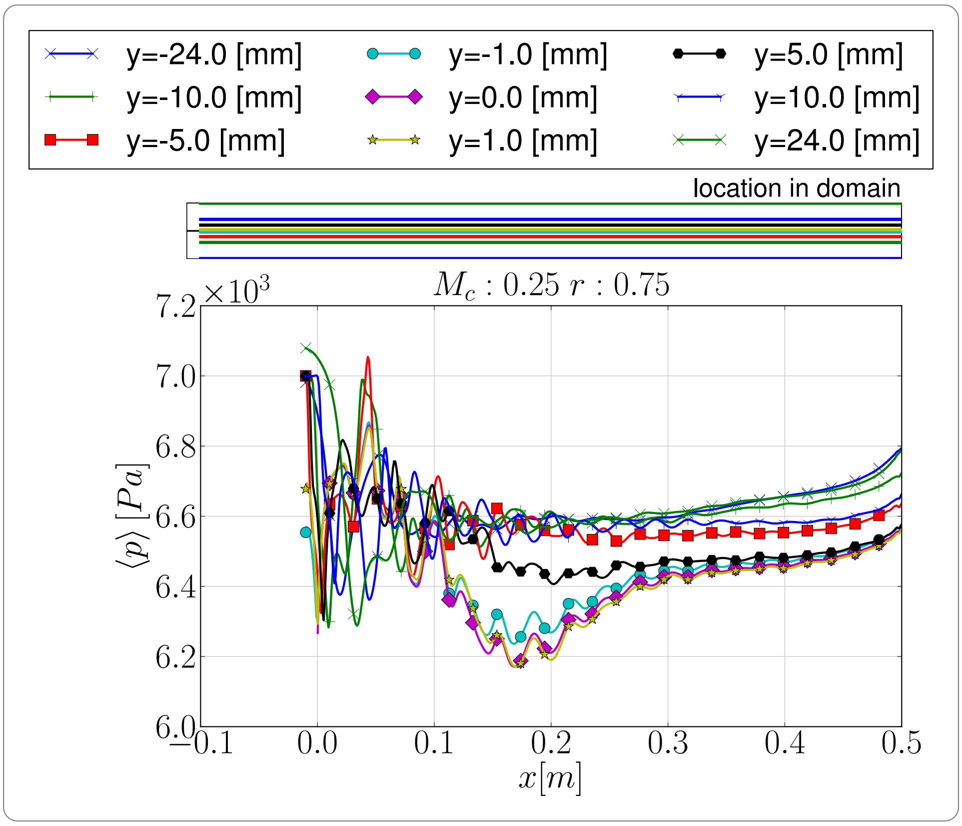

Figure 4.1: Pressure variation in the modified domain
[*Note that stream-wise pressure gradient is almost zero*]

4.4 Integral Source terms for Turbulent Quantities

In the study of the turbulent quantities, it is often better to discuss in terms of the quantities integrated in the cross wise direction. An integration in the cross stream direction eliminates the transport term, in the case of turbulent quantities if we assume a largely turbulence free stream conditions away from the mixing layer. The transport term results only in a redistribution of the parameter under study, and does not modify the total content of the parameter. In the case of temporal mixing layers, usually a similar integration is performed in the self similar coordinate, which is analogous to y (example Pantano and Sarkar [2002], Vreman [1995]).

The integral term of any turbulent parameter at a stream-wise location stations may be thought of as a measure of the total content of that quantity crossing that section. Furthermore, the difference in its value at two stream-wise stations must be the sum effect of the source terms present between the stations.

4.4.1 Diagonal component

The total source terms for all the cases of the diagonal components are shown in **Fig 4.2**. The plots are non-dimensionalized with the average density and the velocity difference.

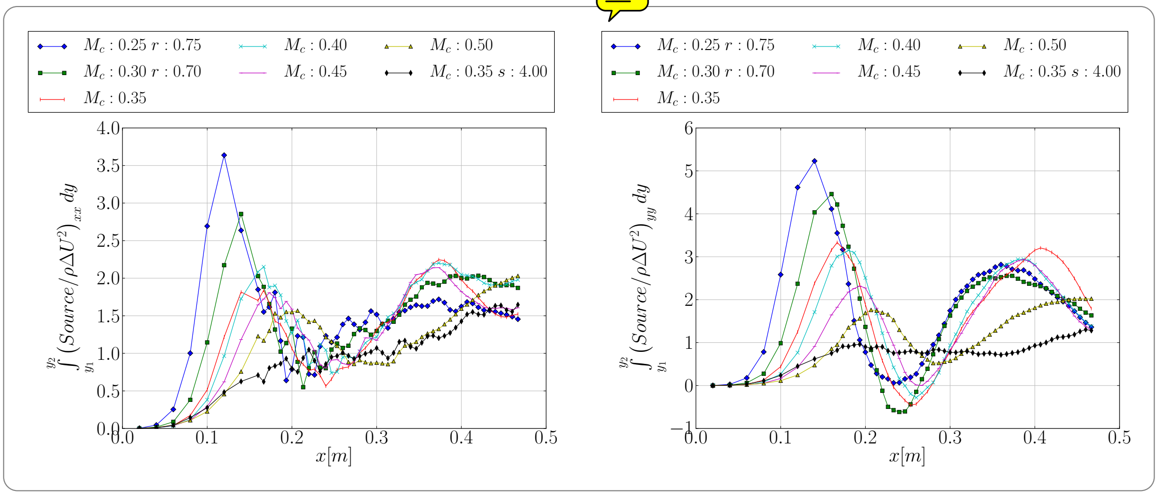

Figure 4.2: Source of symmetric components changes across M_c
[**Left**:*the $_{xx}$ component*, **Right**: *the $_{yy}$. Note that the delay and the decrease in the growth in the source terms with increasing M_c*]

The following observation can be made from the plots

- It is seen that increasing M_c causes a *delay* in the growth of the source terms, that is, the greater the value of M_c the greater is the distance at which the source terms start growing. This is true for all the components. That the stability of the flow increases with M_c is clearly seen, because the amplification of the turbulence occurs later in the flow in the case where the flow has a greater M_c.
- The magnitude of the source terms decreases with the increasing M_c. This further goes to explain the reduction in the growth rate.

The effect of this difference in the source term is directly seen in the values of the turbulent quantities along the stream wise direction. This is plotted in **Fig 4.3**.

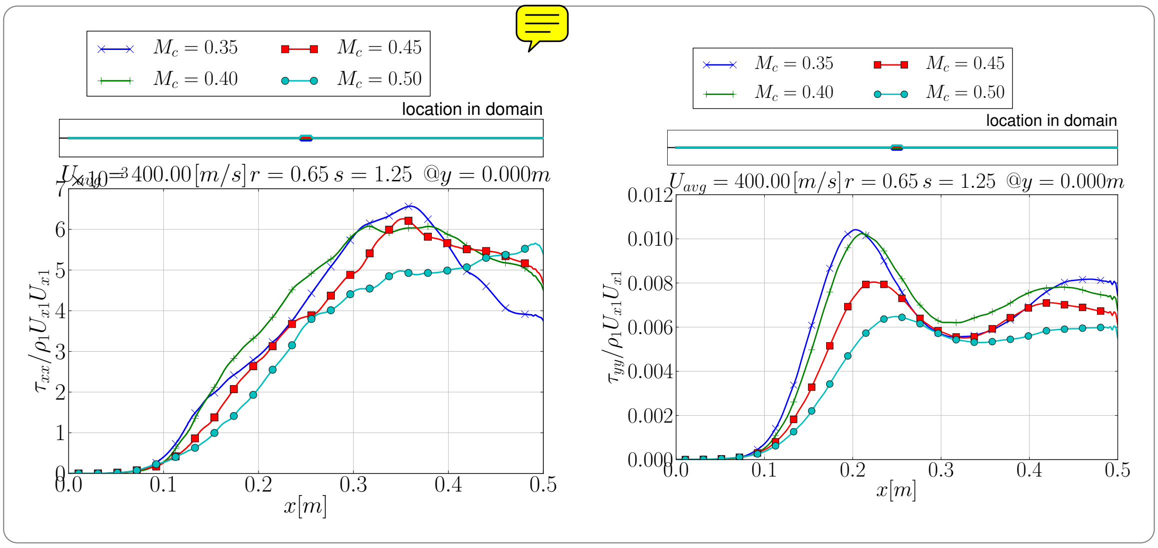

Figure 4.3: Variation of τ_{xx} and τ_{yy} with x for different M_cs along the centerline [*There is a tendency to decrease in the value of non-dimensionalized τ_{xx} and a clear trend of decrease in τ_{yy} with increase in M_c*]

A very similar result was obtained by the experiments of Goebel and Dutton [1990a], which shows a clear trend of decrease of non-dimensionalized τ_{yy} with increase in M_c and no clear trend of decrease in τ_{xx} with M_c. Elliott and Samimy [1990] found decreasing trend in both the τ_{xx} as well as the τ_{yy} components in experiments with increasing M_c.

4.4.2 Shear component

The shear component is related directly to the growth rate and hence has relevance in the mechanics of the decrease in the growth rate with increasing M_c. The normalized source term for the shear component is plotted in **Fig 4.4**

The influence of this can be directly seen on the value of τ_{xy} plotted along the centerline, in **Fig 4.5**. To clearly see the effect of the latter on the growth of the mixing layer, **Fig 4.5** also shows the measured value of δ which is scaled to remove the effects of r and s.

- There is a decrease and a delay in the value of the source terms for τ_{xy}

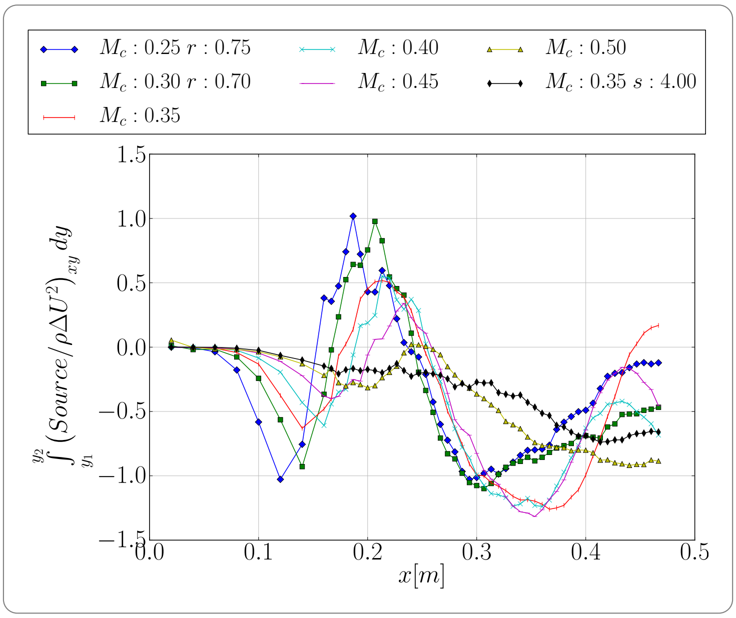

Figure 4.4: Normalized Shear component of the Source
[*The delay and the reduction in the value of the source is apparent*]

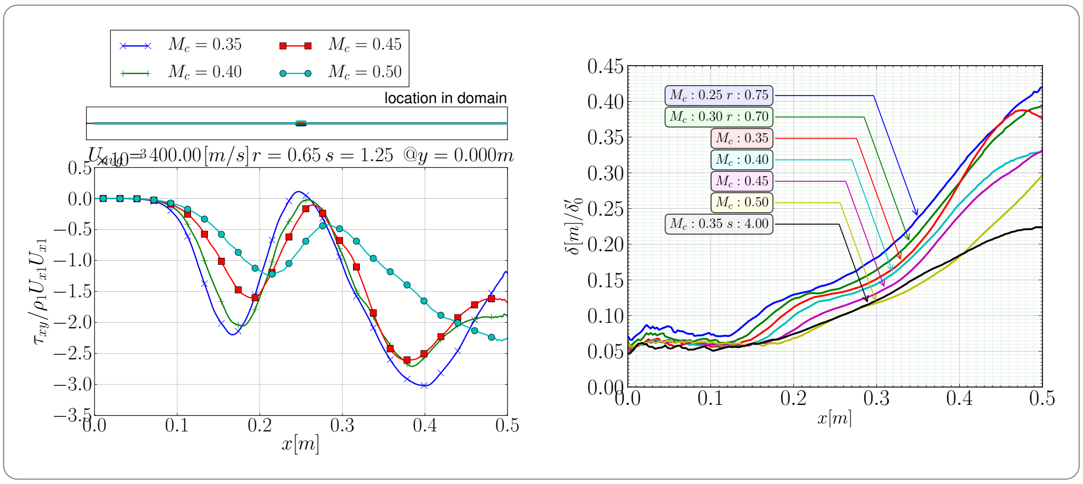

Figure 4.5: Normalized shear stress and growth rates
[*The* **left** *side presents τ_{xy} vs x at $y = 0$ and the* **right** *side presents the growth rates are scaled to remove the effect of r, and s. A clear trend is seen of decrease of τ_{xy} corresponding to a decrease in δ*]

with increasing M_c

- This trend in the profile of source of τ_{xy} is clearly reflected in the actual value of τ_{xy} at the centerline

- The growth pattern matches with the pattern of the turbulence source, especially the shear mode, in which it is seen that the growth rate is greater in the region of larger source of τ

- It is also seen that the effect of the increasing M_c is seen in the reduced growth *rate* but more importantly of the delayed growth. The decreased growth (in contrast to the *growth rate*) is of a greater importance for combustion applications, and this seems to be drastically smaller in the case of higher M_cs.

It is quite interesting to note the trend of each of the components of the source term, that is Σ, B, π and X^{diss}. This is done in the following section.

4.5 The components of the source term

4.5.1 Symmetric components

The production term Σ

First we shall have a look at the production term of the symmetric components.

The following observations are made

- It is clearly seen from **Fig 4.6** that the production term for τ_{xx} decreases with increasing M_c. It is also clear that there is a delay in the distance it takes for the production term to rise. Both these contribute to the increased stability of the flow.

- The production of the τ_{yy} component however does not show much of a trend, as far as the magnitude is concerned. However, a delay is definitely seen in the start of increase of the production rise. It is also seen that this component is of a relatively much small magnitude.

From the definition Σ_{ij} is proportional to the product of the prevalent gradient of velocity and the turbulence present. The most dominant velocity gradient is the gradient of the stream-wise velocity in the cross stream direction, and this gives the large production of energy of the flow in the xx direction. On the other hand, the cross-wise direction velocity is small, and hence the large difference in the magnitudes is expected.

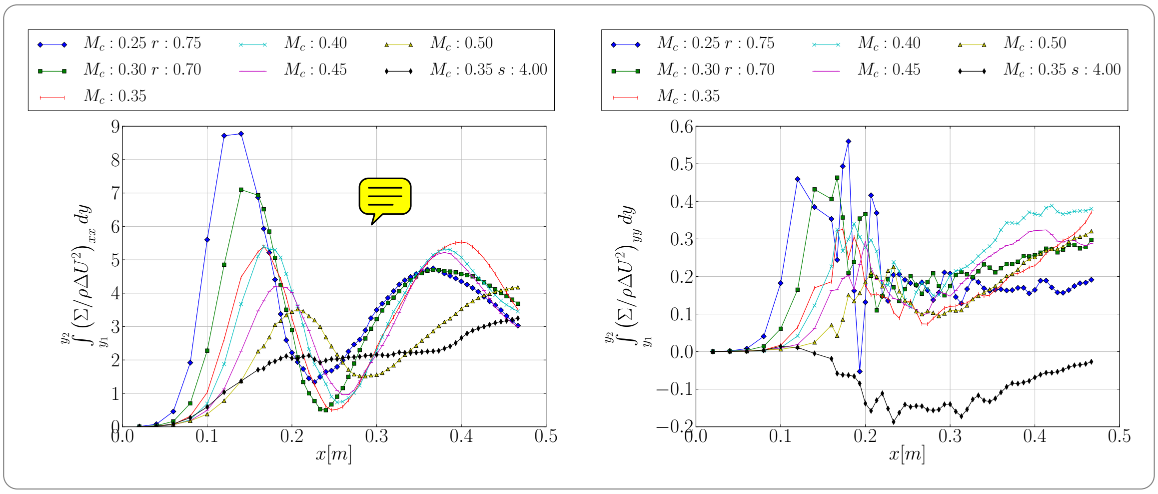

Figure 4.6: Symmetric components of production term, and its changes with M_c [*Note that the delay and reduced magnitude in the growth of the production term with increasing* M_c]

The pressure - velocity correlation terms

It can be seen from **Fig 4.7** that the pressure strain term (π_{xy}) is positive in the xx direction and negative in the yy direction. Since π is a negative source in the evolution equation (**Eqn A.56**), it acts as a sink of energy from the xx direction, and adds this energy to the yy component. As one can see, the values if π_{xx} and π_{yy} are equal and opposite. This pressure strain term is hence the main source of energy for the yy direction, which itself lacks the production.

Thus, in summary, as depicted in **Fig 4.8**, it is seen that with the increase in the M_c, the production term decreases in the xx direction, which leads to a decrease in the source of τ_{xx} and the pressure strain term decreases causing a decrease in the source of τ_{yy}.

Shown in **Fig 4.9** is the figure extracted from Pantano and Sarkar [2002]. This is the result of a temporal mixing layer, which shows that the production

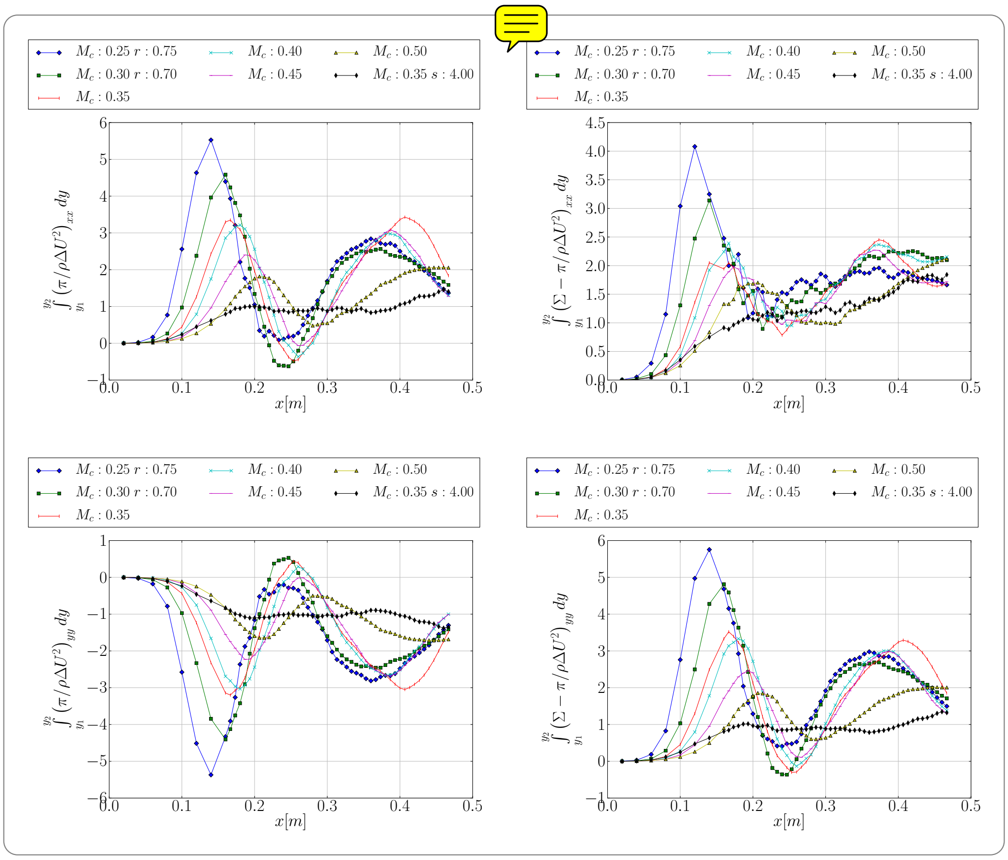

Figure 4.7: The pressure strain term

[*The pressure strain term (left) is positive in the xx direction(top) and negative in the yy direction(bottom). Also the magnitude decreases with increase in the M_c*]

terms being smaller for higher M_c values at a given instant. It can be seen that the current simulations agree with the findings, that the increase in the value of M_c cause a distinct decrease in the value of Σ.

The unscaled values shows a large value for Σ_{xy} even for high M_c because higher M_c is also accompanied by an increase in the difference in the velocities. This is compounded by a smaller δ which in effect causes a large increase in the gradients across the mixing layer.

Sarkar [1995] has attributed the stabilizing effect wholly to the production term, whereas Pantano and Sarkar [2002] acknowledge the difference caused by the pressure strain terms also. *The current work supports the latter viewpoint from the point that the pressure strain terms and the production terms are of similar order of magnitude and* ***both*** *show increased stability at higher M_c*

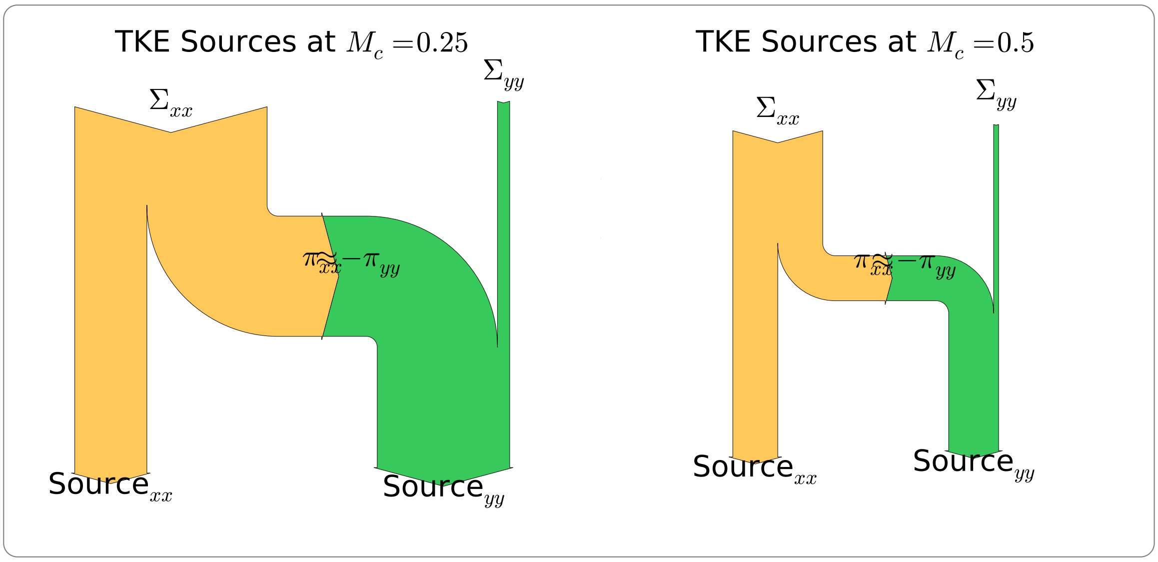

Figure 4.8: Flow of Energy in the TKE Equation
[*The widths are proportional to the peak values*]

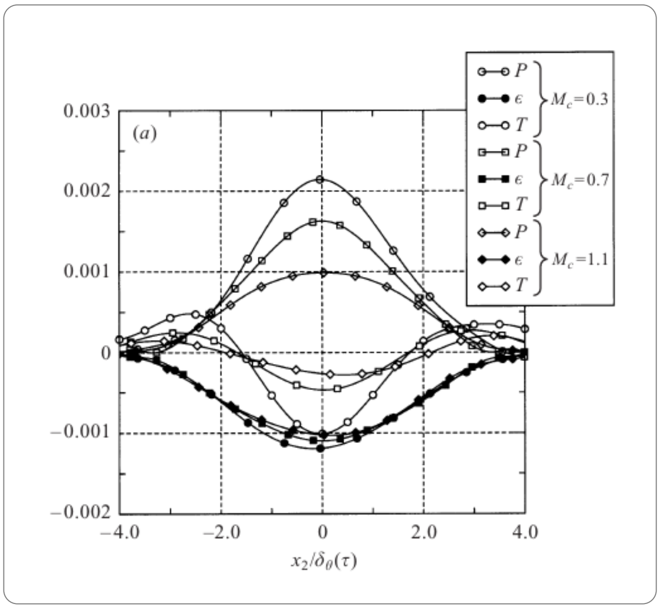

Figure 4.9: Production terms in Pantano and Sarkar [2002]
[*Extracted from Pantano and Sarkar [2002]*]

values.

The dissipation term

The dissipation term, plotted in the **Fig 4.10**, shows that the magnitude is much smaller than the pressure velocity term and the production term, and that its magnitude decreases (in the negative sense) with increasing M_c.

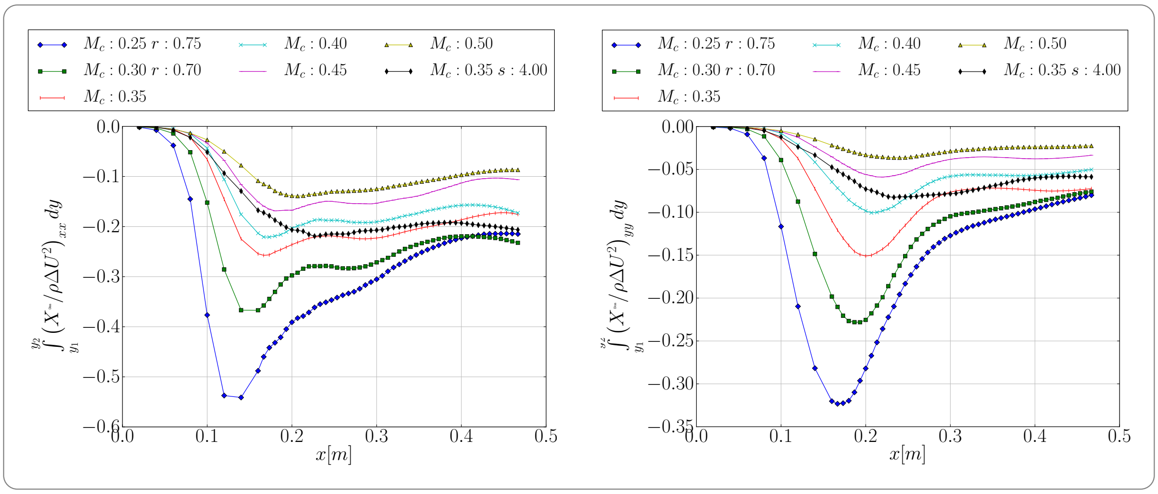

Figure 4.10: The dissipation term
[*The dissiaption is of a much lower value than the other major term, and it generally shows a greater dissipation for smaller* M_c]

This is not in line with the findings of Pantano and Sarkar [2002], who found no trend, in the dissipation.

4.5.2 Asymmetric component

Figure 4.11 shows the different components of the source of the shear (τ_{xy}) component.It can be seen without doubt that the increase in the values of M_c result in decrease in the production term scaled with the average density and the velocity difference.

- The decrease in the source of production with increasing M_c is very pronounced
- The point of start of increase of production is delayed in the case of high M_c

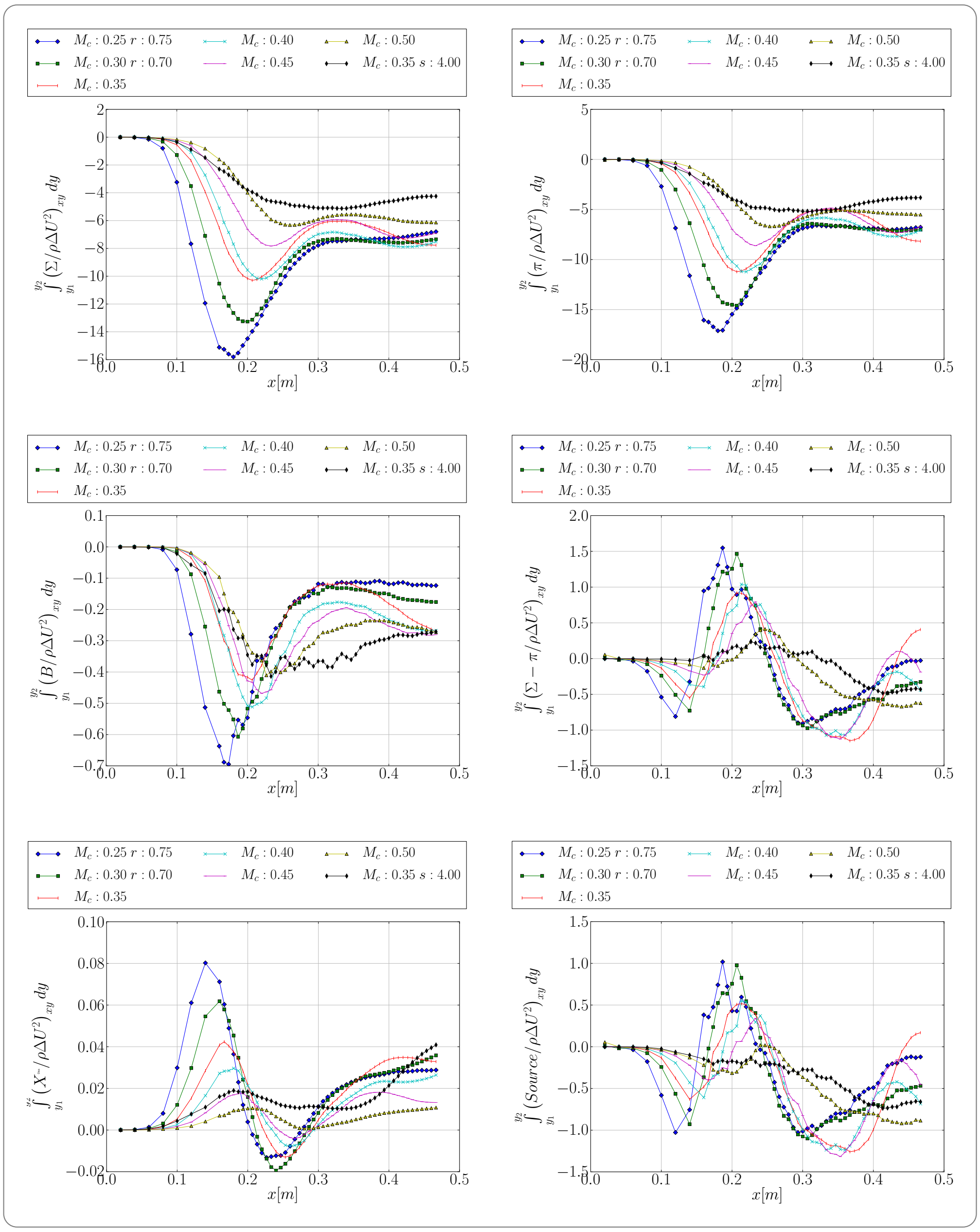

Figure 4.11: Components of the source term in the xy direction

Pressure-Velocity terms π and B

It can be seen from **Fig 4.11** that

- π_{xy} is of an order similar to that of Σ_{xy}, where as B is of a smaller magnitude.

- However, the magnitude of B is similar to $\Sigma - \pi$ hence it cannot be neglected as it was done in the case of the xx and the yy components.
- Both B and π shows an increased stability with increasing M_c.
- It can be seen that the dissipation is much smaller in magnitude than the other terms. Hence it can be concluded to be having a minimal, if any, effect on the stability of the mixing layer.

4.6 The significance of the pressure strain term

The source of the Π term has

$$\left\langle p_{,j} u_i''' \right\rangle = \langle p' u_i'' \rangle_{,j} - \left\langle p' u_{i,j}'' \right\rangle \tag{4.20}$$

The first term on the RHS is a diffusion term and can be taken on the LHS of the evolution equation of τ_{ij}, however the second term is the pressure strain term.

We have seen in **Sect 4.5.1** that the π term plays a very important role in the transfer of energy from the τ_{xx} equation to the τ_{yy} equation, and that this is the main source of the turbulence in the τ_{yy} direction, being negative in the xx equation and positive by almost the same amount in the yy equation.

This is one of the main reason for RANS turbulence models based on k (like the $k - \epsilon$ or the $k - \omega$ models) to not to be able to capture the reduction in the growth rate.

However, it can be seen that when we compute the trace of this term, it reduces to $\langle p' \nabla u'' \rangle$. This term is very small because being positive and negative of roughly the same amount in the xx and the yy directions. Thus the turbulent kinetic energy (k) equation has no means to capture this influence.

4.7 Conclusions

In this chapter, the root cause for the decrease in the turbulent quantities was sought out for, by the analysis and the careful calculation of each of the source terms in the evolution equation of the turbulent quantities. It is concluded that the production term is the dominant source in the case of the xx component, where as a substantial part of the energy is carried over by the pressure strain term π to the yy direction. Both these terms tend to decrease with increasing M_c, and hence both components show a decreasing trend with increasing M_c.

In the shear component too a strong trend of decrease in the production term with increase in M_c is seen, a similar increase in the π term decreases the effect of M_c, and makes the values similar in magnitude to the mean pressure-velocity fluctuation term B. Overall, even for this component, a decrease in the source is seen with increasing M_c which shows the reason for the increased stability with increase in M_c.

Chapter 5

RANS Modelling

5.1 Introduction

In the previous chapter, a detailed description of how the measures of turbulence vary with M_c was presented. LES has an advantage of being able to simulate most of the momentum, energy, and species carrying large scale eddies which do most of the turbulent mixing, and as seen in the previous chapters, LES has been successful in predicting most of the features of the mixing layers, measured experimentally as well as those observed in previous DNS simulations.

However, LES computation is computationally more intensive to qualify as a development tool. It is therefore thought appropriate to evolve a simpler computational tool based on RANS to enable faster and accurate calculations to help system development.

RANS simulations are generally conducted on a much coarser grid as well as much larger time steps, and a possibility of mimicking the behaviour in RANS would be a very useful development tool.

It was realized from **Sect 4.6** that RANS simulations which have the turbulence modelling based on k are ill poised to predict the growth rate reduction effect of a compressible mixing layer. A more detailed description of the same is presented in **Sect 5.2**. Besides, in problems involving heat and mass transfer, it is customary to invoke the Reynold's analogy for turbulent flows, and defining constants $\mathrm{Pr_t}$ (turbulent Prandtl number) and $\mathrm{Sc_t}$ (turbulent Schmidt number), analogous to their laminar counterparts, and solve the respective evolution equations with this assumption. It is however neither certain, nor necessary for the $\mathrm{Pr_t}$ and $\mathrm{Sc_t}$ to be constants, which is the usual assumption.

5.2 The possibilities

RANS refers to generic Reynold's Averaged Navier Stokes equation. When the averaging is thought of as a time average, it yields the Steady-State RANS usually called S-RANS, and when the average means ensemble average, it leads to an unsteady, time-accurate solutions known as Unsteady-RANS or URANS.

Bardina et al. [1997] presents an excellent classification of the existing turbulence models. The basic classification of the turbulence models is as

Reynolds Stress Models Which model directly the Reynolds Stress. These set of models require to model each component of the stress tensor. Most often this involves solving additional convective equations equal to the number of components.

Algebraic Models These are also called zero equation models, which relate the shear stress to the mean flow parameters with an algebraic equation.

Eddy Viscosity Models This group of models model the eddy viscosity, a scalar, which relates the stress tensor to the strain tensor. Most often this estimation requires solving a single convective equation (one equation models), or two convective equations (two equation models). Prominent examples being the $k-\epsilon$ model, the $k-\omega$ model. These have a reputation of being robust, and have been widely used.

Launder et al. [1972] had shown that the classical $k - \epsilon$ model shows a greater spreading rate than what is expected. **Figure 5.1** from Bardina et al. [1997] shows that *none of the classical models* are able to capture the reduced growth rate effect.

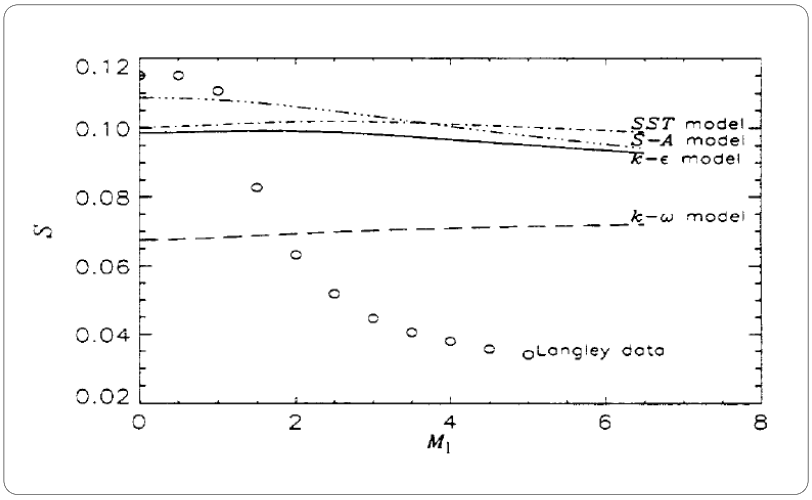

Figure 5.1: Performance of classical turbulence models from Bardina et al. [1997] [*None of the classical models are able to capture the reduced growth rate effect with increasing* M_c]

The equation for the turbulent kinetic energy (k) involves taking a trace of **Eqn A.56**. This process leads to

$$\begin{aligned} \langle\rho\rangle \left\{ \frac{\langle D\rangle k}{\langle D\rangle t} + D_{xx} + D_{yy} \right\} &= (\Sigma_{xx} + \Sigma_{yy}) + (B_{xx} + B_{yy}) \\ &- \underbrace{(\pi_{xx} + \pi_{yy})}_{=0} + (X_{ij}^{\mathrm{Diss}}) + \tfrac{2}{3}\delta_{ij} \langle p' u_{k,k}{}'' \rangle \end{aligned} \tag{5.1}$$

The third term on RHS (π_{ij}), was found in the LES analysis, to be a very significant term in both the τ_{xx} equation, appearing as a sink, as well as τ_{yy} equation, appearing as a source. It was shown that the values of both these are quite close in magnitude. This term which (along with Σ_{xx}) decreases with M_c. This has also been the finding of Vreman et al. [1996] and Pantano and Sarkar [2002] that this term provided an anisotropic effect which allowed the energy transport from the stream-wise to the cross-wise direction. However, when a trace is taken of the τ equation, it leads to the nullification of the π term itself. This implies that the anisotropy arising out of the pressure velocity correlation is lost in the process.

Thus calculation of k implies the loss of information of this pressure velocity relation. Many methods were suggested to correct this problem, most of which were aimed at decreasing the turbulent kinetic energy by increasing the dilatation dissipation ([Sarkar et al., 1991b], [Zeman, 1990]). This approach was however found to be incorrect by Sarkar [1995] who found that it was the production term and not the dissipation which decreases with increased M_c. But in the present work, X_{ij}^{Diss} was found to have a small influence. It has also been confirmed by Pantano and Sarkar [2002], who too found not much of a trend for dissipation with M_c. Hence *any technique intending to correct k using modification to the dissipation term is bound to be flawed in physics.* Wilcox [1998] too has found that this technique is flawed.

The possibility of this feature to be incorporated in any RANS model based on an isotropic μ_t has no possibility of introducing the effect of anisotropy. In the present work, however as new and a rather simpler approach is presented. We first find the most important terms to be modelled for obtaining the growth rate, and then model that with the help of results of LES.

5.3 Terms contributing to the momentum equation

To be able to model the stresses, it is necessary to know, which term is the most significant contributer to the respective momentum equations. This is done using the results obtained using LES. But before that, which term is important can be immediately estimated using a simple integral analysis.

5.3.1 Integral analysis

In Appendix **A.4** on Page**193** integration of the momentum equation is provided, and this analysis connects the growth rate to the integrals of the mean flow and the shear stress which is

$$\delta' \left(\begin{array}{c} \int\limits_{-\infty}^{0} fg(g-r)d\eta + \int\limits_{0}^{\infty} fg(1-g)d\eta \\ + \int\limits_{-\infty}^{0} \left(\underline{\langle p \rangle} - p_\infty - T_{xx}\right) d\eta - \int\limits_{0}^{\infty} \left(\underline{\langle p \rangle} - p_\infty - T_{xx}\right) d\eta \end{array} \right)$$
$$= 2y_0' \left(\underline{\langle p_0 \rangle} - p_\infty - T_{xx0}\right) + 2T_{xy0} \tag{5.2}$$

where,

$$f(\eta) = \underline{\langle\rho\rangle}(x,y) \tag{5.3}$$

$$g(\eta) = \underline{\{u\}}(x,y) \tag{5.4}$$

$$h(\eta) = \underline{\{v\}}(x,y) \tag{5.5}$$

and $\underline{\cdot}$ representing the non-dimensionalized variables with respect to the primary stream variables.

Which on neglecting the pressure terms and y_0' yields

$$\boxed{\delta'\left(\int\limits_{-\infty}^{0} fg(g-r)d\eta + \int\limits_{0}^{\infty} fg(1-g)d\eta\right) = 2T_{xy0}} \tag{5.6}$$

Where

$$T_{xy} \equiv \frac{\left(\underline{\langle\tau_{xy}\rangle} - \langle\rho\rangle\{u''v''\}\right)}{\rho_1 U_1^2} \tag{5.7}$$

and the $T_{xy0} = T_{xy}(y=0)$

In the derivation of the above expression, assumption of the pressure terms and the mixing layer not bending in any direction. So as to check how valid are the assumptions made, the growth rate calculated by the integral analysis and that from actual data were compared. This is shown in **Fig 5.2**, which shows that the error in the predicted values reduces to below 10% when the self similarity is attained. This shows that the assumptions are quite valid.

It was verified that the integrals on the LHS do not vary much, and are more or less dependent only on r and s in the self similar region. The integral analysis clearly leads to the fact that the most important term to the growth rate measurement is T_{xy} which is directly related to τ_{xy}. This particular aspect

5.3.2 The Contributing Terms in the stream-wise momentum equation

First, looking at the x momentum equation, we have the relevant Reynolds stress terms are τ_{xx} and τ_{xy}. τ_{xx} at a location close to the splitter plate and

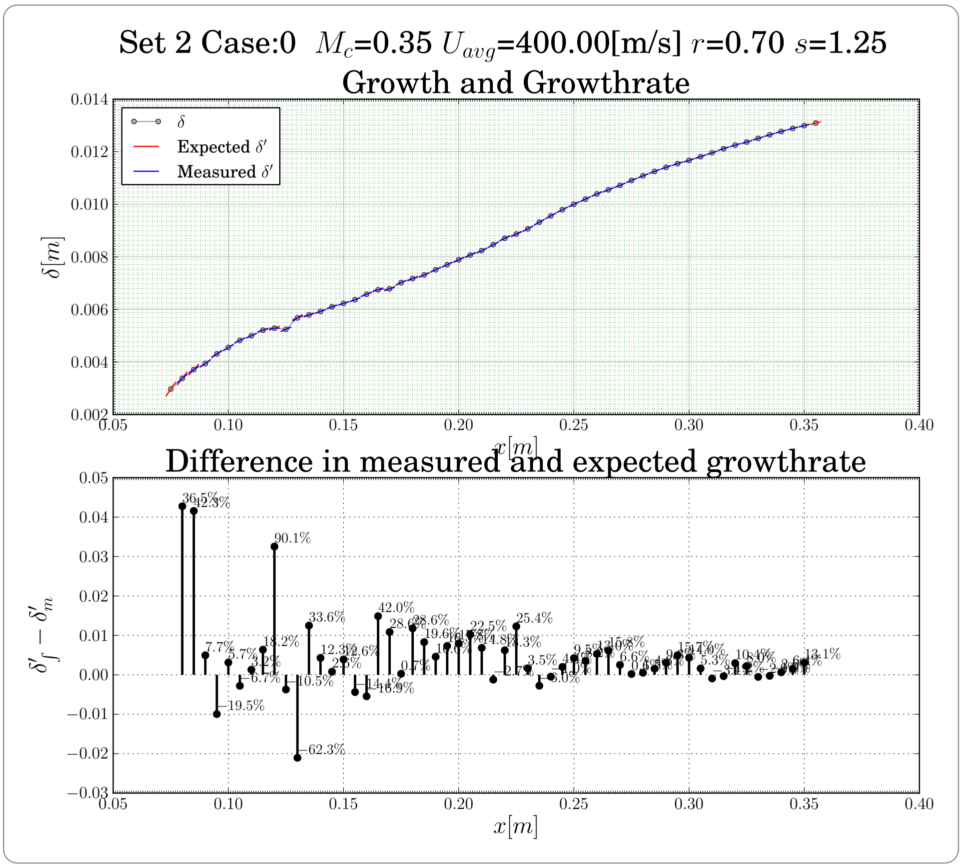

Figure 5.2: Growth rate predicted by integral analysis
[*Notice the regions used for integration and the close match between the measured and the expected growth rates in the self similar region*]

at a location far away is shown in **Fig 5.3**. Similar plots for τ_{xy} is shown in **Fig 5.4**. It can be seen that both of these terms, are of the same order. However what matters more is the actual source in the momentum equation, where it is the cross-wise gradient of τ_{xy} and the stream-wise gradient of τ_{xx} which are present. The relative importance of the quantities can be estimated only through the comparison of this term, which is plotted in **Fig 5.5**.

It is clear from **Fig 5.5** that the contribution of τ_{xy} is an order greater than that of τ_{xx}. This is, of course, not unexpected that this represents the turbulent stresses which transport the most significant momentum in the direction perpendicular, and hence can be expected to be of a greater magnitude. Further, more, momentum mixing in a mixing layer, and the subsequent growth rate of the mixing layer, occurs mainly due to this component. It may hence

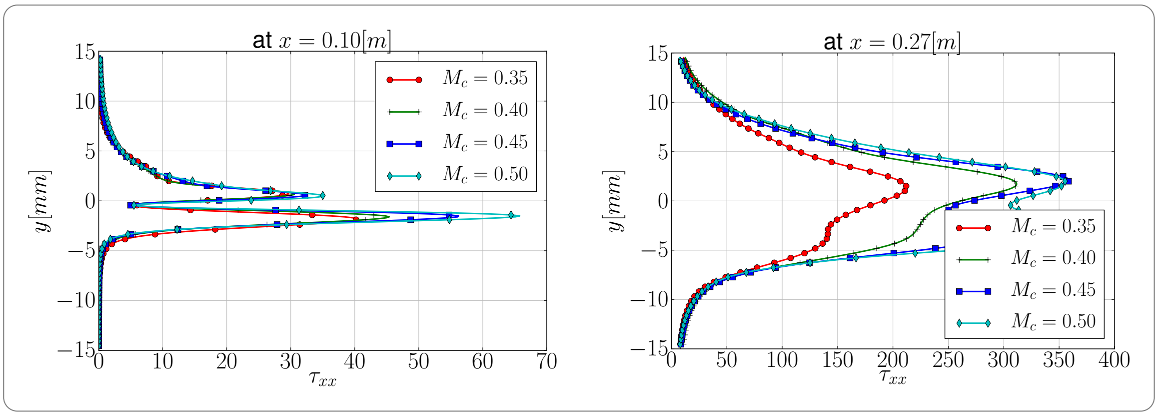

Figure 5.3: τ_{xx} variation in the cross-wise direction
[**Left:** *Typical* τ_{xx} *near the splitter plate, and* **Right:** *at a larger distance downstream*]

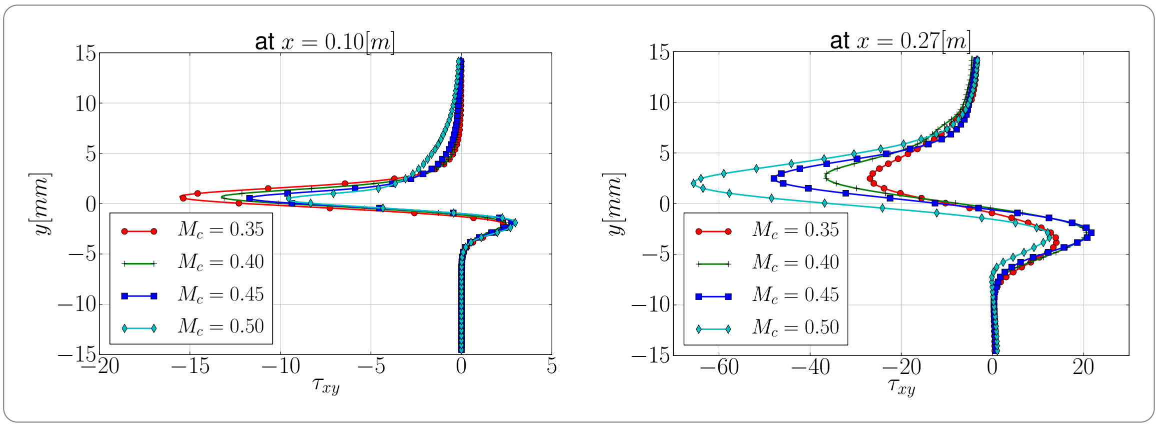

Figure 5.4: Contributing terms of τ_{xy}
[**Left:** *Typical* τ_{xy} *near the splitter plate, and* **Right:** *at a larger distance downstream*]

be said that it is the most important to model τ_{xy} accurately.

5.3.3 The Contributing Terms in the cross direction momentum equation

An examination of the y momentum equation indicates that the relevant Reynolds stress terms are τ_{yy} and τ_{yx}.

τ_{yy} at a location close to the splitter plate and at a location far away is shown in **Fig 5.6**. τ being a symmetric tensor,the observation is the same for τ_{yx} as that of τ_{xy}. As it can be seen, τ_{yy} is larger than τ_{xy}, however it is of the

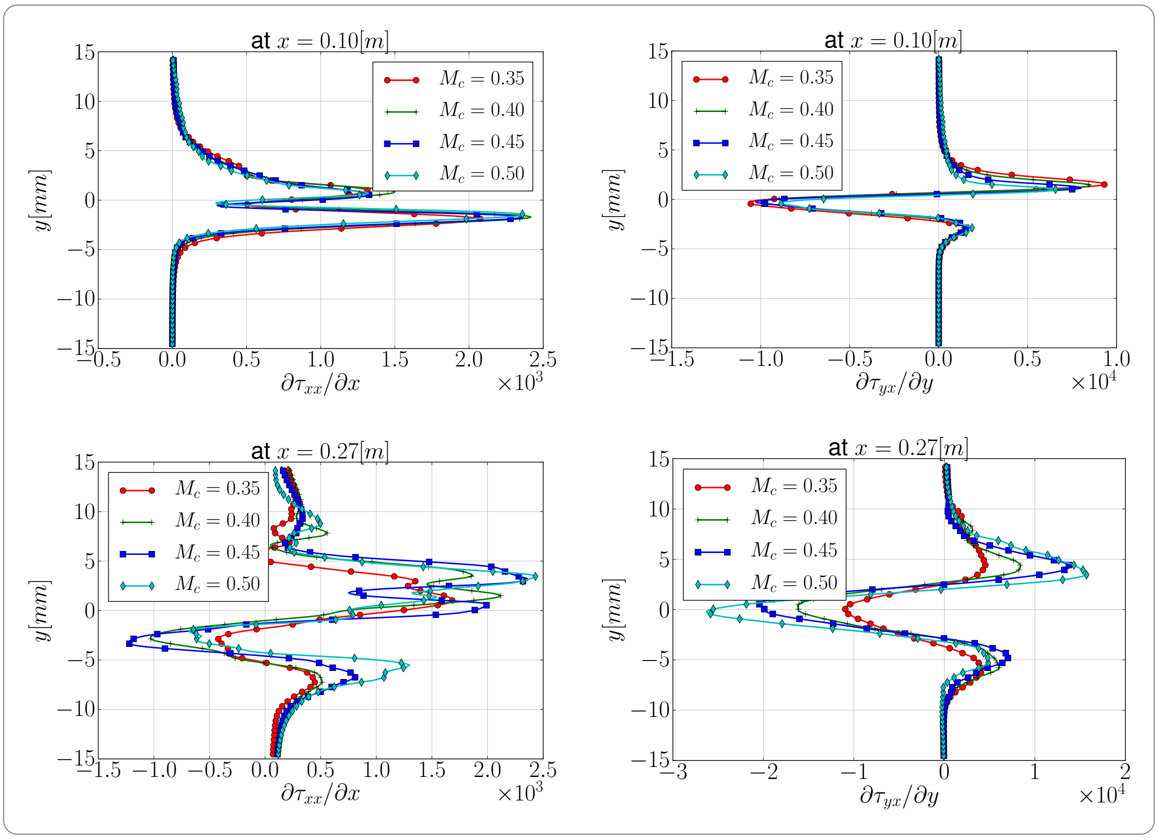

Figure 5.5: Relative contribution of τ_{xx} and τ_{xy} to the momentum equation both near as well as downstream the splitter plate

[*The contribution of* τ_{xy} *is about and order greater than that of* τ_{yy}]

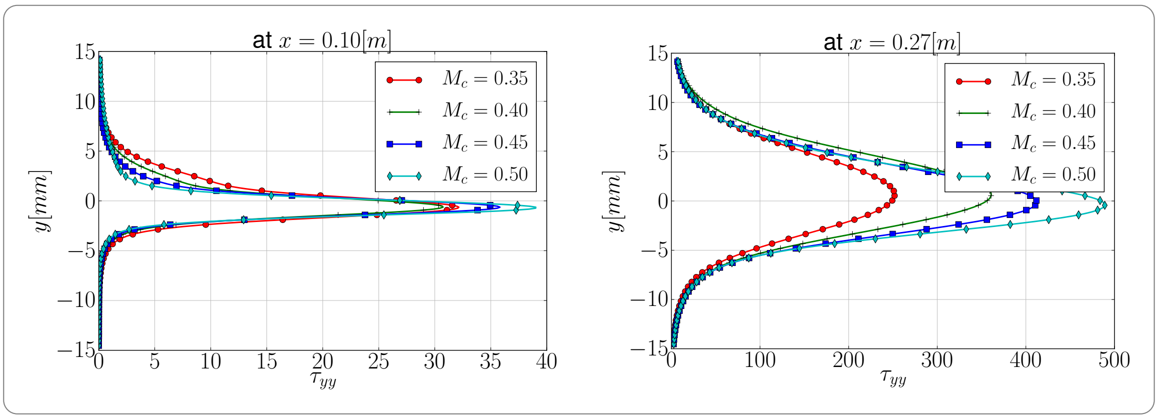

Figure 5.6: τ_{yy} variation in the cross-wise direction

[**Left:** *Typical* τ_{xx} *near the splitter plate, and* **Right:** *at a larger distance downstream*] same order. As before, the contribution to the cross-wise momentum transport is of a greater interest and in that the source terms appear as the cross-wise gradient of τ_{yy} and the stream-wise gradient of τ_{xy}. This is plotted in **Fig 5.7**

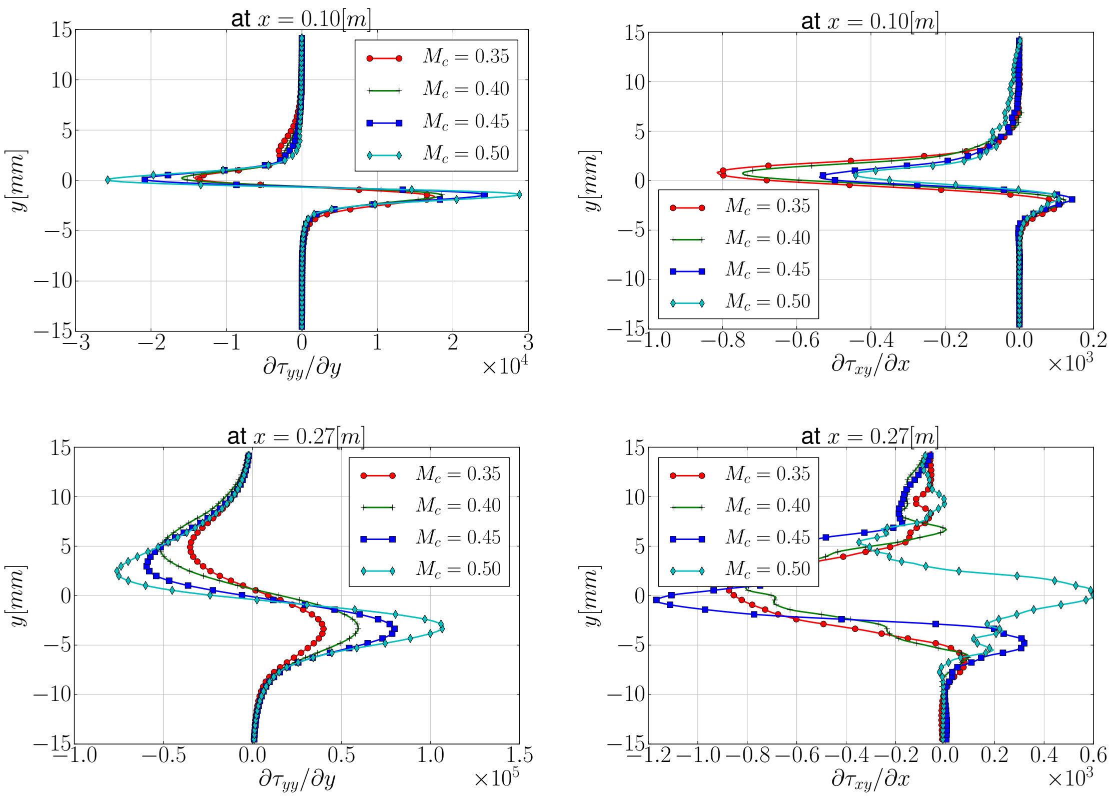

Figure 5.7: Relative contribution of τ_{yy} and τ_{yx} to the y momentum equation both near as well as downstream the splitter plate

[*The contribution of τ_{yy} is about an order greater than that of τ_{yx} in the y momentum equation*]

It is clear from **Fig 5.7** that the contribution of τ_{yy} is an order greater than that of τ_{yx}. And for RANS simulations it is of a greater importance to model τ_{yy} as accurately as possible for the cross-wise momentum equation. However, this term does not directly influence the growth rate, and it is the transport of the non-dominant direction of momentum. Hence the importance of this term cannot be expected to be the same as that of τ_{xy}.

It is thus clear from the above section that the most important parameter for modelling is τ_{xy} and this is followed by τ_{yy}.

5.4 Modelling of τ_{xy} and τ_{yy}

5.4.1 Modelling of τ_{xy}

The aim of this section is to express τ_{xy} as a function of some mean property. The logical choice of such a property is S_{xy}, taking inspiration from the Prantl's mixing length hypothesis. This can be seen qualitatively in **Fig 5.8**.

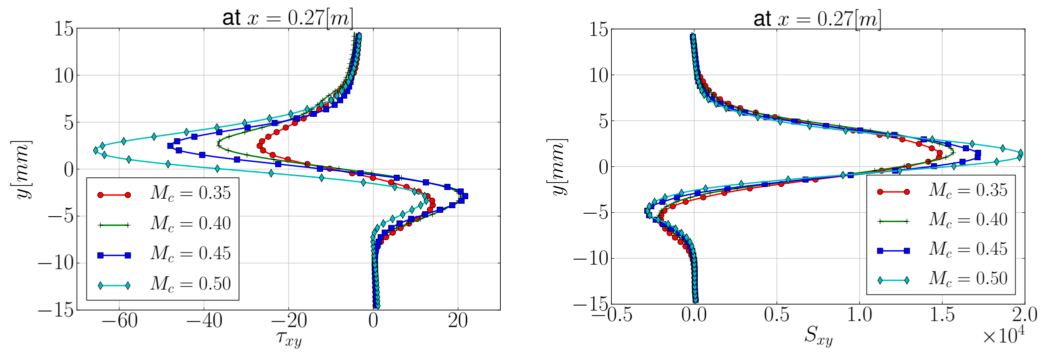

Figure 5.8: τ_{xy} and S_{xy} at the same stream-wise location
[τ_{xy} *profile resembles* $-S_{xy}$]

At once, we can express the relation in terms of non-dimensional parameters as

$$\frac{\tau_{xy}}{\bar{\rho}(\Delta U)^2} = L\frac{S_{xy}}{(\Delta U)/x} \text{ where } \Delta U \text{ is } U_1 - U_2 \text{ and } \bar{\rho} \text{ is } \frac{\rho_1 + \rho_2}{2} \tag{5.8}$$

The above scaling is expected to yield simpler formulation because, it is known that under self similar conditions, τ_{xy} becomes almost a constant, where as S_{xy} linearly decreases with x. Under such conditions, L is expected to be more or less independent of x, however that needs to be verified. Recognizing that S_{xy} can be made scale invariant with the mixing layer thickness and an appropriate velocity scale ΔU, non-dimensionalized quantity $Sxy/(\Delta U)/x$ was chosen after noting that x is the independent variable on which δ depends strongly. This is shown in **Fig 5.9**.

Similarly, with increasing M_c the behaviour of the τ_{xy} vs S_{xy} plot is shown in figure **Fig 5.10** which shows without doubt that *the shear stress in the region of self similarity at least, at all M_cs can be very well approximated by*

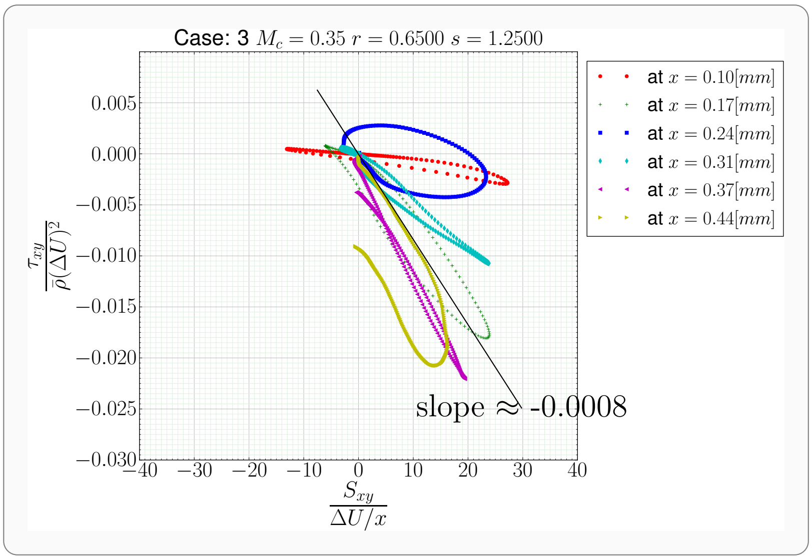

Figure 5.9: Variation of $\tau_x y$ with S_{xy} at various stream-wise locations [**Note:** The plot forms loops with the axis more or less oriented in a single direction except for very small x]

a straight line.

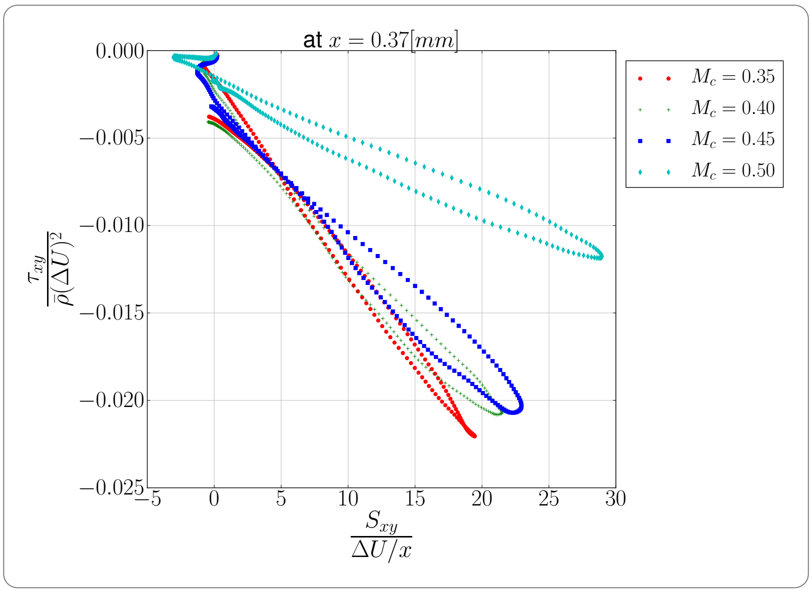

Figure 5.10: Variation of τ_{xy} vs S_{xy} at different M_c values [*The slope clearly decreases with M_c indicating a decreasing L in* **Eqn 5.8**]

This also implies the slope of the τ_{xy} vs S_{xy} plot needs to incorporate the effect of M_c, that is $L = L(M_c)$ which is to be obtained.

From the LES computation, it is seen that L has the form

$$L = Ae^{-BM_c} \tag{5.9}$$

Where $A \approx -0.014$ and $B \approx 6.7$. This relation is used as a initial guess for the RANS computations which follow.

Relation to Prandtl's Mixing length hypothesis

The results obtained in the previous section that

$$\frac{\tau_{xy}}{\bar{\rho}(\Delta U)^2} = L\frac{S_{xy}}{(\Delta U)/x} \tag{5.10}$$

is not surprising. We can write this as

$$\tau_{xy} = L\bar{\rho}\frac{\Delta U}{\delta}\delta^2\frac{x}{\delta}S_{xy} = \frac{L}{\delta'}\delta^2\bar{\rho}\frac{\Delta U}{\delta}S_{xy} \tag{5.11}$$

For a mixing layer, we have from the mixing length hypothesis, $\tau_{xy} \approx \bar{\rho}l_m^2 \left|S_{xy}\right| S_{xy}$. This mixing length ($l_m$) is proportional to δ, say $l_m = c\delta$. Furthermore, the $|S_{xy}|$ is proportional to $\dfrac{\Delta U}{\delta}$. Putting all this together, we obtain

$$c^2 = L/\delta' \tag{5.12}$$

Which means $L = \delta' c^2$. Where c is the ratio of the mixing length to the width of the mixing layer.

5.4.2 Modelling of τ_{yy}

The expected choice of the mean flow parameter to be used for modelling τ_{yy} is **Fig 5.8**. However this turns to be difficult, at least from the measurements of RANS. It can be seen from **Fig 5.11** that though the variation of τ_{yy} is smooth, the variation of S_{yy} is absolutely not so. Furthermore, it is not appropriate to relate S_{yy} to τ_{yy} because of a basic reason that $\tau_{yy} \equiv \langle \rho v'' v'' \rangle \geq 0$ whereas no such requirement is present from S_{xy} which can assume both positive as well as negative values, and in fact it does attain negative values at many locations.

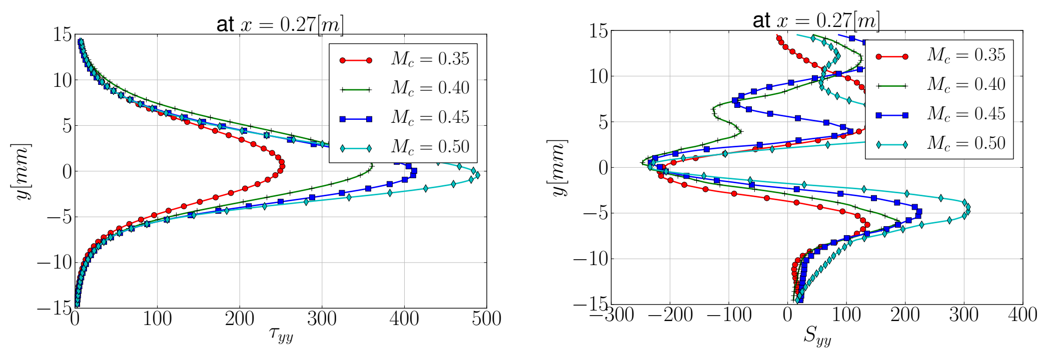

Figure 5.11: τ_{yy} and S_{yy} at the same stream-wise location

It is hence sought to relate τ_{yy} back to S_{xy}, taking inspiration that shear strain is the dominant strain in the mixing layer. Since the shear strain too goes positive as well as negative, it is sought to relate the non-dimensionalized τ_{yy} to non-dimensionalized S_{yy}. The approximate equation so obtained is

$$\boxed{\frac{\tau_{yy}}{\rho \Delta U^2} = A + \frac{B}{\left(\dfrac{M_c + 0.01}{0.25}\right)^2} \left(S^2 (S + 0.4)^2\right)^{0.125} \pm 0.01 \left(S^2 - S^4\right)^{0.125}} \tag{5.13}$$

where $S = \dfrac{S_{xy}}{30(\Delta U/x)}$ and A and B are constants evaluated to be nominally 0.02 and 0.03 respectively from the LES computations.

In the above equation, it must be noticed that S always appears with an even power. This is because τ_{yy} is always positive while S can be both positive and negative. The behavior of τ_{yy} with S is captured through expressing the behavior in terms of an ellipse that has a bias. An examination of an ensemble of the results shows that macro-behavior of the mixing layer is captured with a relatively simple curve fit of the behavior as above.

5.5 Reynold's hypothesis and evolution of $\mathrm{Pr_t}$ and $\mathrm{Sc_t}$

Till this point we concentrated only the momentum equation, however model is required RANS even in the energy and the species conservation equation.

Similar to the momentum equation, the energy equation yields the term

$$- \langle \rho u_i{}'' h'' \rangle$$

Noting that the effect of this term is similar to that of the heat diffusion term, this term is usually written as

$$- \langle \rho u_i{}'' h'' \rangle = \langle \rho \rangle \alpha_\mathrm{t} \frac{\partial \{h\}}{\partial x_i} \tag{5.14}$$

Where α_t is the analogous to the conductivity of the laminar flow, and needs to be modelled.

Reynold's Analogy Reynold's analogy relates the turbulent momentum transfer to the turbulent heat and mass transfer. The assumption that the mechanism of turbulent transfer is the same for all the three (momentum, heat and species) transfers, results in the conclusion that transport coefficient must be similar.

Thus with the definition of turbulent Prandtl number $\mathrm{Pr_t}$ as the ratio of turbulent heat transport to the turbulent momentum transport, we expect $\mathrm{Pr_t}$ to be near unity.

$$\boxed{\mathrm{Pr_t} \equiv \frac{\mu_\mathrm{t}}{\langle \rho \rangle \alpha_\mathrm{t}} = \frac{\langle \rho u'' v'' \rangle}{\langle \rho h'' v'' \rangle} \frac{\dfrac{\partial \{h\}}{\partial y}}{\left(\dfrac{\partial \{u\}}{\partial y} + \dfrac{\partial \{v\}}{\partial x} \right)}} \tag{5.15}$$

On similar lines, we have the diffusion equation, which presents the unresolved term

$$-\left\langle \rho Y_j{}'' u_i{}'' \right\rangle$$

for the j^{th} species. This is considered to be a form of diffusion caused due to turbulence, hence can be written as

$$-\left\langle \rho Y_j{}'' u_i{}'' \right\rangle = \left\langle \rho \right\rangle D_j \frac{\partial Y_j}{\partial x_i} \tag{5.16}$$

Like for the heat transfer, for species we define the turbulent Schmidt number $\mathrm{Sc_t}$ as the ratio of turbulent transport of species to the turbulent transport of momentum. Reynold's analogy expects $\mathrm{Sc_t}$ to be near unity.

$$\boxed{\mathrm{Sc_t} \equiv \frac{\mu_\mathrm{t}}{\left\langle \rho \right\rangle D_t} = \frac{\left\langle \rho u'' v'' \right\rangle}{\left\langle Y_j{}'' v'' \right\rangle} \frac{\dfrac{\partial \left\{Y_j\right\}}{\partial y}}{\left(\dfrac{\partial v}{\partial x} + \dfrac{\partial u}{\partial y}\right)}} \tag{5.17}$$

Other than these we also have the ratio of the heat transport and the species transport due to turbulence. This is the turbulent Lewis number $\mathrm{Le_t}$. Thus

$$\boxed{\mathrm{Le_t} \equiv \frac{\alpha_\mathrm{t}}{D_t} = \frac{\left\langle \rho h'' v'' \right\rangle}{\left\langle \rho Y_j{}'' v'' \right\rangle} \frac{\dfrac{\partial \left\{Y_j\right\}}{\partial y}}{\dfrac{\partial \left\{h\right\}}{\partial y}}} \tag{5.18}$$

5.5.1 Extraction of Turbulent Prandtl Number and Schimdt Number

Extraction of Turbulent Prandtl Number ($\mathrm{Pr_t}$)

From the simulation, the Favre averaged enthalpy, and the Favre averaged velocity field is obtained, whose gradient is computed, from which the gradient of these are computed to obtain

$$\frac{\partial \left\{h\right\}}{\partial y} \text{ and } \frac{\partial \left\{u\right\}}{\partial y} + \frac{\partial \left\{v\right\}}{\partial x}$$

The simulation also computes $\{hU\}$ from which we an obtain

$$\{h''v''\} = \{hU\} - \{h\}\{v\} \tag{5.19}$$

One of the problems in evaluating $\mathrm{Pr_t}$ is that the definition is ill posed near the edges of the mixing layer, and at any location where the velocity gradients are small. To be able to clearly see the distribution of $\mathrm{Pr_t}$, hence it was sought to plot $\tau \dfrac{\partial \{h\}}{\partial y}$ versus $\langle \rho h'' v'' \rangle \left(\dfrac{\partial \{u\}}{\partial y} + \dfrac{\partial \{v\}}{\partial x} \right)$. This is plotted in **Fig 5.12**.

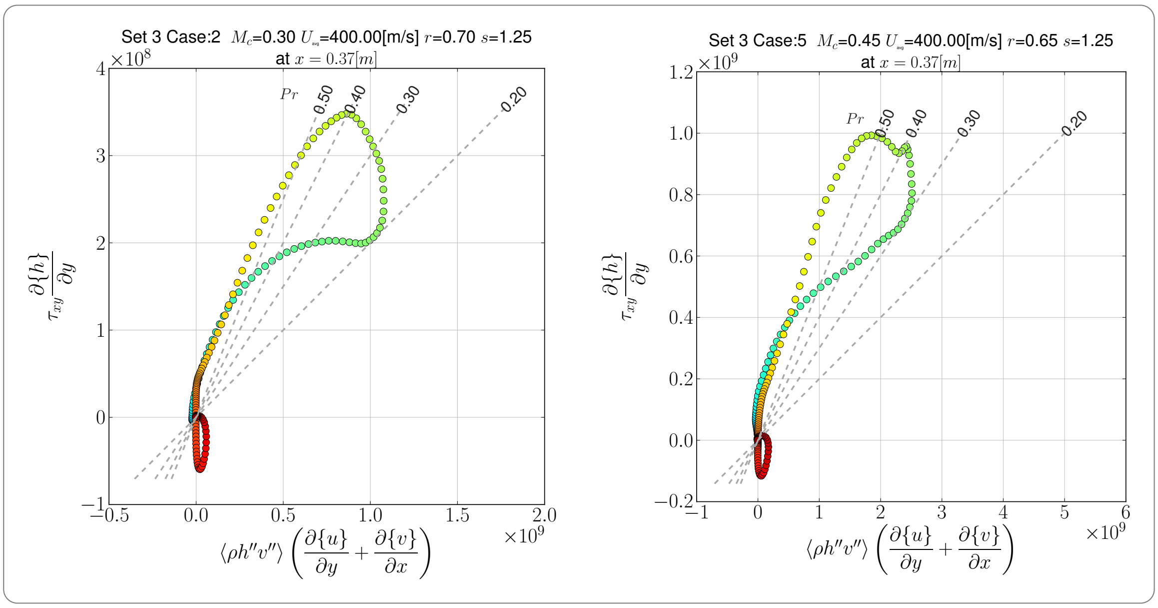

Figure 5.12: Prandtl Number computation
[**Left** *has a lower* M_c *as compared to* **right** *side figure. The Prandtl number is much smaller than unity, and increases downstream.*]

It can be noted from **Fig 5.12** that the value of $\mathrm{Pr_t}$ is significantly lower than unity. Wilcox [1998] suggested a value of $\mathrm{Pr_t} = 0.5$ for a mixing layer. The present simulation shows a value of around 0.2 to 0.5 in most part of the domain, but varies throughout the length. The reason for this behaviour is investigated in **Sect 5.5.2**. From this we can infer that the heat diffusion to heat velocity fluctuation ratio is significantly more than the momentum diffusion to momentum fluctuation ratio. The local ratio of the $\mathrm{Pr_t}$ varies substantially. The value of this seems to be influenced by the flow parameter too. Furthermore it is also seen that the secondary side has a consistently lower $\mathrm{Pr_t}$ as compared to the primary side.

Extraction of Turbulent Schmidt Number ($\mathrm{Sc_t}$)

$\mathrm{Sc_t}$ was calculated in a way similar to $\mathrm{Pr_t}$ by using

$$\{Y_j''v''\} = \{Y_j v\} - \{Y_j\}\{v\} \tag{5.20}$$

Figure 5.13 shows $\tau_{xy}\dfrac{\partial Y_{Ar}}{\partial y}$ plotted against $\langle\rho\rangle\{Y_{Ar}\}\left(\dfrac{\partial\{u\}}{\partial y}+\dfrac{\partial\{v\}}{\partial x}\right)$. Hence the slope of any line passing through a point and the origin is the $\mathrm{Sc_t}$ at that location.

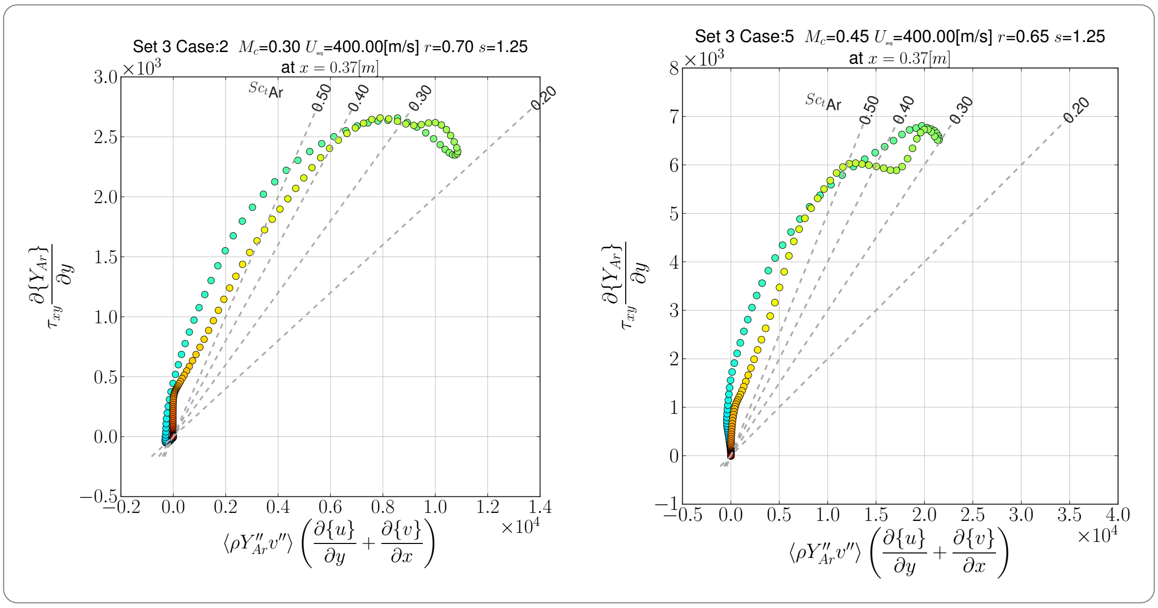

Figure 5.13: Schmidt Number computation
[**Left** *has a lower* M_c *as compared to* **right** *side figure. The value of* $\mathrm{Sc_t}$ *is lower on the primary side and higher on the secondary side. Near splitter plate has a greater spread than further downstream*]

As in the case of $\mathrm{Pr_t}$, **Fig 5.13** shows that the value of $\mathrm{Sc_t}$ is lower than unity, and for most of the domain has a value from 0.2 to 0.8. It can also be noted that this value is slightly lower on the primary side than on the secondary side. Likewise again, like $\mathrm{Pr_t}$, it unlikely to be able to get accurate results by using a constant value for the values of $\mathrm{Sc_t}$, because of its large variation in both the stream wise location as well as the cross wise location.

5.5.2 Reasons for the observed behaviour of $\mathrm{Pr_t}$, $\mathrm{Sc_t}$ and $\mathrm{Le_t}$

The reasoning of the behaviour of the $\mathrm{Pr_t}$, $\mathrm{Sc_t}$ and $\mathrm{Le_t}$ can be inferred from a typical diffusion pattern of the same. To understand this the average profiles of $\{h\}$, $\{T\}$ and $\{U\}$ is plotted in **Fig 5.14**, where the respective quantities are scaled to make them vary from 0 towards $y = -\infty$ and 1 towards $y = \infty$.

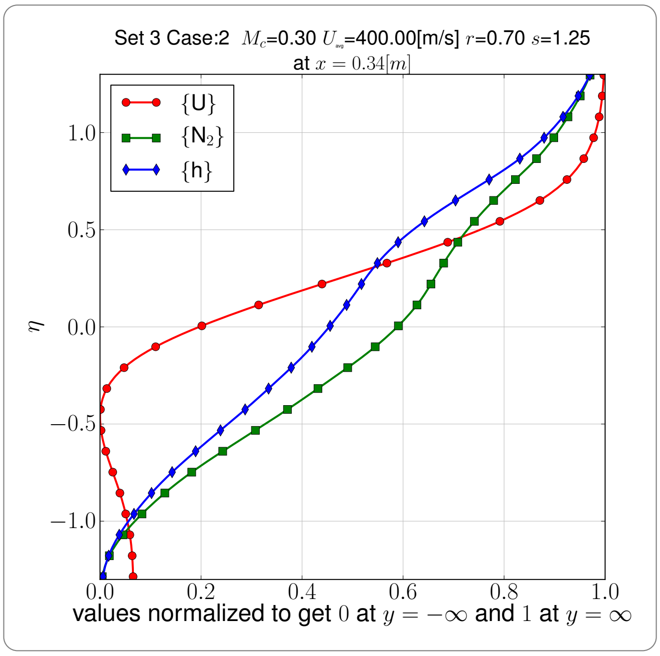

Figure 5.14: Comparing the diffusion of heat, species and momentum
[*The diffusion of heat and species is more than the diffusion of momentum*]

It is quite apparent from **Fig 5.14** that the diffusion of heat and species happens more than the diffusion of momentum. It is also apparent that the diffusion of the species and heat happens in a similar way, albeit there is a clear asymmetry in the patten in the diffusion on the primary side as compared to the secondary side. This difference appears as the difference small deviation in the $\mathrm{Le_t}$ observed.

It is also apparent that the enthalpy and the species profiles become self similar faster than the mean velocity profiles.

5.6 Unsteady RANS computations

Unsteady RANS was used for the computations for the compressible mixing layers, with the turbulence model for τ_{xy} as mentioned in the previous section. These simulations were carried out with the same fluid, Air, in both the streams, and a constant $\mathrm{Pr_t}$ of 0.3 was used. These cases are defined in **Table 5.1**.

With each of these test cases, an unsteady RANS simulation was performed, and averaging was performed over 10 sweeps, and the growth rate was measured. The growth rate showed an almost linear variation with the L. This was used to estimate the value of L which would give the expected growth rate.

5.6.1 RANS Simulation Results

The value of L which provides the expected growth rate is shown in **Fig 5.15**. We proposed earlier an ansatz that the value of L is of the form

$$L \approx Ae^{-BM_c} \tag{5.21}$$

Case	$U_{\text{avg}}[m/s]$	M_c	r	s	$U[m/s]$		$T[K]$		M		$p[Pa]$
					Prm	Sec	Prm	Sec	Prm	Sec	
1 - 7	500	0.27	0.68	1.25	597	402	358.1	286.49	1.58	1.19	7000
8 - 14	500	0.35	0.68	1.25	597	402	213.1	170.49	2.04	1.54	7000
15 - 21	500	0.45	0.68	1.25	597	402	128.9	103.14	2.62	1.98	7000
22 - 28	500	0.55	0.68	1.25	597	402	86.3	69.04	3.20	2.42	7000
29 - 35	500	0.65	0.68	1.25	597	402	61.7	49.43	3.79	2.86	7000
36 - 43	400	0.70	0.60	1.25	500	300	56.6	45.29	3.31	2.22	7000
44 - 49	400	0.75	0.55	1.25	516	283	66.5	53.20	3.16	1.94	7000
50 - 56	400	0.05	0.95	1.25	410	389	116.7	93.37	1.89	2.01	7000
57 - 63	400	0.10	0.90	1.25	421	378	122.9	98.35	1.89	1.91	7000

Note: The seven cases in each row correspond to cases with $M_c <= 0.6$, L was tried with values $[0.01, 0.03, 0.06, 0.1, 0.3, 0.6, 1.] \times 10^{-3}$, and for others $[0.01, 0.03, 0.06, 0.1, 0.3, 0.6, 1.] \times 2 \times 10^{-5}$

Table 5.1: Specifications of RANS Simulations

M_c	$L \times 10^4$
0.05	17.7
0.1	11.4
0.27	5.31
0.35	2.89
0.45	2.50
0.55	1.01
0.70	0.193
0.75	0.134

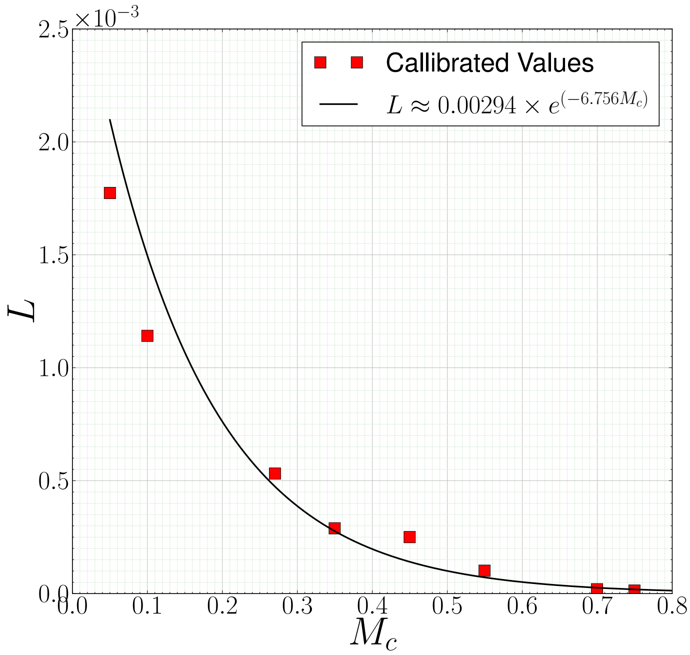

Figure 5.15: Measured and interpolated variation of L with M_c

Which is valid for low M_c to moderately large M_c. With this the best fit for the observed values of L is

$$L \approx 0.00294 e^{(-6.756 M_c)} \tag{5.22}$$

Thus substituting in **Eqn 5.8** we get the model for τ_{xy} as

$$\boxed{\frac{\tau_{xy}}{\bar{\rho}(\Delta U)^2} = \frac{S_{xy}}{(\Delta U)/x} \left(0.003 e^{(-6.76 M_c)}\right)} \tag{5.23}$$

It must be noted that from the experiments of Goebel and Dutton [1990a] the velocity profile and the shear stress can be calculated. Assuming δ/x is the same as $d\delta/dx$ from **Fig 5.16** where we can see that it is about 0.000776 . From the expression we obtain a value of L as 0.00076, which is indeed very close to the experimental value.

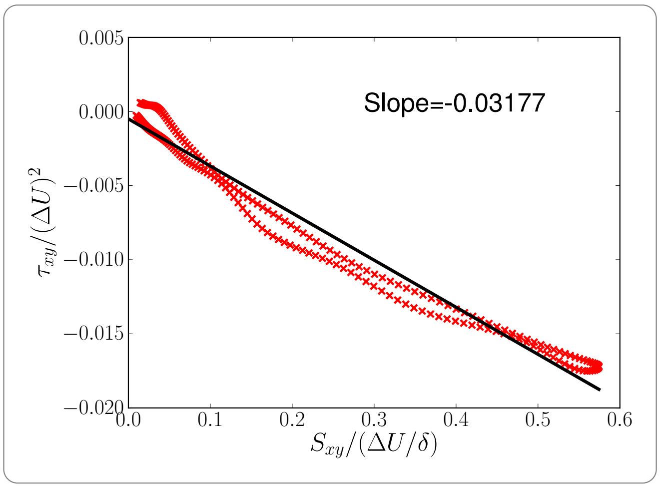

Figure 5.16: Value of μ_t as can be obtained form Goebel and Dutton [1990a]

5.6.2 Simulations with the model values

The simulations were performed with the values predicted from **Eqn 5.23**. The results of these are presented in the following sections.

Growth Rate

The growth rate of the different cases were measured, and were compared with the experimental results. The plot of the growth is shown in **Fig 5.17**. It can be seen that the growth rate of the mixing layer shows a clear decrease with increase in the M_c. Also it is seen that the

Along with the model, it is also necessary to note the sensitivity of the growth rate to the coefficient in the model. This is necessary to know the influence the model has on the mixing mechanism. This is plotted along with other data in **Fig 5.17**

If the sensitivity of the model, defined as the ratio of change of the normalized growth rate to the value of L

$$\frac{\Delta(\delta'/\delta'_0)}{\Delta L/L} \approx 1.5 \tag{5.24}$$

Furthermore, for the same L the effect of variation of A and B from **Eqn**

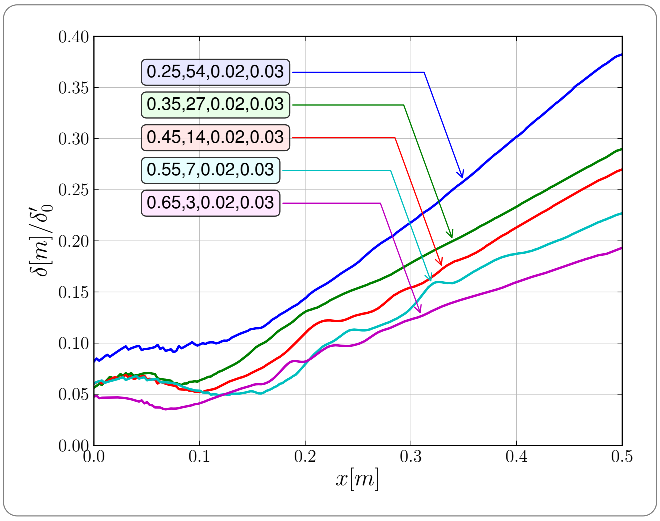

Figure 5.17: Growth of the mixing layer with RANS at different M_cs
[*The clear reduction of the growth and the growth rate with increasing* M_c. *The numbers indicate the* M_c,$L \times 1e5$,A *and* B]

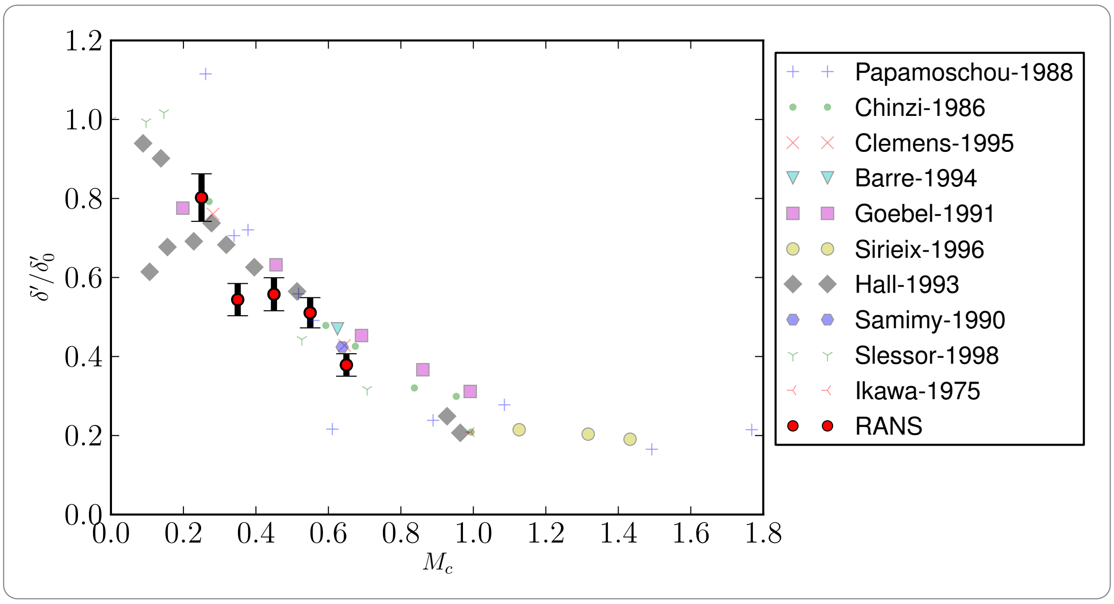

Figure 5.18: Sensitivity of Growth rate with L
[*The error bars show the difference expected in the growth rate for a variation of* $\pm 5\%$ *in the value of L*]

5.13 was studied. This is shown in **Fig 5.19**

It is seen clearly that where as the growth rate is quite sensitive to the selection of the constants for τ_{xy}, it is hardly so in case of the coefficients related to τ_{yy}, unless for the case where the model for τ_{yy} is not made zero. This goes to so that it is not very important to have the model for τ_{yy} extremely accurate, and neither for τ_{xx} needs to be modelled quite accurately, because the growth rate is not very sensitive to the model of shear stress and not to the normal stress.

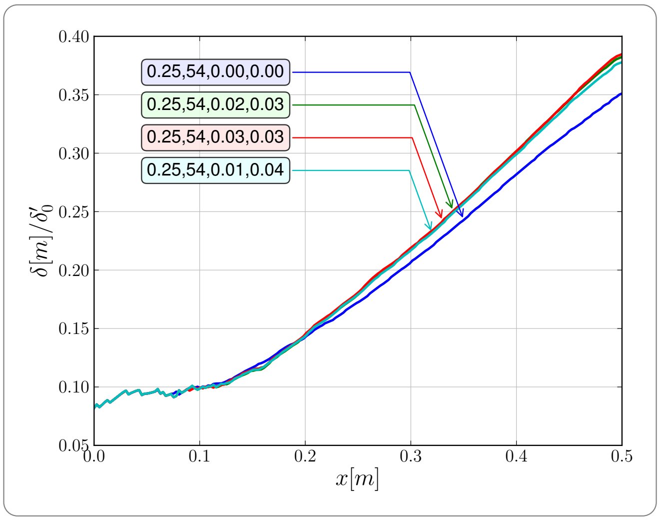

Figure 5.19: Variation of Growth pattern with A and B
[*The value of A and B have little effect when they are non-zero.*]

5.7 Conclusions

It has been known that the k based turbulence models are not suited for good prediction of the mixing layer growth rate. The reason for this was identified from the LES simulations. τ_{xy} was determined to be the most important factor which contributes to the growth of the mixing layer. This was done using integral analysis to come to a rough conclusion, and then through analysis of the data obtained from LES.

It was seen from the analyses that the shear stress scales quite reasonably with the shear strain for most of the mixing layer, and that a simple mixing length approach is expected to yield the mixing layer reduction, albeit the length itself would be a function of M_c. This was estimated from the LES to be roughly an exponential function, and a series of experiments with RANS were tried and the functional form of the mixing length was established and coefficients determined. τ_{yy} at the same time was also related using a suitable algebraic relation to S_{xy}. Furthermore, the LES simulations were analysed to calculate and compare the non-dimensional numbers characterizing the diffusion of momentum, enthalpy and species. It was determined that the values of $\mathrm{Pr_t}$ and $\mathrm{Sc_t}$ are in the range 0.3–0.5. The relation obtained after tuning was seen to predict the growth rates well within the band of experimental results. Further, it was shown that the growth rate was not sensitive to the modelling of τ_{yy}, indicating that a simpler model could have been used.

It must be emphasized no less that the current work does not attempt to model k. If k is to be estimated, it must be solved for independently, perhaps with a classical turbulence model for k. In fact Launder et al. [1972] claimed that the kinetic energy from mixing length models are not very good. The claim made, is that it is sufficient to model the τ_{xy} accurately to obtain the reduction in the growth rate, and this can be adequately be done by a simple zero equation model. This approach is sufficient to give the correct mean flow features. Furthermore, since the measured τ_{xy} from LES was composite effect of the pressure strain term as well as the production term, the behaviour of τ_{xy} with reduction in the value of L with M_c taken into account, would have captured the cumulative effect of decrease of production and pressure strain term.

The fact that the growth rate is not very sensitive to τ_{yy} (and of course τ_{xx}) also opens up the possibility of merging this with $k-\epsilon$ or $k\omega$ model, where in the region of the mixing layer, the shear stress is predicted using the present zero equation model, and the normal stresses predicted by an eddy viscosity model. This will of course still be flawed in that the anisotropy would not be accounted for, even if the measure of the turbulent kinetic energy would roughly be correct. This particular aspect has not been dealt with in the present work.

Chapter 6

Entropy Generation and Trends

6.1 Introduction

When the issues related to mixing layer thickness reduction due to compressibility effects were being internally debated, it was thought if it was useful to explore of ideas of entropy change since mixing implied inherently entropy increase and increased convective Mach number led to reduced mixing. It was clear that this approach could enhance understanding but not add to practice (calculation procedure or predictive schemes) in any sense. It was thought appropriate to use the conservation equations that involve the mixing of two high speed streams with different gases (**Set3** involving argon and nitrogen - see section) by casting them in the entropy format.

The different terms that enter into the picture are: reversible heat transfer, irreversible heat transfer, reversible diffusion, irreversible diffusion, and shear. A different approach to viewing the production of turbulence and the dissipation is considering turbulence as source of entropy production. Fluid flow causes irreversible entropy generation through mixing of different species and through dissipation. In addition, there is also an isentropic or reversible generation or removal of entropy. We shall first write the entropy equation as a convective equation with source terms representing the reversible and the irreversible entropy generation. This will be followed by studying the variation of the same with the flow parameters.

6.2 Governing Equation

To inspect the entropy generation and its convection, we need to develop the equation of entropy in conservation form. It must be appreciated that the entropy is a property of the fluid and this can be calculated knowing the pressure, temperature and species at any given point in the field. However, this method of calculating the entropy, can at best give the difference in the total sum of the generation when contrasted with the free stream values. To be able to decipher this total entropy generation and break it down into it constituent sources, it is necessary to have an evolution equation [1] for entropy. Besides a rough comparison between the value of entropy calculated from the latter approach i.e. the evolution equation and the one obtained from the fluid properties serves as a quick check of the evolution equation.

We start with the energy equation Eqn(**2.9**) on Page(**48**)

$$\rho \frac{De}{Dt} = -p\nabla \cdot \boldsymbol{u} + \sigma : \nabla \boldsymbol{u} - \nabla \cdot \boldsymbol{q} \tag{6.1}$$

where $\boldsymbol{q}$ represents the heat flux due to molecular diffusion (conduction).

Considering energy to be a function of entropy, density and species mole fraction,

$$de = Tds + \frac{p}{\rho^2} d\rho + \sum_j \left(\frac{\partial e}{\partial n_j} \right)_{\rho, s, n_{i \neq j}} dn_j \tag{6.2}$$

And simplifying the terms we finally arrive at the equation (see Appendix **A.5** on Page**203** for the derivation)

$$\boxed{\begin{aligned} \rho \frac{Ds}{Dt} &= -\nabla \cdot \left(\frac{\boldsymbol{q}}{T} \right) + \frac{\lambda}{T^2} \left(\nabla \cdot T \right) \left(\nabla \cdot T \right) \\ &+ \sum_j \nabla \cdot \left(\frac{\mu_j}{W_j T} \right) \boldsymbol{j}_j - \sum_j \frac{R}{W_j Y_j} \nabla Y_j \cdot \boldsymbol{j}_j + RW \sum_i \frac{\nabla Y_i}{W_i} \cdot \sum_j \frac{\boldsymbol{j}_j}{W_j} \\ &+ \frac{1}{T} \sigma : \nabla \boldsymbol{u} \end{aligned}}$$

(6.3)

[1] It is well appreciated that there is not law of conservation of entropy and hence the term *conservative form* for entropy is misleading and rather meaningless. However here we mean the evolution equation written in a form with a part which is conserved as a passive scalar and source terms for all of the part which change entropy.

Terms in **Eqn 6.3** are explained in **Table 6.1**

Term	Name	Significance
$\rho \dfrac{Ds}{Dt}$		Substantial derivative of entropy
$-\nabla \cdot \left(\dfrac{\boldsymbol{q}}{T}\right)$	s_{rc}	Reversible entropy change due to heat transfer
$\dfrac{\lambda}{T^2} (\nabla \cdot T) (\nabla \cdot T)$	s_{ic}	Irreversible entropy change due to heat transfer
$\sum_j \nabla \cdot \left(\dfrac{\mu_j}{W_j T}\right) \boldsymbol{j}_j$	s_{rm}	Reversible entropy change due to mixing
$-\sum_j \dfrac{R}{W_j Y_j} \nabla Y_j \cdot \boldsymbol{j}_j$	s_{im1}	Irreversible entropy change due to mixing
$RW \sum_i \dfrac{\nabla Y_i}{W_i} \cdot \sum_j \dfrac{\boldsymbol{j}_j}{W_j}$	s_{im2}	Irreversible entropy change due to mixing
$\dfrac{1}{T} \sigma : \nabla \boldsymbol{u}$	s_{τ}	Irreversible entropy generation through dissipation

Table 6.1: Terms in **Eqn 6.3**

Each of these terms were implemented in the code, and analysed. These terms match the ones mentioned in Okong'o and Bellan [2000]

6.3 Consistency

As mentioned earlier, entropy is calculated by two techniques. First is to solve the evolution equation and actually *convect* entropy with the fluid along with the source terms. The second technique is to calculate the entropy directly from the fluid properties.

The stream properties are calculated using the coefficients from McBride et al. [1993] as in Eqn(**2.19**) on Page(**49**)

$$\frac{s_0}{R} = a_1 \ln(T) + a_2 T + a_3 \frac{T^2}{2} + a_4 \frac{T^3}{3} + a_5 \frac{T^4}{4} + a_7 \tag{6.4}$$

Figure 6.1 shows the average entropy measured from direct calculation

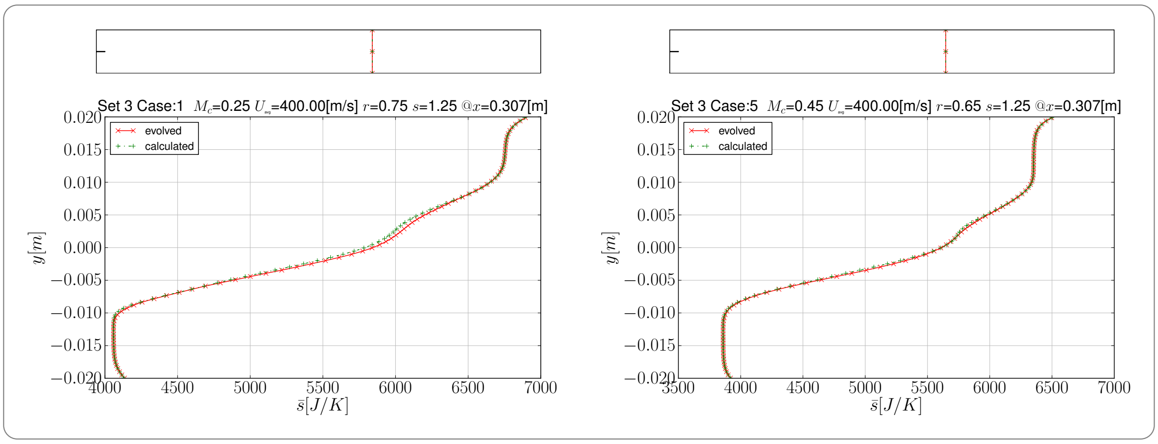

Figure 6.1: The entropy calculated by evolution and by direct calculation almost match each other

[*Consistency of Entropy Calculations*]

and from the evolution equation for two cases at some arbitrary stream-wise location. It can be clearly seen that the entropies measured by either techniques are matching almost perfectly. This confirms the implementation of the entropy code, as well as the derivation of the entropy evolution equation.

6.4 Description of the sources

In this part we shall qualitatively study the various contribution to the entropy due to the different sources, as described in **Table 6.1**. We shall also study the influence M_c has on each of these sources.

6.4.1 Reversible Heat Transfer

General Features

This corresponds to the term

$$s_{\mathrm{rc}} \equiv -\nabla \cdot \left(\frac{\boldsymbol{q}}{T}\right)$$

The s_{rc} term arises from the conduction equation. Conduction, the diffusion of thermal energy from a high temperature side to the low temperature side, involves a decrease in the entropy on the high temperature side, and an increase in the entropy on the low temperature side. The decrease in the entropy is smaller than the increase in the entropy on the low energy side, when there is a finite temperature difference between the source and the sink. Any heat transfer with infinitesimal temperature difference is reversible. It can be seen that this term involves both positive as well as negative values, of similar magnitude, though not exactly same.

Variation with M_c

The comparison for $s_{\rm rc}$ for the cases differing only in M_c is shown in **Fig 6.2**.

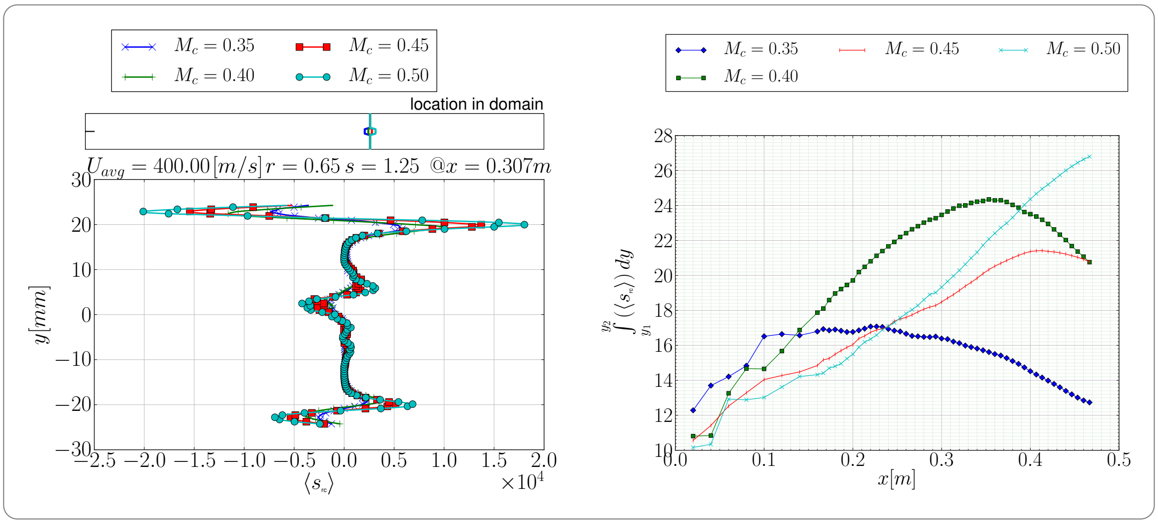

Figure 6.2: Time averaged and cross-wise integrated value of $\langle s_{\rm rc} \rangle$
[**Left**: *The time averaged source of s_{rc} across the stream at a particular stream-wise location, and* **Right**: *integrated quantity in the cross wise direction.*]

From the time average plot, tt can be seen that the sources have quite similar values. It is also seen that the values mostly appear as pairs of positive and negative values of almost the same value, negative on the side of higher temperature and positive on the side of lower temperature. Further the integrated values do not show any clear trend with respect to M_c. Hence it can be concluded that an increase in the M_c does not influence $s_{\rm rc}$ significantly.

6.4.2 Irreversible Heat transfer

General Features

This corresponds to the term

$$s_{\text{ic}} \equiv \frac{\lambda}{T^2}\left(\nabla \cdot T\right)\left(\nabla \cdot T\right)$$

As can be seen from the definition of s_{ic} as well as from the plots, this term is always positive and it only increases the entropy. Also as can be seen from the equation, the contribution is proportional to the gradient of the temperature as well as inversely proportional to the temperature. Hence as can be seen in the source peaks on the primary side.

Variation with M_c

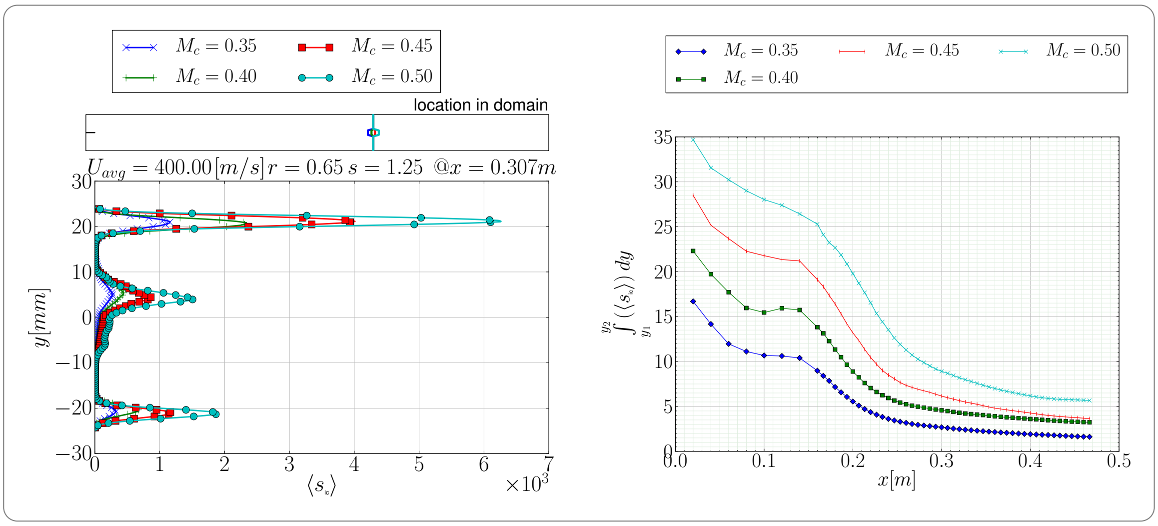

Figure 6.3: $\langle s_{\text{ic}} \rangle$, time averaged plotted at a cross-wise location and cross-wise averaged values in the stream-wise direction
[*The plot shows a distinct increase in the source of entropy with increasing* M_c]

It can be seen that clearly, that greater M_c is resulting in higher values of $\langle s_{\text{ic}} \rangle$. To reason out this, we observe that roughly speaking

$$s_{\text{ic}} \propto \left(\frac{1}{T_1} - \frac{1}{T_2}\right)^2 \left(\frac{T_1 - T_2}{\delta}\right)^2 = \frac{1}{\delta^2}\frac{\left(T_1 - T_2\right)^4}{\left(T_1 T_2\right)^2} \tag{6.5}$$

We note that for the same fluids at different M_c and same velocity ratio s, we have

$$s = \frac{\rho_2}{\rho_1} = \frac{T_1 R_1}{T_2 R_2} \tag{6.6}$$

Thus for the same combination of fluids, and at the same density ratio, the ratio of the temperatures is the same. Hence

$$\left.\left(\frac{(T_1 - T_2)^2}{T_1 T_2}\right)\right|_{\textsf{Case 3}} \approx \left.\left(\frac{(T_1 - T_2)^2}{T_1 T_2}\right)\right|_{\textsf{Case 5}} \tag{6.7}$$

Hence the greater source term is indicative of the smaller growth rate.

6.4.3 Reversible Diffusion

General Features

This corresponds to the term

$$s_{\mathrm{rm}} \equiv \sum_j \nabla \cdot \left(\frac{\mu_j}{W_j T}\right) \boldsymbol{j}_j$$

Reversible entropy change has both positive as well as negative values at different regions of the flow. At the zones of mixing, due to diffusion, there are negative sources adjacent to positive sources. In these it is seen that the usual locations of the negative and the positive sources are separated in the cross wise direction, and hence due to time averaging, they do not cancel out each other. Hence averaging over time shows distinct regions of negative source and positive source.

Variation with M_c

Upon cross-wise integrating, this term more or less cancels out completely. Further, in the stream-wise direction, the integrated source is definitely not single signed. Hence it would be a fair conclusion that this term has an insignificant contribution to the total entropy change, and that this term is not affected by M_c.

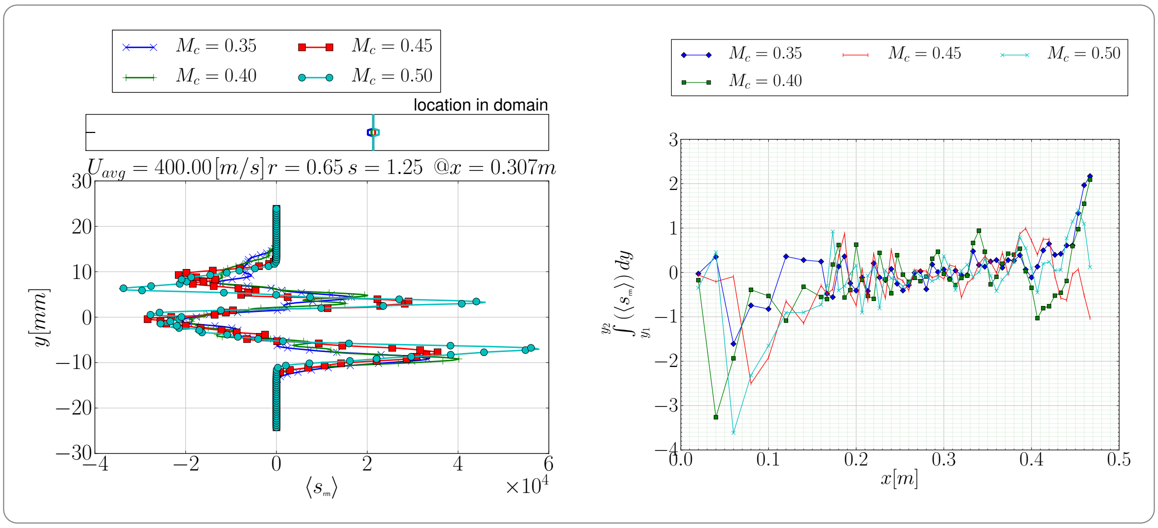

Figure 6.4: $\langle s_{\rm rm} \rangle$, time averaged plotted at a cross-wise location and cross-wise averaged values in the stream-wise direction
[*Note the large negative and positive values*]

6.4.4 Irreversible Diffusion (A)

General Features

This corresponds to the term

$$s_{\rm im1} \equiv -\sum_j \frac{R}{W_j Y_j} \nabla Y_j \cdot \boldsymbol{j}_j$$

. It can be seen from equation since ∇Y_n and $\boldsymbol{j}_j$ have opposite directions, $s_{\rm im1}$ will always be positive. Also as in the case of the other diffusion terms, this term has a larger magnitude near the contact regions between the two fluids. It is important to note that this term is independent of the direct influence of temperature, and is hence present on both the edges of the mixing layer.

Variation with M_c

$s_{\rm im1}$ is a term which is independent of the temperature, and this term is seen in **Fig 6.5** to increase with decrease in the M_c. Also this term can be seen as the most dominant of the irreversible entropy source terms. The decrease in the mixing process with increase in M_c causes this term to decrease with increase in M_c.

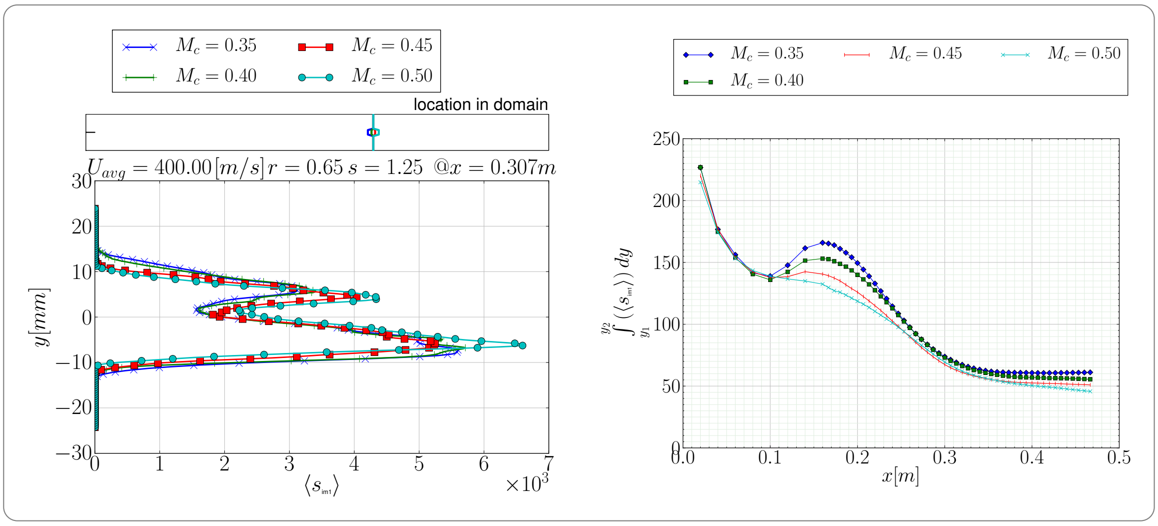

Figure 6.5: $\langle s_{\text{im1}} \rangle$, time averaged plotted at a cross-wise location and cross-wise averaged values in the stream-wise direction
[*Note the decrease in the peak value with increase in* M_c]

6.4.5 Irreversible Diffusion (B)

General Features

This corresponds to the term

$$s_{\text{im2}} \equiv RW \sum_i \frac{\nabla Y_i}{W_i} \cdot \sum_j \frac{\boldsymbol{j}_j}{W_j}$$

It must first be mentioned that his term arises due to difference in the molecular weights. This is observed from the definition of s_{im2} that for streams with the same molecular weight, this term will become 0 because $\sum_j \dfrac{\boldsymbol{j}_j}{W_j} = 0$.

Variation with M_c

Variation of s_{im2} with M_c is shown in **Fig 6.6**

It can be observed at once that though this term is always negative, its magnitude is rather small. It shows a greater negative value for greater M_cs,

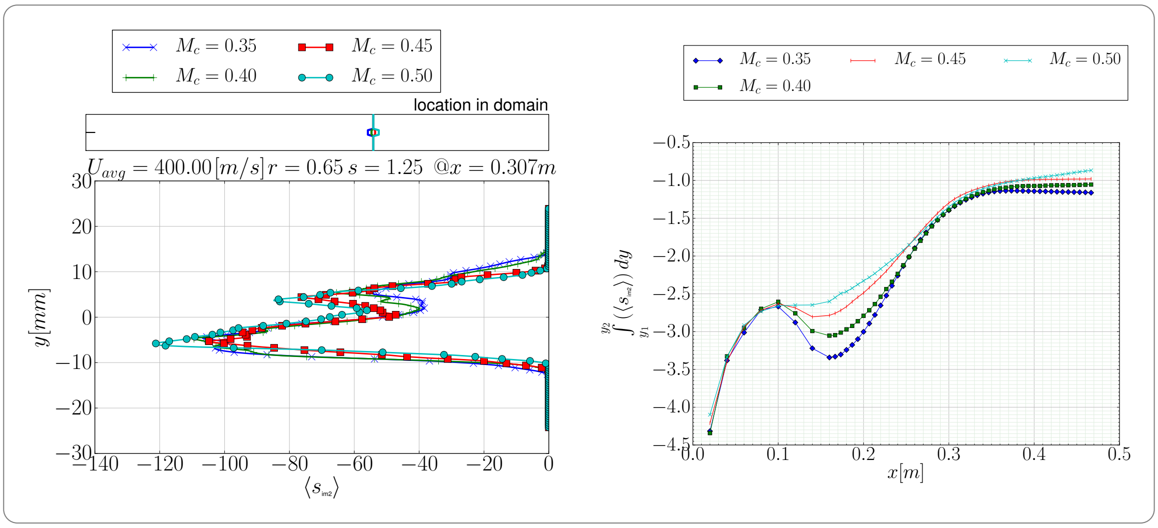

Figure 6.6: $\langle s_{\mathrm{im2}} \rangle$, time averaged plotted at a cross-wise location and cross-wise averaged values in the stream-wise direction
[*Note the always negative and the small magnitude of the values*]

but since the magnitude of this term is small, this influence is insignificant over the effect of s_{im1}

6.4.6 Shear

General Features

This corresponds to the term

$$s_\tau \equiv \frac{1}{T} \sigma : \nabla \boldsymbol{u}$$

This term corresponds to the increase in the entropy due to conversion of kinetic energy to heat (dissipation). The magnitude of this term is large where there is a large shear and is higher with lower temperatures. This term is seen to be always positive, which is expected.

Variation with M_c

The variation of s_τ with M_c is shown in **Fig 6.7**. It can be seen from **Fig 6.7** that the value of the entropy source due to shear actually increases with in-

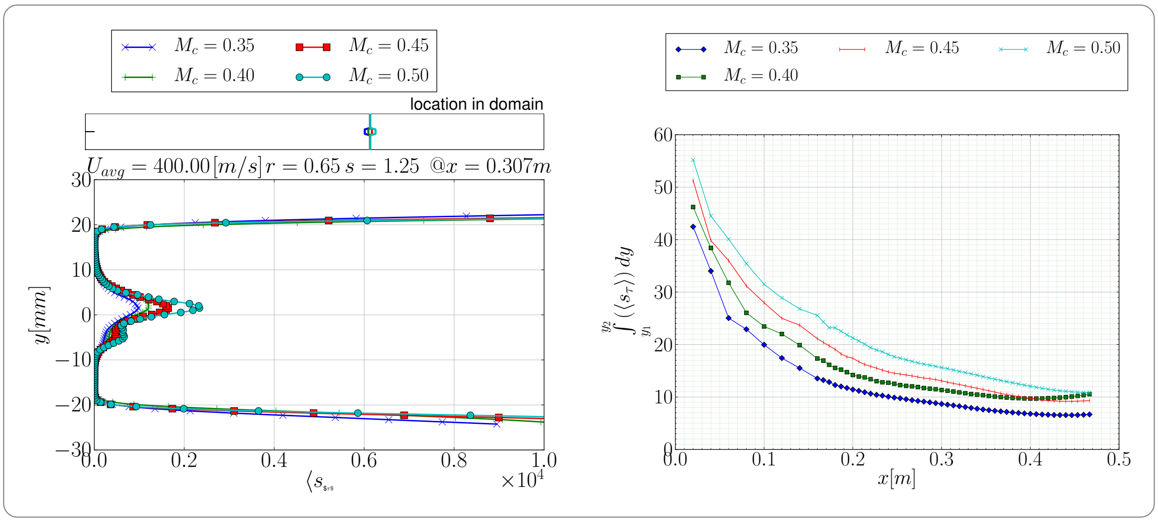

Figure 6.7: $\langle s_\tau \rangle$, time averaged plotted at a cross-wise location and cross-wise averaged values in the stream-wise direction

[*Note that this terms is always positive.*]

crease in the M_c. The basic reason for this being the large gradient of the velocity, the growth rate being small.

6.5 Total Contributions

A histogram of the (rms) contribution of entropy generation is presented in **Fig 6.8**. This shows the total contributions, and in this it is seen that there is no particular trend in the total contribution. This is primarily because if reverse trends in shear an in mixing. The opposite trends cancel out each other and on the whole no specific trend is found with increase in M_c, though individual trends are seen.

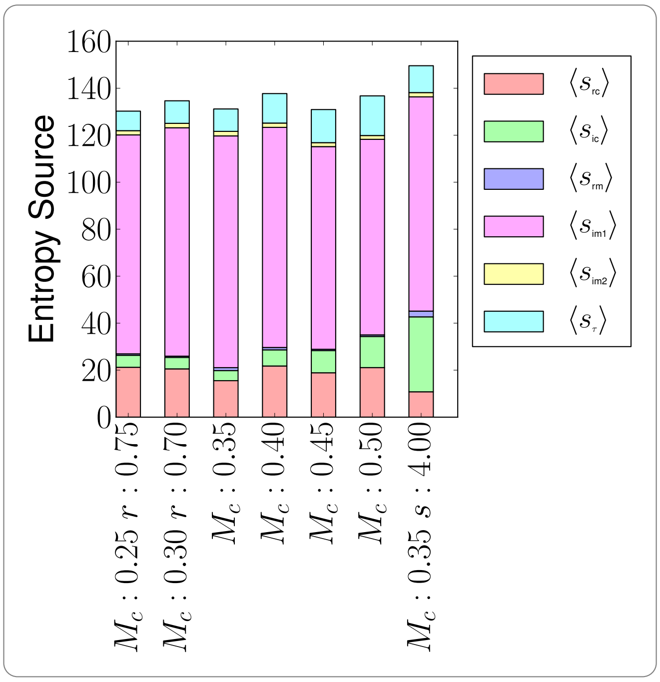

Figure 6.8: Histogram of contribution
[*The specific components show trends, however the overall contribution does not show any clear trend*]

6.6 Conclusions

The detailed study of entropy evolution is studied in this chapter. The evolution equation for entropy is developed, and following this, it was verified that the entropy obtained from the convective solution compares well with the entropy calculated from the fluid properties.

The sources of entropy generation are identified, and analysed for their relative contribution and the variation with M_c. It is seen that s_{im1} is the greatest source of entropy generation in the current set of calculations. It is also seen that the value of this term decreases with increasing M_c. The effect of shear is exactly opposite and that with increasing M_c is accompanied with an increasing entropy source. Even though the two terms cancel out nearly leaving the net effect unaltered with changes in M_c, it is perhaps one of these terms that has greater effect on the mixing layer and hence the observed effect. Quite clearly, the entropy approach in resolving the issue of convective Mach number influence on growth rate is not adequately insightful.

Chapter 7

Overview and future work

This work has been concerned with the behavior of high speed mixing layer as a function of various flow parameters. Placed between ineffective RANS strategy and a vastly time-consuming DNS, the present work has chosen to elucidate the details using LES that has reached maturity in its ability to capture the important scales of the flow. The aim has been to concentrate of the crucial initial development of the flow that emanates from the splitter plate. The boundary layers on the top and the bottom surfaces of the splitter with a wake controlled by the thickness of the splitter plate merge and the minimum velocity in the field keeps increasing as mixing proceeds. This profile with two inflection points controls the instability in the flow. Computational analysis has shown that the distances it takes for the wake region to disappear and self-similarity to appear both increase with convective Mach number. This is consistent with the view point that arises out of theoretical analysis – even of hyperbolic tangent profiles showing that the central issues lie with convective Mach number . While many details of the role of various parameters like stream speed ratio and density ratio are elucidated, what has been found important is to examine the evolution of stresses in the flow field with flow development and convective Mach number. This examination made evident the possibility of simple relationships between the stresses and strain rates, a feature that has been exploited in the development of an unsteady Reynolds averaged Navier-stokes calculation approach. Before embarking on this approach, it was thought prudent to examine why the classical RANS approaches have failed to bring out the effect of convective Mach number. It is found that the field of eddy viscosity in the momentum equation is obtained as a relation between the turbulent kinetic energy and the eddy dissipation and the equation for the kinetic energy has a property that the crucial effect of convective Mach number that occurs as a sum of two stress source terms cancel out. This is the reason why an alternate approach, albeit simpler one is what is adopted here. The eddy viscosity is known to be a simple constant through the mixing layer in incompressible mixing layer and is now modified as a function of convective Mach number, and was used only for the prediction of shear stress. It is important to point out that this is done on the basis of the results of LES simulations. This approach helped by the deduction of a relationship of eddy viscosity for shear stress with convective Mach number leads to expected results. A question that arises now will be: How will the more successful $k - \epsilon$ or $k - \omega$ approaches be integrated into a complex flow field with boundary layers and mixing layers in a high speed flow setting? This needs an approach to identify mixing layer zone and a strategy for switching from the classical methods of estimation of the turbulent shear stress to the present model in the region of mixing layer. This will preserve the dependence of mixing with the convective Mach number, as well as provide the correct k distribution. Perhaps there are other alternatives that need exploration. These constitute the future work of significance.

Part III

Appendices

Appendix A

Details of Derivations and Implementations

A.1 Implementation of the Turbulent Inlet velocity Field

The aim is to implement the generation of a simple (pseudo) random field which imitates turbulence to some extent at least. Turbulence is made of large as well as small eddies, which cause spatio-temporal correlations to be present. Also the specification is for the generation of a field with a prescribed mean ($\langle U \rangle$) and a prescribed standard deviation (σ_U).

The formulation of such a field was

$$U = (1-\alpha)U + \alpha \langle U \rangle \left(1 + \sigma \aleph \mathcal{R}_{-1}^{1}\right) \tag{A.1}$$

Where

U is the current velocity

α is the autocorrelation factor which controls the temporal correlation

$\mathcal{R}_0^1$ is a random number generator from 0 to 1

$\aleph$ is a factor to be multiplied to correct σ_U due to autocorrelation

The following figures indicate the obtained velocity distributions and energy content for various values of α

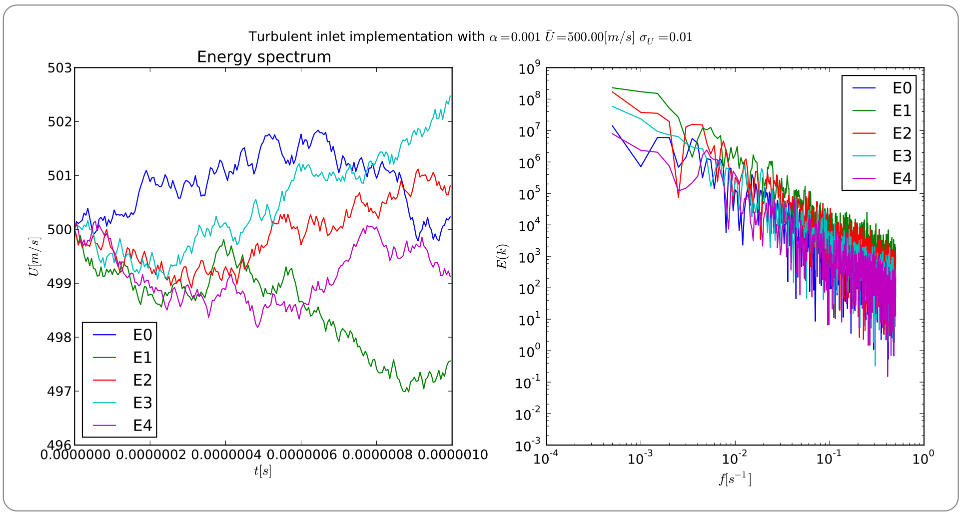

Figure A.1: Inlet for small α

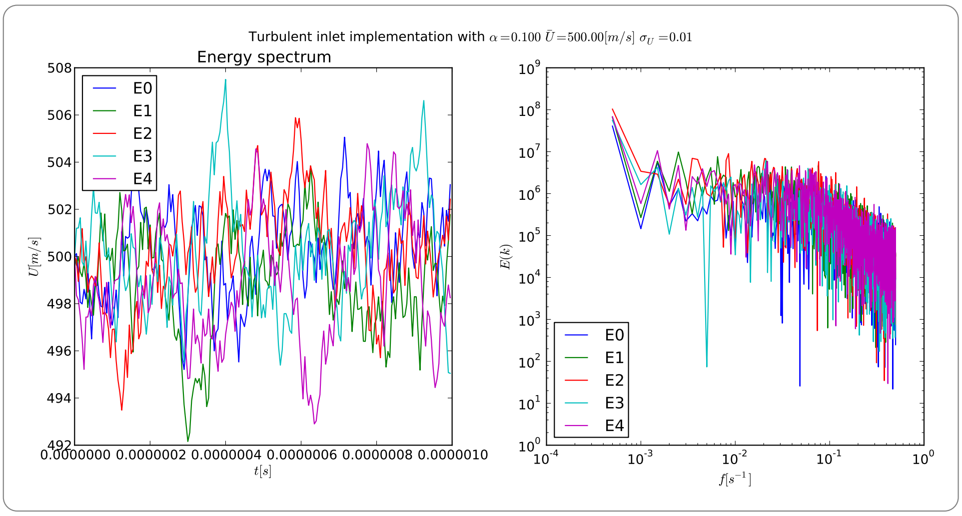

Figure A.2: Inlet for large α

We can see that the energy spectrum is reasonable, with some energy in the larger eddies and successively decreasing energy in smaller structures. It must also be noted that no spatial correlation was implemented. The turbulence in the inlet stream is small, and is only to trip and start off the instability mechanism if the mixing layer, hence not much attention is required to be given to the details of inlet turbulence structure. Referred from Section 2.4.1 on Page 60

A.2 Flow parameters to primitive parameters

We have the definitions

$$M_c \equiv \frac{U_1 - U_2}{a_1 + a_2} \tag{A.2}$$

$$U_{\text{avg}} \equiv \frac{U_1 + U_2}{2} \tag{A.3}$$

$$r \equiv \frac{U_2}{U_1} \tag{A.4}$$

$$s \equiv \frac{\rho_2}{\rho_1} \tag{A.5}$$

Using **Eqn A.4** and **Eqn A.3** we get

$$U_{\text{avg}} = U_1 \frac{(1+r)}{2} \tag{A.6}$$

hence

$$\boxed{U_1 = 2\frac{U_{\text{avg}}}{1+r}} \tag{A.7}$$

And from **Eqn A.4**

$$\boxed{U_2 = 2\frac{U_{\text{avg}} r}{1+r}} \tag{A.8}$$

Substituting the values of U_1 and U_2 into **Eqn A.2** and using $a = \sqrt{\gamma RT}$ we get

$$M_c = \frac{U_{\text{avg}} \frac{1-r}{1+r}}{\sqrt{\gamma RT_1} + \sqrt{\gamma RT_2}} \tag{A.9}$$

Noting that both streams are at the same pressure and for the same gas the ideal gas equation yields

$$s = \frac{\rho_2}{\rho_1} = \frac{T_1}{T_2} \tag{A.10}$$

the denominator of **Eqn A.9** becomes

$$\sqrt{\gamma RT_1} + \sqrt{\gamma RT_2} = \sqrt{\gamma RT_2}\left(s^{1/2} + 1\right) \tag{A.11}$$

Thus

$$\sqrt{T_2} = \frac{U_{\text{avg}}}{M_c\sqrt{\gamma R}\,(s^{1/2}+1)}\left(\frac{1-r}{1+r}\right) \tag{A.12}$$

Squaring both sides we get the relation for T_2 as

$$\boxed{T_2 = \frac{1}{\gamma R}\left(\frac{U_{\text{avg}}}{M_c\,(s^{1/2}+1)}\left(\frac{1-r}{1+r}\right)\right)^2} \tag{A.13}$$

And finally using **Eqn A.10**

$$\boxed{T_1 = \frac{s}{\gamma R}\left(\frac{U_{\text{avg}}}{M_c\,(s^{1/2}+1)}\left(\frac{1-r}{1+r}\right)\right)^2} \tag{A.14}$$

Referred from Section 2.9 on Page 78

A.3 Turbulent Kinetic Energy Balance

This section follows Canuto [1997] initially, but deviates from it as mentioned later. To get the turbulent kinetic energy we shall track the mean flow energy defined as

$$E \equiv \frac{\langle \rho \rangle}{2} \{U_i\} \{U_i\} \tag{A.15}$$

And the turbulent kinetic energy defined as

$$k \equiv \frac{\langle \rho \rangle}{2} \{u_i'' u_i''\} \tag{A.16}$$

A.3.1 Mean Flow Kinetic Energy

To arrive at the mean flow kinetic energy evolution equation we average **Eqn 2.3** to get

$$\frac{\partial \langle \rho U_i \rangle}{\partial t} + \frac{\partial \langle \rho U_i U_l \rangle}{\partial x_l} = -\frac{\partial \langle p \rangle}{\partial x_i} + \frac{\partial \sigma_{il}}{\partial x_l} \tag{A.17}$$

Expanding the convective term and using the definition of Favre averaging (**Eqn 2.32**) we get

$$\frac{\partial \langle \rho \rangle \{U_i\}}{\partial t} + \frac{\partial \langle \rho \rangle \{U_i\} \{U_l\}}{\partial x_l} + \frac{\partial \langle \rho \rangle \{U_i'' U_l''\}}{\partial x_l} = -\frac{\partial \langle p \rangle}{\partial x_i} + \frac{\partial \langle \sigma_{il} \rangle}{\partial x_l} \tag{A.18}$$

We use the following notation

$$\tau_{ij} = \langle \rho \rangle \{U_i'' U_j''\} \tag{A.19}$$

With this the averaged momentum equation becomes

$$\frac{\partial \langle \rho \rangle \{U_i\}}{\partial t} + \frac{\partial \langle \rho \rangle \{U_i\} \{U_l\}}{\partial x_l} = -\frac{\partial \langle p \rangle}{\partial x_i} + \frac{\partial}{\partial x_l} \left(\langle \sigma_{il} \rangle - \tau_{il} \right) \tag{A.20}$$

To arrive at the mean flow energy equation we multiply **Eqn A.20** with $\{U_j\}$ and add it with $\{U_i\} \times$ (**Eqn A.20**) with index i swapped with j) Thus we have

$$
\begin{aligned}
\{U_j\}\frac{\partial\langle\rho\rangle\{U_i\}}{\partial t}+\{U_j\}\frac{\partial\langle\rho\rangle\{U_i\}\{U_l\}}{\partial x_l} &= -\{U_j\}\frac{\partial\langle p\rangle}{\partial x_i}+\{U_j\}\frac{\partial}{\partial x_l}\left(\langle\sigma_{il}\rangle-\tau_{il}\right)\\
&+ \qquad\qquad\qquad\qquad\qquad\qquad\qquad\qquad\qquad \text{(A.21)}\\
\{U_i\}\frac{\partial\langle\rho\rangle\{U_j\}}{\partial t}+\{U_i\}\frac{\partial\langle\rho\rangle\{U_j\}\{U_l\}}{\partial x_l} &= -\{U_i\}\frac{\partial\langle p\rangle}{\partial x_j}+\{U_i\}\frac{\partial}{\partial x_l}\left(\langle\sigma_{jl}\rangle-\tau_{jl}\right)
\end{aligned}
$$

Expanding the terms we get

$$
\begin{aligned}
\cancelto{a}{\{U_j\}\{U_i\}\frac{\partial\langle\rho\rangle}{\partial t}} &+ \{U_j\}\langle\rho\rangle\frac{\partial\{U_i\}}{\partial t}+\cancelto{a}{\{U_j\}\{U_i\}\frac{\partial\langle\rho\rangle\{U_l\}}{\partial x_l}}+\{U_j\}\{U_l\}\langle\rho\rangle\frac{\partial\{U_i\}}{\partial x_l} \qquad \text{(A.22)}\\
&= -\{U_j\}\frac{\partial\langle p\rangle}{\partial x_i}+\{U_j\}\frac{\partial}{\partial x_l}\left(\langle\sigma_{il}\rangle-\tau_{il}\right)\\
&+ \qquad\qquad\qquad\qquad\qquad\qquad\qquad\qquad\qquad \text{(A.23)}\\
\cancelto{b}{\{U_i\}\{U_j\}\frac{\partial\langle\rho\rangle}{\partial t}} &+ \{U_i\}\langle\rho\rangle\frac{\partial\{U_j\}}{\partial t}+\cancelto{b}{\{U_i\}\{U_j\}\frac{\partial\langle\rho\rangle\{U_l\}}{\partial x_l}}+\{U_i\}\{U_l\}\langle\rho\rangle\frac{\partial\{U_j\}}{\partial x_l} \qquad \text{(A.24)}\\
&= -\{U_i\}\frac{\partial\langle p\rangle}{\partial x_j}+\{U_i\}\frac{\partial}{\partial x_l}\left(\langle\sigma_{il}\rangle-\tau_{il}\right)
\end{aligned}
$$

Where (a) and (b) terms become zero on account of the averaged mass conservation equation.

Finally performing the addition we get

$$
\langle\rho\rangle\frac{\partial\{U_i\}\{U_j\}}{\partial t}+\langle\rho\rangle\langle U_l\rangle\frac{\partial\{U_i\}\{U_j\}}{\partial x_l}=\{U_i\}\left(-\langle p_{,j}\rangle+\sigma_{jl,l}-\tau_{jl,l}\right)+\{U_j\}\left(-\langle p_{,i}\rangle+\sigma_{il,l}-\tau_{il,l}\right) \tag{A.25}
$$

To seggregate the terms, and referring to the operator

$$
\frac{\partial}{\partial t}+\langle U_l\rangle\frac{\partial}{\partial x_l}\equiv\frac{\langle D\rangle}{\langle D\rangle t} \tag{A.26}
$$

we get

$$
\langle\rho\rangle\frac{\langle D\rangle}{\langle D\rangle t}\{U_i\}\{U_j\}=-\{U_i\}\tau_{jl,l}-\{U_j\}\tau_{il,l}+\langle F_i\rangle\{U_j\}+\langle F_j\rangle\{U_i\} \tag{A.27}
$$

Where

$$F_i \equiv -\frac{\partial p}{\partial x_i} + \frac{\partial \sigma_{il}}{\partial x_l} \tag{A.28}$$

A.3.2 Turbulent Kinetic Energy equation

For the turbulent Kinetic energy equation we multiply the compressible momentum equation (**Eqn 2.3**) with u_j, and addding with (**Eqn 2.3** with index i swapped with index j) multiplied with U_i

$$\begin{aligned} U_j\frac{\partial \rho U_i}{\partial t} + U_j\frac{\partial \rho U_i U_l}{\partial x_l} &= -U_j\frac{\partial p}{\partial x_i} + U_j\frac{\partial \sigma_{il}}{\partial x_l} \\ &+ \\ U_i\frac{\partial \rho U_j}{\partial t} + U_i\frac{\partial \rho U_j U_l}{\partial x_l} &= -U_i\frac{\partial p}{\partial x_j} + U_i\frac{\partial \sigma_{jl}}{\partial x_l} \end{aligned} \tag{A.29}$$

Simplifying the terms, we get

$$\begin{aligned} &U_j\rho\frac{\partial U_i}{\partial t} + \cancelto{a}{U_jU_i\frac{\partial \rho}{\partial t}} + \cancelto{a}{U_jU_i\frac{\partial \rho U_l}{\partial x_l}} + \rho U_l U_j\frac{\partial U_i}{\partial x_l} + U_i\rho\frac{\partial U_j}{\partial t} + U_iU_j\frac{\partial \rho}{\partial t} + U_i\frac{\partial \rho U_j U_l}{\partial x_l} \\ &= U_j\left(-\frac{\partial p}{\partial x_i} + \frac{\partial \sigma_{il}}{\partial x_l}\right) + U_i\left(-\frac{\partial p}{\partial x_j} + \frac{\partial \sigma_{jl}}{\partial x_l}\right) \end{aligned} \tag{A.30}$$

Where the terms indicated as (a) reduce to zero on account of the continuity equation

Using the definition of F as in **Eqn A.28**, and by simplifying the terms we get

$$\frac{\partial \rho U_i U_j}{\partial t} + \frac{\partial \rho U_i U_j U_l}{\partial x_l} = U_i F_j + F_i U_j \tag{A.31}$$

Before averaging this equation we enlist a few properties of averaging

$$\langle \rho U_i U_j \rangle = \langle \rho \rangle \{U_i\} \{U_j\} + \underbrace{\langle \rho \rangle \overbrace{\{u_i'' u_j''\}}^{R_{ij}}}_{\tau_{ij}} \tag{A.32}$$

And we define the triple correlation term τ_{ijk} as

$$\tau_{ijk} \equiv \langle \rho \rangle \{u_i'' u_j'' u_k''\} \tag{A.33}$$

Using this definition we have the triple velocity correlation as

$$\langle\rho U_i U_j U_k\rangle = \langle\rho\rangle\{U_i\}\{U_j\}\{U_k\} + \tau_{ij}\{U_k\} + \tau_{jk}\{U_i\} + \tau_{ki}\{U_i\} + \tau_{ijk} \tag{A.34}$$

With these definitions, we average the LHS of **Eqn A.31** as

$$\begin{aligned}
\langle \textbf{Eqn A.31}\rangle_{LHS} &= \frac{\partial\langle\rho U_iU_j\rangle}{\partial t} + \frac{\partial\langle\rho U_iU_jU_l\rangle}{\partial U_l} \\
&= \frac{\partial\langle\rho\rangle\{U_i\}\{U_j\}}{\partial t} + \frac{\partial\tau_{ij}}{\partial t} + \frac{\partial}{\partial x_l}\left(\langle\rho\rangle\{U_i\}\{U_j\}\{U_l\} + \tau_{ij}\{U_l\} + \tau_{jl}\{U_i\} + \tau_{li}\{U_j\} + \tau_{ijl}\right) \\
&= \underbrace{\langle\rho\rangle\frac{\partial\{U_i\}\{U_j\}}{\partial t}}_{b} + \cancelto{a}{\{U_i\}\{U_j\}\frac{\partial\langle\rho\rangle}{\partial t}} + \underbrace{\frac{\partial\tau_{ij}}{\partial t}}_{c} + \cancelto{a}{\{U_i\}\{U_j\}\frac{\partial\langle\rho\rangle\{U_l\}}{\partial x_l}} + \underbrace{\langle\rho\rangle\{U_l\}\frac{\partial\{U_i\}\{U_j\}}{\partial x_l}}_{b} \\
&+ \underbrace{\{U_l\}\frac{\partial\tau_{ij}}{\partial x_l}}_{c} + \tau_{ij}\frac{\partial\{U_l\}}{\partial x_l} + \{U_i\}\frac{\partial\tau_{jl}}{\partial x_l} + \tau_{jl}\frac{\partial\{U_i\}}{\partial x_l} + \{U_j\}\frac{\partial\tau_{il}}{\partial x_l} + \tau_{il}\frac{\partial\{U_j\}}{\partial x_l} + \frac{\partial\tau_{ijl}}{\partial x_l}
\end{aligned} \tag{A.35}$$

In the above equations (a) reduces to zero on account of the continuity equation. while $(b) = \langle\rho\rangle\dfrac{\langle D\rangle}{\langle D\rangle t}\{U_i\}\{U_j\}$ whose value is got from **Eqn A.27**, and (c) is $\dfrac{\langle D\rangle\tau_{ij}}{\langle D\rangle t}$ Thus substituting the above and using **Eqn A.27** we get

$$\begin{aligned}
\langle \textbf{Eqn A.31}_{LHS}\rangle \;=\; & \frac{\langle D\rangle\tau_{ij}}{\langle D\rangle t} - \cancelto{a}{\{U_i\}\tau_{jl,l}} - \cancelto{b}{\{U_j\}\tau_{il,l}} + \langle F_i\rangle\{U_j\} + F_j\{U_i\} + \tau_{ij}\{U_{l,l}\} + \cancelto{a}{\{U_i\}\tau_{jl,l}} \\
& + \tau_{jl}\{U_{i,l}\} + \cancelto{b}{\{U_j\}\tau_{il,l}} + \tau_{il}\{U_{j,l}\} + \tau_{ijl,l}
\end{aligned} \tag{A.36}$$

Thus the LHS of **Eqn A.31**, averaged,reduces to

$$\frac{\langle D\rangle\tau_{ij}}{\langle D\rangle t} + \tau_{ij}\{U_{l,l}\} + \tau_{jl}\{U_{i,l}\} + \tau_{il}\{U_{j,l}\} + \langle F_i\rangle\{U_j\} + \langle F_j\rangle\{U_i\} + \tau_{ijl,l} \tag{A.37}$$

Thus we have **Eqn A.31**, averaged

$$\frac{\langle D\rangle\tau_{ij}}{\langle D\rangle t} + \tau_{ij}\{U_{l,l}\} + \tau_{jl}\{U_{i,l}\} + \tau_{il}\{U_{j,l}\} + \langle F_i\rangle\{U_j\} + \langle F_j\rangle\{U_i\} + \tau_{ijl,l} = \langle F_iU_j\rangle + \langle F_jU_i\rangle \tag{A.38}$$

The similar terms are seggregated as

$$\frac{\langle D\rangle\,\tau_{ij}}{\langle D\rangle\,t}+\tau_{ijl,l}=P_{ij}+\langle F_iU_j\rangle-\langle F_i\rangle\{U_j\}+\langle F_jU_i\rangle-\langle F_j\rangle\{U_i\} \tag{A.39}$$

Where

$$-P_{ij}\equiv\tau_{ij}\{U_{l,l}\}+\tau_{jl}\{U_{i,l}\}+\tau_{il}\{U_{j,l}\} \tag{A.40}$$

We can further simplify the RHS of the above equation by noting that

$$\langle F_iU_j\rangle=\langle F_i\left(\{U_j\}+u_j''\right)\rangle=\langle F_i\rangle\{U_j\}+\langle F_i u_j''\rangle \tag{A.41}$$

Thus we have

$$\langle F_iU_j\rangle-\langle F_i\rangle\{U_j\}=\langle F_i u_j''\rangle=\langle\left(-p_{,i}+\sigma_{il,l}\right)u_j''\rangle=-\langle p_{,i}\rangle\langle u_j''\rangle-\langle p_{,i}' u_j''\rangle+\langle\sigma_{il,l}u_j''\rangle \tag{A.42}$$

Substituting back we get

$$\frac{\langle D\rangle\,\tau_{ij}}{\langle D\rangle\,t}+\tau_{ijl,l}=\left(\begin{array}{l} P_{ij}\underbrace{-\left(\langle p_{,j}\rangle\langle u_i''\rangle+\langle p_{,i}\rangle\langle u_j''\rangle\right)}_{B_{ij}} \\ -\underbrace{\left(\langle p_{,j}'u_i''\rangle+\langle p_{,i}'u_j''\rangle\right)}_{\Pi_{ij}}+\underbrace{\left(\langle\sigma_{jl,l}u_i''\rangle+\langle\sigma_{il,l}u_j''\rangle\right)}_{X_{ij}}\end{array}\right) \tag{A.43}$$

We can note that we can also write Π_{ij} as

$$\langle p_{,j}'u_i''\rangle+\langle p_{,i}'u_j''\rangle=\langle p_{,j}'u_i'\rangle+\langle p_{,i}'u_j'\rangle \tag{A.44}$$

We further need to separate the diffusive and the dissipative terms in X_{ij} as

$$\sigma_{jl,l}u_i''=u_i''\frac{\partial\sigma_{jl}}{\partial x_l}=\frac{\partial u_i''\sigma_{jl}}{\partial x_l}-\sigma_{jl}\frac{\partial u_i''}{\partial x_l}=\underbrace{\left(u_i''\sigma_{jl}\right)_{,l}}_{\text{Diffusive}}\underbrace{-\sigma_{jl}u_{i,l}''}_{\text{Dissipative}} \tag{A.45}$$

And similarly

$$\sigma_{il,l}u_j''=\underbrace{\left(u_j''\sigma_{il}\right)_{,l}}_{\text{Diffusive}}\underbrace{-\sigma_{il}u_{j,l}''}_{\text{Dissipative}} \tag{A.46}$$

Thus $\mathcal{X}$ splits as

$$X_{ij} = \underbrace{\left(\langle u_i{''}\sigma_{jl}\rangle + \langle u_j{''}\sigma_{il}\rangle\right)_{,l}}_{X_{ij}^{\mathrm{Diff}}} \underbrace{-\left(\langle u_{i,l}{''}\sigma_{jl}\rangle + \langle u_{j,l}{''}\sigma_{il}\rangle\right)}_{X_{ij}^{\mathrm{Diss}}} \tag{A.47}$$

Thus the energy budget can be written as

$$\frac{\langle D\rangle\, \tau_{ij}}{\langle D\rangle\, t} + \tau_{ijl,l} - X_{ij}^{\mathrm{Diff}} = P_{ij} + B_{ij} - \Pi_{ij} + X_{ij}^{\mathrm{Diss}} \tag{A.48}$$

We now decompose τ as $\tau_{ij} = \langle\rho\rangle \{u_i{''}u_j{''}\}$ to get

$$\frac{\langle D\rangle\, \tau_{ij}}{\langle D\rangle\, t} = \frac{\partial \tau_{ij}}{\partial t} + \{U_l\}\frac{\partial \tau_{ij}}{\partial x_l} = \frac{\partial \langle\rho\rangle R_{ij}}{\partial t} + \{U_l\}\frac{\partial \langle\rho\rangle R_{ij}}{\partial x_l} \tag{A.49}$$

This can be expanded as

$$\langle\rho\rangle \frac{\partial R_{ij}}{\partial t} + R_{ij}\frac{\partial \langle\rho\rangle}{\partial t} + \{U_l\}\langle\rho\rangle\frac{\partial R_{ij}}{\partial x_l} + \{U_l\} R_{ij}\frac{\partial \langle\rho\rangle}{\partial x_l} \tag{A.50}$$

The last term of which can be expanded as

$$\underbrace{\langle\rho\rangle \frac{\partial R_{ij}}{\partial t}}_{b} + \underbrace{\cancelto{0}{R_{ij}\frac{\partial \langle\rho\rangle}{\partial t}}}_{a} + \underbrace{\{U_l\}\langle\rho\rangle\frac{\partial R_{ij}}{\partial x_l}}_{b} + \underbrace{\cancelto{0}{R_{ij}\frac{\partial \{U_l\}\langle\rho\rangle}{\partial x_l}}}_{a} \underbrace{- R_{ij}\langle\rho\rangle\frac{\partial \{U_l\}}{\partial x_l}}_{c} \tag{A.51}$$

In the above expression (a) reduces to zero on account of mass conservation, (b) is $\langle\rho\rangle \frac{\langle D\rangle R_{ij}}{\langle D\rangle t}$ and $(c = \tau_{ij}\{U_{l,l}\})$ is taken on the RHS and added to P_{ij} where

$$\Sigma_{ij} \equiv P_{ij} + \tau_{ij}\{U_{l,l}\} = \cancel{-\tau_{ij}\{U_{l,l}\}} - \tau_{jl}\{U_{i,l}\} - \tau_{il}\{U_{j,l}\} + \cancel{\tau_{ij}\{U_{l,l}\}} = -\tau_{jl}\{U_{i,l}\} - \tau_{il}\{U_{j,l}\} \tag{A.52}$$

Thus

$$\langle\rho\rangle \left\{\frac{\langle D\rangle R_{ij}}{\langle D\rangle\, t} + D_{ij}\right\} = \Sigma_{ij} + B_{ij} - \Pi_{ij} + X_{ij}^{\mathrm{Diss}} \tag{A.53}$$

Finally decomposing Π_{ij} as

$$\Pi_{ij} = \underbrace{\Pi_{ij} - \frac{1}{3}\delta ij \Pi_{kk}}_{\pi_{ij}} + \frac{1}{3}\delta_{ij}\Pi_{kk} \tag{A.54}$$

The last term can be written as

$$\frac{1}{3}\delta ij \Pi_{kk} = \frac{1}{3}\delta_{ij}\left(\langle u_k{}'' p_{,k}{}' \rangle + \langle p_{,k}{}' u_k{}'' \rangle\right) = \frac{2}{3}\delta_{ij}\langle p_{,k}{}' u_k{}'' \rangle = \frac{2}{3}\delta_{ij}\langle p' u_k{}'' \rangle_{,k} - \frac{2}{3}\delta_{ij}\langle p' u_{k,k}{}'' \rangle \tag{A.55}$$

Substituting these, and absorbing the first term on the RHS into D_{ij} the energy budget can be written as

$$\boxed{\langle \rho \rangle \left\{ \frac{\langle D \rangle R_{ij}}{\langle D \rangle t} + D_{ij} \right\} = \Sigma_{ij} + B_{ij} - \pi_{ij} + X_{ij}^{\text{Diss}} + \frac{2}{3}\delta_{ij}\langle p' u_{k,k}{}'' \rangle} \tag{A.56}$$

where we have, to summarize

$$\begin{aligned}
\frac{\langle D \rangle}{\langle D \rangle t} &\equiv \frac{\partial}{\partial t} + \{U_l\}\frac{\partial}{\partial x_l} && \text{(A.57)}\\
R_{ij} &= \{u_i{}'' u_j{}''\} && \text{(A.58)}\\
D_{ij} &= \frac{1}{\langle \rho \rangle}\frac{\partial}{\partial x_l}\left(\tau_{ijk} + \frac{2}{3}\delta_{ij}\langle p' u_l{}'' \rangle - X_{ij}^{\text{Diff}}\right) && \text{(A.59)}\\
\tau_{ijk} &= \langle \rho \rangle \{u_i{}'' u_j{}'' u_k{}''\} && \text{(A.60)}\\
X_{ij}^{\text{Diff}} &= \left(\langle u_i{}'' \sigma_{jl} \rangle + \langle u_j{}'' \sigma_{il} \rangle\right) && \text{(A.61)}\\
\Sigma_{ij} &= -\tau_{jl}\{U_{i,l}\} - \tau_{il}\{U_{j,l}\} && \text{(A.62)}\\
B_{ij} &= -\left(\langle p_{,j} \rangle \langle u_i{}'' \rangle + \langle p_{,i} \rangle \langle u_j{}'' \rangle\right) && \text{(A.63)}\\
\pi_{ij} &= \Pi_{ij} - \frac{1}{3}\delta_{ij}\Pi_{ll} && \text{(A.64)}\\
\Pi_{ij} &= \langle p_{,j}{}' u_i{}'' \rangle + \langle p_{,i}{}' u_j{}'' \rangle && \text{(A.65)}\\
X_{ij}^{\text{Diss}} &= -\left(\langle u_{i,l}{}'' \sigma_{jl} \rangle + \langle u_{j,l}{}'' \sigma_{il} \rangle\right) && \text{(A.66)}\\
& && \text{(A.67)}
\end{aligned}$$

Referred from Section 4.2 on Page 127

A.4 Integral Analysis

The growth rate at any given stream-wise direction is directly related to the profiles of the velocity and the density at that location and the mean shear stress. This derivation is similar to that of the Karman Integral equation for a boundary layer, but taking into consideration a possible pressure gradient and variation in the density.

The continuity equation in two dimensions is given by

$$\frac{\partial \rho}{\partial t} + \frac{\partial \rho u}{\partial x} + \frac{\partial \rho v}{\partial y} = 0 \tag{A.68}$$

Time averaging this equation, we get

$$\frac{\partial \langle \rho \rangle \{u\}}{\partial x} + \frac{\partial \langle \rho \rangle \{v\}}{\partial y} = 0 \tag{A.69}$$

A.4.1 Momentum Equation

The Momentum equation in tensor notation is

$$\frac{\partial \rho u_i}{\partial t} + \frac{\partial \rho u_i u_j}{\partial x_j} = -\frac{\partial p}{\partial x_i} + \frac{\partial \tau_{ij}}{\partial x_j} \tag{A.70}$$

Where

$$\tau_{ij} = 2\mu \left(e_{ij} - \frac{1}{3}\frac{\partial u_k}{\partial x_k}\delta_{ij} \right); e_{ij} = \frac{1}{2}\left(\frac{\partial u_i}{\partial x_j} + \frac{\partial u_j}{\partial x_i} \right)$$

Time averaging this, we get

$$\frac{\partial \langle \rho \rangle \{u_i u_j\}}{\partial x_j} = -\frac{\partial \langle p \rangle}{\partial x_i} + \frac{\partial \langle \tau_{ij} \rangle}{\partial x_j} \tag{A.71}$$

We can decompose $\{u_i u_j\}$ as

$$\{u_i u_j\} = \{u_i\}\{u_j\} + \{u_i'' u_j''\} \tag{A.72}$$

Thus the momentum equation becomes

$$\frac{\partial \langle\rho\rangle \{u_i\} \{u_j\}}{\partial x_j} = -\frac{\partial \langle p\rangle}{\partial x_i} + \frac{\partial \langle\tau_{ij}\rangle - \langle\rho\rangle \{u_i'' u_j''\}}{\partial x_j} \tag{A.73}$$

In particular the x momentum equation is

$$\frac{\partial \langle\rho\rangle \{u\} \{u\}}{\partial x} + \frac{\partial \langle\rho\rangle \{u\} \{v\}}{\partial y} = -\frac{\partial \langle p\rangle}{\partial x} + \frac{\partial \langle\tau_{xx}\rangle - \langle\rho\rangle \{u'' u''\}}{\partial x} + \frac{\partial \langle\tau_{xy}\rangle - \langle\rho\rangle \{u'' v''\}}{\partial y} \tag{A.74}$$

A.4.2 Self Similarity

We shall assume that the solutions are self similar, that is, in the coordinate frame of η defined as

$$\eta \equiv \frac{y - y_0}{\delta(x)} \tag{A.75}$$

the cross wise average profiles non dimensionalized with suitable reference values at any stream wise location fall on a single curve. That is to say that the only independent variable is η. Hence we can convert the equations in terms of η noting that

$$\frac{\partial}{\partial x} = \frac{\partial}{\partial \eta}\frac{d\eta}{dx} = -\frac{1}{\delta}\left(y_0' + \eta\delta'\right)\frac{d}{d\eta} \tag{A.76}$$

[1] Similarly

$$\frac{\partial}{\partial y} = \frac{\partial}{\partial \eta}\frac{d\eta}{dx} = \frac{1}{\delta}\frac{d}{d\eta} \tag{A.77}$$

The reference velocity scale is the primary stream velocity U_1 and the density scale is the primary stream density ρ_1. Thus we have the definitions

$$\underline{\{u\}}(x,y) \equiv \frac{\{u\}(x,y)}{U_1} \quad \text{and because of self similarity} \underline{\{u\}}(x,y) = g(\eta) \tag{A.78}$$

[1] Note that throughout this derivation $'$ represents a derivative with respect to the argument of the function.

Similarly for density, we have

$$\underline{\langle \rho \rangle}(x,y) \equiv \frac{\langle \rho \rangle (x,y)}{\rho_1} \quad \text{because of self similarity} \quad \underline{\langle \rho \rangle}(x,y) = f(\eta) \tag{A.79}$$

And finally for v

$$\underline{\{v\}}(x,y) \equiv \frac{\{v\}(x,y)}{U_1} \quad \text{and because of self similarity} \quad \underline{\{v\}}(x,y) = h(\eta) \tag{A.80}$$

A.4.3 Continuity equation

Using this with the time averaged continuity equation we get

$$-\frac{1}{\delta}\left(y_0' + \eta \delta'\right) \frac{d}{d\eta}(fg) + \frac{1}{\delta}\frac{d}{d\eta}(fh) = 0 \tag{A.81}$$

Simplifying gives

$$(fh)' = \left(y_0' + \eta \delta'\right)(fg)' \tag{A.82}$$

We define

$$A \equiv A(\eta, x) \equiv \left(y_0' + \eta \delta'\right) \text{ and } A' \equiv \frac{dA}{d\eta} = \delta' \tag{A.83}$$

Thus the continuity equation, time averaged and non dimentionalized is

$$\boxed{(fh)' = A\,(fg)'} \tag{A.84}$$

A.4.4 Momentum equation

Time averaged momentum equation when non dimentionalized gives

$$-A(fgg)' + (fgh)' = A\underline{\langle p \rangle}' - A\frac{\left(\underline{\langle \tau_{xx} \rangle} - \langle \rho \rangle \{u''u''\}\right)'}{\rho_1 U_1^2} + \frac{\left(\underline{\langle \tau_{xy} \rangle} - \langle \rho \rangle \{u''v''\}\right)'}{\rho_1 U_1^2} \tag{A.85}$$

Defining

$$\frac{\left(\underline{\langle \tau_{xx} \rangle} - \langle \rho \rangle \{u''u''\}\right)}{\rho_1 U_1^2} \equiv T_{xx} \tag{A.86}$$

And

$$\frac{\left(\underline{\langle\tau_{xy}\rangle} - \langle\rho\rangle\left\{u''v''\right\}\right)}{\rho_1 U_1^2} \equiv T_{xy} \tag{A.87}$$

Thus the momentum equation reduces to

$$\boxed{-A(fgg)' + (fgh)' = A\underline{\langle p\rangle}' - AT'_{xx} + Txy'} \tag{A.88}$$

A.4.5 Integrating the equations

Continuity Equation

Integrating the continuity equation from $\eta = -\infty$ to $\eta = 0$ we get

$$\int_{-\infty}^{0} (fh)' d\eta = \int_{-\infty}^{0} A(fg)' d\eta \tag{A.89}$$

Which yields

$$\left[(fh)\right]\Big|_{-\infty}^{0} = \int_{-\infty}^{0} A(fg - sr)' d\eta \tag{A.90}$$

$$f_0 h_0 - sh_2 = \left[A(fg - sr)\right]\Big|_{-\infty}^{0} - \int_{-\infty}^{0} (fg - sr) A' d\eta \tag{A.91}$$

$$= y'_0(f_0 g_0 - sr) - \delta' \int_{-\infty}^{0} (fg - sr) d\eta \tag{A.92}$$

Thus

$$\boxed{sh_2 = f_0 h_0 + \delta' \int_{-\infty}^{0} (fg - sr) d\eta - y'_0(f_0 g_0 - sr)} \tag{A.93}$$

Integrating from $\eta = 0$ to $\eta = \infty$ we get

$$\int_0^\infty (fh)' d\eta = \int_0^\infty A(fg)' d\eta \tag{A.94}$$

Which yields

$$[(fh)]\Big|_0^\infty = \int_0^\infty A(fg-1)' d\eta \tag{A.95}$$

$$h_1 - f_0 h_0 = [A(fg-1)]\Big|_0^\infty - \int_0^\infty (fg-1)A' d\eta \tag{A.96}$$

$$= -y_0'(f_0 g_0 - 1) - \delta' \int_0^\infty (fg-1) d\eta \tag{A.97}$$

Thus

$$\boxed{h_1 = f_0 h_0 - \delta' \int_0^\infty (fg-1) d\eta - y_0'(f_0 g_0 - 1)} \tag{A.98}$$

Momentum equation

Integrating the momentum equation $\eta = -\infty$ to $\eta = 0$ we get

$$-\int_{-\infty}^0 A(fgg - srr)' d\eta + \int_{-\infty}^0 (fgh)' d\eta = \int_{-\infty}^0 A\left(\underline{\langle p\rangle} - p_\infty\right)' d\eta - \int_{-\infty}^0 AT'_{xx} d\eta + \int_{-\infty}^0 T'_{xy} d\eta \tag{A.99}$$

$$\begin{aligned} &-[A(fgg-srr)]\Big|_{-\infty}^0 & & \left[A\left(\langle\underline{p}\rangle - p_\infty\right)\right]\Big|_{-\infty}^0 - \int_{-\infty}^0 A'\left(\langle\underline{p}\rangle - p_\infty\right) d\eta \\ \therefore\ &+\int_{-\infty}^0 A'(fgg-srr) d\eta &=\ & \\ &+f_0 g_0 h_0 - s r h_2 & & -[AT_{xx}]\Big|_{-\infty}^0 + \int_{-\infty}^0 A' T_{xx} d\eta + [T_{xy}]\Big|_{-\infty}^0 \end{aligned} \tag{A.100}$$

(A.101)

Substituting the limits and noting that $A' = \delta'$, and substituting for sh_2 we get the LHS of the above equation as

$$-y_0'\left(f_0g_0g_0 - srr\right) + \delta' \int\limits_{-\infty}^{0} \left(fgg - srr\right) d\eta + f_0g_0h_0 - r\left(f_0h_0 + \delta' \int\limits_{-\infty}^{0} (fg - sr)d\eta - y_0'(f_0g_0 - sr)\right) \tag{A.102}$$

Which is

$$y_0'f_0g_0\left(r - g_0\right) + \delta' \int\limits_{-\infty}^{0} fg(g-r)d\eta + f_0h_0(g_0 - r) \tag{A.103}$$

And finally the LHS becomes

$$f_0\left(r - g_0\right)\left(y_0'g_0 - h_0\right) + \delta' \int\limits_{-\infty}^{0} fg(g-r)d\eta \tag{A.104}$$

The RHS of the momentum equation evaluates to

$$y_0'\left(\underline{\langle p_0\rangle} - p_\infty\right) - \delta' \int\limits_{-\infty}^{0} \left(\underline{\langle p_0\rangle} - p_\infty\right) d\eta - y_0'T_{xx0} + \delta' \int\limits_{-\infty}^{0} T_{xx}d\eta + T_{xy0} \tag{A.105}$$

Thus

$$\boxed{\begin{aligned} & f_0\left(r - g_0\right)\left(y_0'g_0 - h_0\right) + \delta' \int_{-\infty}^{0} fg(g-r)d\eta = \\ & y_0'\left(\underline{\langle p_0\rangle} - p_\infty\right) - \delta' \int_{-\infty}^{0} \left(\underline{\langle p\rangle} - p_\infty\right) d\eta - y_0'T_{xx0} + \delta' \int_{-\infty}^{0} T_{xx}d\eta + T_{xy0} \end{aligned}}$$

(A.106)

Integrating the momentum equation $\eta = 0$ to $\eta = \infty$ we get

$$-\int_0^\infty A(fgg-1)'d\eta + \int_0^\infty (fgh)'d\eta = \int_0^\infty A\left(\underline{\langle p\rangle} - p_\infty\right)' d\eta - \int_0^\infty AT'_{xx}d\eta + \int_0^\infty (T_{xy})'d\eta \qquad \text{(A.107)}$$

$$\begin{aligned} & -\left[A(fgg-1)\right]\Big|_0^\infty & & \left[A\left(\langle \underline{p}\rangle - p_\infty\right)\right]\Big|_0^\infty - \int_0^\infty A'\left(\langle \underline{p}\rangle - p_\infty\right)d\eta \\ \therefore\ & +\int_0^\infty A'(fgg-1)d\eta & = & \qquad\qquad\qquad\qquad\qquad\qquad \text{(A.108)} \\ & +h_1 - f_0g_0h_0 & & -\left[AT_{xx}\right]\Big|_0^\infty + \int_0^\infty A'T_{xx}d\eta + \left[T_{xy}\right]\Big|_0^\infty \end{aligned}$$

(A.109)

Substituting the limits and noting that $A' = \delta'$, and substituting for h_1 we get the LHS of the above equation as

$$y_0'\left(f_0g_0g_0 - 1\right) + \delta'\int_0^\infty \left(fgg-1\right)d\eta - f_0g_0h_0 + \left(f_0h_0 - \delta'\int_0^\infty (fg-1)d\eta - y_0'(f_0g_0-1)\right) \qquad \text{(A.110)}$$

Which is

$$y_0'f_0g_0\left(g_0-1\right) + \delta'\int_0^\infty fg(g-1)d\eta + f_0h_0(1-g_0) \qquad \text{(A.111)}$$

And finally the LHS becomes

$$f_0\left(y_0'g_0 - h_0\right)\left(g_0-1\right) + \delta'\int_0^\infty fg(g-1)d\eta \qquad \text{(A.112)}$$

The RHS of the momentum equation evaluates to

$$-y_0'\left(\underline{\langle p_0\rangle} - p_\infty\right) - \delta'\int_0^\infty \left(\underline{\langle p_0\rangle} - p_\infty\right)d\eta + y_0'T_{xx0} + \delta'\int_0^\infty T_{xx}d\eta - T_{xy0} \qquad \text{(A.113)}$$

Thus

$$\boxed{\begin{aligned} & f_0\left(y_0' g_0 - h_0\right)\left(g_0 - 1\right) + \delta' \int\limits_0^\infty fg(g-1)d\eta \\ & = -y_0'\left(\underline{\langle p_0\rangle} - p_\infty\right) - \delta' \int\limits_0^\infty \left(\underline{\langle p\rangle} - p_\infty\right)d\eta + y_0' T_{xx0} + \delta' \int\limits_0^\infty T_{xx} d\eta - T_{xy0} \end{aligned}} \tag{A.114}$$

Subtracting A.106 from A.114 gives

$$\cancelto{0}{f_0(2g_0 - (r+1))} + \delta' \left(\int\limits_0^\infty fg(g-1)d\eta - \int\limits_{-\infty}^0 fg(g-r)d\eta \right) \tag{A.115}$$

$$= -2y_0'\left(\underline{\langle p_0\rangle} - p_\infty\right) - \delta' \left(\int\limits_0^\infty \left(\underline{\langle p\rangle} - p_\infty\right)d\eta - \int\limits_{-\infty}^0 \left(\underline{\langle p\rangle} - p_\infty\right)d\eta \right) \tag{A.116}$$

$$+2y_0' T_{xx0} + \delta' \left(\int\limits_0^\infty T_{xx} d\eta - \int\limits_{-\infty}^0 T_{xx} d\eta \right) - 2T_{xy0} \tag{A.117}$$

Thus rearranging the terms we get

$$\begin{aligned} & \delta' \left(\begin{array}{c} \int\limits_{-\infty}^0 fg(g-r)d\eta + \int\limits_0^\infty fg(1-g)d\eta \\ + \int\limits_{-\infty}^0 \left(\underline{\langle p\rangle} - p_\infty - T_{xx}\right)d\eta - \int\limits_0^\infty \left(\underline{\langle p\rangle} - p_\infty - T_{xx}\right)d\eta \end{array} \right) \\ & = 2y_0'\left(\underline{\langle p_0\rangle} - p_\infty - T_{xx0}\right) + 2T_{xy0} \end{aligned} \tag{A.118}$$

Neglecting the pressure terms, and y_0', we get

$$\boxed{\delta' \left(\int\limits_{-\infty}^0 fg(g-r)d\eta + \int\limits_0^\infty fg(1-g)d\eta \right) = 2T_{xy0}} \tag{A.119}$$

A.4.6 Observations

Observing **Eqn 5.6** we note that the growth rate is the ratio of T_{xy0} and the two integrals

$$I_1 \equiv \int_{-\infty}^{0} fg(g-r)d\eta \text{ and } I_2 \equiv \int_{0}^{\infty} fg(1-g)d\eta$$

Thus the growth rate at a given location is influenced by the local stress and the local profile of the flow. To illustrate this point, we plot the actual growth and the expected growth from integral analysis. This is shown in **Fig 5.2**, where it can be seen that the initial error arising out of non self similarity reduces to less than 10% once the flow becomes self similar. Which confirms the relation between the quantities.

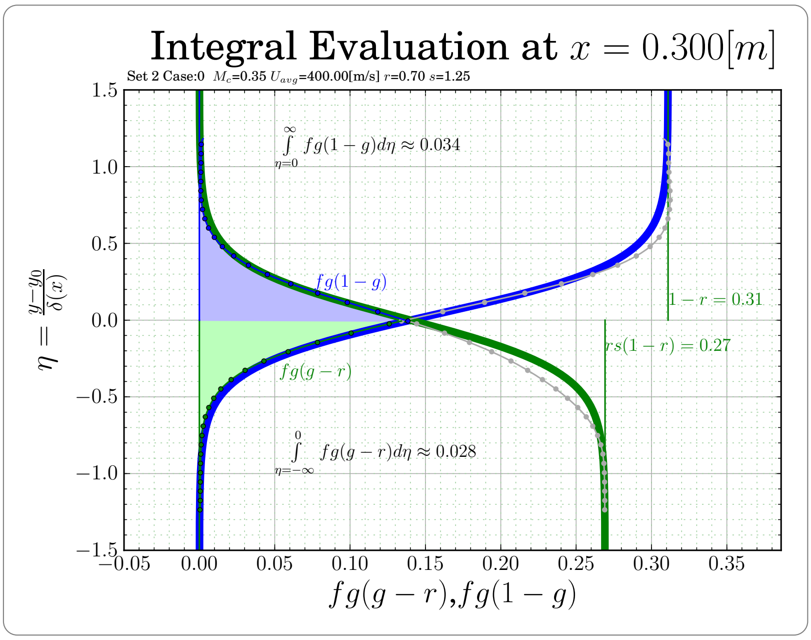

Figure A.3: Evaluation of the integrals
[*Dots represent the actual measurement, lines the approximate self similar profile* (tanh)*. The grey dots are unused.*]

Figure A.3 shows the evaluation of the integrals. This figure shows that the integrands are quite close to the self similar profiles, especially in the respective domains of integration. It is also quite apparent that the integration is a strong function of r and s.

Referred from Section 5.3.1 on Page 146

A.5 The entropy transport equation

We have the energy equation Eqn(**2.9**) on Page(**48**) as

$$\rho \frac{De}{Dt} = -p\nabla \cdot \boldsymbol{u} + \sigma : \nabla \boldsymbol{u} - \nabla \cdot \boldsymbol{q} \tag{A.120}$$

Also considering energy to be a function of entropy, density and species mole fraction, We get

$$de = Tds + \frac{p}{\rho^2} d\rho + \sum_j \left(\frac{\partial e}{\partial n_j}\right)_{\rho, s, n_{i\neq j}} dn_j \tag{A.121}$$

Where the summation is carried over all the species. The chemical potential of the j^{th} species is defined as

$$\mu_j \equiv \left(\frac{\partial e}{\partial n_j}\right)_{\rho, s, n_{i\neq j}} \tag{A.122}$$

Hence the entropy equation turns out to be

$$de = Tds + \frac{p}{\rho^2} d\rho + \sum_j \mu_j dn_j \tag{A.123}$$

Substituting this in the energy equation we get

$$\rho T \frac{Ds}{Dt} + \rho \sum_j \mu_j \frac{Dn_j}{Dt} + \frac{p}{\rho^2} \frac{D\rho}{Dt} = -p\nabla \cdot \boldsymbol{u} + \sigma : \nabla \boldsymbol{u} - \nabla \cdot \boldsymbol{q} \tag{A.124}$$

From the mass conservation equation Eqn(**2.1**) on Page(**48**)

$$\frac{D\rho}{Dt} = -\rho \nabla \cdot \boldsymbol{u} \tag{A.125}$$

Thus the entropy equation becomes,

$$\rho T \frac{Ds}{Dt} + \rho \sum_j \mu_j \frac{Dn_j}{Dt} = +\sigma_{ij} \frac{\partial u_j}{\partial x_i} + \frac{\partial}{\partial x_i} k \frac{\partial T}{\partial x_i} \tag{A.126}$$

Next we use the species diffusion equation

$$\rho \frac{Dn_j}{Dt} = \frac{1}{W_j} \nabla \cdot \boldsymbol{j_j} \tag{A.127}$$

Where $\boldsymbol{j}_i$ is the diffusive mass flux of species i Thus the entropy equation becomes.

$$\rho \frac{Ds}{Dt} = \underbrace{\sum_j \frac{\mu_j}{TW_j} \nabla \cdot \boldsymbol{j}_j}_{\text{Mass transfer}} \underbrace{- \frac{1}{T} \nabla \cdot \boldsymbol{q}}_{\text{Heat Transfer}} \underbrace{+ \frac{1}{T} \sigma : \nabla \boldsymbol{u}}_{\text{Shear}} \tag{A.128}$$

We shall now evaluate and separate the production terms as

A.5.1 Heat transfer

The conduction term is

$$\frac{1}{T} \nabla \cdot \boldsymbol{q}$$

This can be written as

$$\nabla \cdot \left(\frac{\boldsymbol{q}}{T} \right) + \frac{1}{T^2} \nabla T \cdot \boldsymbol{q} \tag{A.129}$$

Molecular heat flux happens due to conduction as well as mass transport. Hence

$$\frac{1}{T^2} \nabla T \cdot \boldsymbol{q} = \underbrace{- \frac{\lambda}{T^2} (\nabla \cdot T) (\nabla \cdot T)}_{\text{conduction}} + \underbrace{\sum_j \frac{\nabla T}{T^2} \cdot \frac{H_j}{W_j} \boldsymbol{j}_j}_{\text{species flux}} \tag{A.130}$$

Thus we have

$$\frac{1}{T} \nabla \cdot \boldsymbol{q} = \underbrace{\nabla \cdot \left(\frac{\boldsymbol{q}}{T} \right)}_{\text{reversible}} \underbrace{- \frac{\lambda}{T^2} (\nabla \cdot T) (\nabla \cdot T) + \sum_j \frac{\nabla T}{T^2} \cdot \frac{H_j}{W_j} \boldsymbol{j}_j}_{\text{irreversible}} \tag{A.131}$$

A.5.2 Mixing

The term due to mixing is

$$\sum_j \frac{\mu_j}{TW_j} \nabla \cdot \boldsymbol{j}_j$$

We can reduce this as

$$\frac{\mu_j}{T} \nabla \cdot \boldsymbol{j}_j = \nabla \cdot \left(\frac{\mu_j \boldsymbol{j}_j}{T} \right) - \nabla \left(\frac{\mu_j}{T} \right) \cdot \boldsymbol{j}_j \tag{A.132}$$

Noting that

$$\mu_j = H_j - TS_j^0 + RT \ln \left(\frac{p_j}{p_0} \right) + RT \ln X_j \tag{A.133}$$

Where p_j is the partial pressure of the j^{th} species The last term on the right hand side can be evaluated for the j^{th} species as

$$\nabla \left(\frac{\mu_j}{T} \right) = -\frac{H_j}{T^2} \nabla T + \frac{R}{Y_j} \nabla Y_j - RW \sum_i \frac{\nabla Y_i}{W_i} \tag{A.134}$$

Thus we have

$$\frac{\mu_j}{T} \nabla \cdot \boldsymbol{j}_j = \underbrace{\nabla \cdot \left(\frac{\mu_j \boldsymbol{j}_j}{T} \right)}_{\text{reversible}} \underbrace{+ \frac{H_j}{T^2} \nabla T \cdot \boldsymbol{j}_j - \frac{R}{Y_j} \nabla Y_j \cdot \boldsymbol{j}_j + RW \left(\sum_i \frac{\nabla Y_i}{W_i} \right) \cdot \boldsymbol{j}_j}_{\text{irreversible}} \tag{A.135}$$

Substituting the above relations into the entropy equation we get

$$\begin{aligned} \rho \frac{Ds}{Dt} &= \sum_j \frac{1}{W_j} \left(\nabla \cdot \left(\frac{\mu_j \boldsymbol{j}_j}{T} \right) + \frac{H_j}{T^2} \nabla T \cdot \boldsymbol{j}_j - \frac{R}{Y_j} \nabla Y_j \cdot \boldsymbol{j}_j + RW \left(\sum_i \frac{\nabla Y_i}{W_i} \right) \cdot \boldsymbol{j}_j \right) \\ &- \left(\nabla \cdot \left(\frac{\boldsymbol{q}}{T} \right) - \frac{\lambda}{T^2} \left(\nabla \cdot T \right) \left(\nabla \cdot T \right) + \sum_j \frac{\nabla T}{T^2} \cdot \frac{H_j}{W_j} \boldsymbol{j}_j \right) \\ &+ \frac{1}{T} \sigma : \nabla \boldsymbol{u} \end{aligned} \tag{A.136}$$

The above can be simplified and segregated as

$$
\begin{aligned}
\rho \frac{Ds}{Dt} &= -\nabla \cdot \left(\frac{\boldsymbol{q}}{T}\right) + \frac{\lambda}{T^2} \left(\nabla \cdot T\right) \left(\nabla \cdot T\right) \\
&+ \sum_j \nabla \cdot \left(\frac{\mu_j}{W_j T}\right) \boldsymbol{j}_j - \sum_j \frac{R}{W_j Y_j} \nabla Y_j \cdot \boldsymbol{j}_j + RW \sum_i \frac{\nabla Y_i}{W_i} \cdot \sum_j \frac{\boldsymbol{j}_j}{W_j} \\
&+ \frac{1}{T} \sigma : \nabla \boldsymbol{u}
\end{aligned}
$$

(A.137)

Referred from Section 6.2 on Page 168

Bibliography

[**Abramowitz, 1963**] G. Abramowitz. The theory of turbulent jets, 1963.

[**Andrews, 1994**] E. Andrews. Nasa's hypersonic project research - a review. *NASA-TM-107759*, October 1994.

[**Bardina et al., 1980**] J. Bardina, J. H. Ferziger, and W. C. Reynolds. Improved subgrid scale models for large eddy simulation. *AIAA, Fluid & Plasma Dynamics Conference*, 1980.

[**Bardina et al., 1997**] J. Bardina, P. Huang, and T. Coakley. Turbulence modeling validation. *AIAA paper*, 2121:1997, 1997.

[**Barre et al., 1994**] S. Barre, C. Quine, and J. Dussauge. Compressibility effects on the structure of supersonic mixing layers: experimental results. *Journal of Fluid Mechanics*, 259:47–78, 1994.

[**Billig, 1993**] F. Billig. Scram: a supersonic combustion ramjet missile. In *at 29th AIAA/SAE/ASME/ASEE Joint Propulsion Conference, AIAA*, pages 93–2329, 1993.

[**Birch et al., 1972**] S. Birch, D. Rudy, and D. Bunshell. Nasa langley free turbulent shear flows conference proceedings, vol. i , nasa sp-321. 1972.

[**Blumen, 1970**] W. Blumen. Shear layer instability of an inviscid compressible fluid. *Journal of Fluid Mechanics*, 40(4):769–781, 1970.

[**Blumen et al., 1975**] W. Blumen, P. Drazin, and D. Billings. Shear layer instability of an inviscid compressible fluid. part 2. *Journal of Fluid Mechanics*, 71(2): 305–316, 1975.

[**Bogdanoff, 1983**] D. Bogdanoff. Compressibility effects in turbulent shear layers. *AIAA journal*, 21:926, 1983.

[**Bradshaw, 1977**] P. Bradshaw. Compressible turbulent shear layers. *Annual Review of Fluid Mechanics*, 9(1):33–52, 1977.

[**Brown and Roshko, 1974**] G. Brown and A. Roshko. On density effects and large structure in turbulent mixing layers. *Journal of Fluid Mechanics*, 64(4): 775–816, 1974.

[**Canuto, 1997**] Canuto. Compressible turbulence. *The Astrophysical Journal*, (482): 827– 851, 1997.

[**Chinzei et al., 1986**] N. Chinzei, G. Masuya, T. Komuro, A. Murakami, and K. Kudou. Spreading of two-stream supersonic turbulent mixing layers. *Physics of Fluids*, 29:1345, 1986.

[**Clemens and Mungal, 1995**] N. Clemens and M. Mungal. Large-scale structure and entrainment in the supersonic mixing layer. *Journal of Fluid Mechanics*, 284 (1):171–216, 1995.

[**Clemens and Mungal, 1990**] N. T. Clemens and M. G. Mungal. Two and three dimensional effects in the supersonic mixing layer. *AIAA*, 1990.

[**Curran, 2001**] E. Curran. Scramjet engines: the first forty years. *Journal of Propulsion and Power*, 17(6):1138–1148, 2001.

[**Curran et al., 1996**] E. Curran, W. Heiser, and D. Pratt. Fluid phenomena in scramjet combustion systems. *Annual review of fluid mechanics*, 28(1):323–360, 1996.

[**Demetriades and Brower, 1990**] A. Demetriades and T. Brower. Experiments on the free shear layer between two supersonic streams. *AIAA*, 1990.

[**Dimotakis, 1984**] P. Dimotakis. Entrainment into a fully developed, two dimensional shear layer. *AIAA*, 1984.

[**Dimotakis, 1986**] P. Dimotakis. Two-dimensional shear-layer entrainment. *AIAA journal*, 24(11):1791–1796, 1986.

[**Drazin and Davey, 1977**] P. Drazin and A. Davey. Shear layer instability of an inviscid compressible fluid. part 3. *Journal of Fluid Mechanics*, 82(2):255–260, 1977.

[**Dubief and Delcayre, 2000**] Y. Dubief and F. Delcayre. On coherent-vortex identification in turbulence. *Journal of Turbulence*, page N11, 2000. doi: 10.1088/1468-5248/1/1/011.

[**Edwards, 1974**] C. L. W. Edwards. A forebody design technique for highly integrated bottom-mounted scramjets with application to a hypersonic research airplane. *NASA TM X-71971*, 1974.

[**Elliott and Samimy, 1990**] G. Elliott and M. Samimy. Compressibility effects in free shear layers. *Physics of Fluids A: Fluid Dynamics*, 2:1231, 1990.

[**Erdos et al., 1992**] J. Erdos, J. Tamango, R. Bakos, and R. Trucco. Experiments on shear layer mixing at hypervelocity conditions. *30. American Institute of Astronautics and Aeronautics (AIAA) aerospace sciences meeting and exhibit*, 6(9), 1992.

[**Erlebacher et al., 1992**] G. Erlebacher, M. Hussaini, C. Speziale, and T. Zang. Toward the large-eddy simulation of compressible turbulent flows. *Journal of Fluid Mechanics*, 238(1):155–185, 1992.

[**Favre, 1964**] A. Favre. The mechanics of turbulence. *Gordon and Breach, New York*, 1964.

[**Favre, 1971**] A. Favre. Équations statistiques aux fluctuations turbulentes dans les écoulements compressibles: cas des vitesses et des températures. *Comptes Rendus des Séances de lAcadémie des sciences de Paris*, 273:1087–93, 1971.

[**Ferri, 1959**] A. Ferri. Trends in experimental hypersonic research. Technical report, 1959.

[**Ferri and Fox, 1969**] A. Ferri and H. Fox. Analysis of fluid dynamics of supersonic combustion process controlled by mixing. In *Symposium (International) on Combustion*, volume 12, pages 1105–1113. Elsevier, 1969.

[**Ferri et al., 1962**] A. Ferri, P. Libby, and V. Zakkay. Theoretical and experimental investigation of supersonic combustion. Technical report, 1962.

[**Fjortoft, 1950**] R. Fjortoft. Application of integral theorems in deriving criteria of stability for laminar flows and for the baroclinic circular vortex. *Geofys. Publ*, 17(6):1–52, 1950.

[**Germano et al., 1991**] M. Germano, U. Piomelli, P. Moin, and W. H. Cabot. A dynamic subgrid-scale eddy viscosity model. *Physics of Fluids*, 1991.

[**Germano et al., 1992**] M. Germano, U. Piomelli, P. Moin, and W. Cabot. Turbulence: the filtering approach. *J. Fluid Mech*, 238:325–336, 1992.

[**Goebel and Dutton, 1990a**] S. G. Goebel and J. C. Dutton. Experimental study of compressible turbulent mixing layers. *AIAA Journal*, 8:538, 1990a.

[**Goebel and Dutton, 1990b**] S. G. Goebel and J. C. Dutton. Velocity measurements of compressible, turbulent mixing layers. *AIAA*, 709:1990, 1990b.

[**Harsha et al., 2005**] P. Harsha, L. Keel, A. Castrogiovanni, and M. Sherrill. X-43a vehicle design and manufacture. *AIAA/CIRA 13th International Space Planes and Hypersonics Systems and Technologies, Capua, Italy*, 2005.

[**Heppenheimer, 2007**] T. Heppenheimer. *Facing the Heat Barrier: A History of Hypersonics*. National Aeronautics and Space Administration, NASA History Division, Office of External Relations, 2007.

[**Herrmann Schlicting, 2000**] K. G. Herrmann Schlicting. *Boundary Layer Theory*. Springer, 2000.

[**Ikawa, 1973**] H. Ikawa. *Turbulent mixing layer experiment in supersonic flow*. PhD thesis, 1973.

[**Ikawa and Kubota, 1975**] H. Ikawa and T. Kubota. Investigation of supersonic turbulent mixing layer with zero pressure gradient. *AIAA Journal*, 13(5), 1975.

[**Issa, 1986**] R. Issa. Solution of the implicitly discretised fluid flow equations by operator-splitting. *Journal of computational physics*, 62(1):40–65, 1986.

[**J. L. Hall, 1991**] H. R. J. L. Hall, P. E. Dimotakis. Experiments in non-reacting compressible shear layers. *AIAA*, 1991.

[**Jasak et al., 2007**] H. Jasak, A. Jemcov, and Z. Tukovic. Openfoam: A c++ library for complex physics simulations. In *International Workshop on Coupled Methods in Numerical Dynamics, IUC, Dubrovnik, Croatia*, 2007.

[**Jimenez and Moser, 2000**] J. Jimenez and R. Moser. Large-eddy simulations: Where are we and what can we expect? *AIAA journal*, 38(4):605–612, 2000.

[**John and Griffin, 1973**] R. H. John and Y. A. Griffin. Design considerations for the airframe integrated scramjet. *NASA TM X-2895*, 1973.

[**Kim and Menon, 1999**] W. Kim and S. Menon. An unsteady incompressible navier–stokes solver for large eddy simulation of turbulent flows. *International journal for numerical methods in fluids*, 31(6):983–1017, 1999.

[**Konrad, 1977**] J. Konrad. An experimental investigation of mixing in two-dimensional turbulent shear flows with applications to diffusion-limited chemical reactions. 1977.

[**Launder et al., 1972**] B. E. Launder, A. Morse, W. Rodi, and D. B. Spalding. *The Prediction of Free Shear Flows: A Comparison of the Performance of Six Turbulence Models*. National Aeronautics and Space Administration, 321 edition, 1972.

[**Leonard, 1974**] A. Leonard. Energy cascade in large-eddy simulations of turbulent fluid flows. *Adv. Geophys*, 18(3):237, 1974.

[**Lilly, 1992**] D. Lilly. A proposed modification of the germano subgrid-scale closure method. *Physics of Fluids A: Fluid Dynamics*, 4:633, 1992.

[**Lucor et al., 2007**] D. Lucor, J. Meyers, and P. Sagaut. Sensitivity analysis of large-eddy simulations to subgrid-scale-model parametric uncertainty using polynomial chaos. *Journal of Fluid Mechanics*, 585:255–280, 2007.

[**Lumley, 1986**] J. Lumley. Evolution of a non-self-preserving thermal mixing layer. *Physics of Fluids*, 29(12):3976–3981, 1986.

[**MacBride, 1963**] B. MacBride. *Reportnr. NASA SP 3001.* Office of Technical Services, 1963.

[**Maydew and Reed, 1963**] R. Maydew and J. Reed. Turbulent mixing of axisymmetric compressible jets (in the half jet region) with quiescnet air. Technical report, 1963.

[**McBride et al., 1993**] B. McBride, S. Gordon, and M. Reno. Coefficients for calculating thermodynamic and transport properties of individual species', nasa report tm-4513. *NASA (October 1993)*, 1993.

[**Messersmith et al., 1988**] N. Messersmith, S. Goebel, W. Frantz, E. Krammer, J. Renie, J. Dutton, and H. Krier. Experimental and analytical investigations of supersonic mixing layers. *AIAA*, 1988.

[**Miller et al., 1993**] M. Miller, T. Island, B. Yip, C. Bowman, M. Mungal, and R. Hanson. An experimental study of the structure of a compressible, reacting mixing layer. *AIAA, Aerospace Sciences Meeting*, 1993.

[**Miller et al., 1994**] M. Miller, T. Island, J. Seitzman, C. Bowman, M. Mungal, and R. Hanson. An experimental investigation of supersonic reacting mixing layers. *AIAA, Aerospace Sciences Meeting and Exhibit, 32 nd, Reno, NV*, 1994.

[**Oh and Loth, 1994**] C. Oh and E. Loth. A numerical investigation of supersonic turbulent shear layers- compressibility effects. In *AIAA, Fluid Dynamics Conference, 25 th, Colorado Springs, CO*, 1994.

[**Okong'o and Bellan, 2000**] N. Okong'o and J. Bellan. Entropy production of emerging turbulent scales in a temporal supercritical n-heptane/nitrogen three-dimensional mixing layer. *Proceedings of the Combustion Institute*, 28(1): 497–504, 2000.

[**Pantano and Sarkar, 2002**] C. Pantano and S. Sarkar. A study of compressibility effects in the high-speed turbulent shear layer using direct simulation. *J. Fluid Mech*, 451:329–371, 2002.

[**Papamoschou, 1990**] D. Papamoschou. Communication paths in the compressible shear layer. *AIAA*, 1990.

[**Papamoschou, 1993**] D. Papamoschou. Total-pressure loss in supersonic parallel mixing. *AIAA*, 1993.

[**Papamoschou and Roshko, 1988**] D. Papamoschou and A. Roshko. The compressible turbulent shear layer: an experimental study. *Journal of Fluid Mechanics Digital Archive*, 197(-1):453–477, 1988. doi: 10.1017/S0022112088003325.

[**Patankar, 1980**] S. Patankar. *Numerical heat transfer and fluid flow*. Hemisphere Pub, 1980.

[**Paull et al., 1995**] A. Paull, R. Stalker, and D. Mee. Experiments on supersonic combustion ramjet propulsion in a shock tunnel. *Journal of Fluid Mechanics*, 296:6, 1995.

[**Piomelli, 1997**] U. Piomelli. Large-eddy simulation: Present state and future perspectives. *AIAA*, 1997.

[**Pope, 2000**] S. B. Pope. *Turbulent Flows*. Cambridge University Press, 2000.

[**Rayleigh, 1879**] L. Rayleigh. On the stability, or instability, of certain fluid motions. *Proceedings of the London Mathematical Society*, 1(1):57, 1879.

[**Sagaut, 2006**] P. Sagaut. *Large Eddy Simulation for Incompressible Flows: An Introduction*. Springer, 2006.

[**Samimy and Elliott, 1990**] M. Samimy and G. Elliott. Effects of compressibility on the characteristics of free shear layers. *AIAA journal*, 28(3):439–445, 1990.

[**Sandham and Reynolds, 1989**] N. D. Sandham and W. C. Reynolds. A numerical investigation of the compressible mixing layer. *NASA STI/Recon Technical Report N*, 90, Sept. 1989.

[**Sankaran and Menon, 2005**] V. Sankaran and S. Menon. Les of scalar mixing in supersonic mixing layers. *Proceedings of the Combustion Institute*, 30(2): 2835 – 2842, 2005. doi: 10.1016/j.proci.2004.08.027.

[**Sarkar, 1995**] S. Sarkar. The stabilizing effect of compressibility in turbulent shear flow. *Journal of Fluid Mechanics*, 282:163–186, 1995.

[**Sarkar et al., 1991a**] S. Sarkar, G. Erlebacher, and M. Hussaini. Direct simulation of compressible turbulence in a shear flow. *Theoretical and Computational Fluid Dynamics*, 2(5):291–305, 1991a.

[**Sarkar et al., 1991b**] S. Sarkar, G. Erlebacher, M. Hussaini, and H. Kreiss. The analysis and modelling of dilatational terms in compressible turbulence. *Journal of Fluid Mechanics*, 227(1):473–493, 1991b.

[**Schumann, 1975**] U. Schumann. Subgrid scale model for finite difference simulations of turbulent flows in plane channels and annuli. *Journal of computational physics*, 18(4):376–404, 1975.

[**Sirieix and Solignac, 1966**] M. Sirieix and J. Solignac. Contribution a letude experimentale de la couche de melange turbulent isobare dun ecoulement supersonique. *Separated Flows, AGARD CP4*, 1966.

[**Slessor, 1998**] M. Slessor. Aspects of turbulent-shear-layer dynamics and mixing. Technical report, 1998.

[**Slessor et al., 2000**] M. D. Slessor, M. Zhuang, and Dimotakis. Turbulent shear-layer mixing: growth-rate compressibility scaling. *J. Fluid Mech*, 2000.

[**Smagorinsky, 1963**] J. Smagorinsky. General circulation experiments with the primitive equations. *Monthly weather review*, 91(3):99–164, 1963.

[**Sosounov, 1993**] V. Sosounov. *Research and Development of Ram/Scramjets and Turboramjets in Russia*. AGARD lecture series. AGARD, 1993. ISBN 978-92-8350732-1.

[**Sutherland, 1893**] W. Sutherland. Lii. the viscosity of gases and molecular force. *The London, Edinburgh, and Dublin Philosophical Magazine and Journal of Science*, 36(223):507–531, 1893.

[**Tennekes and Lumley, 1972**] H. Tennekes and J. Lumley. *A first course in turbulence*. MIT press, 1972.

[**Vreman, 1995**] A. Vreman. *"Direct and Large-Eddy Simulation of the Compressible Turbulent Mixing Layer," PhD thesis*. 1995.

[**Vreman et al., 1996**] A. Vreman, N. Sandham, and K. Luo. Compressible mixing layer growth rate and turbulence characteristics. *Journal of Fluid Mechanics*, 320(1):235–258, 1996.

[**Vreman et al., 1995**] B. Vreman, B. Geurts, and H. Kuerten. Subgrid-modelling in les of compressible flow. *Applied scientific research*, 54(3):191–203, 1995.

[**Wilcox, 1998**] D. C. Wilcox. *Turbulence modeling for CFD*, volume 2. DCW industries La Canada, 1998.

[**Yoshizawa and Horiuti, 1985**] A. Yoshizawa and K. Horiuti. A statistically-derived subgrid-scale kinetic energy model for the large- eddy simulation of turbulent flows. *Physical Society of Japan, Journal*, 54:2834–2839, 1985.

[**Zeman, 1990**] O. Zeman. Dilatation dissipation: The concept and application in modeling compressible mixing layers. *Physics of Fluids A: Fluid Dynamics*, 2:178, 1990.

[**Zhuang and Dimotakis, 1995**] M. Zhuang and P. Dimotakis. Instability of wake-dominated compressible mixing layers. *Physics of Fluids*, 7(10):2489–2495, 1995.